INSTITUTO DE PESQUISAS ENERGÉTICAS E NUCLEARES
Autarquia Associada à Universidade de São Paulo

Development of functional layers for direct ethanol solid oxide fuel cells

MARINA MACHADO LIVINALLI

Tese apresentada como parte dos requisitos para obtenção do Grau de Doutor em Ciências na Área de Tecnologia Nuclear - Materiais

Orientador:
Prof. Dr. Fabio Coral Fonseca

São Paulo
2022

INSTITUTO DE PESQUISAS ENERGÉTICAS E NUCLEARES
Autarquia Associada à Universidade de São Paulo

Development of functional layers for direct ethanol solid oxide fuel cells

Versão Corrigida

MARINA MACHADO LIVINALLI

Tese apresentada como parte dos requisitos para obtenção do Grau de Doutor em Ciências na Área de Tecnologia Nuclear - Materiais

Orientador:
Prof. Dr. Fabio Coral Fonseca

São Paulo
2022

Fonte de Financiamento: FAPESP 2016/07156-4, 2019/04499-6, 2019/21159-4

Como citar:

MACHADO LIVINALLI, M. ***Development of functional layers for direct ethanol solid oxide fuel cells***. 2022. 195 f. Tese (Doutorado em Tecnologia Nuclear), Instituto de Pesquisas Energéticas e Nucleares, IPEN-CNEN, São Paulo. Disponível em: ‹http://repositorio.ipen.br/› (data de consulta no formato: dd/mm/aaaa)

Ficha catalográfica elaborada pelo Sistema de geração automática da Biblioteca IPEN, com os dados fornecidos pelo(a) autor(a).

Machado Livinalli, Marina
Development of functional layers for direct ethanol solid oxide fuel cells / Marina Machado Livinalli; orientador Fabio Coral Fonseca. -- São Paulo, 2022.
195 f.

Tese (Doutorado) - Programa de Pós-Graduação em Tecnologia Nuclear (Materiais) -- Instituto de Pesquisas Energéticas e Nucleares, São Paulo, 2022.

1. solid oxide fuel cell (SOFC). 2. cerium oxide. 3. shape-controlled synthesis. 4. sintering aid. 5. ethanol steam reform reaction. I. Coral Fonseca, Fabio, orient. II. Título.

APPROVAL SHEET

Author: MARINA MACHADO LIVINALLI

Title: *Development of functional layers for direct ethanol solid oxide fuel cells*

Thesis presented as part of the requirements for obtaining the degree of Doctor of Science in the Field of Nuclear Technology - Materials

Date: 09/06/2022

Thesis Committee

Prof. Dr: Marc Torrell Faro

Institution: Institut de Recerca en Energia de Catalunya

Judgement: Approved

Prof. Dra: Lisiane Veiga Mattos

Institution: Universidade Federal Fluminense

Judgement: Approved

Prof. Dr: Everton Bonturim

Institution: Universidade Presbiteriana Mackenzie

Judgement: Approved

To my bone marrow donor.

Acknowledgements

Primeiramente, gostaria de agradecer ao meu orientador Prof. Dr. Fabio Coral Fonseca pela confiança, pelas oportunidades enriquecedoras e pelas importantes lições. Foram anos conturbados e você sempre me apoiou.

Gostaria de agradecer à FAPESP que financiou meu trabalho e me deu a oportunidade de comparecer em congressos e realizar um ano de estágio de pesquisa no exterior.

I would also like to thank Dr. Marc Torrell, Dr. Albert Tarrancón and Dr. Federico Baiutti for receiving me at IREC in Barcelona, for the teachings, valuable contributions and above all for the enthusiasm that inspired me. Thanks to my friends and colleagues at the nanoionics group at IREC, for the scientific support and friendship: Juande, José, Carol, Natalia, Marc N., Lucille, Marco, Simone, Ariana, e minha maior cúmplice Maritta.

Meus agradecimentos também vão aos professores e funcionários do IPEN que colaboraram para a realização deste trabalho, pelo auxílio, ensinamentos e análises realizadas. Obrigada Dra. Dolores, Dra. Eliana, Dr. Muccillo, Valter, Francisco, Rene, Coutinho, Glauson, Sabrina e Shirley.

Aos amigos que fiz no IPEN, por todos os momentos de descontração dividindo almoços, cafezinhos, risadas e desabafos. Agradeço especialmente a Natália, Joana, Vinicius, Fernando, Amon, Daniel, Miguel e Marcela. Meus maiores agradecimentos a minha parceira científica desde o princípio Leticia e a Lays que veio um pouco depois, e tanto me ajudaram. Ao nosso maravilhoso grupo de laboratório, e meus queridos amigos Robson, Tamara, Vivian, Vanessa, Jessica, Fernando e ao “pessoal da Beth”, Andrey, Bianca, Ana, Juliano e Eli e Mari por serem, todos vocês, minha família em SP.

A toda equipe do Einstein e ao Redome que cuidaram tão bem de mim e fizeram este doutorado ser possível. A Tia Isa e companhia que me acolheram em São Paulo, muito obrigada. A minha família: minha vovó Tela, meus tios e primos, não tenho palavras para agradecer vocês, só amor.

Thank you to all my dear friends from around the globe, I am, who I am because of you.

Agradeço ao Vinicius, meu grande amor, por ser meu maior parceiro e motivador. Aos meus queridos Juleide e Miguel, obrigada por todo carinho e dedicação. E a minha familinha, papai, mamãe, Tito, Vinicius, Val e agora Miguel e Uririm também. Vocês são a minha base, o meu lugar de amor e segurança. Obrigada por estarem presentes e me incentivarem a ser sempre melhor.

Resumo

Livinalli, Marina M. Desenvolvimento de camadas funcionais para células a combustível de óxidos sólidos a etanol direto. 2022. 195 p. Tese (Doutorado em Tecnologia). Instituto de Pesquisas Energéticas e Nucleares – IPEN-CNEN/SP.

Esta tese explora a síntese e aplicação do óxido de cério como material em células a combustível de óxido sólido (SOFC) com propriedades adequadas para diminuir a temperatura de processamento e melhorar a eficácia das reações catalíticas e eletroquímicas. Três abordagens foram investigadas: i) uma rota de precipitação para a síntese de céria dopada com gadolínio (CGO) com um auxiliar de sinterização, ii) controle morfológico de nanocéria por uma rota hidrotermal e aplicação dos materiais como eletrólito e como camada catalítica para operação de uma SOFC com etanol, iii) aplicação de uma camada de barreira de céria dopada e uma camada nanoestruturada por método de deposição física. A rota de precipitação se mostrou eficiente para a síntese de céria nanométrica e a adição de Fe_2O_3 potencializou o mecanismo de sinterização. Inferiu-se que o Fe segrega nas interfaces do contorno de grão do CGO, diminuindo a energia de contorno de grão e favorecendo a eliminação da interface sólido-gás. No entanto, os precipitados ricos em Fe favoreceram a contribuição eletrônica do CGO, assim, seu uso como auxiliar de sinterização em eletrólitos à base de céria deve ser controlado para evitar alterações no transporte de carga do eletrólito. A rota hidrotermal foi investigada como uma nova abordagem para controlar o mecanismo de densificação do material. Através desta rota simples, nanobastões e nanocubos de CGO foram sintetizados por controle de temperatura. Os nanobastões de CGO exibiram alta energia de superfície, promovendo difusão de massa em temperaturas mais baixas, levando a uma rápida densificação e, portanto, foram aplicados com sucesso como material eletrolítico em uma SOFC totalmente sinterizada a 1150 °C. Por outro lado, os nanocubos de CGO exibiram uma atividade de sinterização muito baixa, atribuída à maior estabilidade superficial dos nanocubos. Os nanobastões e os nanocubos de CGO sintetizados foram avaliados como suportes para catalisadores à base de Ni na reação de reforma a vapor do etanol em temperatura intermediária. O catalisador de Ni suportado nos nanobastões de CGO apresentou a maior atividade após um tratamento térmico similar ao do processamento de uma SOFC, portanto, foi empregado como camada catalítica em uma SOFC operando diretamente com etanol. Foi demonstrado que a célula a combustível permaneceu estável em condições de operação com fluxo contínuo de etanol anidro. Camadas funcionais de céria dopadas nanoestruturadas depositadas por laser pulsado (PLD) foram aplicadas como camada de barreira e como camada funcional de cátodo. A deposição de tais camadas funcionais melhorou o desempenho da célula, tendo um papel importante tanto no aumento da durabilidade, quanto no aumento dos sítios de reação de redução de oxigênio. Em resumo, esta tese contribui para o desenvolvimento de nanomateriais com propriedades adequadas para aplicação em camadas funcionais de uma SOFC de alto desempenho.

Palavras-chave: célula a combustível de óxido sólido (SOFC); óxido de cério; síntese com controle morfológico; auxiliar de sinterização; reação de reforma a vapor.

Abstract

Livinalli, Marina M. Development of functional layers for direct ethanol solid oxide fuel cells. 2022. 195 p. Thesis (Ph.D. in Nuclear Technology). Instituto de Pesquisas Energéticas e Nucleares – IPEN-CNEN/SP. São Paulo.

This thesis explores the synthesis and application of cerium oxide as a material in solid oxide fuel cells (SOFC) with tailored properties to decrease the processing temperature and improve the effectiveness of the catalytic and electrochemical reactions. Three approaches were investigated: i) a precipitation route for the synthesis of gadolinium doped ceria (CGO) with a sintering aid, ii) shape control of nanoceria by a hydrothermal route and application of the materials as an SOFC electrolyte and as catalytic layer for direct operation of an SOFC with ethanol, and iii) the application of a doped ceria barrier layer and nanostructured layer by a physical deposition method. The precipitation route showed to be efficient for the synthesis of nanometric ceria and the addition of Fe_2O_3 enhanced the sintering mechanism. It was inferred that Fe mostly segregates at the grain boundary interfaces of CGO, therefore, decreasing the grain boundary energy and favouring the elimination of the solid-gas interface. Nonetheless, Fe-rich phase precipitates were found to enhance the electronic contribution of CGO. Thus, the use of transition metal oxide as a sintering aid in ceria-based electrolytes should be controlled to avoid changes in charge transport in the electrolyte. The hydrothermal route was investigated as a novel approach to controlling the densification mechanism in the material. Through this simple route, CGO nanorods and nanocubes were synthesized by controlling the temperature. The CGO nanorods exhibited high surface energy, promoting mass diffusion at lower temperatures leading to a rapid densification and were therefore successfully applied as an electrolyte material in an electrolyte supported SOFC fully sintered at 1150 °C operating at intermediate temperature. On the other hand, the CGO nanocubes had a very low sintering activity, attributed to their higher surface stability. The CGO nanorods and the CGO nanocubes were further evaluated to be applied as support materials for Ni-based catalysts in the steam reforming reaction of ethanol at intermediate temperature. The Ni catalyst on the CGO nanorod support displayed the highest activity after a heat treatment analogous to that for processing SOFCs. Hence, it was employed as a catalytic layer in an SOFC operating directly with ethanol. It was demonstrated that the fuel cell remained stable under operating condition with a continuous flow of anhydrous ethanol. Nanostructured doped ceria functional layers deposited by pulsed laser deposition (PLD) were applied as a barrier layer and as a cathode interlayer. The deposition of such functional layers was shown to enhance the cell's performance, having a role in both the durability, and increasing the oxygen reduction reaction sites. In summary, this thesis contributes towards the development of nanomaterials with tailored properties for application as functional layers of high performance SOFC.

Keywords: solid oxide fuel cell (SOFC); cerium oxide; shape-controlled synthesis; sintering aid; ethanol steam reforming reaction.

List of Figures

Fig. 1.1 Schematic representation of an SOFC. Adapted from [17]. 3

Fig. 1.2 Illustration showing a single fuel cell, a stack and a module with the estimated power output for a state-of-the-art SOFC providing a power density of 1 $W \cdot cm^{-2}$. Adapted from [18]. 4

Fig. 1.3 Ideal and actual current-voltage (I-V) characteristics of a fuel cell. Adapted from [20]. 7

Fig. 1.4 Arrhenius plot of the electrical conductivities of selected oxide electrolytes [22]. 9

Fig. 1.5 Unit cell of CeO_2 and structural changes in the unit cell after doping with gadolinium. Obtained through Vesta software [26]. Adapted from [27]. 10

Fig. 1.6 Diagram showing the ORR occurring in the TPB between the different phases in a cathode. Adapted from [43]. 12

Fig. 1.7 Perovskite unit cell with A and B cations and oxygen anions forming an octahedron. Obtained through Vesta software [26]. 13

Fig. 1.8 Schematic representation of SOFC cathodes (a) porous single-phase electronically conductive oxide, such as LSM and (b) porous single-phase mixed conductor, such as LSCF. Adapted from [43]. 14

Fig. 1.9 Schematic representation of an SOFC with doped ceria barrier layer between YSZ electrolyte and LSCF cathode. Adapted from [58]. 15

Fig. 1.10 Schematic representation of an SOFC with catalytic layer for direct internal reforming reaction of ethanol. Adapted from [81]. 20

Fig. 1.11 Diagram describing the nucleation process by the classical theory, showing the critical radius and critical free energy [99]. 24

Fig. 1.12 Schematic representation of (a) nucleation and diffusion growth, (b) and (c) particle growth by Ostwald ripening and oriented attachment mechanisms, respectively. Adapted from [27,106]. 26

Fig. 1.13 Illustration of a PLD system. Adapted from [118]. 30

Fig. 1.14 Schematic representation of the tape-casting technique. 32

Fig. 2.1 TGA, with mass and the derivative of mass, of the as-synthesized powder of CGO, 1Fe-CGO and 5Fe-CGO. 41

Fig. 2.2 XRD patterns of CGO and Fe-doped CGO. 42

Fig. 2.3 STEM EELS of CGO 50

Fig. 2.4 STEM EELS of 5 mol% Fe-doped CGO. 50

Fig. 2.5 Shrinkage curves profiles (top) and the differential shrinkage with respect to time (bottom) for CGO, 1Fe-CGO, and 5Fe-CGO samples. 52

Fig. 2.6 SEM images with inset of great magnification of polished and thermally etched cross-sections of (a) CCO, (b) 1Fe-CGO and (c) 5Fe-CGO, all sintered at 1200 °C. 53

Fig. 2.7 SEM images of polished and thermally etched cross-sections of (a) CCO, (b) 1Fe-CGO and (c) 5Fe-CGO, all sintered at 1400 °C. 55

Fig. 2.8 SEM images of polished and thermally etched cross-sections and corresponding EDS elemental mapping of (a) 1Fe-CCO and (b) 5Fe-CGO, both sintered at 1400 °C. 55

Fig. 2.9 EIS diagrams of CGO and Fe-doped CGO samples measured under synthetic air flow (a) at 300 °C, (b) at 600 °C and (c) of Fe-doped CGO samples measured under 4% H_2/Ar at 600 °C. 58

Fig. 2.10 Arrhenius conductivity plots of CGO and Fe-doped CGO samples sintered at 1400 °C measured under synthetic air flow and of under 4% H_2/Ar. ...60

Fig. 3.1 (a) Image of the cell with gold paste and wire current collection and (b) image of the cell with deposition of catalytic layer. 73

Fig. 3.2 Images of the set-up of the cell with (a) quartz fibre and gold mesh anode side (b) cell with Thermiculite® cathode side (c) alumina felt sealing the cell. 74

Fig. 3.3 TGA, with mass and the derivative of mass, of the of as-prepared CGO-NR and CGO-NC 75

Fig. 3.4 Secondary-electrons SEM images of the as-prepared powders of (a) CGO-NR and (b) CGO-NC. 76

Fig. 3.5 XRD patterns of CGO-NR and CGO-NC. 77

Fig. 3.6 TEM images of CGO-NR (a) and CGO-NC as-prepared (c) and after heat treatment at 500 °C (e). The corresponding HRTEM images of the highlighted regions of CGO-NR (b) and CGO-NC and as-prepared (d) and after heat treatment at 500 °C (f) with insets of FFT.....79

Fig. 3.7 Densification curves (a) and rate of densification curves (b) of CGO-NR and CGO-NC.....81

Fig. 3.8 SEM images of fractured surfaces pellets after dilatometry analysis (1400 °C) of (a) CGO-NR and (b) CGO-NC. 82

Fig. 3.9 XRD patterns of (a) CGO-NR and (b) CGO-NC at 850 °C, 1050 °C and 1400 °C. The inset tables list the calculated average crystallite sizes.....83

Fig. 3.10 Secondary-electrons SEM images of CGO-NRs (a), (b), (c) and CGO-NCs (d), (e) and (f) heated to 850 °C, 1050 °C and 1400 °C. 85

Fig. 3.11 EIS diagrams measured under synthetic air at (a) 250 °C and (b) 500 °C of CGO-NR sintered at 1200 °C and commercial CGO sintered at 1500 °C. 87

Fig. 3.12 Arrhenius conductivity plots of CGO-NR sintered at 1200 °C and commercial CGO sintered at 1500 °C. 88

Fig. 3.13 Secondary electron SEM images of a fracture of the cell sintered at 1150 °C showing: (a) a general view of the full cell, (b) a section of the anode (Ni/CGO) side and (c) a section of the cathode (LSCF) side. 89

Fig. 3.14 Current-voltage (I-V) and current-polarization (I-P) curves of the NR-cell supported on a 1 mm thick electrolyte at 700, 650, 600 and 550°C under synthetic air and dry hydrogen. 90

Fig. 3.15 Current-voltage (I-V) and current-polarization (I-P) curves of the NR-cell supported on a 0.6 mm thick electrolyte at 700, 650, 600 and 550°C under synthetic air and dry hydrogen. 91

Fig. 3.16 EIS diagrams at OCV of the NR-cell supported on a 0.6 mm thick electrolyte at 700, 650, 600 and 550°C under synthetic air and dry hydrogen. 92

Fig. 3.17 Arrhenius plots of the ohmic conductivity extracted from R_s from impedance data of the NR-cell and total conductivity of CGO-NR pellet sintered at 1200 °C. 93

Fig. 3.18 Raman spectra corresponding to different CGO nanostructures. 95

Fig. 3.19 XRD patterns of 5Ni/CGO-NC and 5Ni/CGO-NR calcined and after heat treatment. 96

Fig. 3.20 H_2-TPR of the calcined 5Ni/CGO-NC and 5Ni/CGO-NR catalysts. 97

Fig. 3.21 TEM images of (a) 5Ni/CGO-NC calcined, (b) 5Ni/CGO-NC after heat treatment at 800 °C, (c) 5Ni/CGO-NR calcined, (d) 5Ni/CGO-NR after heat treatment at 800 °C and (e) 5Ni/CGO-NR after heat treatment at 900 °C. 99

Fig. 3.22 TEM-EDS mapping for 5Ni/CGO-NC catalyst after heat treatment at 800 °C. 100

Fig. 3.23 TEM-EDS mapping for 5Ni/CGO-NR catalyst after heat treatment at 800 °C. 101

Fig. 3.24 Ethanol conversion obtained for the catalysts after ethanol steam reforming reactions at 600 °C and H_2O/EtOH molar ratio of 3. 102

Fig. 3.25 Product distribution obtained for the catalysts after ethanol steam reforming reactions at 600 °C and H_2O/ethanol molar ratio of 3, for (a) 5Ni/CGO-

NC, (b) 5Ni/CGO-NC-800 °C, (c) 5Ni/CGO-NR, (d) 5Ni/CGO-NR-800 °C and (e) 5Ni/CGO-NR-900 °C. 104

Fig. 3.26 TGA, with mass and derivative of mass of spent 5Ni/CGO-NC and 5Ni/CGO-NR catalysts after ESR at 600 °C. 105

Fig. 3.27 Secondary electron SEM images of a fractured surface of the 5Ni/CGO-NR catalytic layer deposited the anode and heated at 800 °C. The dotted line indicates the thickness of the catalytic layer..... 106

Fig. 3.28 Durability test of the anode-supported single cell with the 5Ni/CGO-NR catalytic layer, 130 h at 700 °C, applied voltage of 0.6 V, under 6 $L \cdot h^{-1}$ synthetic air at the cathode side and at the anode side dry hydrogen for the first 20 h, then dry ethanol for the next 110 h and finishing with hydrogen. A total flux of 6 $L \cdot h^{-1}$ was flown through the anode compartment. 108

Fig. 3.29 Electrochemical characterization of the fuel cell under hydrogen before and after the durability test of 130 h operation (20 h H_2 and 110 h EtOH) at 700 °C under 0.6 V polarization: (a) I-V curve and (b) complex impedance diagrams at 0.6 V..... 110

Fig. 3.30 Electrochemical analyses of the cell under ethanol at the start of the ethanol introduction (after 20 h under H_2) and after (20 h H_2 and 110 h EtOH) with 0.6 V polarization at 700 °C (a) I-V curve starting at 0.6 V (b) EIS diagrams at 0.6 V..... 112

Fig. 3.31 Secondary electron SEM image of the fractured cell showing the interface between 5Ni/CGO-NR catalytic layer and the anode support after the durability test at 700 °C under ethanol. The dotted line indicates the thickness of the catalytic layer. 113

Fig. 4.1 Schematic representation of the three symmetrical cells (a) YSZ/LSM-SDC/LSCF, (b) YSZ/SDC/LSM-SDC/LSCF, and (c) YSZ/LSCF. 119

Fig. 4.2 Schematic representation of the complete cell Ni-YSZ/YSZ/SDC/LSM-SDC/LSCF. 120

Fig. 4.3 XRD patterns of PLD layers on YSZ. Top to bottom: SDC, SDC+LSM-SDC and LSM-SDC as-deposited. 121

Fig. 4.4 XRD patterns of LSM-SDC layers on YSZ treated at different temperatures (900, 1000 and 1100 °C). 122

Fig. 4.5 (a) Cross-sectional SEM image of SDC BL and LSM-SDC NFL deposited on YSZ support with LSCF sintered at 1000 °C (b) STEM image of the cross-section with EDSmapping of the deposited thin films. 123

Fig. 4.6 (a) EIS diagrams of the symmetrical cells with NFL (YSZ/LSM-SDC/LSCF) sintered at different temperatures measured at 750 °C. The inset shows the high-frequency portion of the diagrams. (b) equivalent circuit used to fit

the impedance data. (c) and (d) Arrhenius plots of the series and polarization ASR, respectively, of the symmetrical cells. 125

Fig. 4.7 (a) EIS diagrams of the symmetrical cells with BL + NFL (YSZ/SDC/LSM-SDC/LSCF) and without the bilayer sintered at 1000 °C. The inset shows the expanded high frequency portion of the diagram. (b) Arrhenius plots of the total ASR of the symmetrical cells with NFL +BL and without the bilayer sintered at 1000 °C. (c) Arrhenius plots of the series and polarization ASR of the symmetrical cell with BL+NFL sintered at 1000 °C. 127

Fig. 4.8 (a) I-V curve and EIS diagrams at (b) OCV and (c) 0.2 $A \cdot cm^{-2}$ of the anode-supported single cell with the BL+ NFL interlayers at 700, 750, and 800 °C under synthetic air and dry hydrogen. 129

Fig. 4.9 (a) Long-term durability test of the anode-supported single cell with the BL+NFL interlayers for 700 h at 750 °C, a current density of 0.3 $A \cdot cm^{-2}$, under synthetic air and dry hydrogen, (b) I-V curves and (c) EIS diagrams at 0.2 $A \cdot cm^{-2}$ of the cell at 0 h and 700 h of operation measured at 750 °C under the same conditions. 131

Fig. 4. 10 TEM images and EDS mapping of the anode-supported single cell with the BL+NFL and LSCF cathode before (a) and after (b) 700 h of operation at 750 °C and 0.3 $A.cm^{-2}$. 133

Fig. A1.1 Tape casting system (left) and doctor blade (right). 139

Fig. A1.2 TGA analysis, with mass and the derivative of mass, of the electrolyte and anode tape obtained under synthetic airflow and 10 $°C \cdot min^{-1}$ heating rate. .142

Fig. A1.3 Secondary electron SEM images of a fractured cross-section of the YSZ electrolyte with a magnified view of the porosity of the electrolyte. 143

Fig. A1.4 Secondary electron SEM images of a fractured cross section of the ESC.....143

Fig. A1.5 Secondary electron SEM images of a fractured cross section of the tape casted ASC (a) general view (b) detail of the anode (c) anode and cathode interfaces, and (d) detail of the electrolyte. 145

Fig. A1.6 Current-voltage (I-V) and current-polarization (I-P) curves of the ESC and ASC at 850 °C under synthetic air and dry hydrogen. 146

Fig. A1.7 EIS diagrams at OCV of the ESC and ASC at 850 °C under synthetic air and dry hydrogen. 147

List of Tables

Table 2.1 Chemical composition of the CGO powders determined by ICP-OES..43

Table 2.2 Crystallite sizes, lattice parameters, density, specific surface area, total specific area, specific GB area, and SGB/SSA ratio of CGO and Fe-doped CGO samples.....47

Table 2.3 Fe, Gd, and Ce surface excess of CGO and Fe-doped CGO samples. 49

Table 3.1 Resulting fitting parameters of series resistances (R_s) and total polarization resistances (R_{ptotal}) of the EIS diagram of the NR-cell at OCV at 700, 650, 600 and 550°C. 92

Table 3.2 Specific BET area and chemical composition (wt%) of the catalysts. ...94

Table 3.3 Resulting fitting parameters of series resistances (R_s) and total polarization resistances (R_{ptotal}) and total resistances (R_{total}) of the EIS diagram of the anode supported cell with catalytic layer at 700 °C under 0.6 V, with H_2 and ethanol as fuels, at the start and at the end of the durability test. 113

Table 4.1 Fitting parameters of series resistances (R_s), polarization resistances (R_{p1} and R_{Pp2}) and capacitances (C_{p1} and C_{p2}) at OCV and at 0.2 $A{\cdot}cm^{-2}$ of the EIS diagram of the anode-supported single cell with the BL+ NFL interlayers at 700, 750, and 800 °C. 129

Table A1.1 Resulting fitting parameters of series resistances (R_s), polarization resistances (R_{p1} and R_{p2}) and total resistance (R_{total}) of the ESC and ASC at OCV, at 850 °C. 147

List of Equations

Equation 1.1	$O_2 + 4e^- \rightleftharpoons 2O^{2-}$
Equation 1.2	$2H_2 + 2O^{2-} \rightleftharpoons 2H_2O + 4e^-$
Equation 1.3	$W = -2FE$
Equation 1.4	$E^o = -\frac{\Delta\overline{g}_f}{2F}$
Equation 1.5	$E_{nernst} = E^o - \frac{RT}{2F} ln\left(\frac{P_{H_2} P_{O_2}^{\frac{1}{2}}}{P_{H_2O}}\right)$
Equation 1.6	$\varepsilon_t = \frac{\Delta\overline{g}_f}{\Delta\overline{h}_f}$
Equation 1.7	$\varepsilon_V = \frac{E}{E^o}$
Equation 1.8	$E = E_{nernst} - iR_{ohmic} - \eta_{cath} - \eta_{an}$
Equation 1.9	$R = \rho\frac{l}{A}$
Equation 1.10	$Y_2O_3 \xrightarrow{ZrO_2} 2Y'_{Zr} + 3O_o^x + V_o^{\cdot\cdot}$
Equation 1.11	$4Ce_{Ce} + 2O_O \overset{\Delta H_{O_2}}{\Longleftrightarrow} O_2 + 4Ce'_{Ce} + 2V_o^{\cdot\cdot}$
Equation 1.12	$Gd_2O_3 \xrightarrow{2CeO_2} 2Gd'_{Ce} + 3O_O^x + V_o^{\cdot\cdot} + {}^1/_2\, O_2$
Equation 1.13	$\sigma T = Ae^{(-E_a/kT)}$
Equation 1.14	$\delta \approx \sqrt{\frac{(1-\epsilon)}{\tau}}\frac{L_c}{a}$
Equation 1.15	$CH_3CH_2OH + 3H_2O \leftrightharpoons 6H_2 + 2CO_2$
Equation 1.16	$CH_3CH_2OH + 1.5O_2 \leftrightharpoons 3H_2 + 2CO_2$
Equation 1.17	$CH_3CH_2OH + 2H_2O + 0.5O_2 \leftrightharpoons 5H_2 + 2CO_2$
Equation 1.18	$CO + H_2O \leftrightharpoons H_2 + CO_2$
Equation 1.19	$C + H_2O \leftrightharpoons CO + H_2$
Equation 1.20	$\Delta G = 4\pi r^2\gamma + \frac{4}{3}\pi r^3 \Delta G_v$
Equation 1.21	$\Delta G_v = \frac{-k_B T ln(S)}{v}$
Equation 1.22	$\Delta G_c^{hetero} = \Phi \Delta G_c^{homo}$

Equation 1.23 $$C_6H_{12}N_4 + 6H_2O \rightarrow 6H_2CO + 4NH_3$$

Equation 1.24 $$NH_3 + H_2O \rightarrow NH_4OH$$

Equation 1.25 $$NH_4OH + H_2O \rightarrow NH_4 + +OH^-$$

Equation 2.1 $$\Delta H_{seg} = \Delta H_\sigma + \Delta H_\varepsilon + \Delta H_\omega + \Delta H_\phi$$

Equation 2.2 $$\sigma T = Ae^{-(E_a/kT)}$$

Equation 2.3 $$d_t^n - d_0^n = kD\sigma_i(t - t_0)$$

Equation 2.4 $$\sigma_i = \sigma_0 - \Gamma_i \Delta H_{seg}$$

Equation 2.5 $$TSA = \frac{6}{\rho D}$$

Equation 2.6 $$SGB = \frac{(TSA - SSA)}{2}$$

Equation 2.7 $$\Gamma = n/SSA$$

Equation 3.1 $$D = \frac{0.9\lambda}{\beta \cos(\theta)}$$

Equation 3.2 $$\rho_{rel} = \frac{[L_0/(\Delta L + L_0)]^3 \rho_0}{\rho_t}$$

Equation 3.3 $$\rho_t = \left(\frac{4}{N_A \times a^3}\right)[0.99M_{Ce} + 0.1M_{Gd} + (2 - \delta)M_O]$$

Equation 3.4 $$X_{ethanol} = \frac{(n_{ethanol})_{fed} - (n_{ethanol})_{exit}}{(n_{ethanol})_{fed}} \times 100$$

Equation 3.5 $$S_{xl} = \frac{(n_x)_{produced}}{(n_{total})_{produced}} \times 100$$

Equation 3.6 $$\sigma_\Omega = \frac{l}{\mathrm{R_s}}$$

Equation 3.7 $$\mathrm{CH_3CH_2OH} \rightleftharpoons \mathrm{CO + H_2 + CH_4}$$

Equation 3.8 $$\mathrm{C_2H_5OH} \rightleftharpoons \mathrm{C_2H_4O + H_2}$$

Equation 3.9 $$C_2H_4O + H_2O \rightleftharpoons 2CO + 3H_2$$

Equation 3.10 $$CO + H_2O \rightleftharpoons CO_2 + H_2$$

Equation 4.1 $$C_p = Q^{1/n} \times R_{pi}^{(1-n)/n}$$

List of Acronyms

ASC	Anode Supported Cell
ASR	Area Specific Resistance
BET	Brunauer, Emmett-Teller Method
BL	Barrier Layer
CCL	Current Collector Layer
CGO	Ceria Doped with Gadolinium
CHP	Combined Heat and Power
CPE	Constant Phase Element
DIR	Direct Internal Reforming
EDS	Energy Dispersive Spectroscopy
EELS	Electron Energy Loss Spectroscopy
EIS	Electrochemical Impedance Spectroscopy
ESC	Electrolyte Supported Cell
ESR	Ethanol Steam Reforming
FFT	Fast Fourier Transform
FL	Functional Layer
GB	Grain Boundary
GIR	Gradual Internal Reforming
H_2-TPR	Temperature-Programmed Reduction with Hydrogen
HMTA	Hexamethylenetetramine
HRTEM	High-Resolution Transmission Electron Microscopy
ICP-OES	Inductively Coupled Plasma Atomic Emission Optical Spectroscopy
I-P	Current-Power
IPCC	Intergovernmental Panel on Climate Change
IT-SOFC	Intermediate Temperature SOFC
I-V	Current-Voltage
LSCF	Strontium-Doped Lanthanum Cobalt Ferrite
LSM	Strontium-Doped Lanthanum Manganite
MIEC	Mixed Ionic and Electronic Conductivity
NC	Nanocube

NFL	Nanostructured Functional Layer
NR	Nanorod
OCV	Open-Circuit Potential
ORR	Oxygen Reduction Reaction
OSC	Oxygen Storage Capacity
PLD	Pulsed Laser Deposition
SDC	Ceria Doped with Samarium
SEM	Scanning Electron Microscopy
SGB	Specific GB Interface Area
SoA	State-of-the-Art
SOFC	Solid Oxide Fuel Cell
SR	Steam Reforming
SSA	Specific Surface Area
STEM	Scanning Transmission Electron Microscopy
TEM	Transmission Electron Microscopy
TGA	Thermogravimetric Analysis
TMA	Thermomechanical Dilatometry Analysis
TMO	Transition Metal Oxide
TPB	Triple-Phase Boundary
TSA	Total Specific Surface Area
VAN	Vertically Aligned Nanocomposite
WDXRF	Wavelength Dispersive X-Ray Fluorescence
XRD	X-Ray Diffraction
YSZ	Yttria-Stabilized Zirconia

Table of Contents

Chapter 1 1
Introduction 1

1.1. Motivation 1

1.2. Fundamentals of solid oxide fuel cells 3

1.2.1. Background 3

1.2.2. Thermodynamics of a fuel cell 5

1.2.3. Overpotential of a fuel cell 6

1.3. Materials in an SOFC 8

1.3.1. Electrolyte 8

1.3.2. Cathode 12

1.3.3. Anode 16

1.4. Alternative fuels for SOFC 17

1.5. Controlled synthesis techniques of nanomaterials 22

1.5.1. Background 22

1.5.2. Chemical synthesis methods 23

1.5.2.1. Synthesis by precipitation 26

1.5.2.2. Hydrothermal synthesis 27

1.5.3. Physical synthesis methods 28

1.5.3.1. Pulsed Laser Deposition (PLD) method 29

1.6. Processing techniques of SOFC 31

1.6.1. Background 31

1.6.2. Tape casting 31

1.6.3. Sintering 32

1.7. Scope 35

Chapter 2 37
Synthesis of CGO by precipitation and addition of Fe_2O_3 as a sintering aid 37

2.1. Introduction 37

2.2. Experimental 39

2.3. Results and discussion 41

2.4. Summary 60

Chapter 3 62
Shape-controlled synthesis of CGO by hydrothermal route and application as electrolyte and as catalyst for direct use of ethanol in SOFCs 62

3.1 Introduction 62

3.1.1 Shape-controlled synthesis of CGO by hydrothermal route 62

3.1.2 Application of CGO nanorods as electrolyte support in an SOFC 63

3.1.3 Evaluation of Ni/CGO nanocubes and nanorods as catalyst for ethanol steam reforming and application as catalytic layer for SOFC 64

3.2 Experimental 66

3.2.1 *Synthesis of CGO nanorods and nanocubes* 66

3.2.2 *Characterization of CGO nanorods and nanocubes* 67

3.2.3 *Application of CGO nanorods as electrolyte support in an SOFC* 69

3.2.4 *Synthesis of Ni/CGO nanocubes and nanorods catalysts* 70

3.2.5 *Characterization and evaluation of Ni/CGO nanocubes and nanorods catalysts for ethanol steam reform reaction* 71

3.2.6 *Application of Ni/CGO nanorods as a catalytic layer in an SOFC* 72

3.3 Results and discussion 75

3.3.1 Shape-controlled synthesis of CGO by hydrothermal route 75

3.3.2 Application of CGO nanorods as electrolyte support in an SOFC 88

3.3.3 Evaluation of Ni/CGO nanocubes and nanorods as catalyst for ethanol steam reforming and application as catalytic layer for SOFC 94

3.4 Summary 114

3.4.1 Shape-controlled synthesis of CGO by hydrothermal route 114

3.4.2 Application of CGO nanorods as electrolyte support in an SOFC 114

3.4.3 Evaluation of Ni/CGO nanocubes and nanorods as catalyst for ethanol steam reforming and application as catalytic layer for SOFC 115

Chapter 4 116
Functional ceria-based thin film deposited by pulsed laser deposition as cathode/electrolyte interlayers 116

4.1 Introduction 116

4.2 Experimental 118

4.3 Results and discussion 121

4.4 Summary 133

Conclusion 135

Appendix 1 137
Development of the tape casting technique for SOFC electrolytes and anode supported SOFC fabricated through lamination and co-sintering. 137

A1.1 Introduction 137

A1.2 Experimental 138

A1.3 Results and discussion 141

A1.4 Conclusion 148

Scientific contribution 149
References 151

Chapter 1

Introduction

1.1. Motivation

The most challenging global threat is the eminent climate crisis that has been building itself up for centuries and has shown its potential to have a devastating effect on humanity. In 1896, Svante Arrhenius was the first scientist to acknowledge that a rise in atmospheric CO_2 levels could contribute to climate variation [1]. Later that hypothesis was validated by numerous scientific research. The Intergovernmental Panel on Climate Change (IPCC) report of 2021 [2] analysed 14 thousand scientific studies and unequivocally states that the emissions of greenhouse gases from human activities, especially CO_2 emission from the burning of fossil fuels, are the main responsible for the rise in global temperature of around 1.1 °C. The report states that very probably this temperature will exceed 1.5 °C and that drastic and immediate actions are needed to reduce the emissions of CO_2 and other greenhouse gases “to limit the temperature increase to 1.5 °C above pre-industrial levels”, as established by the 2015 United Nations Paris Agreement [3]. The decrease in emissions of greenhouse gases by reducing energy consumption in chemical processes, using renewable energy sources, and employing new and more efficient materials in energy systems is crucial in the battle against climate change.

Some of the existing renewable energy sources, such as wind and solar, are intermittent. Thus, efforts are needed to keep the power-grid load balanced. Indeed, the rising electricity demand requires the development of a combination of technologies that will convert, store, and transport energy. Electrochemical devices, such as fuel cells, are of great interest as they directly convert stored chemical energy, mainly in the form of H_2, to electrical energy. The high-temperature fuel cell, the solid oxide fuel cell (SOFC), also has the advantage of being fuel flexible and can operate directly with different fuels, such as hydrocarbon and alcohol. A greater benefit of the technology is attained when these fuels are from renewable sources such as bioethanol and biogas. Besides, generating electrical energy, the SOFC can operate on an integrated system in a combined heat and power (CHP) generation plant. The advances brought by the

efficient use of SOFC technology are important additions towards sustainable energy generation and to the plan to mitigate climate change.

The challenges for the wide commercialization of SOFCs lie in the necessary advances to minimize their degradation, reduce their cost, improve their performance, and adapt them to the use of alternative fuels to hydrogen, such as ethanol and biogas [4–6]. An important strategy to minimize the cost of SOFC and increase the cell's durability is to lower both processing and operation temperatures [7–9]. Decreasing sintering temperature and developing low-cost processing techniques for fabrication of multi-functional layer ceramic components with controlled microstructure are current challenges for SOFC scalable production. In addition, reducing the SOFC operating temperatures is pursued to minimize the thermally activated degradation process aiming to increase durability. However, at intermediate temperatures (500 - 750 °C) the electrochemical reactions and charge transport are less efficient. Therefore, the development of nanomaterials and the use of advanced technologies are important allies to increase the efficiency of an SOFC operating at intermediate temperatures. For the operation of a cell at intermediate temperatures, electrolytic materials with high ionic conductivity, electrodes with high reaction activity, efficient catalysts, and a decrease in the interfacial resistance between the cell’s components are necessary. A material that has gained prominence for use in intermediate temperature SOFCs (IT-SOFCs) is cerium oxide [10–13].

This doctoral work proposes to advance the application of cerium oxide obtained through different synthetic routes and processing methods in distinct functional layers of an SOFC. The experimental results show that through adjustments of synthesis and processing, it is possible to decrease the fabrication costs of an SOFC and to adjust cerium oxide’s properties for application in an SOFC’s electrolyte, anode, cathode, and as a catalyst for direct use of ethanol in the cell. Thus, this study aims to demonstrate that by using advanced techniques such as the synthesis of shape-controlled nanomaterials and by physical depositions strategies of a key component material (cerium oxide) it is possible to minimize processing steps, attaining enhanced durability and fuel flexibility. In a broader context, such results contribute to expand SOFC applications for clean

energy conversion, contributing to the reduction of the emission of greenhouse gases.

1.2. Fundamentals of solid oxide fuel cells

1.2.1. Background

Fuel cells are highly efficient electrochemical devices that convert chemical energy into electrical energy via a combination of fuels and oxidants that by redox reactions produce an electrical current. In 1839, Sir William Grove published his findings on the first operational fuel cell that consisted of a dilute sulfuric acid electrolyte producing a small current at room temperature [14]. High-temperature ceramic fuel cells were later reported: in 1892, Nernst discovered solid oxide electrolytes, and in 1936 Baur and Preis presented the first ceramic fuel cell operating at 1000 °C [15].

There is a wide variety of fuel cells. They all take their name upon the chemical characteristics of the electrolyte by which they are made [16]. The high-temperature ceramic fuel cells, solid oxide fuel cells, have a ceramic material as their electrolyte, which acts as an oxygen ion conductor. **Fig. 1.1** shows a schematic diagram of an SOFC where the ion-conducting electrolyte is sandwiched between two porous electrodes, the cathode, and the anode.

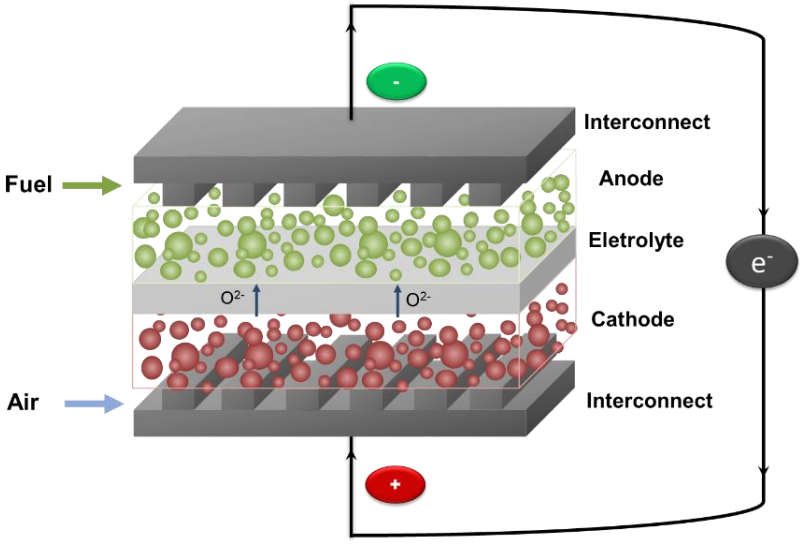

Fig. 1.1 Schematic representation of an SOFC. Adapted from [17].

The electrochemical redox reactions occur between the interfaces of the component of the cell. The O_2 from the air is reduced by electrons at the cathode forming O^{2-} species via the charge-transfer reaction (Equation 1. 1)

$$O_2 + 4e^- \rightleftharpoons 2O^{2-} \tag{1.1}$$

The fuel passes through the anode and is oxidized catalytically at the interface between the anode and the electrolyte, to form H^+ and electrons. The electrolyte is electronically insulating and ionically conductive. The O^{2-} ions from the cathode flow through the electrolyte to the anode where they react with H^+ forming H_2O and other by-products such as CO_2 if hydrocarbon fuels are used (Equation 1.2).

$$2H_2 + 2O^{2-} \rightleftharpoons 2H_2O + 4e^- \tag{1.2}$$

The electrochemical reactions occur while the electrons flow through the external circuit carrying out work. The induvial cells are combined in stacks via interconnects that provide gas flow between the cells and electrical contact. A combined series of stacks can be arranged in a module (**Fig. 1.2**) to provide the needed power outputs for several applications such as in portable devices, transportation, and stationary power generation.

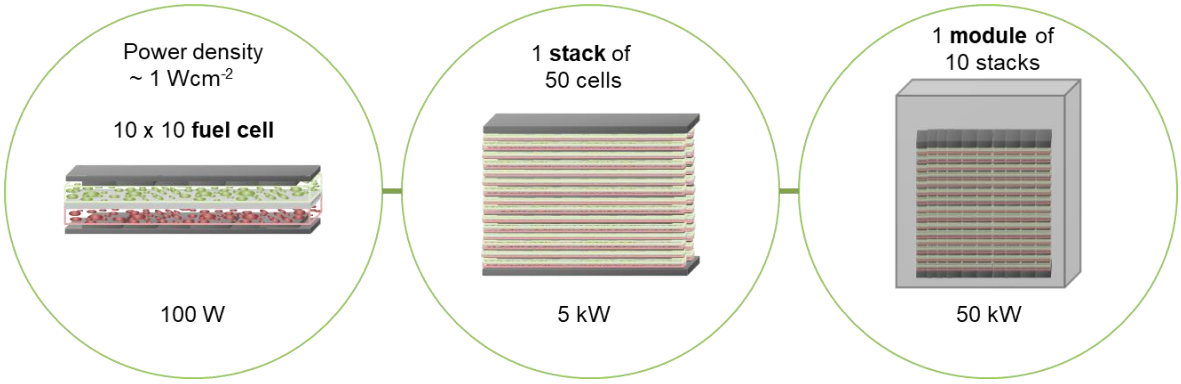

Fig. 1.2 Illustration showing a single fuel cell, a stack, and a module with the estimated power output for a state-of-the-art SOFC providing a power density of 1 W·cm^{-2}. Adapted from [18].

1.2.2. Thermodynamics of a fuel cell

When the fuel cell operates with H_2, water is formed. To form one molecule of H_2O two electrons are needed, then the electrical work (W) of passing the electrons across anode and cathode will be related to the charge of two moles of electrons ($-2FE$) and the potential (E), as seen in Equation 1.3:

$$W = -2FE \tag{1.3}$$

The chemical energy available for the reaction is the Gibbs free energy of formation (ΔG_f), if the reaction is reversible such that there are no energy losses then the Gibbs free energy will be equal to the electrical work, thus, the value of the standard potential E^o (Equation 1.4).

$$E^o = -\frac{\Delta G_f}{2F} \tag{1.4}$$

However, the ideal difference of potential depends on the electrochemical reactions that occur with different fuels and oxygen. The Nernst Equation (Equation 1.5) provides a relationship between the ideal standard E^o and the ideal equilibrium potential (E) related to reaction pressure and concentration.

$$E_{nernst} = E^o - \frac{RT}{2F} ln\left(\frac{P_{H_2} P_{O_2}^{\frac{1}{2}}}{P_{H_2O}}\right) \tag{1.5}$$

The thermodynamic efficiency of the process measures how efficiently the chemical energy from the fuel is converted to electrical energy rather than heat and will be the ratio between the energy produced (ΔG_f) relative to the change in enthalpy of formation (ΔH_f) between product and reactants in a reversible process. If using the maximum work rate, the one of a reversible process, then the maximum theoretical efficiency of the system (ε) can be written as the Equation 1.6:

$$\varepsilon_t = \frac{\Delta G_f}{\Delta H_f} \tag{1.6}$$

The thermodynamic efficiency justifies the development of fuel cells over conventional heat engines, as the heat engine's thermal efficiency will be limited to the Carnot efficiency that considers the temperature change (wasted heat) [19].

1.2.3. Overpotential of a fuel cell

To obtain the actual value of the fuel cell's efficiency the different efficiencies must be combined: the heating efficiency, the voltage efficiency, and the fuel utilization efficiency. A common method to calculate a fuel cell's efficiency is by using the voltage's efficiency (Equation 1.7).

$$\varepsilon_V = \frac{E}{E^o} \tag{1.7}$$

A voltameter connected to the cathode and to the anode is used to measure the electrical potential of the cell (E). When there is no flow of current through the cell the voltage is the open-circuit potential (OCV). For a fuel cell with hydrogen as a fuel, the OCV is very close to the Nernst potential calculated by Equation (1.5). However, as the current flow increases there are internal losses such that there is a drop in potential. Under operation, when an electrical current is drawn from a fuel cell, some of the chemical potential available must be used to overcome the irreversible internal losses, that potential is the overpotential of the cell. The voltage will therefore be dependent on the total ohmic losses of the cell (R_{ohmic}) with current (i) and the polarization losses associated with the electrodes (η_{cath} and η_{an}), as in Equation 1.8 [20].

$$E = E_{nernst} - iR_{ohmic} - \eta_{cath} - \eta_{an} \tag{1.8}$$

The performance of an SOFC is often represented by a current–voltage characteristic (I-V) curve as shown in **Fig. 1.3**. An I-V curve shows how the current changes with voltage due to irreversible losses associated with the physicochemical processes in the cell. In an I-V plot different parts of the curve are

equivalent to different losses in each process. The voltage drop can be divided into three regions, at low current, at intermediary current and at high current. At low current, the drop is associated with the activation polarization related to the activation energy for the charge-transfer reactions taking place at the electrodes. At intermediary current, the loss is associated with the ohmic losses caused by the ionic resistance of the electrolyte and the electronic resistance of the electrodes (very small), of the current collectors and interconnects. At high current, there are concentration losses resulting from diffusion resistance of gas-phase reactants through the electrodes.

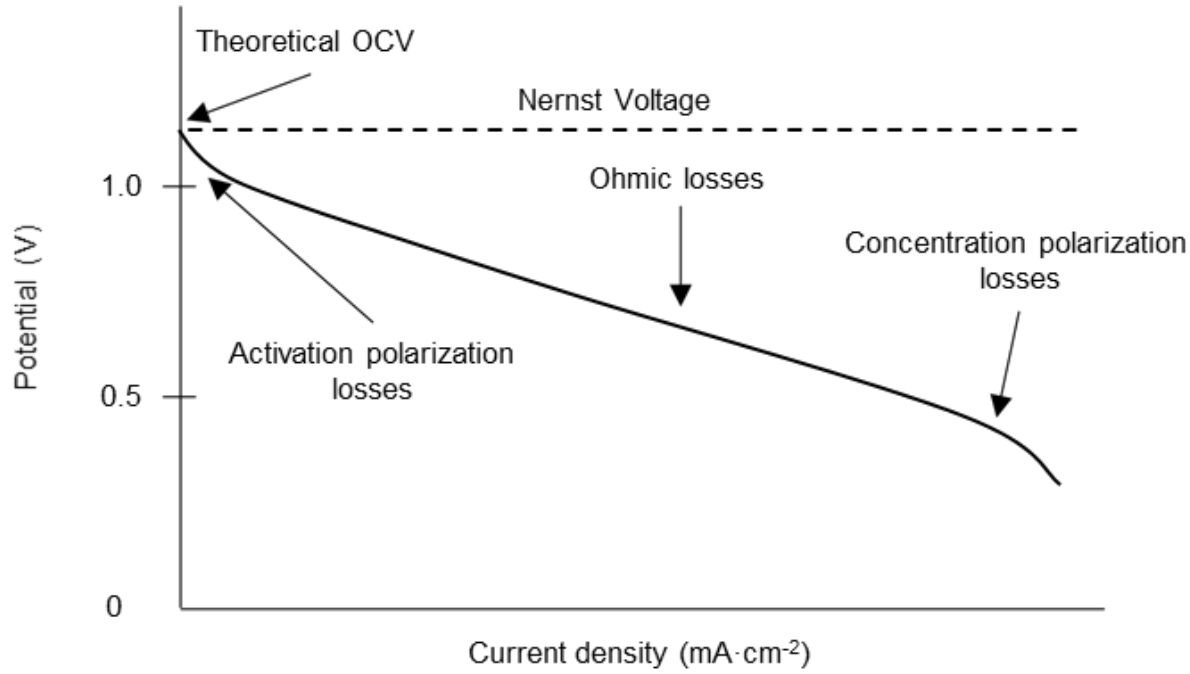

Fig. 1.3 Ideal and actual current-voltage (I-V) characteristics of a fuel cell. Adapted from [20].

Besides measuring the I-V characteristic of the cell a powerful tool to characterize electrochemical phenomena that increase the losses of the cell is electrochemical impedance spectroscopy (EIS). The I-V characteristic of the cell and the EIS analysis are essential to evaluate the electrochemical behaviour of the cell's components, providing means to improve the performance of the cell.

To increase the performance of an SOFC and maximize its efficiency, the losses in each component must be minimized. In the next section the properties of the main components and the state-of-the-art (SoA) materials used in each

component of the cell will be reviewed. Although polarizations losses cannot be eliminated, correct material choice and electrode designs can contribute to their minimization.

1.3. Materials in an SOFC

1.3.1. Electrolyte

In an SOFC the electrolyte is responsible for the ionic charge transport between the electrodes such that its material must have high ionic conductivity as well as a low electronic conductivity to force the electron flow through the external circuit. The electrolyte should be highly dense to make it gas impermeable, and the material should show chemical stability under operation, and in both reducing and oxidizing environments. Another important property is that the material needs to be thermally compatible with the other components of the cell, even more significant when the components are co-sintered [21].

The ohmic resistance (R_{ohmic}) includes all the components of the cell, but it is more relevant for the electrolyte as compared to the other components of the cell that exhibit electronic conductivity Thus, the ohmic resistance of the cell will be mainly affected by the ionic resistance of the electrolyte. The resistance of the electrolyte will be affected by its thickness, so to minimize the ohmic resistance electrolyte should be thin components of a fuel cell. The resistance of a material is measured in terms of its resistivity (ρ), area (A) and thickness (l) related to the charge transport, as shown in Equation 1.9:

$$R = \rho \frac{l}{A} \tag{1.9}$$

Besides controlling the thickness of the electrolyte to decrease the resistance, the ionic conductivity of the electrolyte will be important to determine the operation temperature of the fuel cell. Various oxide ions (O^{2-}) conductors have been researched. The conventional electrolyte material in an SOFC is yttria-stabilized zirconia (YSZ). Zirconia has a fluorite structure at high temperatures; however, it has low ionic conductivity and is not stable under operating conditions. Yttria is the most used zirconia dopant, substituting Y^{3+} for Zr^{4+} increases not only

ionic conductivity but also the stability of fluorite zirconia at room temperature and both oxidizing and reducing atmosphere. The ionic conductivity is increased by creating a large concentration of oxygen vacancies due to charge balance as shown in the following Kröger-Vink notation (Equation 1.10):

$$Y_2O_3 \xrightarrow{ZrO_2} 2Y'_{Zr} + 3O_o^x + V_o^{\cdot\cdot} \qquad (1.10)$$

Other than YSZ there is ongoing research on alternative electrolyte materials to lower the operating temperature of the SOFC. In the **Fig. 1.4**, the temperature dependence of the electrical conductivity of some electrolyte materials is shown. Compared to stabilized zirconia, doped ceria shows higher ionic conductivity and enhanced electrode reaction kinetics under the same operational condition, as well as excellent electrode chemical compatibility

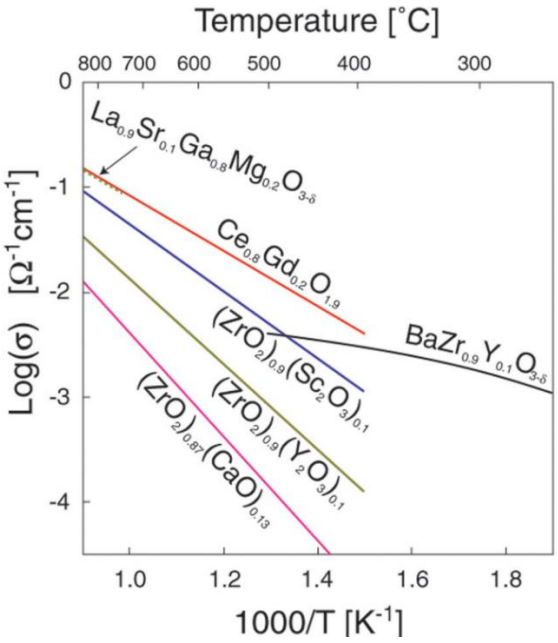

Fig. 1.4 Arrhenius plot of the electrical conductivities of selected oxide electrolytes [22].

Doped cerium oxide is another fluorite, a candidate as an electrolyte material. The ionic conductivity of ceria doped with gadolinium (CGO) is an order of magnitude higher than the conventional electrolyte YSZ (**Fig. 1.4**). Cerium oxide (CeO_2) also has a high oxygen storage capacity (OSC) due to its double oxidation

state, from (IV) to (III), which allows ceria to release oxygen under reducing conditions and adsorb oxygen under oxidizing conditions. The change of valence of cerium oxide can be expressed in the following Kröger-Vink notation (Equation 1.11):

$$4Ce_{Ce} + 2O_O \overset{\Delta H_{O_2}}{\Longleftrightarrow} O_2 + 4Ce'_{Ce} + 2V_o^{\cdot\cdot} \tag{1.11}$$

The reduction of ceria increases the concentrations of electronic defects and induces phase changes [23]. The ionic conductivity of ceria can be increased by doping ceria with a rare earth an aliovalent cation such as Gd^{3+} or Sm^{3+} [24]. Doping with a trivalent cation creates extrinsic charge compensation defect as oxygen vacancies, increasing the mobility of the species [11,25]. Accordingly, Gd^{3+} substitutes Ce^{4+} and an oxygen vacancy is formed as outlined in **Fig. 1.5**. The formation of oxygen vacancies by doping with gadolinium oxide can be expressed by the following Kröger-Vink notation, Equation 1.12:

$$Gd_2O_3 \xrightarrow{2CeO_2} 2Gd'_{Ce} + 3O_O^x + V_o^{\cdot\cdot} + {}^1/_2\, O_2 \tag{1.12}$$

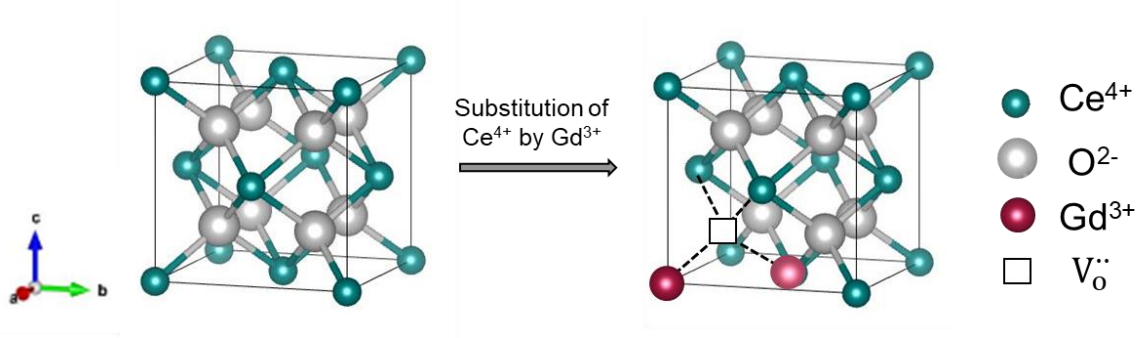

Fig. 1.5 Unit cell of CeO_2 and structural changes in the unit cell after doping with gadolinium. Obtained through Vesta software [26]. Adapted from [27].

The temperature-dependent oxygen ion conductivity for YSZ and doped ceria systems is due to the oxygen vacancies charge carriers and the following Arrhenius relationship can be applied (Equation 1.13).

$$\sigma T = Ae^{(-E_a/kT)} \tag{1.13}$$

where σ is the ionic conductivity, A the preexponential factor and E_a is the activation energy. Materials with lower E_a will facilitate ionic conductivity at lower temperatures. In doped ceria and YSZ, the E_a will be equivalent to the migration barrier of the doped oxide and the dissociation energy to break the defect associations, which hinders the vacancies mobility [28–30]. Grain boundary, grain size, composition, surface segregation, impurity level, starting powder microstructure and processing will have an impact on the electrical conductivity of the material. [11] The oxygen ion conductivity varies as dopant concentration changes. For the yttria-zirconia system, 8-10 mol% yttria-stabilized zirconia has shown the greatest stability and oxygen ion conductivity. For the ceria-based compound a doping with 10 mol% of gadolinium oxide or samarium oxide has shown the best properties to be used as an electrolyte in SOFC [25,30,31].

As observed in **Fig. 1.4** doped ceria shows higher oxygen ion conductivity than YSZ in the 500 - 750 °C temperature range. However, at high temperatures and at a reducing atmosphere, such as that present at the anode, ceria undergoes reduction to Ce^{3+}, which introduces n-type conductivity, lowering the efficiency of the SOFC. Efforts have been made to increase the ionic conductivity of ceria and minimize its electronic conductivity under SOFC operating temperature [32]. Approaches that develop ceria electrolyte with more than one dopant [12,33], add a second phase to the ceria-electrolyte [34] and enhance ceria electrical conductivity (without doping) by surface defects and band energy alignment have been considered [35,36]. One solution that has gained significant attention is to use a bilayer electrolyte consisting of a layer of YSZ and a second one of doped ceria. This configuration allows the use of the conventional stable YSZ material at the anode side and doped ceria at the cathode side when cathodes for intermediate temperature are used. A challenge for the bilayer electrolyte is the reduction of the thickness of the layers to reduce the ohmic resistance [5,37], as well as the sintering temperature of the electrolyte materials, as high sintering temperature induces the formation of an interdiffusion resistive layer due to reaction between YSZ and ceria [38,39].

1.3.2. Cathode

The reduction of the electrolyte's thickness to reduce the ohmic resistance of the fuel cell is being developed through advanced thin film deposition technologies [40,41]. At intermediary temperature, a significant contribution to the polarization losses in the fuel cell is the kinetics of the reactions in the electrodes. In the cathode the oxygen reduction reaction (ORR) (Equation 1.1) takes place. The reactions occur in the area called the triple-phase boundary (TPB). Which are the active areas located between the three phases: gas phase and the electrode material and the electrolyte material as illustrated in **Fig. 1.6**. The oxygen diffuses through the open pores in the cathode and is reduced consuming electrons and producing oxygen ions and at the vicinity of the TPB, those oxygen ions are then transported through the electrolyte [42].

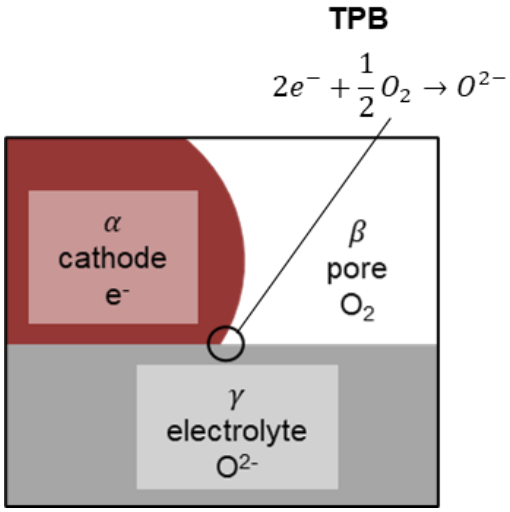

Fig. 1.6 Diagram showing the ORR occurring in the TPB between the different phases in a cathode [43].

The most common cathode material in SOFC is from the perovskite structure ABX_3 shown in **Fig. 1.7**, where X is oxygen, A site element coordinates to 12 oxygen ions and B is bonded to 6 oxygen atoms. The A site is usually occupied by a mixture of rare earth metals (typically La) and alkaline earth metals (such as Sr, Ca, and Ba), whereas the B site is occupied by one or several mixed-valence transition metal ions (such as Mn, Co, Fe, and Ni) [44].

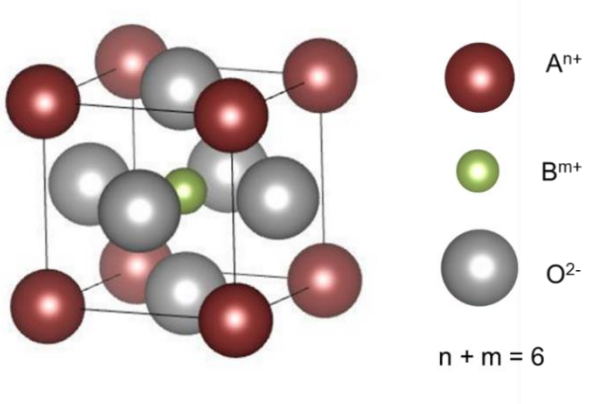

Fig. 1.7 Perovskite unit cell with A and B cations and oxygen anions forming an octahedron. Obtained through Vesta software [26].

The oxygen transport in a perovskite material is described by the oxygen surface exchange coefficient (k), diffusivity, and the chemical diffusion coefficient (D). The ratio between D and k is the critical length parameter (L_c) which expresses the relative control of the transport either by bulk diffusion or surface exchange. Adler [42] used this ratio to qualitatively calculate the penetration depth (δ) (Equation 1.14), which corresponds to the extension of the reaction beyond the TPB:

$$\delta \approx \sqrt{\frac{(1-\epsilon)}{\tau}}\frac{L_c}{a} \qquad (1.14)$$

where ϵ corresponds to the porosity, τ to the tortuosity and a is the surface. Through the proposed model, the penetration depth of the reaction of various perovskite cathodes was calculated to help define the location of the reaction in the cathodes.

The traditional porous electronic conducting cathode is $La_{1-x}Sr_xMnO_3$ (LSM). The LSM presents chemical and thermal compatibility with the conventional YSZ electrolyte, has good stability under oxidizing conditions and is a good electrical conductor at > 800 °C [45,46]. However, LSM has a poor ionic conductivity, and a small penetration depth, limiting the ORR to a very specific point at the TPB as shown in **Fig. 1.8** (a) [43]. This is detrimental for fuel cells operating at temperatures lower than 800 °C. An alternative to the LSM cathode is perovskites

with mixed ionic and electronic conductivity (MIEC). On those materials the reaction sites can be extended over to the bulk of the MIEC's material, with higher penetration depth, such that there are more active sites for the ORR to occur (**Fig. 1.8** (b)) [42]. The expansion in the active area will improve the fuel cell's performance.

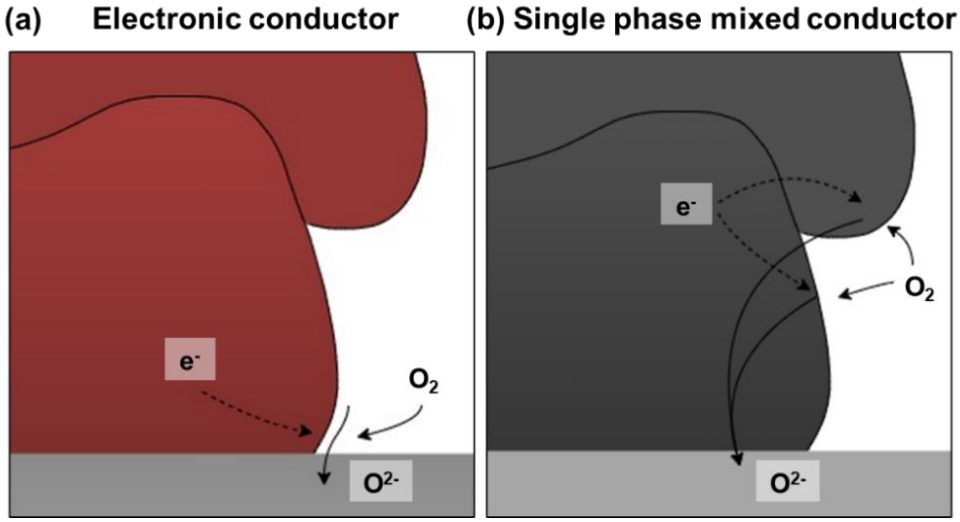

Fig. 1.8 Schematic representation of SOFC cathodes (a) porous single-phase electronically conductive oxide, such as LSM and (b) porous single-phase mixed conductor, such as LSCF. Adapted from [43].

MIECs with the perovskite structure are generally composed of more than two cation substitution at both A and B sites creating charge compensation mechanisms to increase electronic and ionic conductivity. The SoA MIEC cathode is the strontium-doped lanthanum cobalt ferrite ($La_{1-x}Sr_xCo_{1-y}Fe_yO_3$) (LSCF). The LSCF has a high oxygen surface exchange rate and electronic conductivity. The material offers a compromise between thermal compatibility, catalytic properties, and stability at high temperatures [47–51].

The main drawback of using LSCF as the SOFC cathode is related to its higher reactivity with the YSZ. The chemical reactions at the interface of the LSCF cathode and the YSZ involve the formation of insulating phases such as $SrZrO_3$ and La_2Zr_2O, which are responsible for an increase in resistance and a cause for cell degradation [52–54]. An approach to mitigate the formation of resistive phases during both the processing and the operation is to introduce a diffusion barrier layer between the YSZ electrolyte and the cathode (as shown in **Fig. 1.9**). A

proposed material is a ceria-based barrier layer because LSCF is better chemically compatible with ceria than YSZ at processing and operational temperatures [54,55]. However, at temperatures above 1200 °C the interdiffusion of YSZ and CGO species occurs causing the formation of resistive phases, thus increasing ohmic resistance [56,57].

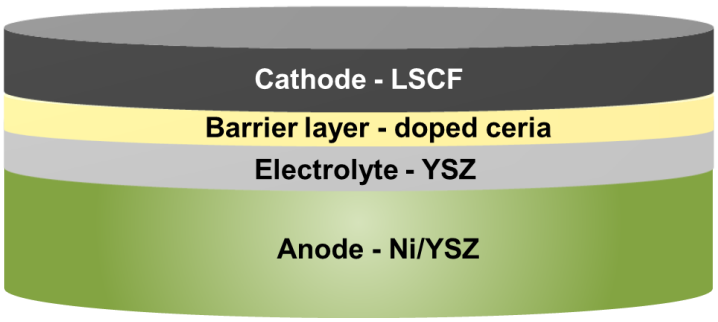

Fig. 1.9 Schematic representation of an SOFC with doped ceria barrier layer between YSZ electrolyte and LSCF cathode. Adapted from **[58]**.

Many studies have been devoted to understanding the interactions between the electrolyte and cathode during processing and operation. The processing of electrolytes usually requires a high sintering temperature of ~1500 °C for the layers to densify. It is usually during the high-temperature processing of the ceramics that cations diffusion occurs to form the resistive phase [59]. The main challenge of using LSCF as a cathode material in SOFC lies in minimizing the cation migration through the interfaces. Several approaches have been proposed to improve interfacial stability between cathode and electrolyte. One approach to avoid interface reactions between electrolyte and cathode and improve the ORR is to use a nanocomposite cathode and separate the processing of the chemically stable ceramic, the scaffold, and the reactive catalytic cathode material, which can then be impregnated into the scaffold at a lower temperature [4,60,61]. An alternative explored is to reduce the sintering temperature of the electrolyte components by morphological control of the starting powder [27]. Advanced techniques have also been suggested such as nanoengineering of the interface by the deposition of thin-film cathodes and barrier layer by the pulsed laser deposition method which require a lower deposition temperature [62,63].

In this Ph.D. work, the fabrication of dense ceria-based diffusion barrier layers was investigated using advanced methods, ranging from chemical synthesis to physical vapour deposition, aiming at minimizing the undesired reaction between YSZ and the ceria layer during the high temperature sintering step. To decrease the sintering temperature of dense ceria layers the studied methods were the controlled shape of nanoparticles, the use of a sintering aid, and the pulsed laser deposition.

1.3.3. Anode

In the anode the fuel diffuses through the open pores and is oxidized by the oxide ion delivered through the electrolyte, water is formed, and electrons are released through the external circuit. The anode material should be porous exhibiting both electronic and ionic conductivities to allow the oxidation reactions to occur beyond the triple-phase boundary. These functional aspects together with the reducing environment of the anode are the major factors for the selection of the anode's material. The reducing environment limits the selection of anode materials to metals and few conductive oxides [64].

The anode must have thermal and chemical compatibility with the electrolyte material and be made of a low-cost material. Therefore, for a SOFC with a YSZ electrolyte the most common anode is the cermet of nickel oxide (NiO) and YSZ [65]. NiO is a relatively low-cost material and acts as an electrocatalyst for the oxidation of hydrogen and electronic conductivity of the anode. The YSZ ceramic is essential to guarantee the dispersion of the metal particles, to maximize the TPB [64,66]. and to reduce the anode thermal expansion coefficient. Due to the relatively low cost of the Ni/YSZ cermet, the anode is often used as the mechanical support for the cell [67]. The anode supported SOFC (ASC) configuration has a lower ohmic loss than an electrolyte supported cell (ESC). SOFC anodes are commonly produced with two layers, one is the functional layer (FL) with a fine microstructure, which corresponds to lower porosity, smaller pore size, and lower Ni volume fraction than that of the current collector layer (CCL). The anode FL has a high surface area to maximize the active region for the electrochemical oxidation reaction, and the thicker anode support CCL with coarse particles and pores to provide mechanical strength and electronic current collection [68].

Besides being a good catalyst for hydrogen oxidation, nickel is also active for the steam reforming (SR) reaction of methane to produce syngas. However, there are thermodynamic limitations to those reactions and SR usually occurs at high temperatures > 900 °C and a high ratio of steam to methane is needed to prevent carbon formation on the surface of the anode. Ni catalyses the decomposition of methane to form carbon filaments under reducing conditions. Avoiding carbon deposition, also known as coking, is even more important in the presence of higher hydrocarbons and alcohols, such as ethanol. Deposition of carbon on the anode can lead to severe cell degradation leading to failure. Hence, when using carbon-containing fuels, alternative anodes, with lower susceptibility to coking have been proposed. In the next section the use of carbon-containing fuels will be reviewed and an alternative to the direct utilization of ethanol will be proposed.

1.4. Alternative fuels for SOFC

The ability of SOFCs to use different fuels is advantageous to the system, especially when the fuel comes from a renewable source such as ethanol obtained from the fermentation of sugarcane. In Brazil ethanol is an economically viable source of energy as the country already has the infrastructure for the production and distribution of fuel for vehicles [69]. Moreover, ethanol is a liquid fuel making it easier to store and transport [70].

Ethanol has been used to obtain H_2 through SR (Equation 1.15), partial oxidation (Equation 1.16), and oxidative steam reforming (Equation 1.17). The SR provides a higher yield of hydrogen. However, it is a highly endothermic reaction, requiring a high operating temperature. Therefore, the SR reaction is suitable for ethanol conversion in the SOFC anode in a direct internal reforming reaction (DIR). Ideally, such reaction would only yield CO_2 and H_2; however, by-products such as CH_4 and CO and intermediate non-reformed by-products (e.g., acetaldehyde and ethylene) are formed reducing the yield of H_2 and leading to carbon deposition on the surface of the cell or of the catalyst compromising the performance of the cell.

$$CH_3CH_2OH + 3H_2O \leftrightharpoons 6H_2 + 2CO_2 \quad (1.15)$$

$$CH_3CH_2OH + 1.5O_2 \leftrightharpoons 3H_2 + 2CO_2 \quad (1.16)$$

$$CH_3CH_2OH + 2H_2O + 0.5O_2 \leftrightharpoons 5H_2 + 2CO_2 \quad (1.17)$$

The Ni/YSZ cermet containing a high Ni content (> 30 vol%) is usually the anode material in an SOFC. When ethanol is directly purged into the conventional anode material, several reactions take place simultaneously. The high carbon content of the fuel and the low oxygen partial pressure favours thermodynamically the deposition of carbon on the surface of the anode leading to a fast and irreversible deactivation of the fuel cell [71]. The carbon formation in the anode will depend on the reaction temperature, the ratio of steam to ethanol for the SR reaction, the composition of the anode, and the use and composition of the catalyst [72]. Carbon deposition on metal surfaces and on the support exposed to hydrocarbons has been extensively explored. Great emphasis is given on finding the carbon source (decomposition of hydrocarbons, CO disproportion, and olefins polymerization), and the type of the carbonaceous deposit, as it can be found with an amorphous and filamentous (ordered) structure [72–75].

Several strategies have been proposed to minimize carbon deposition on an SOFC. One strategy is to use a higher water to fuel ratio that allows carbon gasification and avoids the thermodynamic condition in which carbon deposition is favoured. This is because the SR and water gas-shift reactions (Equation 1.18) are in thermodynamic equilibria. However, large amounts of water in the system lead to a reduction in Nernst potential as represented by the overall efficiency of the fuel cell [76].

$$CO + H_2O \leftrightharpoons H_2 + CO_2 \qquad (1.18)$$

Another way to avoid carbon deposition is to formulate anode materials with a lower Ni relative volume fraction. Decreasing the Ni content increases the dispersion of the metal through the support and therefore increases its catalytic activity which in turn reduces the formation of carbon [77–79]. However, there is a compromise between metal content and electrical conductivity. A low metal content decreases the electronic conductivity of the material and disrupts the current collection. Other materials besides Ni/YSZ have been suggested as anodes for DIR [80]. Still a Ni/YSZ anode offers advantages due to its stability,

electrochemical properties, and low cost [81]. Moreover, Ni/YSZ has the highest performance on hydrogen.

Besides decreasing the Ni ratio, altering the composition of the support to one that is catalytically more active can reduce carbon deposition [82–84]. Redox supports, such as ceria-based oxides have higher oxygen storage-release capacity promoting mechanism for carbon removal, which in turn should contribute to the stability of the catalysts on ethanol conversion reactions [85].

Previous studies reported that ceria-based supports with metallic nanoparticles can be efficient for ethanol-fuelled SOFC. A fuel cell was tested with anhydrous ethanol. The anode was based on a ceria support with Co and Cu, the cell remained stable for 24 h at 850 °C under constant current, and no carbon formation was observed on the bimetallic anode [86]. Another study proposed a cermet anode with 50 wt% Ni on a CGO support as a catalyst for the steam reforming reaction of ethanol [87]. It was observed that at all tested temperature (600, 700, and 800 °C) there was deactivation of catalyst; however, at 800 °C there was a slower deactivation and carbon formation was not observed. They attributed this result to methane reforming reactions occurring at this temperature and to the high oxygen mobility of ceria at high temperatures promoting carbon gasification reaction (Equation 1.19).

$$C + H_2O \leftrightharpoons CO + H_2 \qquad (1.19)$$

Another interesting approach when carbon-containing fuels are used, is to functionalize different layers of the anode. In this strategy a catalytic layer can be used solely for the SR reaction of ethanol while the standard NiO/YSZ anode can be maintained as the anode support layer and for current collection [88,89]. The concept has been named gradual internal reforming (GIR) [90]. In this process a porous catalytic layer is used on top of the anode. The fuel is gradually reformed in the active sites of the catalytic layer before getting in contact with the anode layer, while at the anode the electrochemical oxidation of hydrogen occurs producing water vapor necessary for the SR reaction in the catalyst layer. In this configuration no additional input of water is necessary but the cell needs to be

constantly under load, producing electrical current and water to avoid carbon deposition due to the lack of an oxidizing agent [86].

Furthermore, the catalyst layer material can be chosen according to the fuel (ethanol, methane, etc.) to ensure the highest possible hydrogen conversion while the other components of the cell can be the state-of-the-art materials. A schematic representation of the SOFC with a catalytic layer is shown in **Fig. 1.10**.

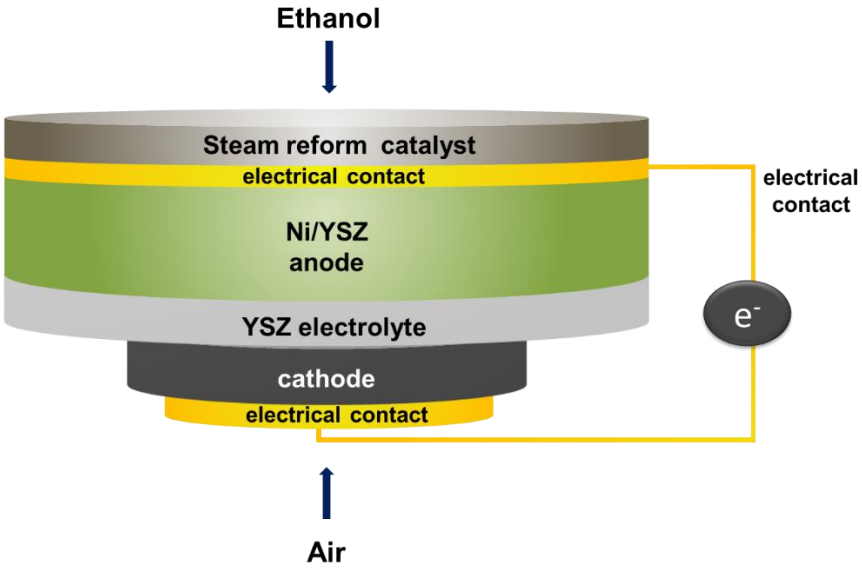

Fig. 1.10 Schematic representation of an SOFC with catalytic layer for direct internal reforming reaction of ethanol. Adapted from [81].

The GIR concept was demonstrated to ethanol to operate a cell for 100 h [88] and 400 h [91] at 850 °C without additional water with a catalytic layer containing 0.1 wt% Ir on a CGO support. The cell remained stable, and no carbon formation was observed. For the GIR reaction to occur the cell needs to be constantly polarized, such that it is drawing continuously electrical current and forming steam at the anode side. The steam is essential for ethanol SR (Equation 1.15) and for carbon gasification reaction (Equation 1.19). Steil et al [70] operated an anode supported cell with the 0.1 wt% Ir on CGO support catalytic layer for 700 h at 850 °C. And a post-test analysis of the cell showed a small formation of non-graphitic deposits that do not represent harm to the cell during the operation. Iridium, however, is not readily available and is regarded as a noble metal. Therefore a nickel catalyst is a more viable option for application in SR on an

industrial-scale, even though it is more prone to carbon formation than noble metal catalysts [85,92–94].

A Ni-based catalyst containing 18 wt% Ni on a ceria support was proposed [81]. The catalytic layer underwent a high temperature heat treatment compatible with ceramic processing conditions for evaluation of its stability for ethanol steam reforming and for GIR in an SOFC at 850 °C [81]. The fuel cell showed stable performance for 100 h of continuous operation under dry ethanol indicating that the formation of water by the hydrogen oxidation reaction sustained the catalytic steam reforming.

In the previous studies of ethanol DIR, the operating temperature of the fuel cell is in the high temperature range (> 800 °C). Such a high-temperature range is not consistent with the trend to decrease the fuel cell's operating temperature using SoA materials and configuration.

Liao et al. [95] fabricated a SoA anode-supported SOFC with a catalyst layer containing 20 wt% Ni on a CeO_2–ZrO_2 substrate and operated the cell with a high flow of steam and ethanol at 550, 600, 650 and 700 °C. They obtained comparable results to the cell operating with hydrogen, but they used a higher stoichiometry of H_2 while operating with ethanol than with H_2 and did not carry out a durability test to evaluate carbon deposition (degradation) with operation time.

In this Ph.D. work, CGO is studied as a functional layer for ethanol DIR SOFC. Nickel-based catalysts dispersed on CGO support are tested for the SR reaction of ethanol. The shape of the CGO support was controlled (nanocubes and nanorods) and different heat treatments were employed to evaluate how the morphology, grain growth, and Ni dispersion influence the catalyst activity. A catalytic layer of Ni/CGO was deposited on the anode of anode supported SOFC (as shown in **Fig. 1.10**) to analyse the stability of the cell under anhydrous ethanol.

1.5. Controlled synthesis techniques of nanomaterials

1.5.1. Background

A well-accepted definition of nanomaterial is a material composed of particles with dimensions below 100 nm and a structure and properties different than the bulk phase [96]. Due to their specific property, nanomaterials have helped improve existing technologies and develop new scientific fields. Nanomaterials have been applied in a variety of applications such as in medicine, biotechnology, engineering, electronics, etc. There is a vast interest in the use of nanomaterials in solid oxide devices due to their large surface area and specific surface and interface properties. In an SOFC, the use of nanoscaled electrolyte and barrier layer thin films is effective in reducing the ohmic resistance of the fuel cell and nanostructured functional layers can improve reaction kinetics at the interfaces by increasing TPB [40,59]. Furthermore, the use and adjustments of the precursors nanopowders can influence the reactivity, electrical conductivity, and catalytic activity. Fine-tuning the morphology of the nanoparticles affects the microstructure of the layers, such as porosity, specific surface area, and pore distribution. The overall performance of the SOFC will be strongly dependent on the composition of the component materials but also on its microstructure, which can be adjusted by synthesis and processing techniques.

Depending on the application a diverse number of methods can be used to synthesize nanomaterials with the desirable size, surface area, and properties The methods can be broadly divided into three: chemical, physical and bio-assisted methods [97]. There are two main different approaches to prepare nanoparticles. One starts with particles in the macroscopic scale, which are then reduced to the nanoscale. This approach is known as top-down. The second one is the bottom-up approach in which atoms or molecules are assembled to generate the nanoparticles. In this study the bottom-up approach was used to synthesize the precursor powders by the chemical methods of precipitation and hydrothermal synthesis. And the top-down approach was used to structure nanolayers by the physical method of pulsed laser deposition (PLD).

1.5.2. Chemical synthesis methods

The synthesis of ceramic nanopowders can be carried out by processes occurring inside a solution. Examples are precipitation, sol-gel, and hydrothermal routes. The synthesis can then be followed by washing and drying procedures and a calcination step for to form the metal oxide. The reaction occurs by the formation of a solid phase in a liquid medium, and the steps involved are nucleation and grain growth. The nucleation and growth kinetics of the particle formation is crucial to control the morphology and size of nanomaterials.

Nucleation is the process of formation of a new phase nucleus from an old phase whose free energy has become higher than the emerging phase. The free energy variation will depend on a component from the bulk ΔG_v and another from the surface ΔG_s [98]. Such that in a classical view, for a spherical particle of radius r, surface energy γ and free bulk energy ΔG_v then the free energy variation ΔG is given by (Equation 1.20):

$$\Delta G = 4\pi r^2\gamma + \frac{4}{3}\pi r^3 \Delta G_v \qquad (1.20)$$

The free bulk energy ΔG_v is dependent on the Boltzmann's constant, the temperature T, the supersaturation of the solution S, and its molar volume v (Equation 1.21).

$$\Delta G_v = \frac{-k_B T ln(S)}{v} \qquad (1.21)$$

From this Equation ΔG_v has a negative value whereas the first term in Equation 1.20, associated with the interfacial free energy ΔG_s ($4\pi r^2\gamma$) always has a positive value. Thus, the sum of the contributions from the surface and the bulk, considering spherical radius, can be plotted as shown in **Fig. 1.11.** In the plot the maximum is given by $d\Delta G/dr = 0$, which is equivalent to the critical energy ΔG_c and the critical radius r_c, corresponds to the energy and radius required to obtain thermodynamically stable particles within the solution.

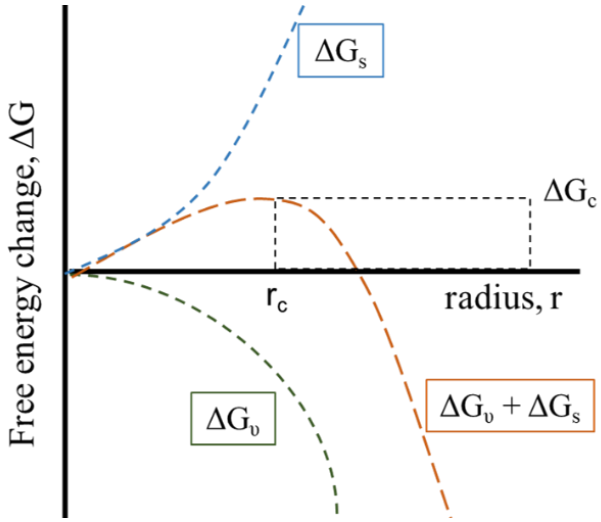

Fig. 1.11 Diagram describing the nucleation process by the classical theory, showing the critical radius and critical free energy [99].

Equation 1.20 expresses the Gibbs free energy for homogeneous nucleation, which occurs when the nuclei form throughout the old phase. The formation of nuclei at the vessel's interface, impurities, grain boundaries, and dislocations is known as heterogeneous nucleation. This type of nucleation is the most common in a liquid phase and industrial environments [99]. It has a lower energy barrier (ΔG_c) which facilitates the nucleation process. Unlike homogeneous, the heterogeneous nucleation does not occur by sphere formation but rather by the formation of a semi-circular nucleus on a substrate with a specific wetting angle, thus different interfacial energies. Accordingly, the heterogeneous nucleation is equal to the product of homogeneous nucleation by a factor Φ which is a function of the contact angle (θ ≤ π) (Equation 1.22)

$$\Delta G_c^{hetero} = \Phi \Delta G_c^{homo} \tag{1.22}$$

From a classical point of view [100], above r_c nucleation will occur following spontaneous process of nucleus growth, controlled by the diffusion of monomers from solution onto the surface of the nucleated particle. However, this approach does not consider the non-uniform growth and different sizes of particles during growth. Various models attempt to explain the mechanism involved in the further growth of a particle. And often it is assumed that more than one growth mechanism is involved. There are two well-known mechanisms commonly noted

for the growth of particles in the synthesis of ceramic nanopowders: Ostwald ripening and oriented attachment [101,102].

Ostwald ripening is a classical crystal growth mechanism [103]. It is caused by the change in solubility of nanoparticles depending on their size. Smaller particles have high surface energy and a high solubility and, therefore, redissolve creating a solute gradient within the solution. The redissolved ions diffuse through regions with higher solute concentration and precipitate on larger particles, allowing the larger particles to grow even more.

A non-classical mechanism that has been recognized to describe crystal growth and yield unique morphology is the oriented attachment process [104]. This process is based on the growth of particles by coalescence of crystals with similar crystallographic orientation. This mechanism is seen to be relevant in cases where particles have a high degree of freedom. In this system the particles undergo continuous rotation and have contact with each other until the crystallographic orientation of the two crystals is matched and they finally attach and grow together [104]. In **Fig. 1.12**, the mechanism of nucleation, diffusion growth, Ostwald ripening and oriented attachment are illustrated. It is often the case that in a solution several particle growth mechanisms, as well as heterogeneous nucleation, coexist and can occur simultaneously [101,105].

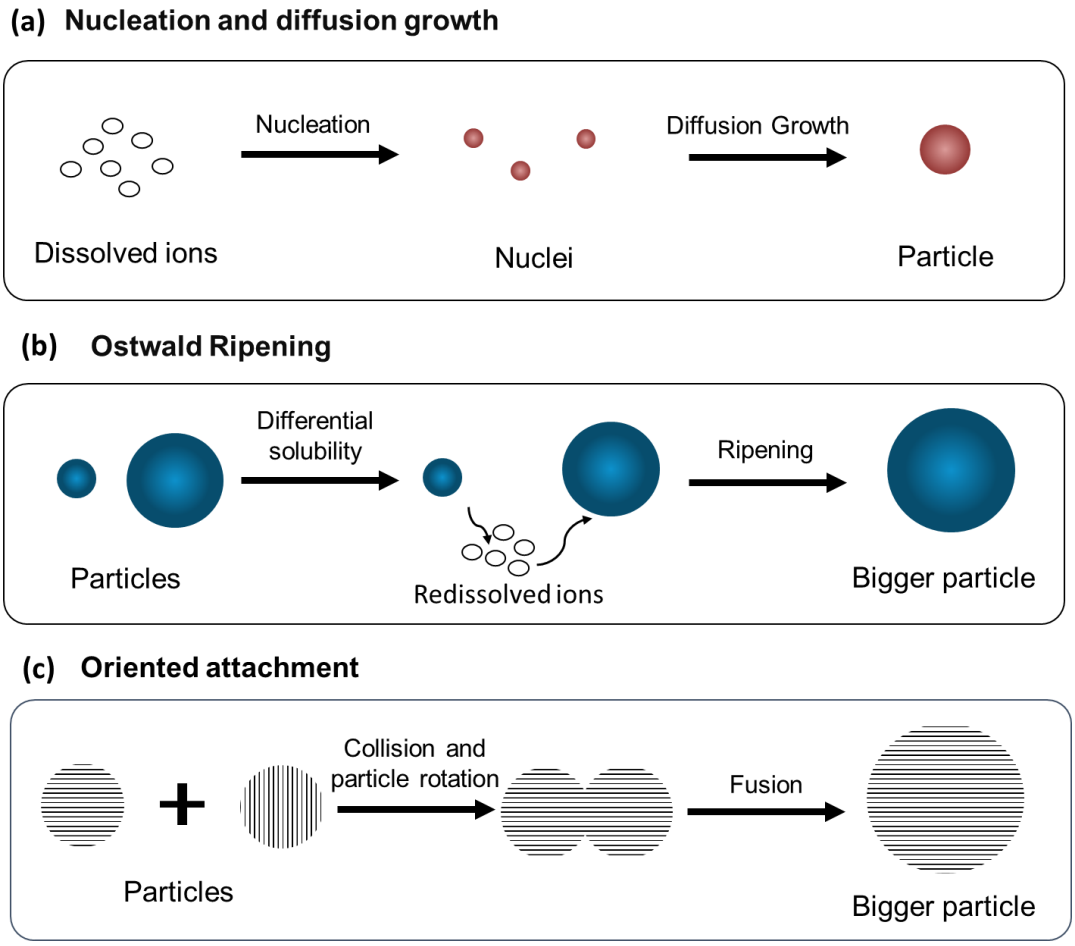

Fig. 1.12 Schematic representation of (a) nucleation and diffusion growth, (b) and (c) particle growth by Ostwald ripening and oriented attachment mechanisms, respectively. Adapted from [27,106].

In this thesis, cerium oxide doped with gadolinium was synthesized via two methods: by precipitation and in hydrothermal conditions. The synthesis used and the parameters, such as pH and temperature, influence nanocrystal formation, from nucleation to growth, affecting the crystallographic orientation, the morphology of the particles and therefore their properties.

1.5.2.1. Synthesis by precipitation

The precipitation route is widely employed as it is relatively fast, simple, and has a high yield. However, reaction parameters need to be finely controlled due to the dependence of the solid formation on conditions such as concentration, precipitation rate, temperature, pH, duration of reaction, etc. The precipitation of a metal hydroxide will occur once it has reached its solubility limit, which will be dependent on the temperature, pressure, and pH. In the precipitation route, the

concentration of the reaction and precipitation agent used will define the solution's pH and therefore the hydroxide formation [107].

Various precipitation agents have been studied to synthesize nanopowders used in components of an SOFC [36,107]. Ceria has been synthesized using a hydrolysing agent, such as urea [108] or hexamethylenetetramine (HMTA) [109–111], under continuous stirring for precipitation to occur. In such a reaction the nucleation occurs slowly and uniformly through the solution. In this work, HMTA-based precipitation was used. HMTA hydrolyses to produce formaldehyde and ammonia under acidic circumstances gradually releasing OH^-, as shown in the Equations below. A higher temperature is needed for such reactions to occur at a faster rate [110].

$$C_6H_{12}N_4 + 6H_2O \rightarrow 6H_2CO + 4NH_3 \quad (1.23)$$

$$NH_3 + H_2O \rightarrow NH_4OH \quad (1.24)$$

$$NH_4OH + H_2O \rightarrow NH_4 + OH^- \quad (1.25)$$

In this thesis, ceria nanopowder doped with gadolinium was synthesized by an HMTA-based precipitation and studied for its microstructural and electrochemical properties. Fe_2O_3 was then added to the precipitation as a sintering aid of the cerium oxide.

1.5.2.2. Hydrothermal synthesis

The hydrothermal route refers to chemical processes carried out in a sealed and heated aqueous solution held above the boiling point of water. Consequently, the pressure within the reaction is increased above atmospheric pressure. In most hydrothermal synthesis processes the solid is precipitated within the liquid, and a precipitation agent is required as in the precipitation method. But due to the high pressure and temperature, interactions between reactants are facilitated, and products with higher crystallinity compared to the precipitation method can be obtained. Therefore, in the hydrothermal route the solid oxide can be formed within the solution without the need for further calcination step [107]. This method can be used to control particle morphology and crystalline phase by regulating reaction temperature, solvent properties, and time of aging [112].

The hydrothermal method is often used for the synthesis of nanocomposites containing ceria for application as catalytically active species [113]. Mai et al. [114] used to hydrothermal method to synthesize ceria with different morphologies and exposed crystal planes by changing the NaOH concentration and the reaction temperature. It was found that the (100)/ (110) planes found on the surface of ceria with nanorod and nanocube morphologies have higher OSC than the (111) planes found in ceria with polyhedron morphology. Papadopoulos et al. [115] employed a hydrothermal method for the synthesis of copper-ceria catalysts, it was observed that strong interactions between the copper and ceria and the even distribution of copper on the surface of ceria played a more important role in increasing the CO oxidation activity of the catalyst as compared to specific surface area and oxygen vacancy concentration. Yang et al. [116] synthesized ceria doped with copper oxide with different morphology by different synthesis methods to be used as a catalyst for the reaction of methanol steam reforming. The results have shown that ceria with the nanorod morphology prepared by hydrothermal synthesis exhibited the highest catalytic activity due to the stronger interaction between copper oxide and the ceria support and the highest content of oxygen vacancy on the surface of the catalyst. Rodrigues et al. [77] reported a synthesis of ceria doped with samarium nanowires via the hydrothermal route, which was then impregnated with Ni to be used as a catalyst in the ethanol steam reforming reaction. The catalyst synthesized exhibited dispersed Ni particles over the ceria support, a high surface area, and a high concentration of oxygen vacancies, properties that have enhanced the catalyst stability and performance for the SR of ethanol.

In this work, the hydrothermal method is used in the synthesis of CGO with nanorod and nanocube morphologies, which have been studied for its sintering, electrochemical and catalytic behaviour to be applied as an electrolyte and a catalytic layer in an SOFC.

1.5.3. Physical synthesis methods

Physical methods are often used to prepare nanomaterials and consist of the application of mechanical pressure, radiations, and thermal or electrical energy to produce a plasma. These methods have the advantage of not generating chemical contamination; however, they are more energetically consuming and usually

require more advanced equipment than the chemical methods. Examples of physical methods are high energy ball milling, inert gas condensation, flash spray pyrolysis, and physical vapor deposition [97]. The physical vapor deposition method consists of various vacuum deposition techniques used to produce thin films. In the SOFC context the use of thin films as components of the cell is of utmost interest to enhance performance and as a strategy to functionalize the materials [117]. In this project, the physical vapor deposition method by pulsed laser deposition (PLD) has been used to fabricate functional nanolayers in an SOFC.

1.5.3.1. Pulsed Laser Deposition (PLD) method

The PLD method consists of ablating a target material, a solid source, with a high-energy pulsed laser. Each pulse of the laser melts, vaporizes, and ionizes a small amount of material on the target's surface generating a plasma plume in the vacuum chamber, consisting of atoms, electrons, ions, molecules, and clusters. The plasma plume is propagated above the substate material where the species condense and start nucleating and growing. The repetition in the pulse of the laser starts the formation of thin films on the substrate's surface.

The PLD system is shown in **Fig. 1.13**. A typical PLD system is mainly composed of a high-energy laser, an optical system, a deposition chamber, a heating system, a substrate stage, and a target holder. Most of the lasers of the PLD system are excimer gas lasers. The laser beam is focused onto the target by the optical lenses. The target is usually set in motion (rotational and raster) to avoid repeated laser pulses on the same area creating defects on the target. The substrate holder is set parallel to the target at a fixed distance and heated at the desired temperature. The vacuum chamber is maintained under low pressure with a set flow of oxygen. Under this set up the deposition can lead to high-purity thin films with the desired structural arrangement and complex stoichiometry. The conditions set for the deposition will influence the final film characteristic such as phase, composition, and structure.

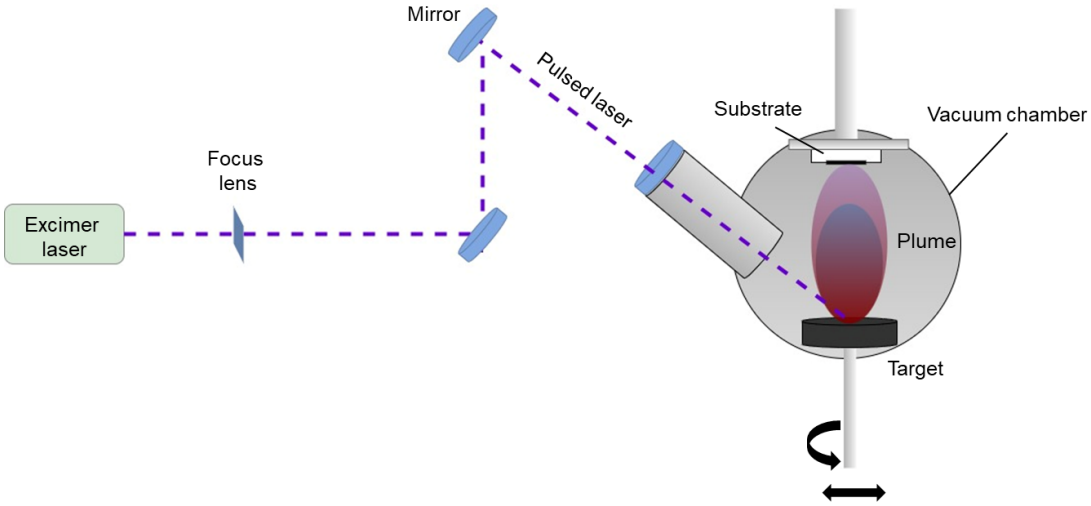

Fig. 1.13 Illustration of a PLD system. Adapted from [118].

The PLD method allows precise control over the stoichiometry and microstructure of the deposited materials and layers of higher density and degree of crystallinity can be achieved. This method has been thoroughly studied for the deposition of thin-film ceria barrier layers in SOFC exhibiting improvements over conventional deposition methods mainly attributed to the low thin thickness and to its high density achieved at a low temperature [57,119]. Besides its use in applying thin electrolyte layer, the PLD method has been investigated for the deposition of functional perovskite cathodes [63,120,121], composite anodes [122] as well as in the manufacture of μ-SOFC [123] for application in portable devices.

In this thesis, the PLD method was used to deposit a thin-film barrier layer of ceria doped with samarium (SDC) and a cathode nanocomposite functional layer of LSM/SDC.

1.6. Processing techniques of SOFC

1.6.1. Background

In a standard SOFC configuration one of the components of the cell is used as the structural material that acts as the mechanical support for the other layers, it is usually the thickest component of the cell. In a ceramic supported SOFC it is advantageous to have an anode support due to both a lower ohmic resistance and cost than the cathode. In this configuration the electrolyte can be made thinner and reduce ohmic losses due to ionic conduction. Conventional ceramic processing techniques can be used to fabricate the green substrate of the cell i.e., pressing and tape casting, followed by sintering to obtain the ceramic scaffold or substrate. Such processing steps can then be combined with deposition techniques such as screen printing, sputtering, dip coating, spin coating, spray coating, sputtering and the PLD, which then usually require a heat treatment to obtain the final body of the ceramic SOFC

In this thesis the uniaxial pressing and the tape casting techniques followed by sintering were used for substrate production and the subsequent functional layers were deposited by spin coating, spray coating, or PLD. In the following sections the tape casting and sintering techniques will be further detailed.

1.6.2. Tape casting

Tape casting is a low cost easily scalable process that allows the production of large-area ceramic tapes with various morphologies: from dense electrolytes to porous electrodes. The technique is well established and has been used to commercially produce electrolyte and anode substrates.

For the tape casting technique, a slurry is prepared with ceramic powder and organic materials such as solvent, plasticizers, binders, dispersants, and pore formers, if necessary. The preparation of the ceramic suspension is the most critical step in obtaining a resistant tape. The suspension must be homogeneous, with dispersed particles, where the ceramic grains are at a uniform distance and interact by polarization with the solvent. The dispersant is used in the suspension as an additive, which is adsorbed to the particles, promoting an increase in repulsion forces. The binder is used to form organic bridges between the particles, improving the green mechanical strength of the product. Plasticizers modify the

viscoelastic properties of the binder-particle system, lower the glass transition temperature of the binder, and ensure tape flexibility. The solvent is responsible for dissolving all the material and is evaporated after the formation of the tape. The rate of evaporation and diffusion of the solvent through the tape needs to be controlled when gluing the tape. Pore formers are added when the material needs porosity, and in turn are removed along with the other additives during calcination [124].

The milling step used in preparing the ceramic suspension aims to make the slip homogeneously and rheologically stable with a deagglomerated powder. The shear force promotes the dispersion of particles that break the agglomerates held together by Van der Waals forces.

After the milling step the slurry is deposited on a reservoir and cast on a polyester film carrier which is set in motion. The thickness of the tape is controlled by the doctor blade's gap. The casting process is illustrated in **Fig. 1.14**.

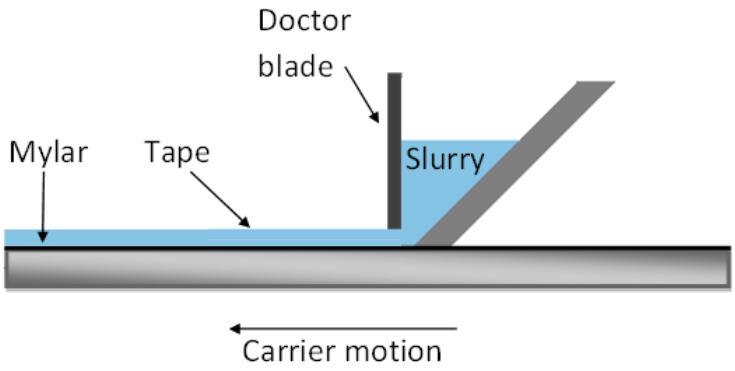

Fig. 1.14 Schematic representation of the tape-casting technique.

The development of the tape casting technique for both the electrolyte and the anode-supported half-cell was shared with a simultaneous M.Sc. project dedicated on developing the tape casting in our group at IPEN [125,126].

1.6.3. Sintering

Sintering is an essential processing step in the fabrication of ceramic components. Sintering consolidates a powder compact by the application of thermal energy. Such high temperature process involves grain growth and densification mechanisms, which are driven by thermodynamics and kinetic

processes. Sintering can be separated into two main categories: solid phase and liquid phase [127]. Several other types of sintering, such as cold, flash (electric field-assisted), transient liquid phase, and viscous flow sintering can be used [127]. In this study the focus will be on solid state sintering.

The driving force of sintering is the reduction of the system's surface energy by minimization of surface area. In solid-state sintering it is the replacement of solid/vapor interfaces with solid/solid which occur by grain growth and densification. Solid-state sintering is usually simplified and divided into three overlapping stages. In the initial stage the particles get in contact with each other, and necks start forming between the particles until reaching an equilibrium. There is not much densification occurring in the first stage. During the intermediate stage most of the densification occurs. Then grain growth and interconnection of porosity lead to the final stage where there is absence of interconnected porosity, pores become isolated and can then be annihilated.

There are various models for sintering mechanisms that consider distinguishable diffusions mechanisms such as surface diffusion, lattice diffusion, vapor transport, grain boundary diffusion and plastic flow [128–131]. Those mechanisms are divided into the densifying mechanisms (grain boundary diffusion, lattice diffusion from the grain boundary to the neck, and plastic flow) and the non-densifying mechanisms (vapor transport, surface diffusion, and lattice diffusion from the particle surfaces to the neck). which lead to neck growth and coarsening of the particles without densification. Such that if the non-densifying mechanisms dominate, there will be grain growth and no densification leading to a porous matrix, whereas if the densifying mechanisms are favoured then the material will be dense.

However, those models have high degrees of uncertainty and require several assumptions, and in many conditions, they are unable to capture all the features of real systems. Those models establish the mechanism of mass transport as the driving force and propose that the kinetics of the processes lead to densification [132]. Castro and Gouvêa [133,134] proposed an approach emphasizing the effects of the thermodynamics of the interfaces (grain boundary and surface area) in the sintering mechanism. They have demonstrated that by introducing a dopant, the surface, and grain-boundary energies are changed, as the dopant is likely to

segregate in these areas and control the sintering [135]. However, in systems composed of random-sized nanoparticles with a high surface area it becomes even harder to predict the sintering mechanisms. It is proposed that a thermo-kinetic correlation considering both interfacial energies and diffusion coefficients define the sintering mechanisms of densification or non-densification [136,137].

The understanding of sintering thermodynamics and kinetics and its application in the design of microstructure is an important tool to enhance the material's performance and drive the cost of the processing lower, as a lower densifying sintering temperature leads to energy savings. In this context, experimental investigation of the sintering behaviour of CGO with sintering aids and through morphological control were investigated.

1.7. Scope

This doctoral work aims at the study and development of nanometric cerium oxide, with morphological control, obtained through chemical synthesis methods and by the advanced physical deposition method. The work proposes to demonstrate that through synthesis and processing adjustments, it is possible to control the sintering properties of ceria such that it can be optimized for different functional layers of SOFC, including as a diffusion barrier layer, electrolyte, and as a catalytic layer in ethanol fuelled SOFC. Such developments are discussed in the following chapters.

In the first part of this work (***Chapter 2***), we proposed a simple low temperature chemical precipitation route for the synthesis of nanometric CGO. The use of Fe_2O_3 as a dopant of CGO was investigated as a strategy to enhance densification. A thorough powder characterization was carried out to elucidate the mechanisms by which Fe_2O_3 acts as a sintering aid. This study advanced the understanding of the role of the dopant in enhancing the sintering behaviour.

In the second part of this thesis (***Chapter 3***), shape-controlled CGO, was synthesized through a hydrothermal synthesis. The hydrothermal synthesis yielded CGO nanorods and nanocubes, with unique properties. Morphological control is originally proposed as an alternative method to enhance or inhibit densification mechanisms. Exploring the distinct mass diffusion properties of shape controlled nanoceria, we demonstrate different applications for such material in SOFCs.

The first proposed application was the use of the CGO nanorods as an electrolyte in an SOFC fully sintered at the low temperature of 1150 °C. Such pioneering development is possibly the lowest sintering temperature achieved for an SOFC fabricated through chemical synthesis methods.

The second application approached was the use of the CGO nanorods and nanocubes as support materials for Ni-based catalysts for the steam reforming of ethanol. The catalytic activity is evaluated, and the catalyst is further applied as a catalytic layer of an SOFC. The Ni catalyst supported on the CGO nanorods was employed as a catalyst in SOFC fuelled by anhydrous ethanol and showed stability through operation. This work shows an SOFC operating by direct ethanol internal reforming at reduced temperatures compared to previous results. The

experimental results emphasize the importance of the ceria support morphology in the catalytic reaction.

In ***Chapter 4,*** the physical deposition method of PLD was applied to deposit nanostructured bilayers consisting of a barrier layer of SDC and self-assembled LSM-SDC composite nanofunctional layer as functional cathode in an SOFC. The experimental results indicated that the microstructural control of thin functional layers has a great potential to enhance SOFC durability.

Finally, ***Chapter 5*** reports the scientific contributions, final remarks, and the conclusions of the work carried out in this doctorate.

In ***Appendix* 1,** the early developments of the tape casting technique in our group at IPEN are exhibited. Traditional electrolyte and anode supported cells were fabricated through lamination and co-firing. Herein, the group intends to advance the fabrication of SoA fuel cells to be tested directly with ethanol and methane.

Chapter 2

Synthesis of CGO by precipitation and addition of Fe_2O_3 as a sintering aid

2.1. Introduction

The main drawback of cerium-based oxides in a multi-layered device is the high sintering temperature (usually ≥1500 °C) needed to obtain a dense layer [9,138,139]. Besides representing a costlier process, it can turn co-firing of the SOFC unviable by promoting both unwanted reactions between the fuel cells components and poor mechanical properties due to large grain size [140]. On the other hand, keeping a high surface area in high temperature applications, such as in chemical looping and heterogeneous catalysis, in which the catalytic activity of ceria depends on the active surface area is a major concern in increasing the durability of devices using this material [77,141]. Therefore, controlling the energetics of the high-surface area ceria nanoparticles is of crucial importance for several emerging technologies related to new energies and sustainable development.

Several techniques have been investigated to improve the sintering of cerium oxides, generally involving the control of the precursor ceramic powders [142,143]. The main ones include adding sintering additives, controlling the size and the morphology of the material [144–147]. Wet chemistry synthesis usually results in nanometric powders with high activity towards densification mechanisms. Moreover, densification temperature can further be reduced by the addition of transition metal oxides (TMOs) additives [148–151]. A particularly interesting TMO additive is Fe_2O_3, which besides acting as a sintering aid, has also shown to improve the grain boundary conductivity of ceria [152–154]. Additionally, Fe is present in the interconnect material used in SOFC and metal-supported cells [155]. Therefore, it is also important to study how Fe doping can affect the electrochemical behaviour of the fuel cell components.

The analysis of the distribution of the dopants in the staring powder of ceria is valuable to understand the sintering behaviour of ceria. And the dopant's distribution after sintering is important to evaluate the electrical behaviour of the material. Many researchers have studied TMO-doped CGO, for instance, Avila-Paredes et al. [156] have doped CGO with a small amount (<0.5 mol%) of iron oxide, and after sintering, no additional phases were detected. Pérez-Coll et al.

[157] and Taub et al. [145] have found that Co segregates at the grain boundaries of CGO at low sintering temperatures, which modifies the grain boundary conductivity and reduces the sintering temperature of CGO by over 150 ºC. Such studies have focused on the sintering and conductivity behaviour towards TMO-doped CGO. On the other hand, a more detailed characterization of the distribution of the dopants in the powders is missing. Such characterization is an important step to further understand the behaviour of the dopants upon sintering and their effect on the electrical properties.

The sintering additive added to a nano-oxide can follow distinct paths: form a solid solution, segregate at interfaces, or precipitate a second phase. However, the exact path varies from system to system and relating the amount of additive to the preferred equilibrium state cannot be predicted with certainty. The extension of the bulk solubility, for instance, relies on the enthalpy of mixing, the enthalpy of segregation, and the availability of the grain boundaries (GB) since the total energy of the system accounts for the bulk volume and the total interfacial areas [158]. The enthalpy of interface segregation (ΔH_{seg}) (Equation 2.1) can be associated with different parameters such as the difference in interface energy between the dopant and the host (ΔH_{σ}), the elastic solute strain energy owing to the size difference between the dopant and host ions (ΔH_{ε}), the solute-solvent interaction (ΔH_{ω}), and the electrostatic potential/charge compensation (ΔH_{ϕ}) [159].

$$\Delta H_{seg} = \Delta H_{\sigma} + \Delta H_{\varepsilon} + \Delta H_{\omega} + \Delta H_{\phi} \qquad (2.1)$$

The additive is expected to segregate at the interface with higher energy to minimize the system's overall energy [160]. Thus, if the dopant preferably segregates at the grain boundary it will decrease the grain boundary energy favouring densification. Therefore, the segregation of species in nano-oxides plays a crucial role in the microstructural evolution during sintering.

In this study, the sintering and electrical behaviour of CGO doped with approximately 0, 1, and 5 mol% Fe_2O_3 were evaluated. The surface segregation of the dopant was determined by the superficial lixiviation method, which helped to understand the higher densification of the doped samples during sintering. The

electrochemical analyses showed that the doped material is suitable to use as a functional layer in a solid oxide fuel cell.

2.2. Experimental

Gadolinium-doped (10 mol%) ceria (CGO), CGO doped with 1 mol% Fe_2O_3 (1Fe-CGO), and CGO doped with 5 mol% Fe_2O_3 (5Fe-CGO) were synthesized using an aqueous precipitation method [161]. The precursors used were cerium (III) nitrate, ($Ce(NO_3)_3 \cdot 6H_2O$, 99%), gadolinium (III) nitrate ($Gd(NO_3)3 \cdot 6H_2O$, 99.9%), and iron (III) nitrate ($Fe(NO_3)_3 \cdot 9H2O$, 98%), all from Sigma Aldrich. An aqueous solution was prepared with stoichiometric amounts of cations. Hexamethylenetetramine (HMT, 99%, Sigma Aldrich) was slowly added to the solution under constant stirring for 3 h at 85 °C to obtain the precipitated oxides. The products were washed by successive rounds of centrifugation with water and isopropyl alcohol and dried at 100 °C for 12 h and then calcined in air at 500 °C for 2 h. The calcination temperature was established by a thermogravimetric analysis (TGA, Setaram Labsys), between room temperature and 800 °C with a heating rate of 10 °C min^{-1} under synthetic air flow.

The powder X-ray diffraction (XRD) patterns were obtained using a Philips X'Pert-MPD diffractometer with Cu K_α radiation over the 5-90° 2θ range at 0.02° 2θ steps per second. The diffractograms were analysed using the X´Pert Highscore software, which was used to calculate the lattice parameters and crystallite sizes by the Rietveld method using $MgAl_2O_4$ as standard.

The chemical compositions were determined by inductively coupled plasma atomic emission optical spectroscopy (ICP-OES) using a Spectro Across spectrometer. The densities of the powders were determined using a Micrometrics AccuPyc II 1340 gas pycnometer after 200 purges for degassing. The specific surface areas (SSAs) of the samples were determined by nitrogen gas adsorption measurements (at 77 K) (Micromeritics Gemini VII) according to the Brunauer, Emmett-Teller (BET) method. Before the analysis, all samples were degassed under vacuum at 300 °C for ~18 h in a Micromeritics VacPrep 061. The morphology of the powders was analysed by scanning transmission electron microscopy (STEM) using a JEM-2100 (Jeol) microscope operated with a parallel beam at 200 kV, equipped with a 4kx4k (TVIPS) camera. The distribution of the

atomic elements of the CGO and 5Fe-CGO samples was qualitatively analysed by electron energy loss spectroscopy (EELS) mapping images.

Cylindrical pellets of 6 mm in diameter of CGO, 1Fe-CGO, and 5Fe-CGO were prepared by uniaxial pressing (1 ton·cm^{-2}) and were sintered at 1200 ºC and 1400 ºC, 1 h dwelling, for microstructural analysis. The microstructures of the sintered samples were analysed by scanning electron microscopy (SEM, Inspect F50) with a secondary and backscattered electron detector. The SEM analyses were carried out in polished and thermally etched (1100 ºC and 1300 ºC for the samples sintered at 1200 ºC and 1400 ºC, respectively) surfaces. The average grain sizes were evaluated by using the ImageJ software. The energy dispersive spectroscopy (EDS) elemental mapping of the CGO samples sintered at 1400 ºC was obtained with the SEM JSM-6010LA microscope.

The surface excess of Fe_2O_3 in CGO nanoparticles was determined by the superficial lixiviation method following a protocol described elsewhere [160,162,163]. Typically, the experiment was performed by ultrasonicating ~100 mg of the as-prepared powder with 2 g of 0.1 M HNO_3 solution (pH = 1) for 1 h. Next, the separation of supernatant and powder was carried out by centrifuging at 13,000 rpm for 1 h. Subsequently, ~1 g of the supernatant solution was collected and diluted in ~10 g of H_2O. These solutions were analysed by ICP-OES to determine the precise composition, providing the quantity of lixiviated ions from the surface of the nanoparticles.

Cylindrical pellets of 6 mm in diameter of CGO, 1Fe-CGO, and 5Fe-CGO were prepared by uniaxial pressing (1 ton·cm^{-2}) for thermomechanical dilatometry analysis (TMA). The analysis was carried out by the Setaram Labsys equipment between room temperature and 1400 °C with a heating rate of 10 °C·min^{-1} under synthetic air flow of 50 ml·min^{-1}.

The electrical properties of cylindrical pellets (typically, 10 mm diameter and 2 mm thick) sintered at 1400 ºC, 1 h dwelling, were analysed by electrochemical impedance spectroscopy measurements (EIS), under synthetic air flow, in the temperature range of 300 °C – 800 °C. The impedance measurements were performed by the Novocontrol frequency analyser (Alpha A), using a frequency between 10 MHz and 1 Hz and an ac amplitude of 100 mV. A high-purity gold paste was used to prepare the electrodes in Au/CGO/Au symmetric cell

configuration. The collected diagrams were analysed with the Zview software. Total resistance was measured by EIS including both the bulk and grain boundary contributions, and the total conductivity values were calculated by normalization of the sample's dimensions. The activation energy of the electrical conductivity (σ) of samples was calculated through the Arrhenius Equation 2.2:

$$\sigma T = Ae^{-(E_a/kT)} \tag{2.2}$$

where A is the pre-exponential factor, E_a is the activation energy, k is the Boltzmann constant and T is the absolute temperature.

2.3. Results and discussion

Thermogravimetric analyses (**Fig. 2.1**) of the as-synthesized powders of CGO, 1Fe-CGO and 5Fe-CGO were carried out to establish the calcination temperature. The materials exhibited a similar mass loss behaviour with increasing temperature. A greater mass loss is observed for the iron doped compounds. It was verified by the TGA and derivative curves that the total mass loss up to 800 °C occurred in two main stages: i) between 30-150 °C associated with the release of residual water, and ii) between 180-400 °C a ~10% mass loss attributed to the complete release of nitrate ions and organics in the form of CO_2. A calcination at 500 °C for 2 h was defined as from this temperature onwards there is no significant mass loss.

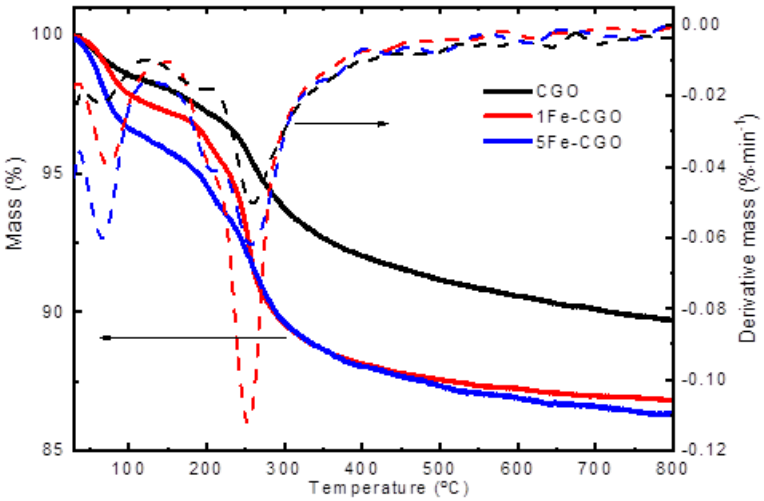

Fig. 2.1 TGA, with mass and the derivative of mass, of the as-synthesized powder of CGO, 1Fe-CGO and 5Fe-CGO.

The X-ray diffraction (XRD) patterns of the studied samples are shown in **Fig. 2.2**. The diffractograms were indexed as the single-phase fluorite structure of ceria (ICDD 96-900-9009). No second phase was detected by the XRD, suggesting that both the gadolinium and iron were either dissolved in solid solution or segregated at the interfaces of ceria nanoparticles. Broad peaks typical of nanosized crystallites can be observed. Increasing Fe content resulted in an increased broadening of the diffraction peaks, indicating decreased crystallite sizes, as shown in **Table 2.2.**

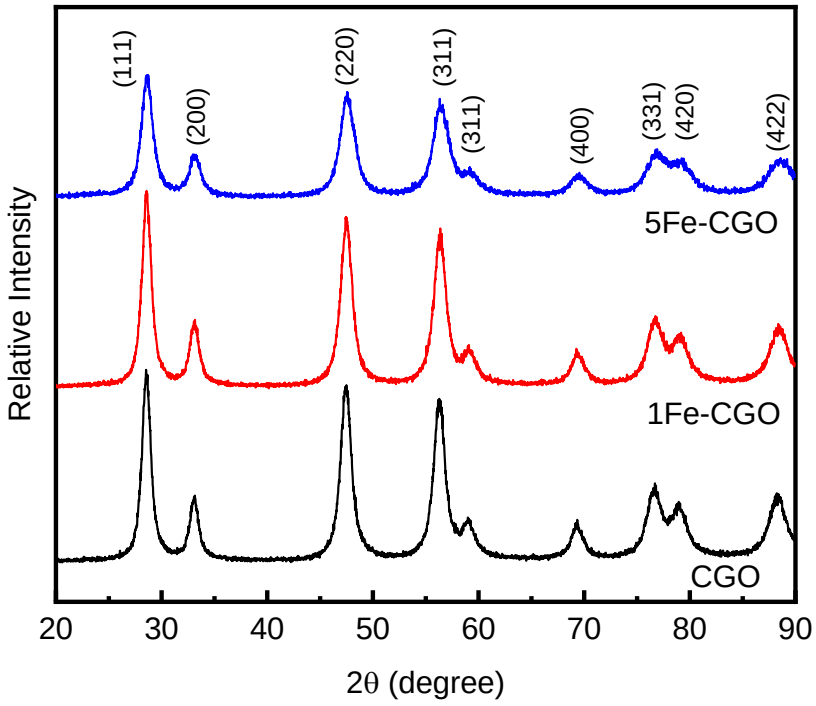

Fig. 2.2 XRD patterns of CGO and Fe-doped CGO.

The chemical composition of the CGO powders analysed by ICP-OES are shown in **Table 2.1**. The results show that the measured amount of gadolinium was close to the nominal 10 mol% for all samples. The 1Fe-CGO and 5-Fe-CGO samples contained 1.5 mol% and 4.4 mol% Fe_2O_3, respectively.

Table 2.1 Chemical composition of the CGO powders determined by ICP-OES.

Sample	Fe (mol%)	Gd (mol%)	Fe_2O_3 (mol%)	Gd_2O_3 (mol%)
CGO	0.0	10.6	0.0	5.3
1Fe-CGO	3.0	10.4	1.5	5.2
5Fe-CGO	8.8	9.0	4.4	4.5

By using the XRD and BET data the crystallite size, lattice parameter, density, specific surface area (SSA), total specific surface area (TSA), specific GB interface area (SGB), and SGB/SSA ratio of samples were determined, as listed in **Table 2.2**. The crystallite sizes decreased as the iron content increased, a feature associated with the effect of segregated dopants on reducing the interfacial energies [164–167]. According to coarsening models, during the isothermal growth of nanoparticles, the average particle size (d_t) dependence with time (t) follows a general law of growth (Equation 2.3).

$$d_t^n - d_0^n = kD\sigma_i(t - t_0) \tag{2.3}$$

where, d_0 is the average particle size at t_0; D is the diffusion coefficient; σ_i is the interface energy; k is a constant that depends on the approach to develop the kinetic equation; the exponent n =2, 3, …, generally reflects the growth mechanism [168]. According to Equation 2.3 a small crystallite size can be favoured at a given temperature if the σ_i is reduced.

The reduction in interfacial energy is intrinsically connected to interfacial segregation as described in Equation 2.4, which is based on an extension of the Gibbs adsorption isotherm [169,170].

$$\sigma_i = \sigma_0 - \Gamma_i \Delta H_{seg} \tag{2.4}$$

where σ_i is the interface energy of doped material, σ_0 represents the interface energy of the undoped material, ΔH_{seg} is the enthalpy of segregation, and Γ_i is the solute excess at the interface, expressed by n/A , in which n is the amount of the component at the interface and A the interface area. Equation 2.3 holds for both

the solid-vapor (surface) and solid-solid (grain boundary) interfaces. However, such a relation is strictly valid for systems with a single-phase and low concentration of dopants [160]. Based on Equation 2.3 and Equation 2.4, and the decreased crystallite size upon Fe addition, it is possible to expect that the interface excess is likely to take place in the Fe-doped CGO samples.

The calculated cubic lattice parameter of the CGO sample was 5.4277 ± 0.0017 Å. The CGO lattice parameter is slightly higher than that of CeO_2 (a = 5.4110 Å, ICDD 96-900-9009). Such lattice expansion is due to the difference in the ionic radius of Gd^{3+} (0.105 nm) and Ce^{4+} (0.097 nm) with coordination number VIII [151]. Previous studies of similar CGO samples have reported lattice parameter in the range of 5.4166 Å to 5.42 Å [151,171–173]. The lattice parameters of Fe-doped CGO linearly decreased as the amount of iron increased in the sample. This linear relationship can be fitted as $a = 5.427 - 0.1733x$. The observed decrease of lattice parameter is possibly attributed to the smaller radius of Fe^{3+} (0.078 nm) than that of Ce^{4+} (0.097 nm) and Gd^{3+} (0.105 nm) [160,172].

The densities of the Fe-CGO powders measured by gas pycnometry are shown in **Table 2.2**. The pycnometry uses the gas displacement method to accurately measure the volume of the sample. The measurement procedure includes consecutive purges to ensure a clean surface, free of water and other possible adsorbed species before data collection. The measured density of the CGO powder (5.397 g·cm^{-3}) was much lower than the ~7.2 g·cm^{-3} theoretical density (CeO_2 – 7.22 g·cm^{-3}; Gd_2O_3 – 7.41 g·cm^{-3}). On the other hand, the density of the CGO sample calculated from XRD data was 7.149 g·cm^{-3}. Such a difference suggests that pycnometry density is possibly affected by the surface of the nanoparticles. In addition, nano-oxides with small crystallite sizes (≤ 20 nm) have been reported to exhibit smaller measured densities as compared to the theoretical ones [160,163,174]. Such an effect is still unclear, but was attributed to a surface structure disorder, which forms a superficial layer with a lower density, decreasing the overall density of the system [163]. As smaller crystallite size represents a high percentage of the total volume of the particle, surfaces with high number of defects are likely to induce a decreased overall density. Such an effect is more pronounced in the Fe-doped samples 1Fe-CGO and 5Fe-CGO, which have measured densities of 5.366 g·cm^{-3} and 4.746 g·cm^{-3} respectively. The

addition of iron can contribute to the decreased density of the CGO by a lower theoretical density of iron oxide (5.24 $g \cdot cm^{-3}$), but, more importantly, by the effect of decreased crystallite size due to segregated iron cations on the surface of the ceria crystal.

The BET measured SSAs of CGO, 1Fe-CGO, and 5Fe-CGO samples were 111.4, 106.9, and 108.1 $m^2 \cdot g^{-1}$, respectively. The incorporation of iron into the CGO system slightly decreased the SSA. This SSA reduction can be associated with the dopant's distribution into the CGO matrix. It can be better interpreted along with the calculated total specific surface area (TSA), specific GB interface area (SGB), and SGB/SSA ratio, shown in **Table 2.2**. The TSA was calculated using Equation 2.5, assuming spherical grains, by:

$$TSA = \frac{6}{\rho D} \tag{2.5}$$

where ρ is the density (**Table 2.2**) and D is the average crystallite size. The TSAs of all samples were higher than the SSA, which indicates that the particles agglomerated. The higher the difference between SSA and TSA, the higher the specific GB area, which can be calculated according to Equation 2.6.

$$SGB = \frac{(TSA - SSA)}{2} \tag{2.6}$$

The (TSA-SSA) difference is divided by two due to the intersection of at least two grains. The SGB increased as the amount of iron increased in the system. This behaviour indicates a possible preference of the dopant towards the GB segregation. As shown in Equation 2.4, the interface energy is directly related to interface segregation. Thus, if the SGB area increases, the GB becomes more thermodynamically stable compared to the surface, which indicates a reduction in the GB energy and an increase in GB excess [133,160].

The addition of Fe in the CGO resulted in single phase compounds, *i.e.*, no secondary phase was detected by the XRD (**Fig. 2.2**). Such a behaviour indicates that the dopant is either dissolved in solid solution or segregated at the interfaces. Although it is difficult to precisely determine the solubility limit of Fe_2O_3 into CGO

nanoparticles, similar systems, *e.g.,* Fe_2O_3-doped SnO_2, pointed out to a very low iron solubility, with the major fraction of the dopant segregated at the grain boundaries [162].

Table 2.2 Crystallite sizes, lattice parameters, density, specific surface area, total specific area, specific GB area, and SGB/SSA ratio of CGO and Fe-doped CGO samples.

Sample	Crystallite sizes (nm)	Lattice parameters (Å)	Density ($g \cdot cm^{-3}$)	Specific surface area ($m^2 \cdot g^{-1}$)	Total specific area ($m^2 \cdot g^{-1}$)	Specific grain boundary area ($m^2 \cdot g^{-1}$)	SGB/SSA ratio
CGO	8.5±0.1	5.4277±0.0017	5.397±0.027	111.4±0.6	130.8±1.7	9.7±0.9	0.09±0.01
1Fe-CGO	7.8±0.1	5.4213±0.0016	5.366±0.012	106.9±0.5	143.3±1.9	18.2±1.0	0.17±0.01
5Fe-CGO	6.5±0.1	5.4144±0.0020	4.746±0.020	108.1±0.5	194.5±3.1	43.2±1.6	0.40±0.01

To further investigate the distribution of the dopant on the CGO nanoparticles, the surface segregation was directly measured by using the selective solubility method. Such a surface lixiviation method was previously proposed and tested by Gouvêa *et al.* [168]. The method is based on the solubility difference between the dopant and the matrix, in which an acid solution selectively removes the exposed ions from the surface of the nanoparticle. Considering that the acid solution cannot access the ions located in both the GBs and the bulk, it is possible to determine the surface excess by quantifying the ion content in the solution used for the lixiviation of the surface. Following the procedure detailed in the experimental section, the surface excess (Γ) for the present system was calculated according to Equation 2.7:

$$\Gamma = n/SSA \qquad (2.7)$$

where *n* is the number of moles of dopant lixiviated for each sample.

The surface excess was measured for the three metals presented in this system (**Table 2.3**). Only a small amount of cerium (< 0.076 μmol·m^{-2}) was detected in the lixiviated solution, indicating the cerium oxide's stability in nitric acid. It is interesting to observe that ~0.2 μmol·m^{-2} of Gd segregated on the surface of the nanoparticles. The Gd amount was slightly smaller for the undoped CGO sample, and it was kept constant upon the addition of iron in the system. Thus, as a first result of this study it is shown that adding a sintering aid in Gd-doped ceria changes the distribution of Gd and possibly the formation of the ceria:gadolinia solid solution. This feature has a direct impact on the electrochemical properties of ceria-based compounds. The increment of Gd on the surface by the introduction of iron indicates a possible change in the Gd solubility affected by the Fe ions. The Fe^{3+} ions surface excess for 1Fe-CGO was very low, suggesting that the dopant's main fraction was segregated in the GBs. However, for 5Fe-CGO, a considerable increment in the amount of iron is detected on the surface, from 0.007 μmol·m^{-2} for 1Fe-CGO to 0.139 μmol·m^{-2} for 5Fe-CGO. In the Fe-CGO system, upon increasing the iron content from 1 mol% Fe_2O_3, the grain boundary reaches saturation and the amount of the dopant on the surface rapidly

increases for the sample with 5 mol% Fe. The lixiviation method showed the interaction of the Gd and the sintering aid and the distribution of the dopants in the material. Such a distribution has a direct impact on the properties of ionic conductors synthesized using simultaneous doping for ionic conductivity (Gd) and as a sintering aid (Fe).

Table 2.3 Fe, Gd, and Ce surface excess of CGO and Fe-doped CGO samples.

Sample	Γ (μmol·m^{-2})		
	Fe	Gd	Ce
CGO	0.001±0.000	0.197±0.001	0.006±0.000
1Fe-CGO	0.007±0.000	0.246±0.001	0.060±0.000
5Fe-CGO	0.139±0.001	0.245±0.001	0.076±0.000

Figs. 2.3 and **2.4** show the STEM-EELS images for CGO and 5Fe-CGO, respectively. The images evidenced that the nanoparticles are highly agglomerated, which confirms the high specific GB area data listed in **Table 2.2**. The EELS mapping images show that the atomic elements were homogenously distributed on the surface of the nanoparticles. For the CGO, iron was not detected, whereas for the 5Fe-CGO sample, iron was equally distributed along with cerium, gadolinium, and oxygen.

The experimental findings indicate that the iron segregated in CGO on both surface and GB, being the last one the dominant. The increased GB area observed in the powders doped with 5 mol% Fe_2O_3 suggests that the dopant can affect the solid-solid interface to facilitate the sintering process.

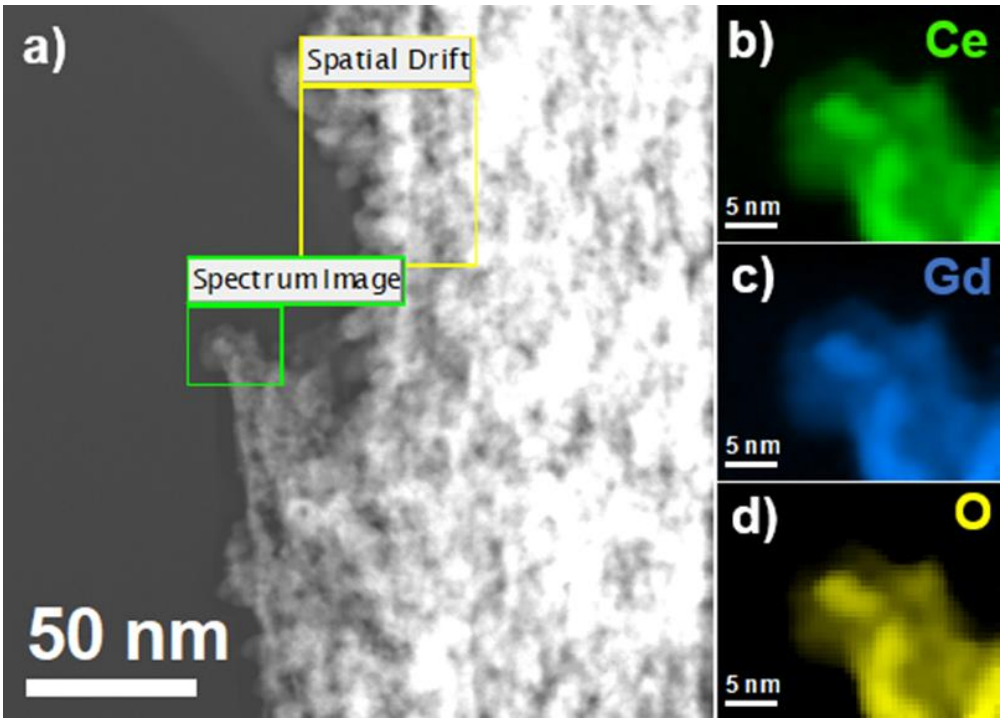

Fig. 2.3 STEM EELS of CGO.

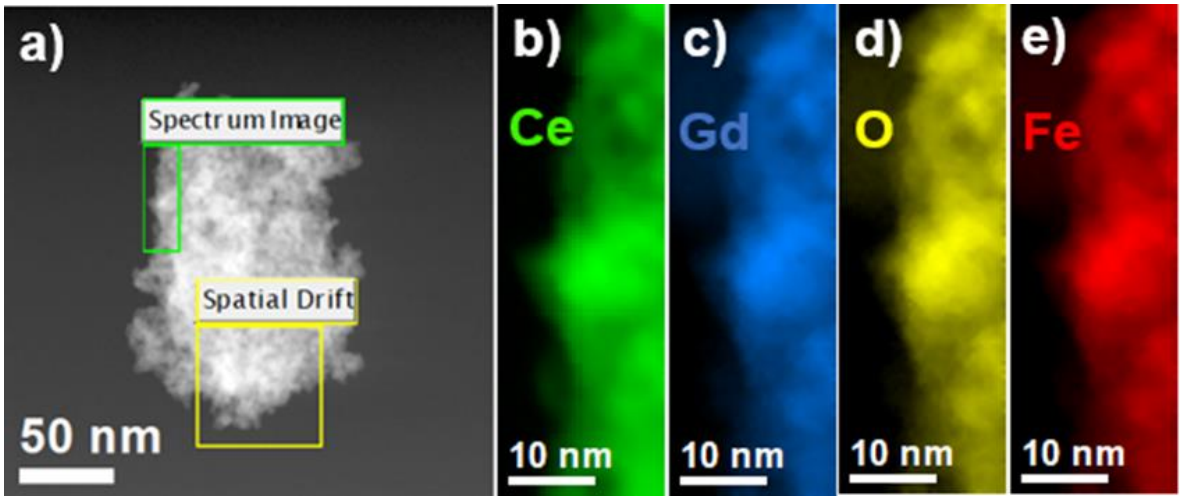

Fig. 2.4 STEM EELS of 5 mol% Fe-doped CGO.

The temperature dependence of the linear shrinkage and shrinkage rate profiles of the samples are shown in **Fig. 2.5**. All samples exhibited an onset of linear shrinkage at ~600 °C. The CGO sample had a temperature-driven retraction of ~20% at 1400 °C while Fe-doped samples had a ~28% retraction at the same sintering temperature. Interestingly, the Fe-doped samples showed two clear rate maxima from the shrinkage rate profiles, indicating a two-stage densification mechanism, usually attributed to composite materials [146,175]. The two well-

defined maxima of linear shrinkage rates for the Fe-doped samples are equivalent to densification and grain growth mechanisms [176]. The 1Fe-CGO sample exhibited the first maximum at ~1100 °C, whereas the 5Fe-CGO had the first significant retraction shifted to lower temperature (~880 °C). The second maximum of both Fe-doped samples coincide at ~1270 °C. It is observed that with increasing Fe_2O_3 content, the activation energy for densification decreased, as there was a displacement of the peaks of maximum shrinkage (sintering activity) to a lower temperature. The shrinkage profiles suggest a change in the densification mechanism upon Fe doping. There is an indication that Fe segregated in the grain boundary, decreasing the grain boundary energy, such that the sintering driving force is the high-energy solid-gas interface, favouring densification. From the experimental results, it is verified that the addition of small amounts of Fe_2O_3 alters the sintering mechanism, increasing the densification rate and reducing the CGO sintering temperature.

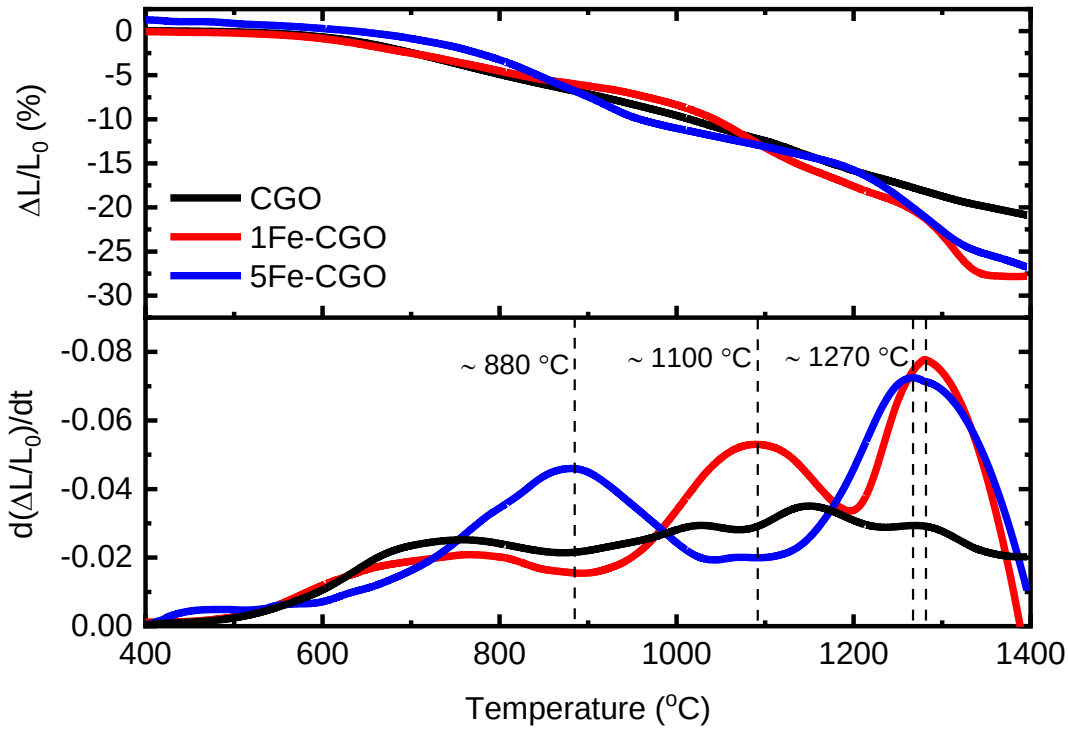

Fig. 2.5 Shrinkage curves profiles (top) and the differential shrinkage with respect to time (bottom) for CGO, 1Fe-CGO, and 5Fe-CGO samples.

In order to further study the effect of Fe doping on CGO, a temperature close to the maximum activity of the CGO sample was chosen, i.e., T = 1200 °C. **Fig. 2.6** shows the microstructural features of the polished and thermally etched samples sintered at 1200 °C. The microstructures agree with the discussed densification processes based on dilatometric analysis (**Fig. 2.5**). The CGO sample sintered at 1200 °C exhibited a porous structure with adherence of the particles forming distinguishable grain boundaries, compatible with an intermediary stage of densification. The images show that the 1Fe-CGO and 5Fe-CGO samples have achieved higher densification (~90% relative density), confirming the effectiveness of Fe_2O_3 as a sintering aid. The CGO, 1Fe-CGO and 5Fe-CGO samples presented average grain sizes of 0.018 ± 0.021 µm, 0.24 ± 0.14 µm and 0.37 ± 0.19 µm, respectively.

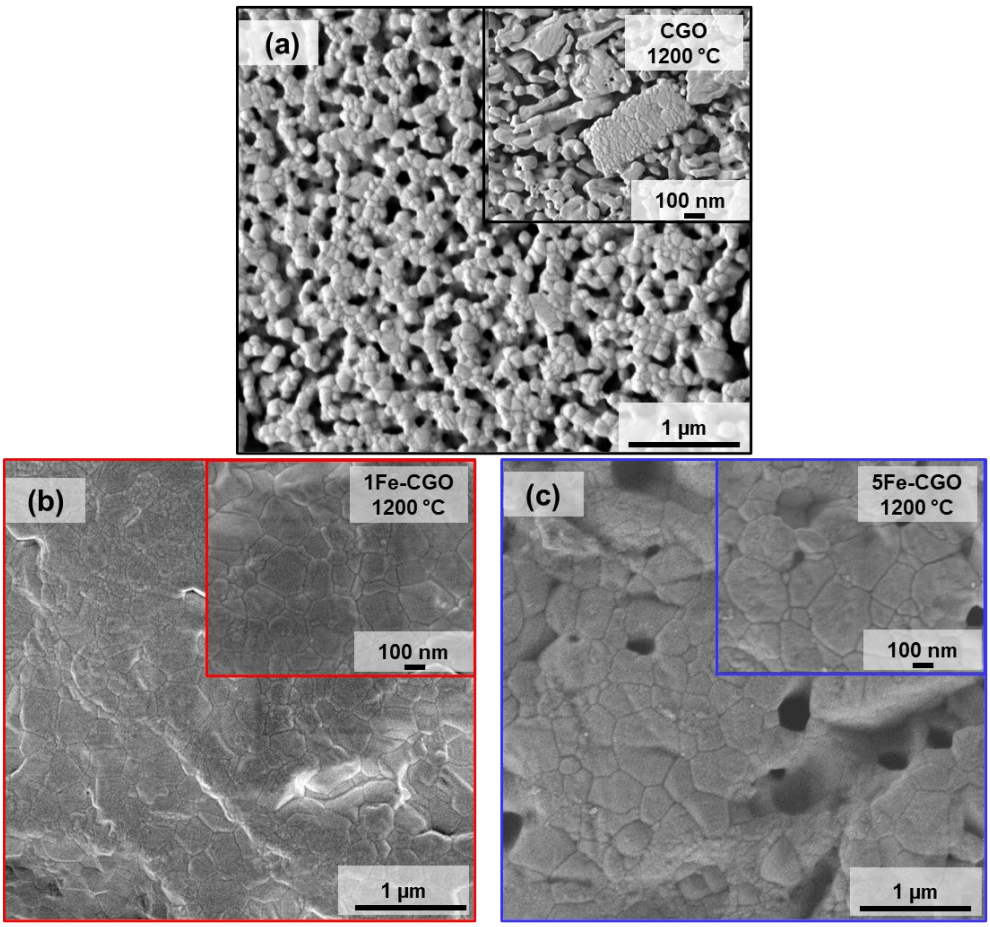

Fig. 2.6 SEM images with inset of great magnification of polished and thermally etched cross-sections of (a) CCO, (b) 1Fe-CGO and (c) 5Fe-CGO, all sintered at 1200 °C.

Fig. 2.7 shows the SEM images of the polished and thermally etched samples sintered at 1400 °C. The CGO sample sintered at 1400 °C exhibited a porous structure, similar to the sample sintered at 1200 °C (**Fig. 2.6**), necking is present through the grains related to an ongoing densification process. The images show that the 1Fe-CGO and 5Fe-CGO samples have achieved higher densification at this temperature (> 95% relative density). The 1Fe-CGO sample exhibited little residual porosity, mostly located at the triple points, while in the 5Fe-CGO sample the pores have been eliminated. The 1Fe-CGO sample presented an average grain size of 2.87 ± 0.98 µm and the 5Fe-CGO sample, an average of 2.69 ± 1.08 µm, representing a ten-fold increase in grain size as compared to the sample sintered at 1200 °C. The similar grain growth for both samples is consistent with the shrinkage profiles (**Fig. 2.5**) that show the maximum shrinkage rate and final stage of sintering activity at the same temperature

(1270 °C), as well as a similar intensity of the peak related to the maximum shrinkage rate.

In **Fig. 2.7** distinctive darker grains were observed in the Fe-doped samples (indicated by yellow arrows). Such darker grains increased with increased Fe doping and were absent in the samples sintered at 1200 °C (**Fig. 2.6**). The EDS analysis was carried out and the resulting elemental distribution maps of the Fe-doped samples are shown in **Fig. 2.8**. A clear correspondence between the EDS and phase contrast in SEM images evidenced that darker grains are isolated Fe-rich grains formed in both 1Fe-CGO and 5Fe-CGO sintered samples. The calculated volumetric fraction of Fe-rich grains was estimated at 1 and 5 vol% for the 1Fe-CGO and 5Fe-CGO samples, respectively equivalent to the molar fraction of Fe_2O_3 in CGO.

The second phase formation at 1400 °C indicates that the system reached a grain boundary saturation state [158]. As the grains grow and grain boundary specific area decreases, the net concentration of dopant increases until it occupies all available sites at the grain boundaries [177]. This increased dopant concentration is caused by the decrease in specific GB area because of the increased sintering temperature, which rapidly increases the concentration of solute atoms segregated at the GBs that induces the formation of a Fe-rich second phase [178].

The use of iron as a dopant in CGO samples facilitates densification during sintering. Firstly, during synthesis, most of the dopant segregates to the GBs, increasing the specific GB area (**Table 2.2**), which aids the densification at lower temperatures during sintering. This phenomenon is evidenced by the shrinkage rate profiles observed in **Fig. 2.5**, in which Fe-doped samples had the first significant retraction at a lower temperature (~880 °C) compared to CGO. As the temperature further increases and GB area decreases, dopant saturation occurs and the second phase forms.

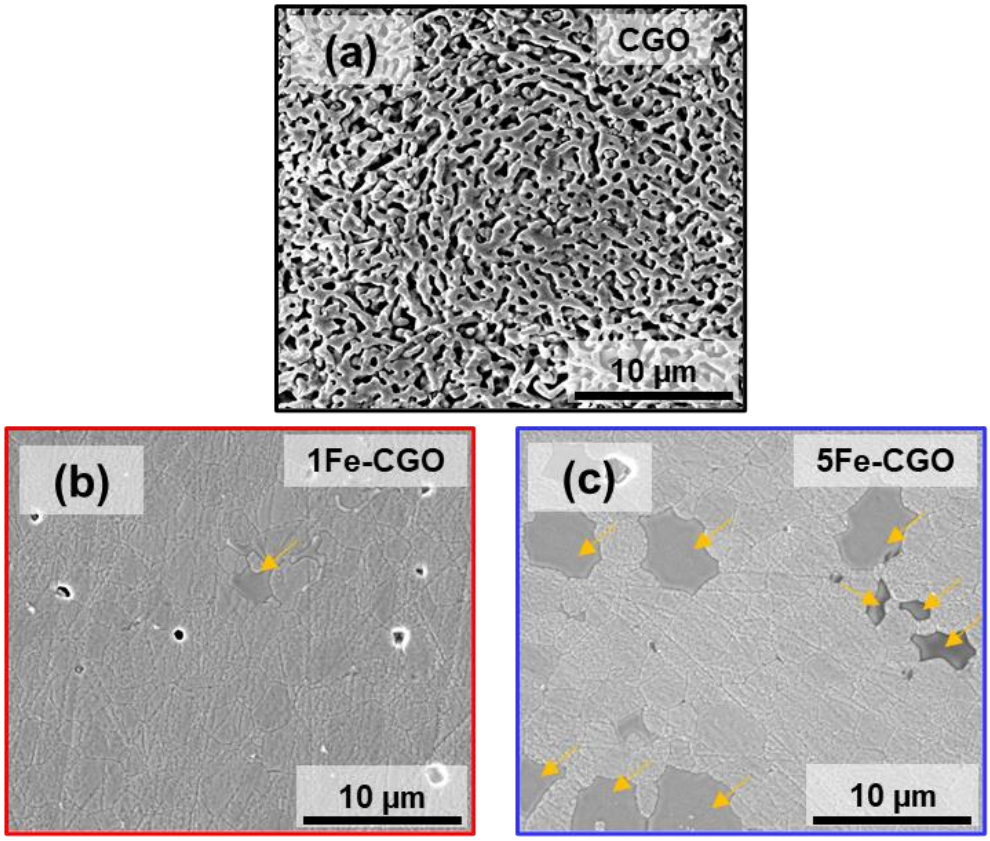

Fig. 2.7 SEM images of polished and thermally etched cross-sections of (a) CCO, (b) 1Fe-CGO and (c) 5Fe-CGO, all sintered at 1400 °C.

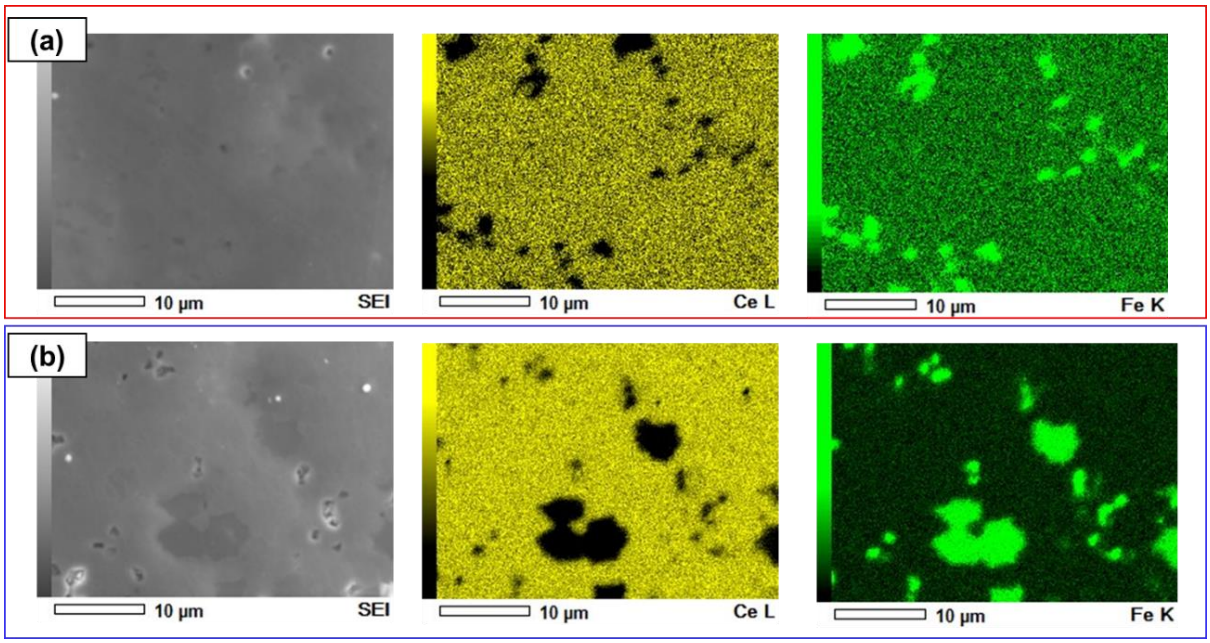

Fig. 2.8 SEM images of polished and thermally etched cross-sections and corresponding EDS elemental mapping of (a) 1Fe-CCO and (b) 5Fe-CGO, both sintered at 1400 °C.

The influence of Fe_2O_3 doping on the electrical properties of the CGO samples sintered at 1400 °C was evaluated through EIS. **Fig. 2.9** (a) and (b) show the EIS of the samples at 300 °C and at 600 °C under synthetic air. At 300 °C, the experimental EIS data show two semi-circles, which can be fitted with the equivalent circuit $(R_bCPE_b)(R_{gb}CPE_{gb})W_o$. Where R_b and CPE_b represent the semicircle related to the bulk resistivity (R_b) and corresponding capacitance in terms of phase constant elements CPE_b, at high frequency (>10^6 Hz). The R_{gb} and CPE_{gb} refer to the semicircle related to the grain boundary resistivity (R_{gb}) and corresponding capacitance CPE_{gb}, found at the intermediary frequency (10^6 – 10^5 Hz). The tail at low frequency was fitted with the Warburg element (W_o) and is due to the high polarization resistance of the electrode and will not be taken into consideration in this study. At 600 °C only one semicircle is observed and the EIS data at were fitted with the equivalent circuit $R_b(R_{gb}CPE_{gb})W_o$. Where R_b is the series resistance equivalent to the intercept of the data with the real axis at high frequency.

The total electrical resistivities of the samples under synthetic air **Fig. 2.9** (a) and (b) agree with the high density observed densities of the samples (**Fig. 2.7**). The undoped CGO sample presented a grain boundary resistivity higher than the Fe-doped samples, which was attributed to its porous microstructure [179]. Furthermore, at 600 °C the grain boundary resistance of the CGO sample is 10 times higher than the Fe-CGO samples. The bulk resistances at 300 °C and at 600 °C of the three samples are in the same order of magnitude revealing that the Fe had a negligible effect on the bulk conductivity. The Fe-doped samples show similar bulk and grain boundary resistance under synthetic air.

The experimental EIS data of the Fe-doped samples at 600 °C under a gas mixture of 4% H_2/Ar are shown in **Fig. 2.9** (c) and were fitted with the equivalent circuit $R_b(R_{gb}CPE_{gb})W_o$. The elements R_b and $R_{gb}CPE_{gb}$ are found in lower frequencies when compared to the spectra at the corresponding temperature under synthetic air (R_b at >10^4 Hz and $R_{gb}CPE_{gb}$ at 10^4 – 10^3 Hz).

The similar microstructure, grain size, and density of samples sintered at 1400 °C allows the evaluation of the CGO ionic conductivity with increasing Fe_2O_3 addition. The EIS measured under 4% H_2/Ar (**Fig. 2.9** (c)) was used to assess the performance of the Fe-doped samples at reducing atmosphere. Under low pO_2,

the bulk (R_b) and GB resistances (R_{gb}) exhibit a mixed ionic-electronic conductivity [180,181]. The increase in Fe content decreased both bulk and GB resistances at low pO_2. It has been reported that under reducing atmosphere iron oxide (Fe_2O_3) reduces to Fe_3O_4 at 300 °C and then to metallic Fe at 450 °C [182]. The secondary Fe-rich phase, observed in **Fig. 2.8**, is prone to reducing and therefore to exhibit a relatively high electronic conductivity. Such that increasing its content also decreases bulk resistance, a feature more pronounced in the reducing atmosphere.

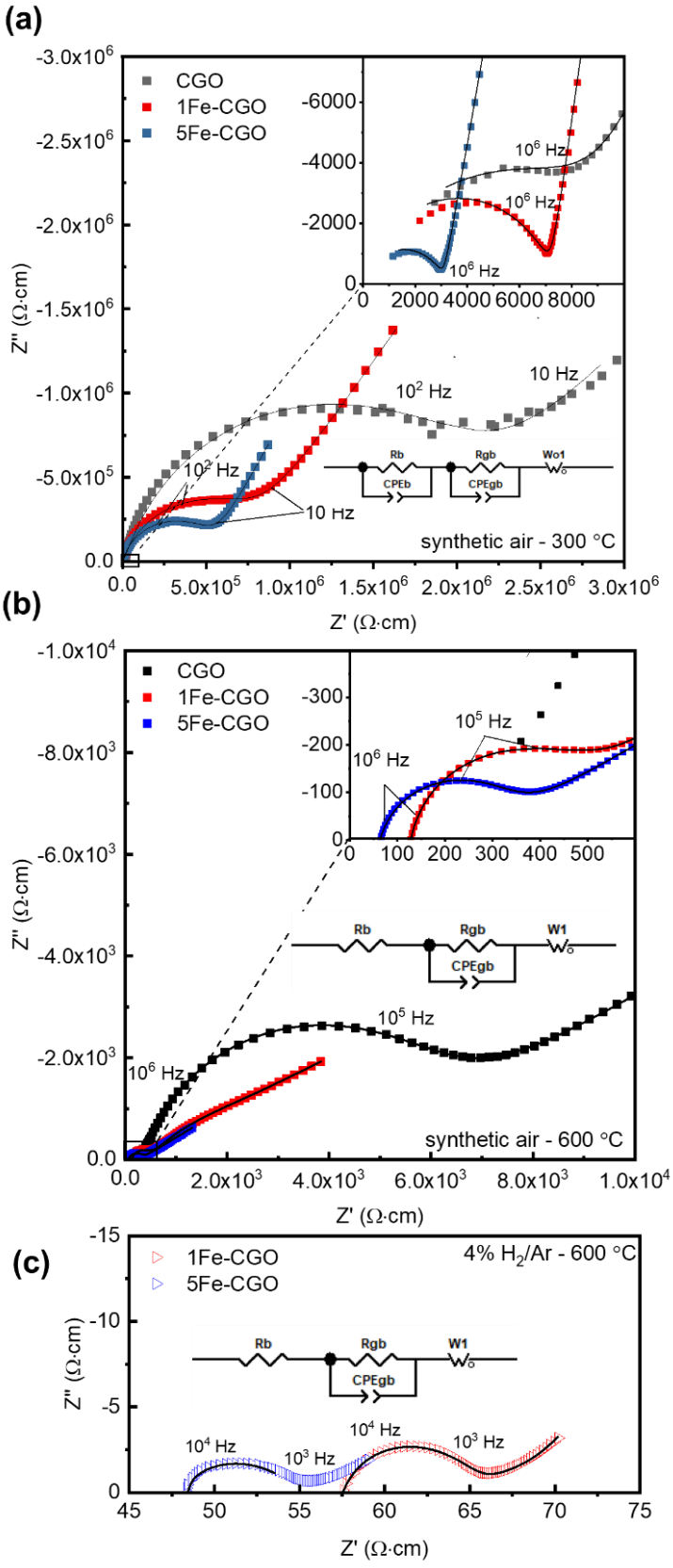

Fig. 2.9 EIS diagrams of CGO and Fe-doped CGO samples measured under synthetic air flow (a) at 300 °C, (b) at 600 °C and (c) of Fe-doped CGO samples measured under 4% H_2/Ar at 600 °C.

Arrhenius plots of the total conductivity obtained under synthetic air and 4% H_2/Ar, are shown in **Fig. 2.10**. The calculated activation energies of CGO were in the same range as reported literature [183]. The addition of Fe increases the density of the samples and therefore it increases the total conductivity of the samples sintered at 1400 °C. The 5Fe-CGO sample presented the highest conductivity in both atmospheres (as seen in **Fig. 2.9** (b), and 4% H_2/Ar, **Fig. 2.9** (c) at the same temperature). The total conductivity of the Fe-doped samples measured in H_2/Ar was close to one order of magnitude higher than in synthetic air. In synthetic air, at 600 °C, the conductivity was of 1.6×10^{-3} $S \cdot cm^{-1}$ for the 1Fe-CGO sample and 2.6×10^{-3} $S \cdot cm^{-1}$ for the 5Fe-CGO sample, whereas under H_2/Ar the conductivities were of 1.5×10^{-2} and 1.8×10^{-2} $S \cdot cm^{-1}$, respectively.

The higher conductivity of ceria under hydrogen is related to the mixed ionic-electronic property of the ceria-based materials. At high temperature and low oxygen partial pressure ceria exhibits an n-type conductivity due to its double valence state [184–186]. In high oxygen partial pressure (synthetic air), the electrical conductivity is mostly ionic, whereas in 4% H_2/Ar, a large fraction of electronic charge carriers develops. The effect of doping CGO with an increased amount of Fe (from 1 to 5 mol%) was similar in both atmospheres causing an increase in both ionic and electronic conductivities.

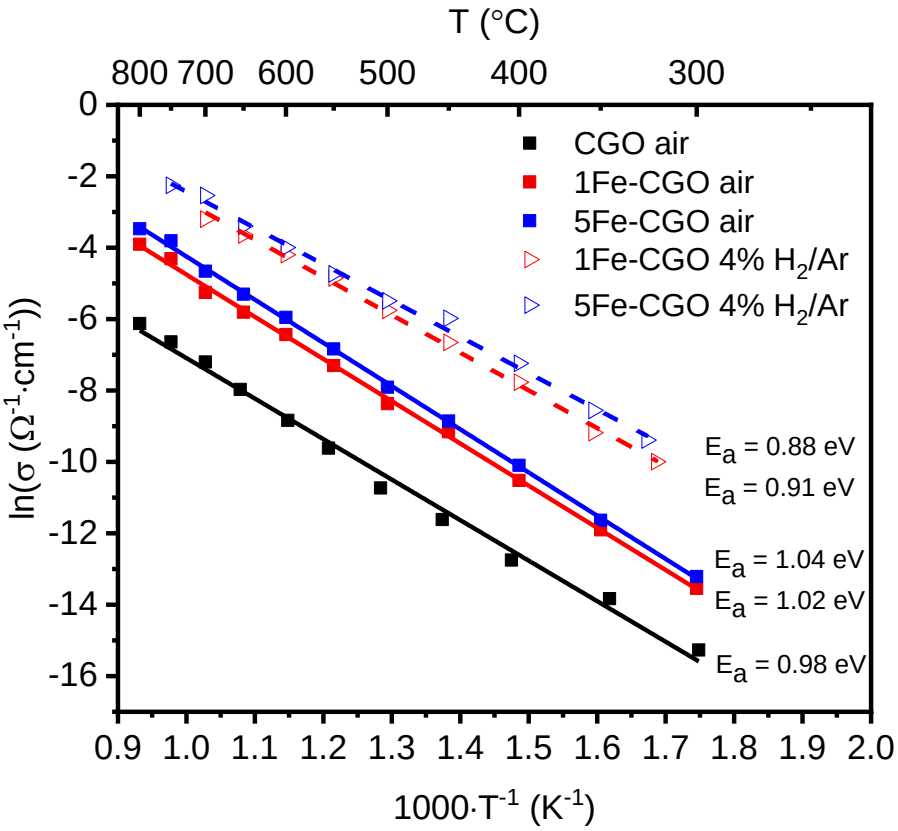

Fig. 2.10 Arrhenius conductivity plots of CGO and Fe-doped CGO samples sintered at 1400 °C measured under synthetic air flow and of under 4% H_2/Ar.

2.4. Summary

The sintering and electrochemical behaviour of Fe-doped CGO were evaluated with an emphasis on the dopant distribution on the precursor powder. The XRD of the Fe-doped CGO samples showed the single-phase fluorite structure of ceria. Segregation of Fe on the surface of CGO nanoparticles was quantified using a selective lixiviation process of Fe on the exposed solid-gas atmosphere. The results revealed a relatively low surface excess (0.139 μmol·m^{-2}) for 5 mol% Fe-doped CGO, which, associated with an increase in the specific GB area suggested that most of the dopant segregated at the solid-solid interface of GBs. The sintering studies showed that Fe significantly increased the densification of CGO at a relatively lower temperature compared to those typically used for ceria-based compounds. Such an effect was clearly related to the segregation of iron at the grain boundary, which favoured the elimination of high-energy solid gas

interfaces. Therefore, the driving force for sintering was enhanced by the mass diffusion process leading to densification. By sintering at the maximum shrinkage temperature 1200 °C Fe-doped samples attained a high relative density (~90%) and grain size ~0.3 μm. Increasing the sintering temperature to 1400 °C induced a ten-fold increase of the average grain size evidencing the effect of Fe in increasing the mass diffusion at the grain boundary of CGO. Such a pronounced increase in the grain size significantly decreased the grain boundary surface area and promoted the precipitation of the Fe-rich phase, possibly forming a CGO-Fe_2O_3 composite. The effect of the dopant on the electrical properties was evaluated by EIS. Under synthetic air, Fe-doped samples presented similar bulk and GB resistance, which in turn are much lower than the corresponding components of the porous CGO sintered at the same temperature. However, The EIS data under 4% H_2 of the sample with increasing volume fraction (5 mol%) of iron revealed a lower total electrical resistivity with decreased activation energy. The reduced resistivity and activation energy indicate a slightly increased electronic contribution to the charge transport that may be related to the formation of Fe-rich grains in the CGO matrix. Thus, using a transition metal oxide as a sintering aid in ceria-based electrolytes must be tuned to control the possible development of electronic transport. Such effect is relevant for the application of ceria as an electrolyte. For iron-doped CGO samples, an optimal concentration in the 1-5 mol% Fe range for attaining high density at sintering temperatures below 1400 °C. For CGO used as either an electrode or as a barrier layer, the enhanced density at a lower sintering temperature than that of CGO is important, whereas an increased electronic contribution of the charge transport can have a minor and eventually positive impact.

Chapter 3

Shape-controlled synthesis of CGO by hydrothermal route and application as electrolyte and as a catalyst for direct use of ethanol in SOFCs

3.1 Introduction

3.1.1 Shape-controlled synthesis of CGO by hydrothermal route

The use of cerium oxide in a wide range of applications leads to the development of strategies to enhance, most notably, its oxygen storage and redox capacities [187]. In an SOFC the possible applications of doped or undoped cerium oxide are noteworthy: it can be applied as an electrolytic barrier layer [59], as catalyst support [81,188] and electrode [63,86]. Therefore, it is fundamental to enhance the specific property of ceria required for each application, with approaches starting at the synthesis step.

Controlling the sintering of ceria-based materials is a relevant topic for both SOFC and catalysis. In ***Chapter 2*** the use of Fe as a sintering aid was discussed as a strategy to improve the densification of CGO, but it was observed that Fe-rich phases can be formed. Besides the use of sintering aids, another approach to enhance the densification mechanism is through morphological control of the precursor powder, which can be used to enhance or hinder sintering mechanisms. Morphology control has an important role, especially in nanometric starting materials, as surface energy will primarily contribute to the diffusion processes leading to sintering [146]. It is known that species with large surface area and surface energy tend to grow rapidly with increasing temperature, while species with low surface energy will be thermodynamically stable [189]. Thus, shape control can be an important tool to dictate surface energy.

The hydrothermal route is often used to synthesize specific morphologies [114,187] due to the capacity to control temperature and thus pressure in the autoclave vessel. The different morphologies, sizes, exposed facets, and degrees of crystallinity can be directed by varying synthesis conditions. Mehmood et al. [190] have shown that morphology control of ceria nanoparticles is dominated by variation in temperature. As reaction temperature increases from lowest to highest, nanoctahedra, nanorods, and nanocubes are obtained. Torrente-Murciano et al.

[191] have elaborated a phase diagram relating base concentration, temperature and ceria morphology and likewise showed that nanocubes are obtained at a higher temperature. They have also shown that the exposed facets vary with morphology and crystallinity and that the ceria nanorods with (110) and (100) preferential planes are the most catalytically active. Xu et al. [187] compiled an extensive review on the formation of ceria nanoparticles with different morphologies through hydrothermal methods. They elaborated a mechanistic description of the grain growth mechanisms and formation of nanoctahedra, nanorods, nanospheres, and nanocubes.

In this present work, shape control by hydrothermal route was originally chosen to synthesize CGO nanorods (CGO-NR) and CGO nanocubes (CGO-NC). The study originally focused on the characterization of the as-synthesized materials to better understand the grain growth mechanisms aiming at controlling the sintering behaviour and the properties of the different initial shapes of the nanoceria. The shape-controlled nanoparticles exhibited interesting properties for application as an electrolyte in an SOFC and as a catalytic layer in an ethanol fuelled SOFC.

3.1.2 Application of CGO nanorods as electrolyte support in an SOFC

One of the key challenges of SOFC processing is the high sintering temperature used, especially to densify the electrolyte and provide mechanical strength (usually ≥1500 °C). Lowering the sintering temperature of both the electrolyte and the electrodes while maintaining the required electrochemical and mechanical properties represent a great cost reduction of the system. Aiming to reduce the fuel cell processing to lower temperatures is in line with the quest for intermediate temperature operation. Decreasing sintering temperature brings more possibilities to explore properties of nanostructured components; for example, to produce electrodes with smaller grain sizes, increasing the surface area for the catalytic and electrochemical reactions and the triple phase boundary length.

Nonetheless an optimal sintering temperature is needed for the electrodes to provide necking between the particles and good adherence between electrode/electrolyte conductivity. It has been reported that LSCF cathodes with sintering temperature ≥1000 °C showed higher area specific resistance to the

oxygen reduction reaction due to the coarsening of the material [192]. Hildebrand et al. [193] noted strong sintering dependence on the cathode activity with LSCF sintered at 1100 °C showing poor adherence to the electrolyte, while cathodes sintered at 1300 °C did not have enough porosity and thus had high polarization resistance. Similarly, better electrochemical performance is observed for the anodes with lower sintering temperatures [194]. A sintering temperature as low as 1100 °C was shown to inhibit Ni grain growth, optimizing the catalytic reactions in the NiO/CGO anode [195]. Oishi et al. [196] optimized the sintering temperature of the NiO/CGO anode to 1150 °C, finding at this temperature adequate mechanical strength as well as uniformly distributed pores.

As an example of using the shape-controlled synthesis of the nano ceria, a solid oxide fuel cell sintered at 1150 °C has been fabricated. For such low sintering temperature to be possible the electrolyte was made of CGO-NR with a high surface energy. An electrolyte supported solid oxide fuel cell was fabricated by painting the electrolyte with anode and cathode inks. The anode consisted of NiO/CGO and the cathode of high activity $La_{0.6}Sr_{0.4}Co_{0.2}Fe_{0.8}O_{3-\delta}$ (LSCF). The electrochemical properties of the fuel cell were tested at temperatures between 550 and 700 °C.

3.1.3 Evaluation of Ni/CGO nanocubes and nanorods as a catalyst for ethanol steam reforming and application as a catalytic layer for SOFC

One of the greatest advantages of an SOFC is its ability to operate with hydrocarbons as fuel, including ethanol. The high operating temperature of an SOFC (<600 °C) favours the direct internal ethanol steam reforming reaction (DIR) (Equation 1.15). However, if ethanol is directly fed into the SOFC, carbon will form due to the high Ni content (>30 vol%) of the state-of-the-art Ni/YSZ anode [72–75,197]. Coke formation on the anode will lead to a rapid and irreversible degradation of the fuel cell performance. As a result, a strategy was proposed to add a catalytic functional layer on top of the SOFC anode to reform the fuel before it gets in contact with the anode layer [70,89,94,198]. In this configuration, the catalyst material can be selected to ensure the highest possible hydrogen conversion. Nonetheless, the catalytic material must meet requirements such as

high stability to the harsh processing and operating conditions of an SOFC, and be compatible with the other materials in the SOFC.

Reportedly, supported noble-metal catalysts such as Ir and Rh exhibit the highest activity towards C-C bond cleavage with negligible coke formation [85,199,200]. However, a transition metal catalyst is a more viable option for industrial-scale application than a noble metal. Low-cost catalysts, based on a support with a low Ni content, are commonly used as they were shown as stable and to have a high activity for H_2 conversion for ethanol steam reforming [94,201–203].

Besides the metal component of the catalyst, the support can have an important role in improving ethanol steam reforming. The use of cerium oxide (CeO_2) as a support has shown to be effective in improving ethanol decomposition and inhibiting carbon formation [85]. CeO_2 has a high oxygen storage capacity (OSC) due to its double oxidation state, from (IV) to (III), which allows ceria to release oxygen under reducing conditions and adsorb oxygen under oxidizing conditions. Doping ceria with a trivalent cation creates extrinsic charge compensation defects as oxygen vacancies increasing the mobility of the species [11,25,204].

Additionally, the morphology of the catalyst support has been shown to have a role in the Ni dispersion. High metal dispersion is correlated with increased active sites for catalytic reaction [116,205]. Moreover, in the case of ceria the oxygen vacancies are morphology dependent. It has been observed that morphologies such as nanosheets, nanorods and nanocubes have exposed planes {110} and {100} and those have higher OSC and higher coke resistance [206,207]. Rodrigues et al. [77] synthesized Ni/$Ce_{0.9}Sm_{0.1}O_{2-\delta}$ nanowires with increased catalytic activity for ethanol conversion compared to a commercial catalyst with the same composition. The increase in activity was attributed to the high surface area of the support, which provided many nucleation sites for the Ni nanoparticles over the whole surface of the support. Moraes et al. [78] synthesized CeO_2 with different morphologies (nanocube, nanorod, flower-like, and random shaped) impregnated with Ni. They observed that the Ni had a smaller crystallite size, which favoured ethanol decomposition on the ceria-based support with adjusted morphology over the one with random-shaped nanoparticles.

An important factor in evaluating a catalyst for an SOFC is to consider the temperature effect on the catalyst. A heat treatment is typically employed for the application of a catalyst directly in an SOFC. The application of the catalyst layer on a SOFC consists of preparing an ink of the catalyst material with organic additives (*i.e*., solvents, pore formers, terpineol, polymers). A high temperature (~800 °C) is usually needed for the removal of the organics and for the attachment of the catalytic layer on the anode [70,81,91,95]. Furthermore, the reduction of the NiO of the anode is typically carried out at a high temperature (>750 °C) before the operation of the fuel cell [81,208]. A high temperature heat treatment alters the microstructure of the material and is associated with particles coarsening and to a decrease in the surface area leading to reduced catalytic activity, hence a higher rate of carbon formation and faster degradation of the cell.

In this present study, the two morphologies, CGO-NRs and CGO-NCs, are impregnated with 5 wt% Ni to evaluate the material as a catalytic layer for ethanol steam reforming aiming at DIR in SOFC. Furthermore, these nanostructured catalysts were heat treated in conditions analogous to the typical conditions for catalytic layer processing and of operation of an SOFC. The suitability of those materials for application on an SOFC is established.

The CGO-NRs are applied as a catalytic layer on a high-performance anode supported SOFC. A schematic representation of a similar cell is shown in **Fig. 1.9**. The cell operated for ~110 h under DIR of anhydrous ethanol at 700 °C. The cell's stability and performance under the harsh operating condition are studied to evaluate the cell's durability at an intermediate operating temperature under anhydrous ethanol.

3.2 Experimental

3.2.1 *Synthesis of CGO nanorods and nanocubes*

The synthesis of $Ce_{0.9}Gd_{0.1}O_{2-\delta}$ nanorods (CGO-NR) and $Ce_{0.9}Gd_{0.1}O_{2-\delta}$ nanocubes (CGO-NC) was adapted from a previously reported synthesis of ceria by the hydrothermal method [77,114,209]. First, a 14 M aqueous sodium hydroxide solution (NaOH, 99%, Sigma-Aldrich) (19.6 g of NaOH dissolved in 35 mL of deionized water) was transferred to a 100 ml Teflon-lined stainless-steel autoclave. Then an aqueous 5 mL solution containing 6.2344 g of cerium nitrate

($Ce(NO_3)_3 \cdot 6H_2O$, 99%, Sigma Aldrich) and 0.7219 g of gadolinium nitrate ($Gd(NO_3)_3 \cdot 6H_2O$, 99.9%, Sigma Aldrich) was gradually added to the NaOH solution under constant magnetic stirring**.** The autoclave was placed in a furnace at 110 °C for 24 h to obtain CGO-NRs and at 180 °C for 24 h to obtain CGO-NCs. After the synthesis, the products were washed by five cycles of centrifugation with water and two cycles with ethanol. Finally, the synthesized material was dried at 120 °C for 2 h in air atmosphere.

3.2.2 *Characterization of CGO nanorods and nanocubes*

Thermogravimetric analyses (TGA) of the as-synthesized material were performed using Setaram Labsys equipment between room temperature and 1200 °C with a heating rate of 10 °C·min^{-1} under 50 ml·min^{-1} synthetic airflow. According to the TGA results, a temperature of 500 °C (heating rate of 10 °C·min^{-1} and dwell time of 1 h) was adopted for calcining the powder of CGO-NR, whereas the CGO-NC did not need to undergo a calcination step.

The images of the calcined CGO-NRs and as-synthesized CGO-NCs were obtained using a scanning electron microscope (SEM) JEOL field emission microscope JSM 6330F operating at 5 kV with a secondary electron detector. The HRTEM (high-resolution transmission electron microscopy) analyses of the powders were carried out by JEOL JEM 2100 transmission electron microscope operated at 200 kV with a high-angle annular dark-field (HAADF) detector. Samples for TEM analyses were prepared by drop-casting an aqueous suspension of the materials over a carbon-coated copper grid, followed by drying under ambient conditions. The samples analysed were CGO-NC as-synthesized, CGO-NR after calcination at 500 °C, and CGO-NC after heat treatment at 500 °C.

X-ray diffraction analyses of the as-synthesized CGO-NC and calcined CGO-NR, powders and of the samples submitted to 1400 °C, 1050 °C and 850 °C were performed by a Miniflex II model diffractometer with Cu Kα radiation source (0.15406 nm) in the range of 20° to 90° 2θ. Mean crystallite sizes (*D*) were calculated using Scherrer Equation 3.1:

$$D = \frac{0.9\lambda}{\beta \cos(\theta)} \tag{3.1}$$

where λ is the electromagnetic radiation wavelength, β is the full width at half maximum of the diffraction peak, and θ is the diffraction angle. The average crystallite sizes were calculated from the (111), (200), and (220) reflections.

Typically, cylindrical pellets of 6 mm in diameter were prepared by uniaxial pressing (1 ton·cm^{-2}) the powder for thermomechanical dilatometry analysis (TMA). The TMA analyses were carried out between room temperature and 1400 °C with a heating rate of 10 °C·min^{-1} under synthetic airflow of 50 ml·min^{-1}. The linear shrinkage values from the TMA were converted into relative density (ρ_{rel}) according to the relation, Equation 3.2:

$$\rho_{rel} = \frac{[L_0/(\Delta L + L_0)]^3 \rho_0}{\rho_t} \tag{3.2}$$

where L_0 is the initial length of the sample, and ΔL is the linear shrinkage. ρ_0 is the apparent green density of the pressed samples determined by the geometrical method and ρ_t is the theoretical density of each sample calculated using the lattice parameter data, a, obtained from the XRD data, following the Equation 3.3:

$$\rho_t = \left(\frac{4}{N_A \times a^3}\right)[0.99M_{Ce} + 0.1M_{Gd} + (2-\delta)M_O] \tag{3.3}$$

SEM images of the sintered samples submitted to 1400, 1050 and 850 °C (heating rate of 10 °C·min^{-1} and dwell time of 1 minute) were obtained, and the mean crystallite sizes were calculated using Scherrer Equation 3.1. The microscopy analyses were performed by JEOL field emission microscope JSM6701F operating at 1.5 kV with a secondary electron detector.

The electrical properties of the CGO-NR sintered at 1200 °C (heating ramp of 10 °C·min^{-1} and dwell time of 1h) were compared with that of a commercial CGO powder ($Ce_{0.9}Gd_{0.1}O_{2-\delta}$ Praxair) sintered at 1500 °C (heating ramp of 10 °C·min^{-1} and dwell of 1 h). Prior to sintering, the pellets were prepared by uniaxially

pressing 10 mm diameter pellets of each sample using 1 ton·cm^{-2} pressure. Gold paste was painted on both pellet's side, followed by curing at 800 °C to ensure electrical contact. The electrochemical impedance characterization was carried out by the Solartron frequency analyser (SI 1260), with frequency ranging from 10 MHz to 1 Hz and ac amplitude of 100 mV in the 200-600 °C temperature range.

3.2.3 *Application of CGO nanorods as electrolyte support in an SOFC*

A solid oxide fuel cell (NR-cell) was prepared using the CGO-NR powder as the electrolyte. The as-synthesized powder was uniaxially pressed (25 mm diameter cylindrical pellet and 1 ton·cm^{-2} pressure) and sintered at 1150 °C for 2 h. The pellet' density was measured through the standard method for apparent density [210].

NiO/CGO and LSCF were used as anode and cathode material, respectively. The anode powder consisted of 60 vol% NiO in CGO, prepared through a liquid mixture technique with ethanol [211,212]. Accordingly, nickel (II) acetate tetrahydrate (99%, Sigma-Aldrich) and 10 mol% gadolinium-doped cerium oxide (99.9%, Praxair) were mixed with 200 mL ethanol and heated under constant stirring at a temperature of ~70 °C until complete evaporation of the ethanol. The powder was then calcined at 450 °C for 5 h. The cathode used was commercial $La_{0.6}Sr_{0.4}Co_{0.2}Fe_{0.8}O_{3-\delta}$ (LSCF, Fuel Cell Materials).

The electrode inks were prepared following a process developed by the group. First, the anode ink was prepared by ball milling for 24 h at 100 rpm the ceramic powders with 1 wt% PVP, 4 wt% ethylene glycol, 2 wt% PVB, 27 wt% terpineol and 30 wt% ethanol. The grinding media consisted of zirconia spheres of 3 mm diameter. Next, the cathode ink was prepared by mixing the 30 wt% LSCF with a commercial ink-vehicle (Fuel Cell Materials) in a planetary mill (Fritsch - Pulverisette), three cycles of 5 minutes at 3000 rpm. The grinding media used were zirconia spheres with ~1 mm diameter.

The electrode layers were hand-painted on each side of the electrolyte support until obtaining a mass of ~200 mg for each layer. Between each deposition the ink was dried under an incandescent lamp (200 W) at a 20 cm distance overnight. After the drying steps, the full cell was sintered at 1150 °C for

2 h. The microstructure of the NR-cell was analysed using a scanning electron microscope SEM JSM-6010LA.

The electrochemical properties of the cell were tested in the open flange test set-up from Fiaxell SOFC Technologies™. The current collection was carried out by gold wires connected to a gold mesh (37 mm diameter) in the air outlet and by a nickel mesh on the fuel side. The electrochemical measurements of the NR-cell supported on a 1 mm thick electrolyte were carried out by a Zahner IM6 electrochemical workstation, and the measurements of the NR-cell supported on a 0.6 mm thick electrolyte were carried out by a PARSTAT® 3000A-DX electrochemical workstation. I-V curves of the cells were measured in the temperature range of 700-550 °C with H_2 as fuel and air as the oxidant, both with a flow rate of 12 $L \cdot h^{-1}$. The anode reduction was carried out at 700 °C, gradually introducing H_2. The impedance under the open circuit conditions was measured at different temperatures in the frequency range of 1 MHz to 1 Hz with an ac amplitude of 10 mV. The fitting of the equivalent circuits on the impedance plots was carried through the Z-view software.

3.2.4 *Synthesis of Ni/CGO nanocubes and nanorods catalysts*

Ni/CGO catalysts were prepared by incipient wetness impregnation of the supports, CGO nanorods (CGO-NRs), and CGO nanocubes CGO-NCs, with an aqueous solution of $Ni(NO_3)_2 \cdot 6H_2O$ in order to obtain 5 wt% Ni in CGO-NRs and CGO-NCs. The impregnation consisted of dissolving the $Ni(NO_3)_2 \cdot 6H_2O$ in an aqueous solution. A volume of the solution matching the pore volume of the support is then slowly added to the support powder, such that the metal ions are adsorbed by the CGO support.

After impregnation, the samples were calcined at 450 °C for 2 h in air. Moreover, the 5NiCGO-NR sample was heated at 800 °C and 900 °C, and the 5NiCGO-NC was heated to 800 °C for 1 h in air atmosphere for evaluation of catalytic activity after the heat treatments.

3.2.5 *Characterization and evaluation of Ni/CGO nanocubes and nanorods catalysts for ethanol steam reforming reaction*

The specific surface areas (SSA) of the samples were determined by nitrogen gas adsorption measurements (at -196 °C) (Micromeritics Gemini VII) according to the Brunauer-Emmett-Teller (BET) method. Before the analysis, all samples were degassed under vacuum at 300 °C for 18 h in a Micromeritics VacPrep 061. The elemental analysis of the catalysts was carried out by wavelength dispersive X-ray fluorescence (WDXRF) on a Rigaku Supermini200 spectrometer.

X-ray diffraction analyses of the calcined powders and of the samples heated at 800 °C and 900 °C were performed using a Miniflex II model diffractometer with Cu Kα radiation source (0.15406 nm) in the range of 20° to 90° 2θ. The average crystallite sizes (*D*) were calculated using Scherrer Equation (Equation 3.1):

The Raman spectrometer (XploRa Plus, Horiba) with a laser wavelength of 785 nm coupled to a microscope with a ×10 objective lens was employed to obtain the Raman spectra of the calcined samples. The measurements were carried out between 200-800 cm^{-1}, with a laser frequency of 45 Hz and 5 s of exposure time and 5 accumulations for each spectrum.

The STEM analysis was carried out by JEOL JEM 2100 transmission electron microscope operated at 200 kV with a high angle annular dark field detector. Samples for STEM, were prepared by drop-casting an aqueous suspension of the materials over a carbon coated copper grid, followed by drying under ambient conditions. And the energy dispersive spectrometry (EDS) analyses of the samples were obtained with JEOL JEM 1011 operating at 100 kV.

Temperature-programmed reduction with hydrogen (H_2-TPR) was carried out in a multipurpose unit with a Pfeiffer Vacuum Prisma detector mass spectrometer. Typically, 0.1 g of a catalyst was dried with He flow at 300 °C for 1 h and then cooled down to room temperature. The H_2-TPR profiles were obtained between 30 and 1000 °C in a flow of 2% H_2/He, the temperature increasing linearly at a rate of 10 °C·min^{-1}.

The steam reforming of ethanol (ESR) was performed in a fixed bed quartz tubular reactor, 6m, inner diameter, packed with 20 mg in a vertical oven at 600 °C. Prior to reaction, the calcined catalysts and heat-treated catalysts were

reduced under pure hydrogen flow (30 ml·min^{-1}) for 1 h at 450 °C for the calcined catalyst and at 800 °C for the catalyst heated, and then purged under N_2 at the same temperature for 15 min. Water and ethanol were fed into the reactor using a system with two saturators to obtain a H_2O/CH_3CH_2OH molar ratio of 3. Nitrogen was used as carrier gas at a total flow rate of 60 ml·min^{-1}. The ethanol conversion and selectivity of the obtained products as a function of the reaction time were determined by (Equation 3.4 and 3.5). The reactants and the reaction products were analysed by gas chromatography (Agilent 7890A), equipped with a thermal conductivity detector (TCD) and a flame ionization detector (FID) connected in series.

$$X_{ethanol} = \frac{(n_{ethanol})_{fed} - (n_{ethanol})_{exit}}{(n_{ethanol})_{fed}} \times 100 \quad (3.4)$$

$$S_{xl} = \frac{(n_x)_{produced}}{(n_{total})_{produced}} \times 100 \quad (3.5)$$

where $(n_x)_{produced}$ = moles of x produced (x = H_2, CO, CO_2, CH_4, acetaldehyde, or ethylene) and $(n_{total})_{produced}$ = moles of H_2 + moles of CO + moles of CO_2 + moles of CH_4 + moles of acetaldehyde + moles of ethylene (i.e., the moles of water produced are not included).

The thermogravimetric analysis (TGA) of the samples after the steam reforming reaction was carried out by the TA Instruments SDT Q600 equipment. The measurements were obtained between room temperature and 800 °C with a heating rate of 10 °C·min^{-1} under 50 ml·min^{-1} airflow.

3.2.6 *Application of Ni/CGO nanorods as a catalytic layer in an SOFC*

The singles cells used were commercial anode supported bottom cells (Fuel Cell Materials) composed of Ni-YSZ/YSZ/CGO/LSC with an active electrode area of 1.2 cm^2. A current collector was placed on the anode side: Au ink was painted on the anode, gold wire was fixed on the paint and cured at 800 °C in air, the cell with the current collector is shown in **Fig. 3.1** (a).

The catalytic ink was prepared by mixing 5Ni/CGO-NR + 10 wt% ethyl cellulose (Sigma Aldrich) with ethanol and polyvinylpyrrolidone (PVP, Sigma Aldrich, Mw ~55000) with the proportion of 1:10:0.1 wt% in a planetary mill (Fritsch - Pulverisette), following two cycles of 5 minutes at 3000 rpm [213]. The grinding media used were zirconia spheres with ~1 mm diameter. After milling the suspension was immediately deposited on the anode. The deposition of the ink (70 mg) was carried out by an airbrush at a distance of ~15 cm of the cell. The cell after deposition of the catalytic layer is shown in **Fig. 3.1** (b).

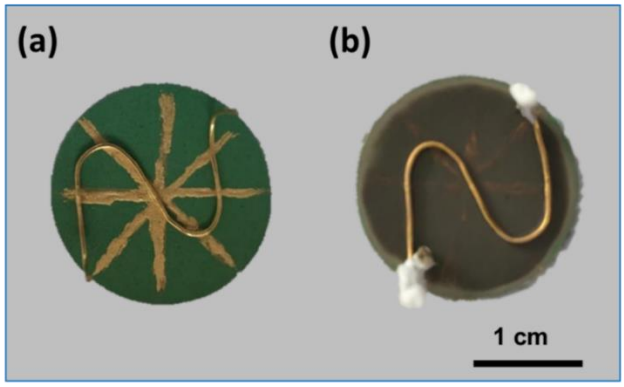

Fig. 3.1 (a) Image of the cell with gold paste and wire current collection and (b) image of the cell with deposition of catalytic layer.

The electrochemical properties of the anode supported cell with the Ni/CGO-NR catalytic layer were tested in the open flange test set-up from Fiaxell SOFC Technologies™. The current was collected by gold wires connected to a gold mesh (37 mm diameter) in the air outlet and one on the fuel side. On the inlet of the fuel side, a quartz fibre was placed (as in the ESR reaction) and then the cell and Thermiculite® plate to promote sealing between the fuel and air compartments. The images of the set-up are shown in **Fig. 3.2**.

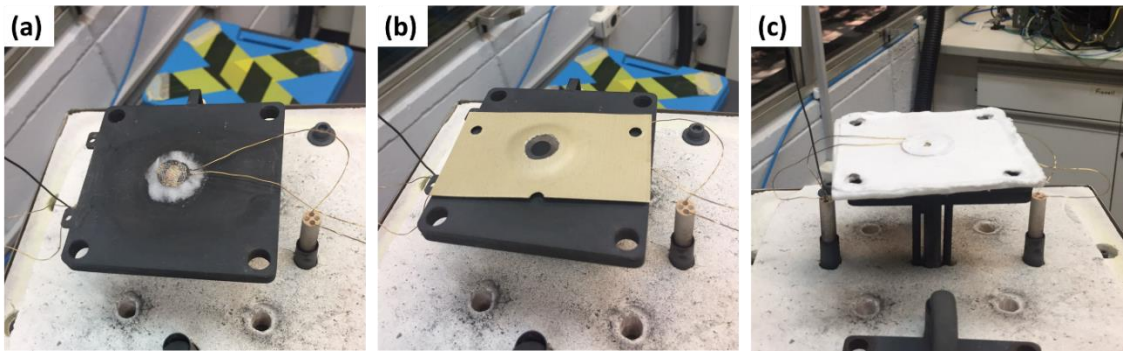

Fig. 3.2 Images of the set-up of the cell with (a) quartz fibre and gold mesh anode side (b) cell with Thermiculite® cathode side (c) alumina felt sealing the cell.

The anode supported cell with the Ni/CGO-NR catalytic layer was heated up to 800 °C under N_2 flow. Then H_2 was gradually inserted until a flow rate of 78 ml·min^{-1} of H_2 and 22 ml·min^{-1} of N_2 for anode reduction and system stabilization. At the cathode, the flow rate was maintained at 100 ml·min^{-1} synthetic air. After 1 h of stabilization the fuel cell was cooled to 700 °C for fuel cells tests. Initial polarization and impedance spectroscopy data under 78% H_2 in N_2 were taken during the initial operation on hydrogen. The fuel cell was polarized at 0.6 V under hydrogen for 20 h and then switched to dry ethanol.

Liquid ethanol was kept in a thermal bath at a controlled temperature and carried by N_2. The bath was set to 48 °C and carried by a flow of 50 ml·min^{-1} of N_2 further diluted with N_2 (50 ml·min^{-1}) to obtain a gas composition of 13% of ethanol in 87% N_2. The total flow on both anode and cathode sides were kept at 100 ml·min^{-1}. The cell operated under 13% ethanol for ~120 h. The stoichiometric ratio of ethanol and hydrogen 1:6 was chosen for the durability test. After operation with ethanol, the cell was switched back to hydrogen for further characterization.

The electrochemical characterization was performed during cell operation under hydrogen and ethanol using a Zahner IM6 Electrochemical Workstation. The polarization measurements under H_2 were taken from OCV to 0.4 V, and under ethanol the curve was limited to the 0.6 V–0.4 V range to ensure continuous water generation at the anode for the steam reforming reaction of ethanol. Impedance spectroscopy data were collected under polarization at 0.6 V, with 10 mV ac amplitude in the 100 kHz −1 Hz frequency range. After the fuel cell stability test, SEM analyses were carried out by JSM-6010LA.

3.3 Results and discussion

3.3.1 Shape-controlled synthesis of CGO by hydrothermal route

CGO-NR and CGO-NC were synthesized by the hydrothermal route. According to the TGA curve of the as-synthesized and dried materials from **Fig. 3.3** there was no mass loss for the CGO-NC between room temperature and 1200 °C whereas the CGO-NR had a 10% mass loss. It is noted that the washing and drying processes were successful in removing all organics of CGO-NC and for the oxide formation, whereas on the CGO-NR sample, there was still presence of adsorbed organic material. In the TGA and the derivative of the thermogravimetric curves of the CGO-NR below 200 °C, there is a drop in mass occurring due to the partial evaporation of water and ethanol, as evidenced by the derivative peak. In the temperature range from 200 – 500 °C, the decomposition of the hydroxides and nitrates occur. To remove all organics from the CGO-NR and for the oxide formation, the temperature of 500 °C was chosen as the calcination temperature, whereas the CGO-NC sample required no calcining step.

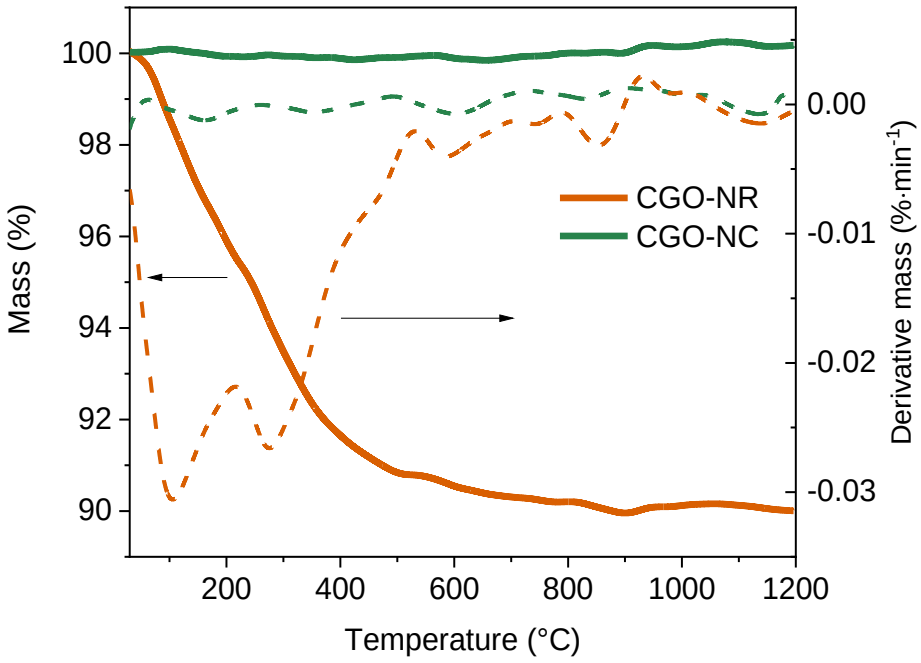

Fig. 3.3 TGA, with mass and the derivative of mass, of the of as-prepared CGO-NR and CGO-NC

The SEM images shown in **Fig. 3.4** confirm that nanorods (CGO-NR) were synthesized in the autoclave at 110 °C and nanocubes (CGO-NC) were synthesized at 180 °C. The nanorods have ~200 nm length and 30 nm cross-section. The edges of the nanocubes have an estimated length of ~100 nm. These different shapes obtained by controlling the synthesis temperature emphasize the importance of the autoclave pressure, which is fixed by temperature. The obtained shapes reflect the trend suggested in the morphological phase diagram of Torrente-Murciano et al. [191]. An increase in temperature is associated with higher energy input leading to the growth of crystals towards greater stability. The cubic shape forms in more stable crystal directions at the higher temperature of 180 °C.

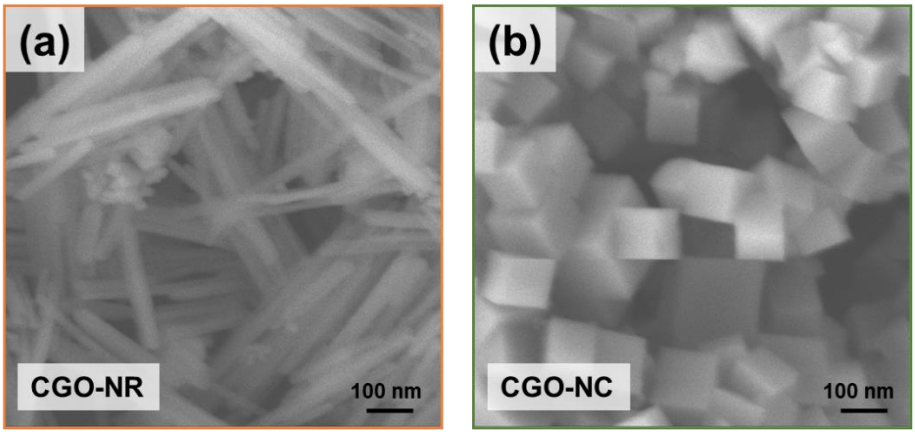

Fig. 3.4 Secondary-electrons SEM images of the as-prepared powders of (a) CGO-NR and (b) CGO-NC.

The X-ray diffraction patterns in **Fig. 3.5** confirm the formation of the fluorite structure of ceria (ICDD 96-900-9009). The diffraction peaks of the CGO-NC sample are narrow, while the CGO-NR sample exhibits broad peaks characteristic of nanomaterials. The peak widths are related to the mean crystallite sizes, calculated by the Scherrer Equation 3.1, and are 67 nm and 17 nm for the NC and NR, respectively. The difference in crystallinity of the sample is reflected in the morphology. The greater intensity of the diffraction peaks of the NC can be attributed to the more ordered structure of the cube, and the estimated sizes of the

cube (SEM) and crystallite size (XRD) have the same order of magnitude, indicating that the NCs are single crystals or are equivalent to a few crystallites.

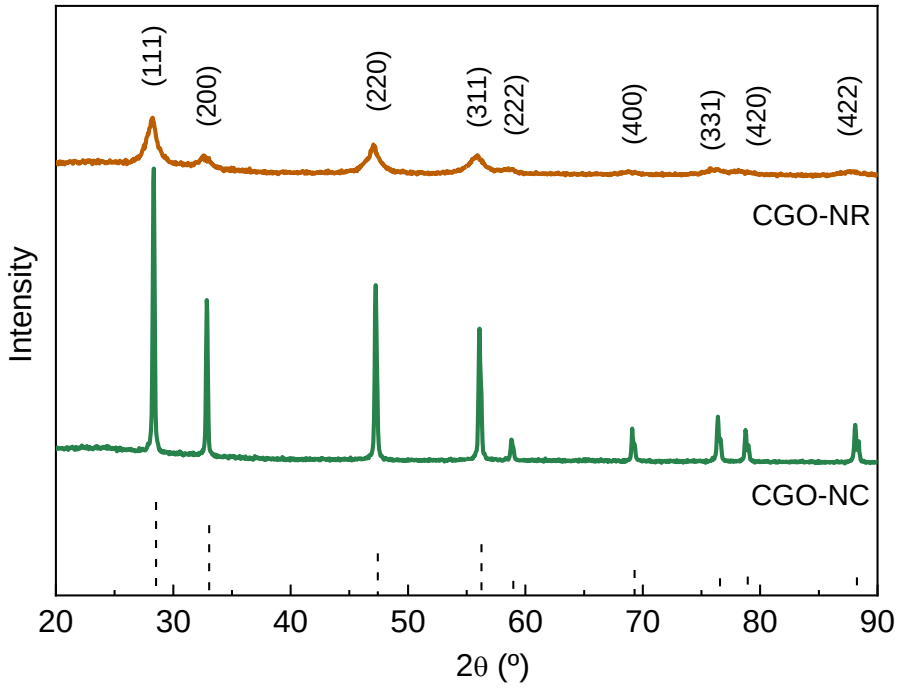

Fig. 3.5 XRD patterns of CGO-NR and CGO-NC.

In order to gain further insight into the morphological features of the nanorods and nanocubes the materials were analysed by TEM as shown in **Fig. 3.6**. The general view images in **Fig. 3.6** (a) and (c) show NRs and NCs with varying sizes. The corresponding high-resolution images reveal the fringes corresponding to the lattice planes of the face-cantered-cubic (*fcc*) ceria structure. The lattices {100}, {110} and {111} are distinctly noted in the Fast Fourier Transform (FFT) analyses of the images in **Fig. 3.6** (b) and (d), corresponding to interplanar distances of 0.19, 0.27 and 0.31 nm, respectively. It has been reported through density functional theory calculations that these planes have surface energies in the order {100} > {110} > {111} [214]. Therefore the {111} has the highest stability and the highest packing density and interplanar spacing [187]. It is then expected that any increase in temperature and pressure during the synthesis and subsequent heat treatment, associated with a higher energy input,

would be reflected in increased stability of the surface and growth in the {111} plane.

Based on the extensive literature on ceria and the observed TEM images of the samples, a growth mechanism can be proposed. Previous studies have shown that nanorods formed by a high concentration of NaOH (>5 M, in this study 14 M was used), showing the exposed planes {100}, {110}, and {111} are formed by simple octahedra crystallites, which assemble and start growing by coalescence and Ostwald Ripening mechanisms [187,214]. By increasing the temperature of the synthesis, the crystallites formed are cuboids that self-assemble and intergrow, forming a single crystal cube [102,105,187,215]. Those single crystals can then grow through different paths: oriented attachment and the adsorption of smaller nanocubes on the surface of a bigger cube [187]. In **Fig. 3.4** (c), smaller cubes can clearly be observed surrounding the larger ones indicating that an adsorption mechanism for crystal growth might occur.

A further study of the NCs was carried out after it was submitted to a heat treatment at 500 °C (the same temperature used for the calcination of the CGO-NRs). The HRTEM images are shown in **Fig. 3.6** (e) and (f). There is no significant modification of the shape and size of the CGO-NC as compared to before the heat treatment. However, on the larger cubes, there is an important presence of the fringes with the lattice {111}, which is the lowest surface energy plane. The energy of formation of {111}, {110} and {100} surfaces of ceria is 9.2, 15.3 and 20.3 $eV \cdot nm^2$ [216]. It has been reported that the {100} and the {110} surfaces are metastable and prone to reconstruction into {111} in an oxidizing environment [217] [218]. Thermomechanical studies were carried out to advance the understanding of the morphology behaviour of the morphologies submitted to increasing temperatures.

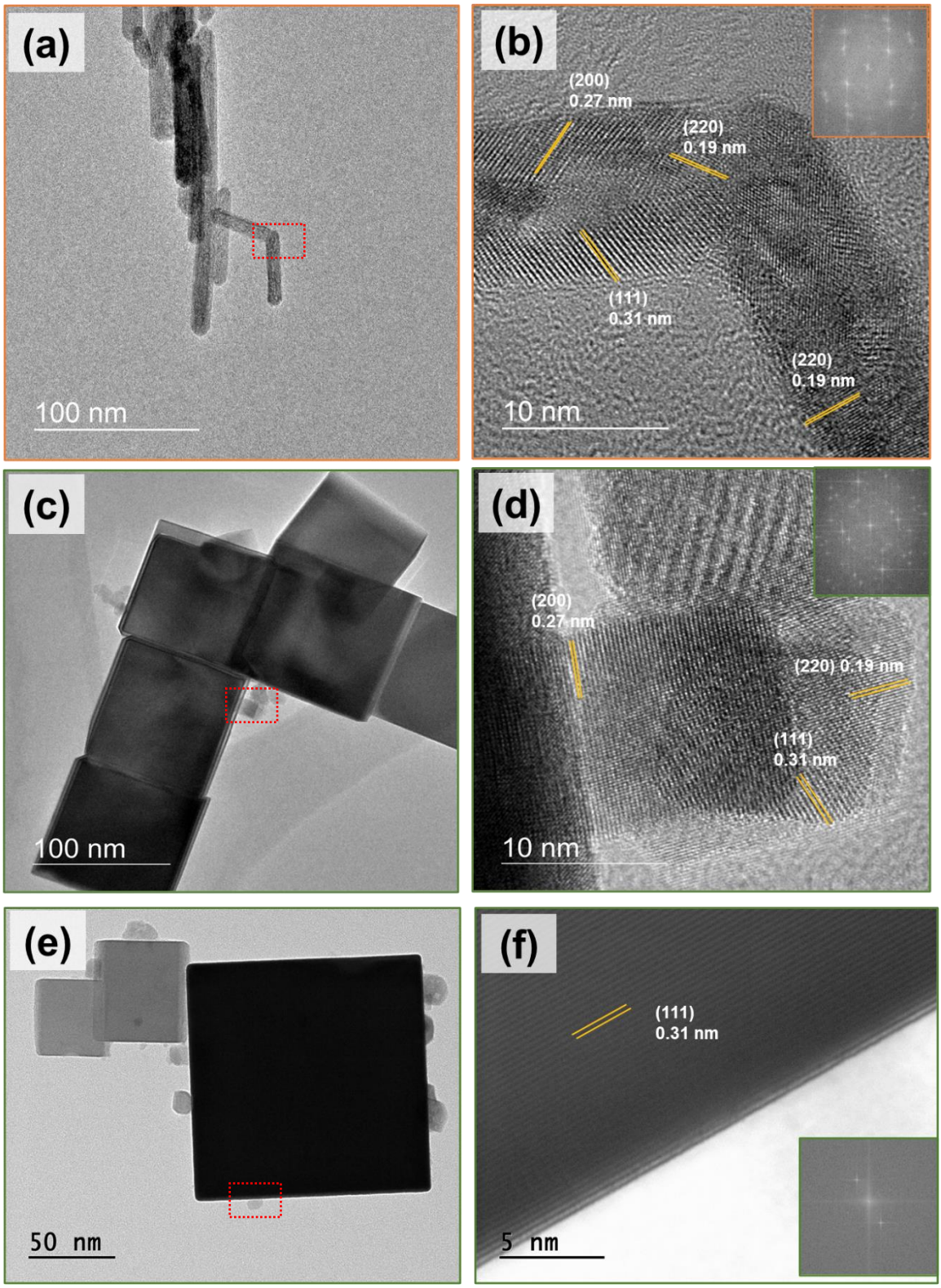

Fig. 3.6 TEM images of CGO-NR (a) and CGO-NC as-prepared (c) and after heat treatment at 500 °C (e). The corresponding HRTEM images of the highlighted regions of CGO-NR (b) and CGO-NC and as-prepared (d) and after heat treatment at 500 °C (f) with insets of FFT.

The densification and densification rate curves, obtained through dilatometry analysis (TMA), of the compacted pellets of CGO-NC and CGO-NR powders are shown in **Fig. 3.7** (a) and (b), respectively. A high green density of ρ_0 ~55% is observed for CGO-NC, while a lower value ρ_0 ~40% was obtained for CGO-NR. The observed differences are attributed to the greater packing of the cubes in relation to the rods in the green ceramic body. A higher green density is attributed to better densification behaviour [219,220]. However, contrary to what is usually observed, the closely packed nanocubes do not show densification during the heat treatment. In contrast, the loosely packed nanorods show a rapid densification that starts at ~500 °C and reaches its final densification stage at 1130 °C. The nanorods exhibit a two-stage (**Fig. 3.7** (b)) diffusion pattern with two maxima occurring at ca. 850 and 1050 °C, where the intensity of the diffusion process is higher at the second maximum, at the highest temperature (1050 °C). It is interesting to note that CGO samples with Fe_2O_3 sintering aid displayed similar retraction curves.

The nanocubes have a preferrable growth in stable crystalline directions. As observed in **Fig. 3.7** (f) when the sample is heated at 500 °C, the cubic shape is retained and there is a tendency for the reconstruction of the (111) lattice plane such that the surface of the nanocubes is stable and has a low surface energy. Nanorods, on the other hand, are less stable, have a high surface area and a defective surface, with high energy surface planes exposed, that favours diffusion processes when submitted to a high temperature.

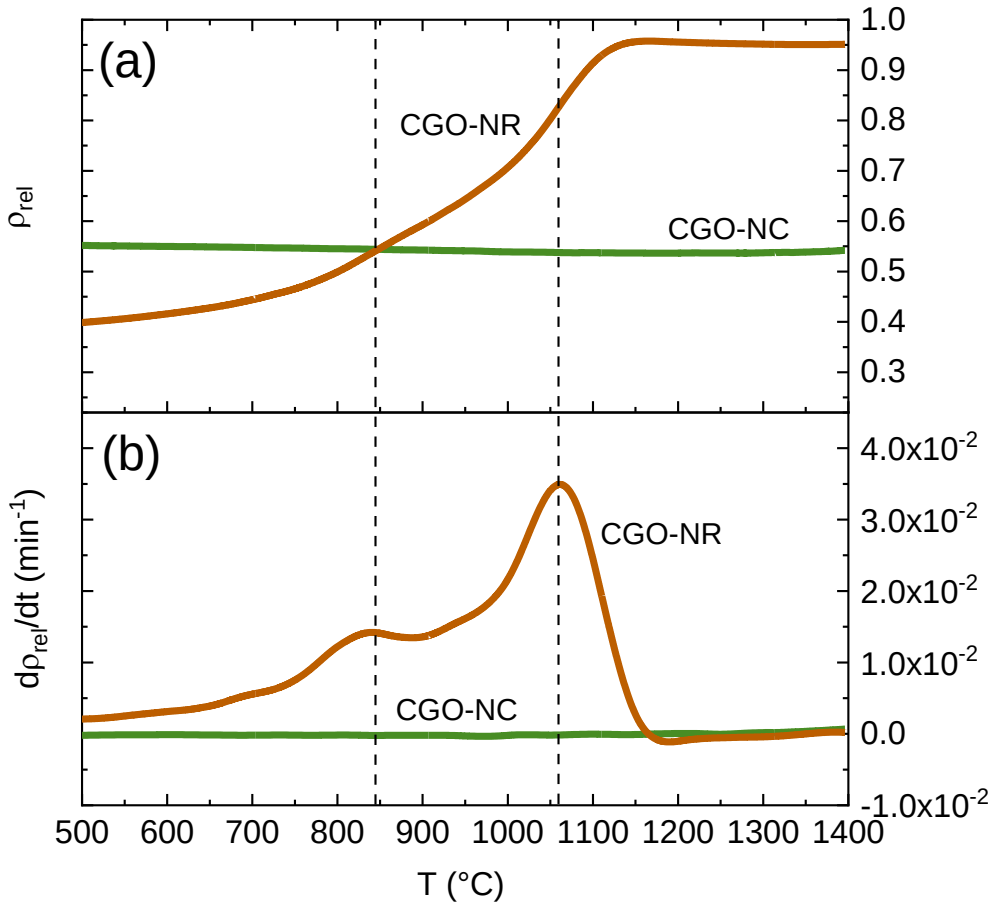

Fig. 3.7 Densification curves (a) and rate of densification curves (b) of CGO-NR and CGO-NC.

The micrographs of the fractured surfaces of the sintered samples, after dilatometry analysis, (**Fig. 3.8)**, exhibit submicron grain sizes and reveal the microstructure of the dense CGO nanorods and the porous CGO nanocube. The nanorods have a homogeneous densified structure, with a typical polyhedron-shaped grain and well-defined grain boundaries. The grain sizes are of ~0.7 µm. From the images, there is no evidence of the previous morphology of the nanorods, and practically no pores are observed (only 0.16% of the area are pores). Furthermore, the grain growth appears to occur in all directions of the nanowires. As for the nanocubes, the diffusion process leads to a porous microstructure. The grain sizes are estimated at ~0.7 µm. There is evidence of a change from cubic to spherical shape by the diffusive process; however, the mass

diffusion does not lead to densification but to the formation of elongated necks and consolidated open porosity; ~15% of the area is porosity.

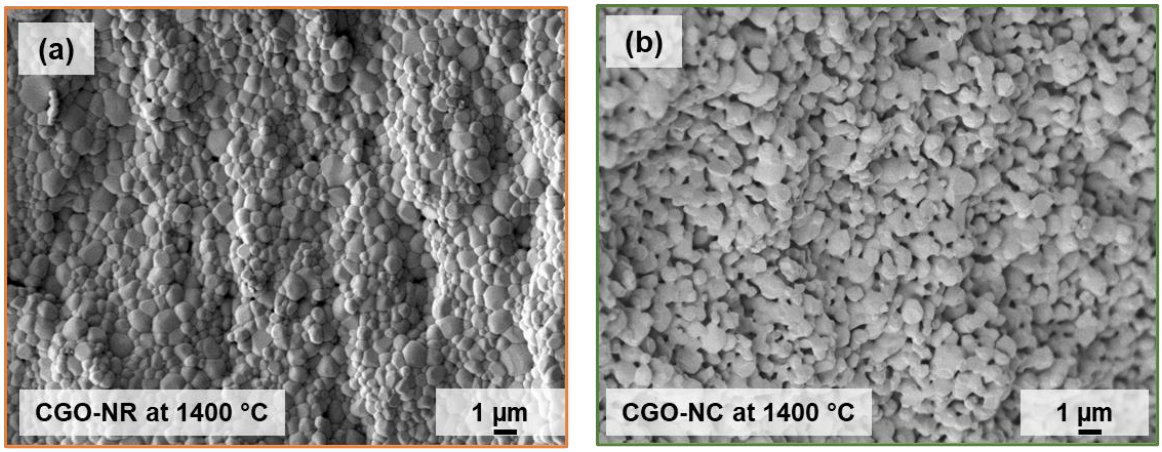

Fig. 3.8 SEM images of fractured surfaces pellets after dilatometry analysis (1400 °C) of (a) CGO-NR and (b) CGO-NC.

The samples were submitted to different sintering temperatures to evaluate the particle's behaviour through heat treatment and thermal evolution of the crystallites. The heat treatments at the intermediary temperatures of 850 and 1050 °C were selected as they correspond to the maximum diffusion peaks of the densification of the NRs sample as shown in **Fig. 3.7**. A short dwell time of 1 minute was chosen to characterize the densification process at those selected stages. **Fig. 3.9** shows the XRD data for CGO-NR and CGO-NC as-synthesized, treated at 850 and 1050 °C, and after TMA (1400 °C). The average crystallite sizes calculated from the XRD data of each sample are shown in **Fig. 3.9**.

The XRD peaks of the CGO-NR samples alter from broad peaks (as-synthesized) to narrow peaks when submitted to the heat treatments, growing from the crystallite size of 17 nm to 51 nm at 850 °C and 62 nm at 1400 °C. The CGO-NC XRD patterns are similar, and there is no significant change in crystallite size upon heating. This data is coherent with the sintering behaviour of the CGO-NC (**Fig. 3.7**), which shows nil densification. To better understand how the shape of the starting powder affects the characteristics of sintered CGO samples, the microstructural analysis of the samples sintered at intermediate temperatures was carried out.

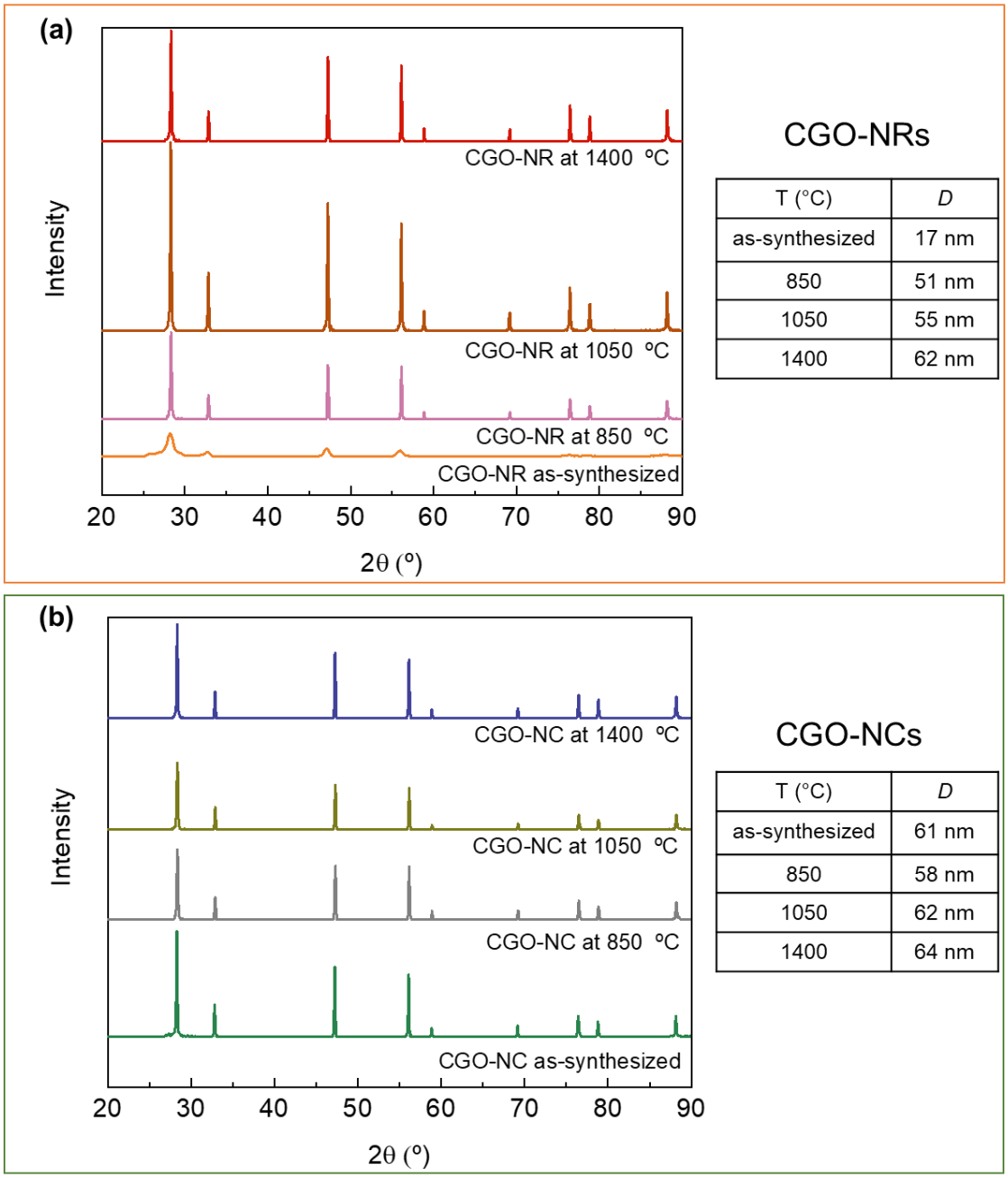

Fig. 3.9 XRD patterns of (a) CGO-NR and (b) CGO-NC at 850 °C, 1050 °C and 1400 °C. The inset tables list the calculated average crystallite sizes.

Fig. 3.10 shows the SEM images of the NRs (left) and NCs samples (right) sintered in air for 0.1 at 850, 1050 and 1400 °C (after TMA analysis). **Fig. 3.10** (a) shows a change of the nanorod shape to a spheroidal shape at 850 °C with only a few visible grains/particles retaining with rod-like shape, the grains are closely packed with a visually estimated size of ca. 200 nm, indicating grain growth and the onset of the densification process. Differently, the nanocube structure is still

clearly visible at 850 °C (**Fig. 3.10** (d)). As the densification progresses at 1050 °C there is a grain growth of the CGO-NR sample reaching an average size of ~500 nm (**Fig. 3.10** (b)). At 1050 °C, there are still some pores in the CGO-NR sample, but there is no evidence of the as-synthesized rod microstructure. Increasing the heating temperature to 1050 °C (**Fig. 3.10** (e)) nanocubes are still distinguishable and maintain the same average size as in 850 °C. At 1050 °C, the edges of the nanocubes are rounded, indicating the beginning of the formation of a spheroidal structure, as evidenced by the microstructural characteristics seen at 1400 °C (**Fig. 3.10** (f)). At 1400 °C the CGO-NR presents a dense structure and an average grain size of ~700 nm.

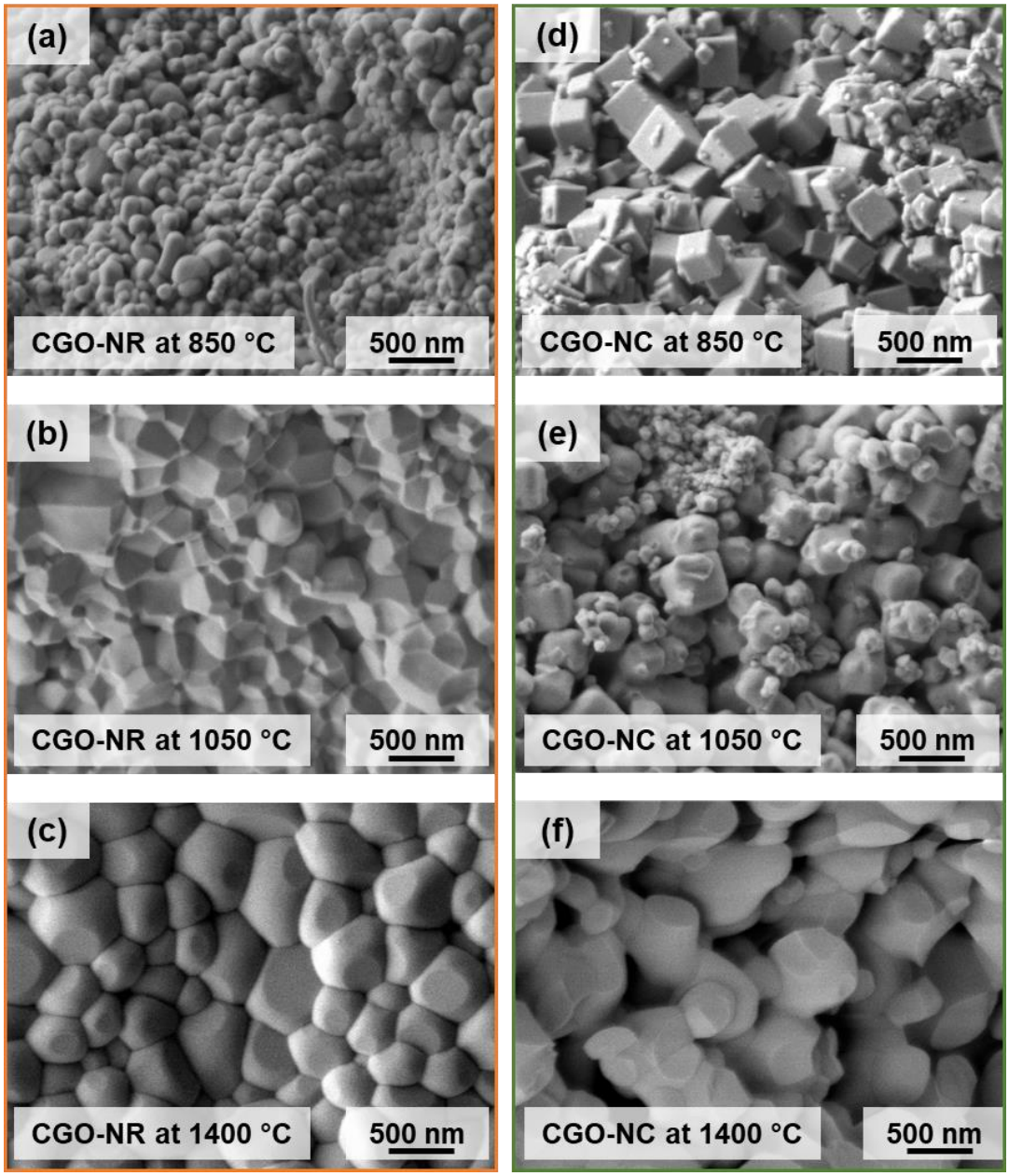

Fig. 3.10 Secondary-electrons SEM images of CGO-NRs (a), (b), (c) and CGO-NCs (d), (e) and (f) heated to 850 °C, 1050 °C and 1400 °C.

Electrochemical impedance spectroscopy (EIS) measurements were carried out of the CGO-NR sample sintered at 1200 °C and of a commercial CGO sample sintered at 1500 °C. Both samples reached similar relative densities of ~96%. The EIS measured at (a) 250 °C and (b) 500 °C are shown in **Fig. 3.11**. At 250 °C EIS diagram shows two components: the high frequency arc that develops at ~1 MHz is related to the bulk conductivity of CGO, and a larger semicircle at 10^4-10^3 Hz frequency range is due to the blocking of charge carriers at the grain

boundary and pores. The spike observed at low frequency is due to the electrode reactions. At 250 °C, the blocking resistance due to grain boundary is greater than the bulk resistance for both samples. The bulk resistance is similar for both samples, which is coherent as they are both related to bulk CGO. At 250 °C the arc due to the grain boundary resistance is clearly distinguishable for the NR sample, whereas for the commercial sample it is less evident. Nevertheless, fitting the semicircles with the equivalent circuit (R_bCPE_b)($R_{gb}CPE_{gb}$) values for the total electrical resistances could be calculated. The obtained conductivities are shown in the Arrhenius plot in **Fig. 3.12**.

At 500 °C, only one semicircle is present at ~10^5 Hz. At this temperature, the bulk resistance is estimated by the equivalent serial resistance as the intercept with the real axis (Z') in the impedance diagram and the grain boundary resistance is equivalent to the arc formed. For the spectra at higher temperatures the R_b($R_{gb}CPE_{gb}$) equivalent circuit was used to fit the data and obtain the total resistance.

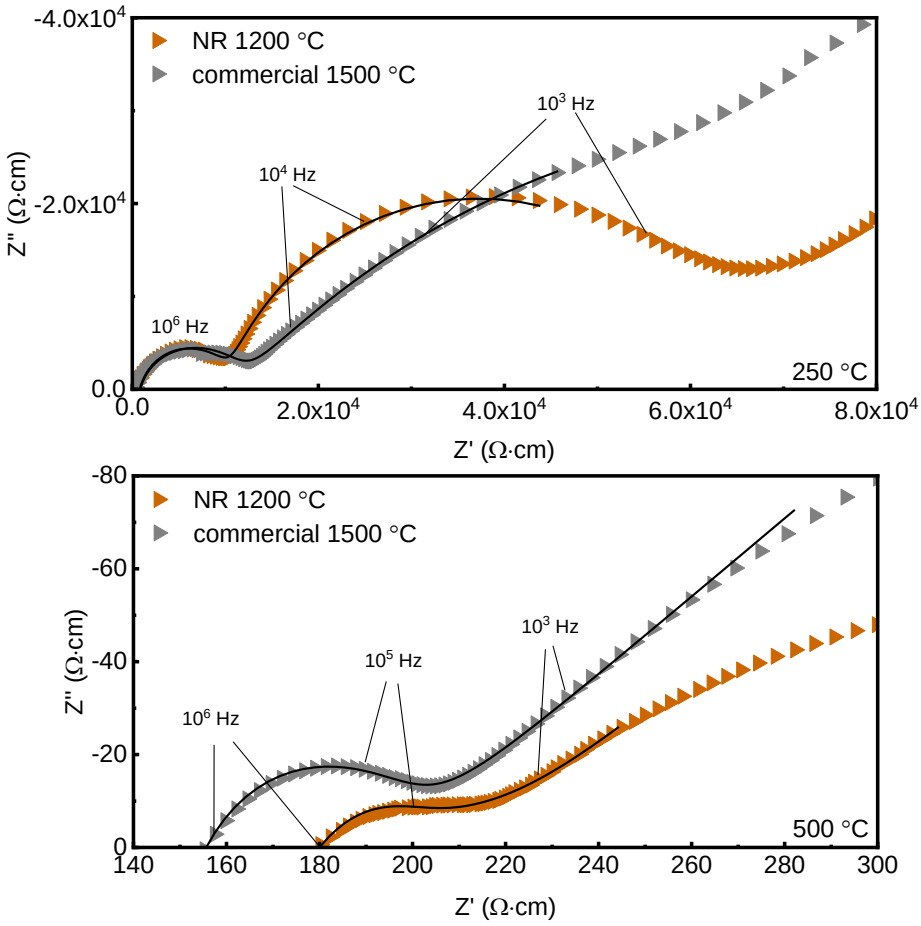

Fig. 3.11 EIS diagrams measured under synthetic air at (a) 250 °C and (b) 500 °C of CGO-NR sintered at 1200 °C and commercial CGO sintered at 1500 °C.

Arrhenius plots of total conductivity extracted from the EIS data measured in the temperature range 200-600 °C are shown in **Fig. 3.12**. The calculated activation energies of CGO were in the same range as previously reported [183]. Both samples exhibit similar conductivities, at 600 °C a conductivity of 1.4 $\times 10^{-2}$ $S \cdot cm^{-2}$ and 2.4 $\times$ 10^{-2} $S \cdot cm^{-1}$ was obtained for the commercial CGO and CGO-NR, respectively, in agreement with reported data [8,33]. Both conductivity and sintering results demonstrate that CGO-NR obtained by the hydrothermal route has equivalent properties to commercially available reference material with 99.9% purity. Moreover, the CGO-NR sintered at 1200 °C exhibited similar electrochemical behaviour to the commercial CGO sintered at 1500 °C.

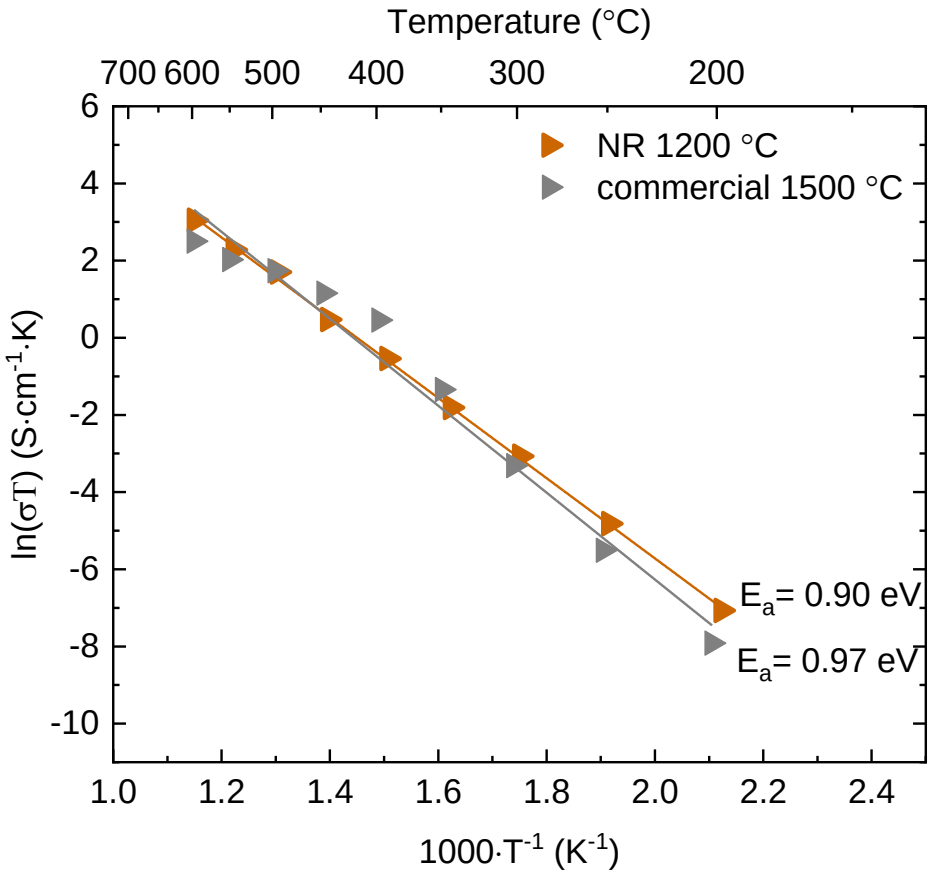

Fig. 3.12 Arrhenius conductivity plots of CGO-NR sintered at 1200 °C and commercial CGO sintered at 1500 °C.

3.3.2 Application of CGO nanorods as electrolyte support in an SOFC

The densification curve analysis in **Fig. 3.7** shows that densification of the CGO-NR occurs up to the temperature of 1130 °C. Thus, to prepare the CGO-NR electrolyte support, a uniaxially pressed pellet was sintered at 1150 °C. The calculated relative apparent density of the CGO-NR support was 95%. This support was used for electrode depositions and co-sintered at 1150 °C.

The SEM images in **Fig. 3.13** show a 0.6 mm thick electrolyte supported cell with the deposited electrodes. The electrolyte is a dense support with a thickness of ~600 µm, and the electrodes are porous layers with ~30 µm thickness. The image shows that the 1150 °C co-sintering steps exhibits the desirable microstructural features of a SOFC.

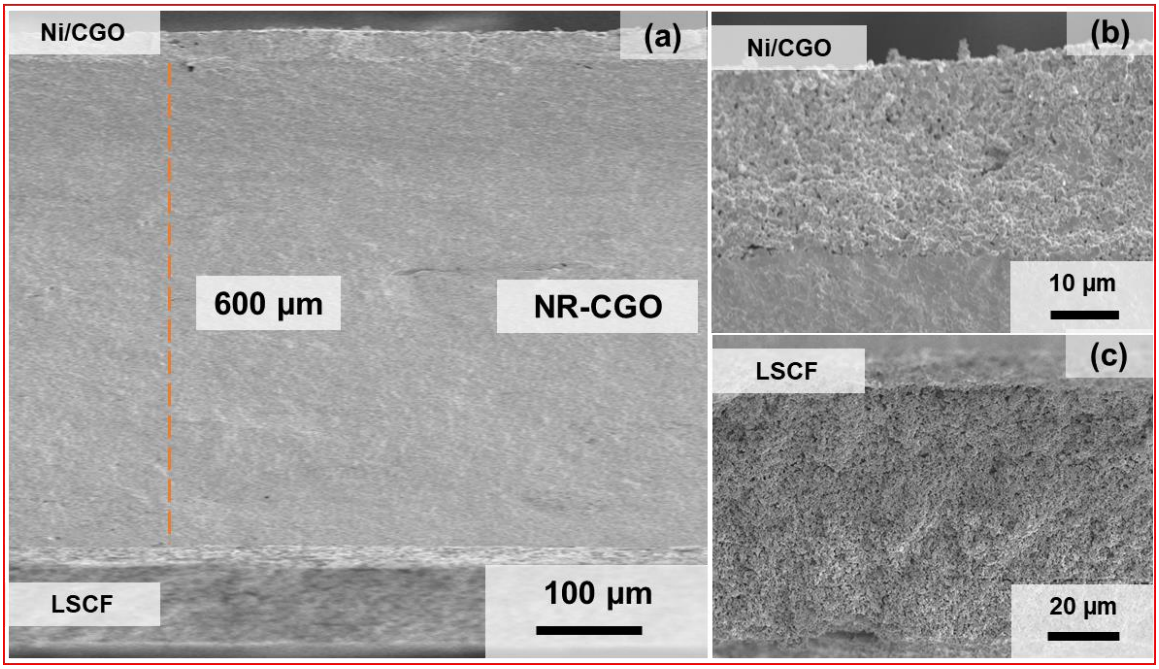

Fig. 3.13 Secondary electron SEM images of a fracture of the cell sintered at 1150 °C showing: (a) a general view of the full cell, (b) a section of the anode (Ni/CGO) side and (c) a section of the cathode (LSCF) side.

At first electrochemical tests were carried out of a NR-cell supported on a 1 mm thick electrolyte. The I-V and I-P curves of the NR-cell supported on an electrolyte of 1 mm in the 700-550 °C temperature range are shown in **Fig. 3.14.** The open-circuit voltage (OCV) was decreased with increasing temperature from 0.98 V at 500 °C to 0.79 V at 700 °C. Such a result is in accordance with the properties of CGO electrolytes, which are known to exhibit electronic defects with increasing temperature (>500 °C) that cause a reduction of cell's OCV. Despite the decreasing OCV, maximum power densities increase with increasing measuring temperature. The highest maximum power density of 104 $mW \cdot cm^{-2}$ was obtained at 700 °C. Nevertheless, I-V curves are linear indicating that ohmic losses are dominating over the performance of the fuel cell. The ohmic losses are usually attributed to the electrolyte.

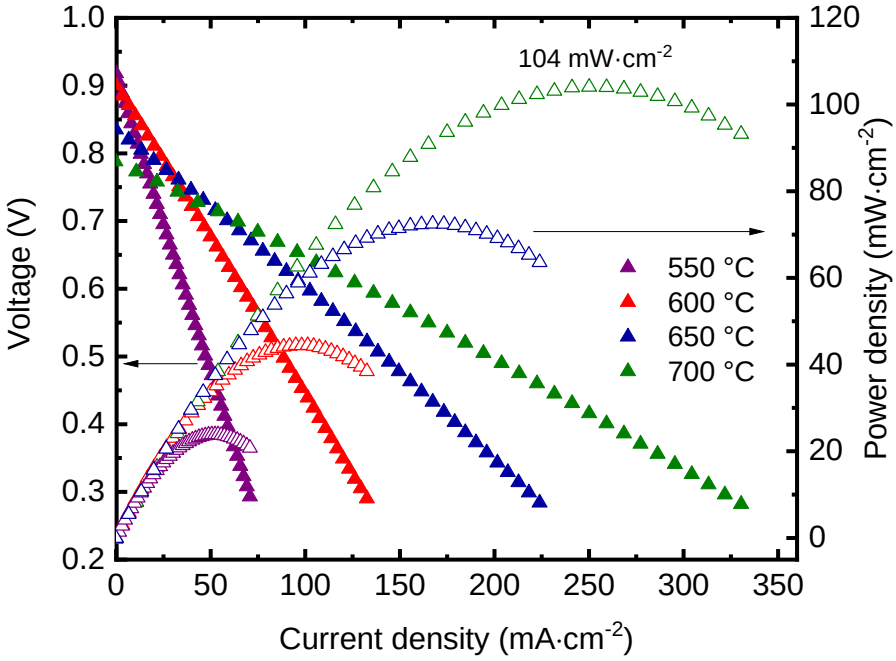

Fig. 3.14 Current-voltage (I-V) and current-polarization (I-P) curves of the NR-cell supported on a 1 mm thick electrolyte at 700, 650, 600, and 550°C under synthetic air and dry hydrogen.

The electrochemical properties of the 0.6 mm thick NR-cell were accessed by the I-V curves in the 700- 550 °C temperature range, as shown in **Fig. 3.15**. The OCV increases with decreasing temperature from 0.85 V at 700 °C to 1 V at 550 °C. The higher OCV of this cell indicated a better gas tightness of the electrolyte for this cell. The highest maximum power density at 700 °C was 164 mW·cm^{-2} higher than the one supported on the 1 mm electrolyte. The I-V curves are still rather linear, suggesting the ohmic resistance as the main source of polarization controlling the performance of the fuel cell.

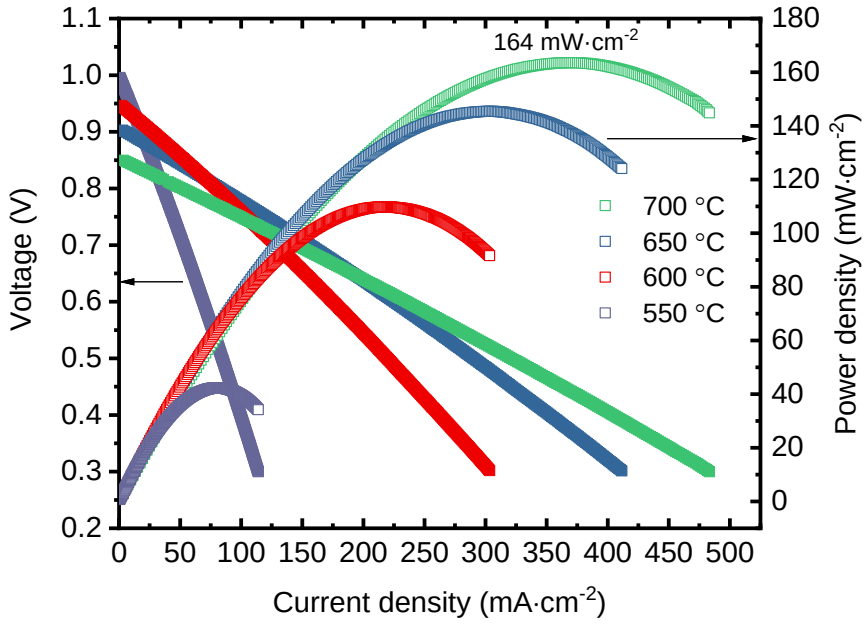

Fig. 3.15 Current-voltage (I-V) and current-polarization (I-P) curves of the NR-cell supported on a 0.6 mm thick electrolyte at 700, 650, 600 and 550°C under synthetic air and dry hydrogen.

The EIS of the 0.6 mm thick NR-cell at the different temperatures is shown in **Fig. 3.16**. The spectra obtained were fitted with the simplest circuit able to fit the data through the Zview software. At 550 °C the spectrum was fitted with the equivalent circuit $LR_s(R_{p1}CPE_{p1})$ $(R_{p2}CPE_{p2})$, whereas the spectra at the other temperatures were fitted with the equivalent circuit $LR_s(R_{p1}CPE_{p1})$, where L refers to the inductive contribution due to the setup, R_s is the serial resistance, and the polarization arcs are fitted with a resistance and a constant phase element (CPE) connected in parallel ($R_{pi}CPE_{pi}$). The serial resistances (R_s) and the total polarization resistances R_{ptotal} obtained through the fitting are shown in **Table 3.1**.

The serial resistance of the cell (R_s), which corresponds to the x-intercept at, is generally attributed to the ohmic resistance of the cell and to the current collection. It is noted that R_s is the main contributor to the total resistance of the cell [221], contributing to, on average, 90% of the total resistance of the cell at different temperatures, in agreement with the observed linearity of the I-V curve. Whereas, the polarization resistances attributed to charge transfer mechanisms, mass diffusion, and reactions occurring at the electrodes are minimal [222–224], emphasizing the high activity of such processes of the materials Ni/CGO in the

anode and LSCF in the cathode and the favourable microstructure of the electrodes achieved at 1150 °C.

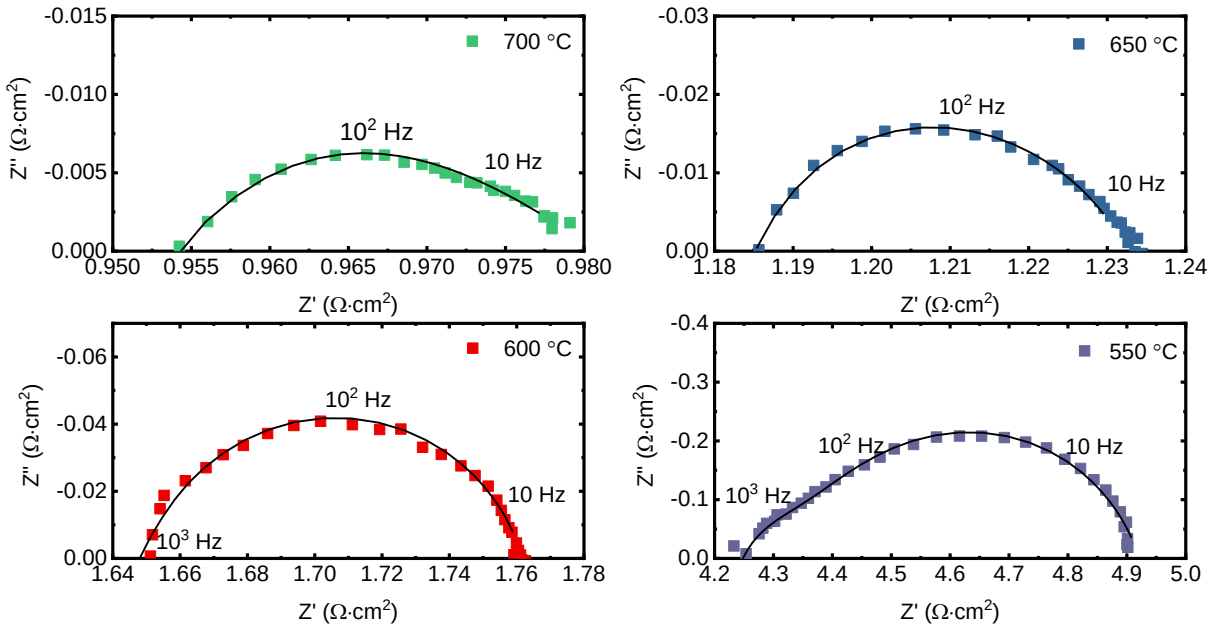

Fig. 3.16 EIS diagrams at OCV of the NR-cell supported on a 0.6 mm thick electrolyte at 700, 650, 600 and 550°C under synthetic air and dry hydrogen.

Table 3.1 Resulting fitting parameters of series resistances (R_s) and total polarization resistances (R_{ptotal}) of the EIS diagram of the NR-cell at OCV at 700, 650, 600 and 550 °C.

T (°C)	R_s (Ω·cm²)	R_{ptotal} (Ω·cm²)
700	8.65E-1	3.58E-02
650	1.06	5.92E-02
600	1.63	1.25E-01
550	4.19	7.34E-01

To verify if the obtained R_s values are determined by the ohmic conductivity (σ_Ω) of the electrolyte, the relation, shown in Equation 3.6, was used:

$$\sigma_\Omega = \frac{l}{R_s} \tag{3.6}$$

where *l* is the length of the electrolyte and **R_s** is the value of area specific resistance in Ω·cm², as shown in **Table 3.1**.

The obtained ohmic conductivity of the cell was plotted in an Arrhenius diagram (**Fig. 3.17**) with the results of the total conductivity of the CGO-NR pellet sintered at 1200 °C, previously shown in **Fig. 3.12**. The experimental data shows both the ohmic conductivity (σ_Ω) from R_s of the cell and the conductivity of the pellet are in excellent agreement. The electrical conductivity of the CGI electrolyte is 3.7 × 10^{-2} S·cm^{-1} at 600 °C and has an activation energy of 0.9 eV. Such results are consistent with previously reported values [12,175] and confirm that the main loss component of the NR-cell is the ohmic resistance due to the rather thick electrolyte support (0.6 mm).

Due to the limitation of the chosen processing technique (uniaxial die pressing) and of the high green density of the NR pellet, it was not possible to manufacture a pellet with a smaller thickness.

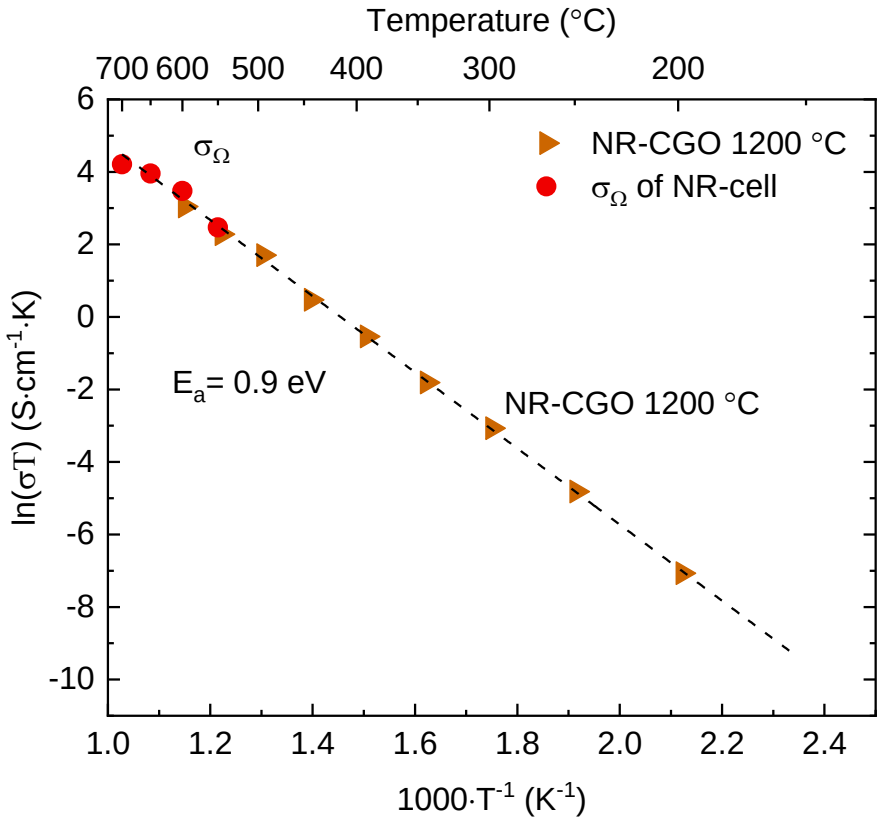

Fig. 3.17 Arrhenius plots of the ohmic conductivity extracted from R_s from impedance data of the NR-cell and total conductivity of CGO-NR pellet sintered at 1200 °C.

3.3.3 Evaluation of Ni/CGO nanocubes and nanorods as a catalyst for ethanol steam reforming and application as a catalytic layer for SOFC

The specific surface area of the 5Ni/CGO-NC and 5Ni/CGO-NR catalysts, both as-prepared and heated at 800 °C, are shown in **Table 3.2**. The BET specific surface area of 5Ni/CGO-NC is considerably lower than that of the CGO-NR. However, the surface area of the nanocubes (~2 $m2 \cdot g^{-1}$) has not been significantly changed after heat treatment at 800 °C. On the other hand, the specific BET area of 5Ni/CGO-NR decrease from 74.3 to 24.6 $m^2 \cdot g^{-1}$ with the same heat treatment.

The chemical composition of the catalyst obtained through WDXRF is shown in **Table 3.2** The Ni contents obtained (~4 wt%) were lower than the nominal ones (5 wt%) for both catalysts, as inferred from the WDXRF data.

Table 3.2 Specific BET area and chemical composition (wt%) of the catalysts.

Sample	BET surface area ($m^2 \cdot g^{-1}$)	Chemical composition (wt%)		
		Ni	**Gd**	**CeO_2**
5Ni/CGO-NC	3	3.6	9.4	87.0
5Ni/CGO-NC (800 °C)	2	-	-	-
5Ni/CGO-NR	74	4.4	9.5	86.1
5Ni/CGO-NR (800 °C)	25	-	-	-

The Raman spectroscopy analyses corresponding to the different Ni/CGO morphologies are shown in **Fig. 3.18**. Similar spectra are obtained for the two different morphologies showing a single predominant band at 456 cm^{-1}. This peak is ascribed to the F_{2g} symmetry mode, characteristic of the CeO_2 vibrations that usually occurs at 465 cm^{-1}. Such mode shifts to lower frequencies upon doping ceria with rare earth elements [225]. There is, however, a large difference in spectrum intensity for the different samples, possibly related to the scattering properties due to the different degrees of crystallinity of the material [226,227].

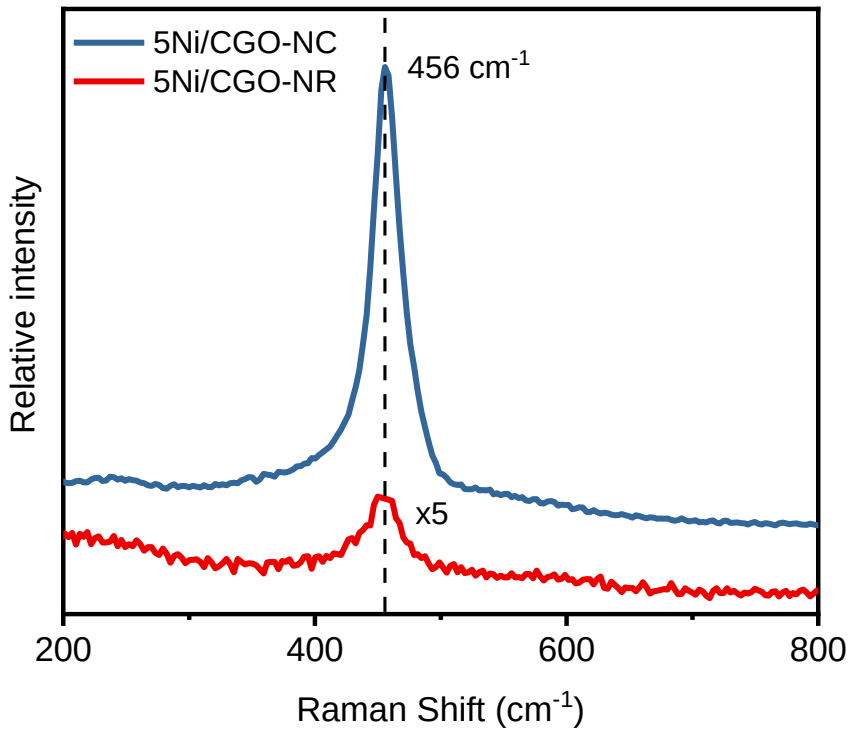

Fig. 3.18 Raman spectra corresponding to different CGO nanostructures.

Fig. 3.19 shows the XRD patterns of 5Ni/CGO-NC and 5Ni/CGO-NR calcined and after heat treatment. All diffractograms exhibited the single-phase fluorite structure of ceria (ICDD 96-900-9009). The shifts in the diffraction peaks are equivalent to the solid solution of CGO. There is no evidence of peaks corresponding to NiO. The 5Ni/CGO-NC catalyst presents more intense diffraction lines than the 5Ni/CGO-NR before heat treatment, showing that the nanostructured CGO support in the form of nanocubes has higher crystallinity. After heat treatment, diffraction lines of 5Ni/CGO-NC catalysts remain practically unchanged. On the other hand, the 5Ni/CGO-NR samples after heat treatment at 800 and 900 °C exhibit more intense diffraction lines, than the as-prepared sample, evidencing the effect of the heat treatment on the nanostructured powders. The average crystallite size was calculated for all catalysts before and after heat treatment. The 5Ni/CGO-NC exhibited average crystallite sizes of 42 nm before and 43 nm after the heat treatment at 800 °C, whereas 5Ni/CGO-NR has crystallite size of 9 nm before heat treatment and 15 and 33 nm after heat treatment at 800 and 900 °C, respectively.

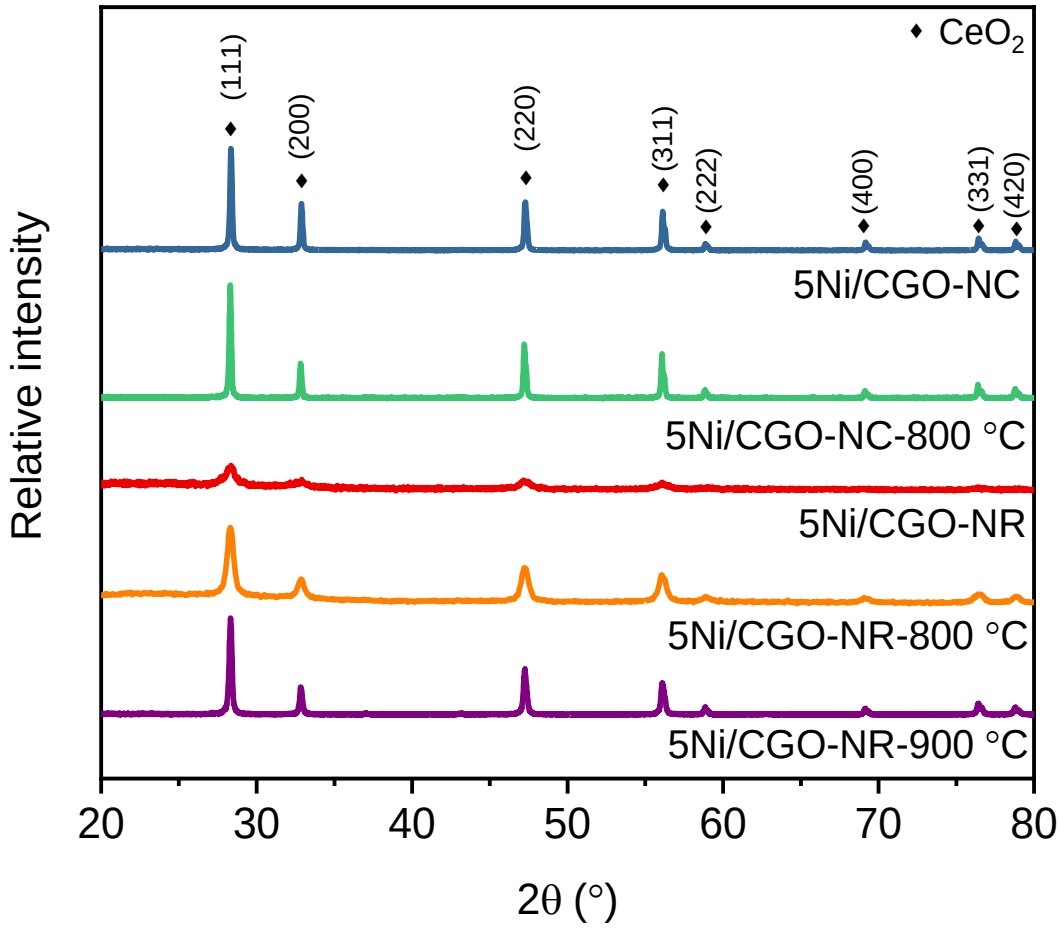

Fig. 3.19 XRD patterns of 5Ni/CGO-NC and 5Ni/CGO-NR calcined and after heat treatment.

Fig. 3.20 shows the H_2-TPR profile of calcined 5Ni/CGO-NC and 5Ni/CGO-NR catalysts. The 5Ni/CGO-NC TPR profile shows four peaks of hydrogen consumption. The first peak at 234 °C, followed by a shoulder at 275 °C, is related to Ni reduction and part of the support reduction promoted by the presence of Ni [75,228]. The third peak at 612 °C is assigned to the reduction of surface CGO and the high temperature peak occurring at 925 °C is related to the reduction of bulk CGO [229,230]. The 5Ni/CGO-NR TPR profile is similar to the 5Ni/CGO-NC, but it presents an additional shoulder at low temperature (160 °C), and broader peaks shifted to lower temperatures than that of the nanocubes-supported catalyst, indicating that the morphology of the support affects the reducibility properties. The main peak at 210 °C is assigned to the reduction of Ni, and the third peak at 240 °C can be related to the reduction of CGO promoted by the presence of Ni [228]. Increasing the reduction temperature reveals two peaks

occurring at 585 and 905 °C that are related to the surface and bulk CGO reduction, respectively [229]. The shift to a lower reduction temperature of the catalyst with the NR suggests a higher active metal dispersion in the support and indicates an increase in its reducibility properties and in its oxygen vacancies [77,231,232].

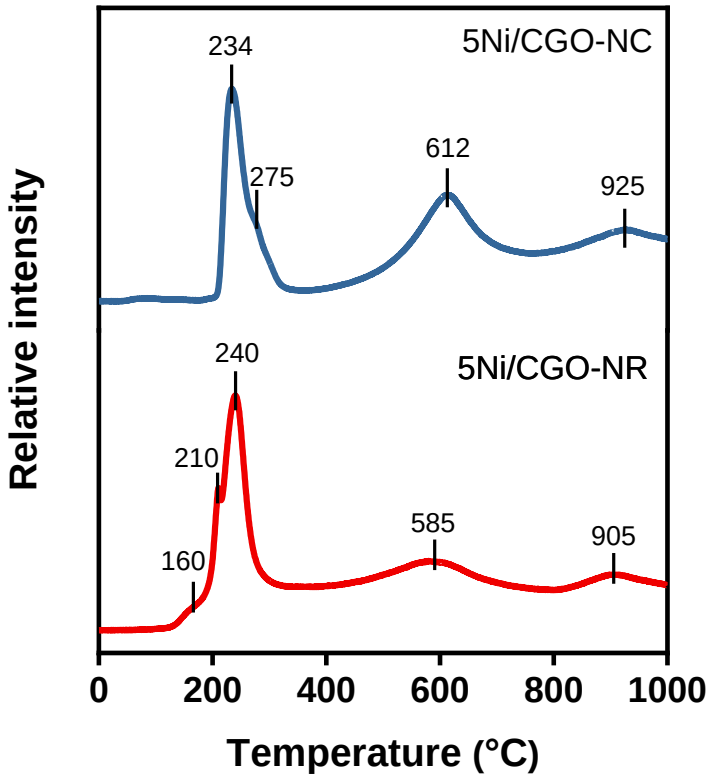

Fig. 3.20 H_2-TPR of the calcined 5Ni/CGO-NC and 5Ni/CGO-NR catalysts.

The TEM image of calcined 5Ni/CGO-NC (**Fig. 3.21** (a)) shows a large distribution of sizes, with the edges of the cubes having an estimated length of ~160 nm. After the heat treatment, as shown in **Fig. 3.21** (b), the nanocubes catalyst presented comparable shapes and sizes (~180 nm length) with slightly more agglomerated and rounded particles with a similar size distribution as compared to the calcined 5Ni/CGO-NC (**Fig. 3.21** (a)) The TEM images of 5Ni/CGO-NR before the heat treatment (**Fig. 3.21** (c)) showed nanorods with a mean length of 80 nm and after heat treatment at 800 °C (**Fig. 3.21** (d)). It is revealed that the nanoparticles retained the rod shape. However, heating at

800 °C caused strong agglomeration and rods became less distinguishable with clearly larger sizes due to coarsening of the rods. Further increasing the temperature of the heat treatment to 900 °C, as shown in **Fig. 3.21** (e), completely changed the shape of the 5Ni/CGO-NR catalyst, and particles assumed a random polyhedron shape with size ~120 nm. This behaviour agrees with the densification behaviour of the CGO-NRs shown in **Fig. 3.7**. In **Fig 3.7**, a first maxima of diffusion occurs at ~850 °C, such that at lower temperatures, the diffusion and particle growth are inactivated. Thus, the morphology changes of 5Ni/CGO-NR catalyst observed at 900 °C agree with the observed morphology of the CGO-NRs pellet heated at 850 °C shown in **Fig. 3.10** (a)

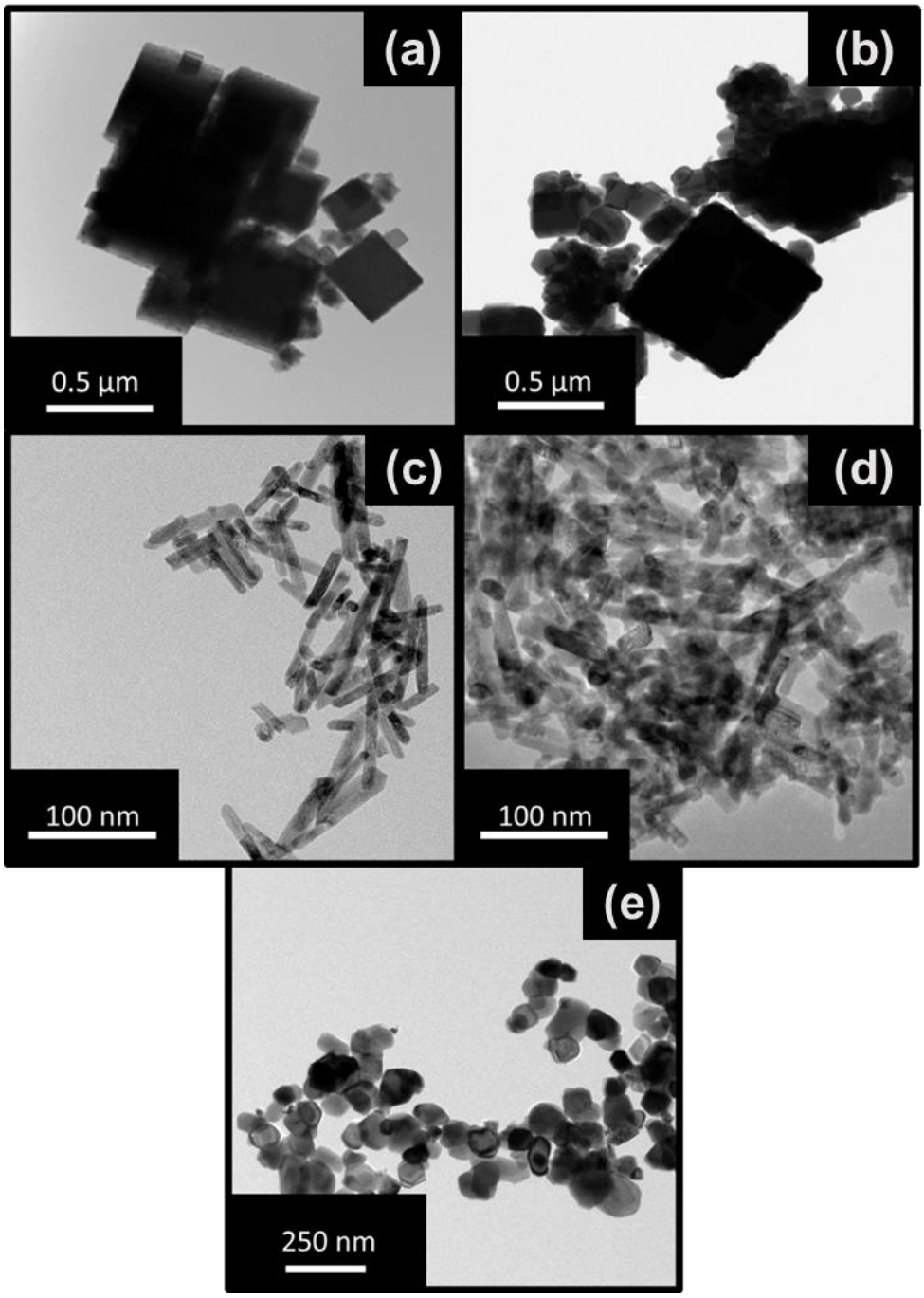

Fig. 3.21 TEM images of (a) 5Ni/CGO-NC calcined, (b) 5Ni/CGO-NC after heat treatment at 800 °C, (c) 5Ni/CGO-NR calcined, (d) 5Ni/CGO-NR after heat treatment at 800 °C and (e) 5Ni/CGO-NR after heat treatment at 900 °C.

The TEM-EDS mapping for 5Ni/CGO-NC (**Fig. 3.22**) and 5Ni/CGO-NR (**Fig. 3.23**) catalyst after heat treatment at 800 °C shows that Ni nanoparticles with mean size of 20 nm are well dispersed on the surface of the catalysts. A more dispersed distribution of Ni particles with a lower mean size is observed in the

5Ni/CGO-NR catalyst in agreement with its larger specific BET area (24.6 $m^2 \cdot g^{-1}$) than the 5Ni/CGO-NC catalyst (2 $m^2 \cdot g^{-1}$).

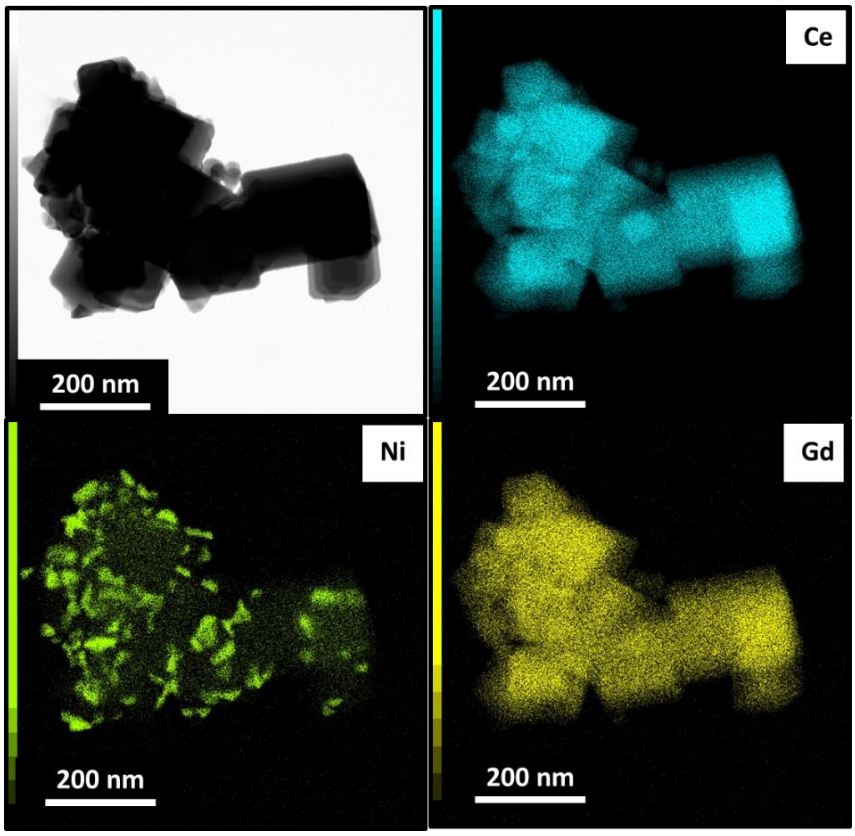

Fig. 3.22 TEM-EDS mapping for 5Ni/CGO-NC catalyst after heat treatment at 800 °C.

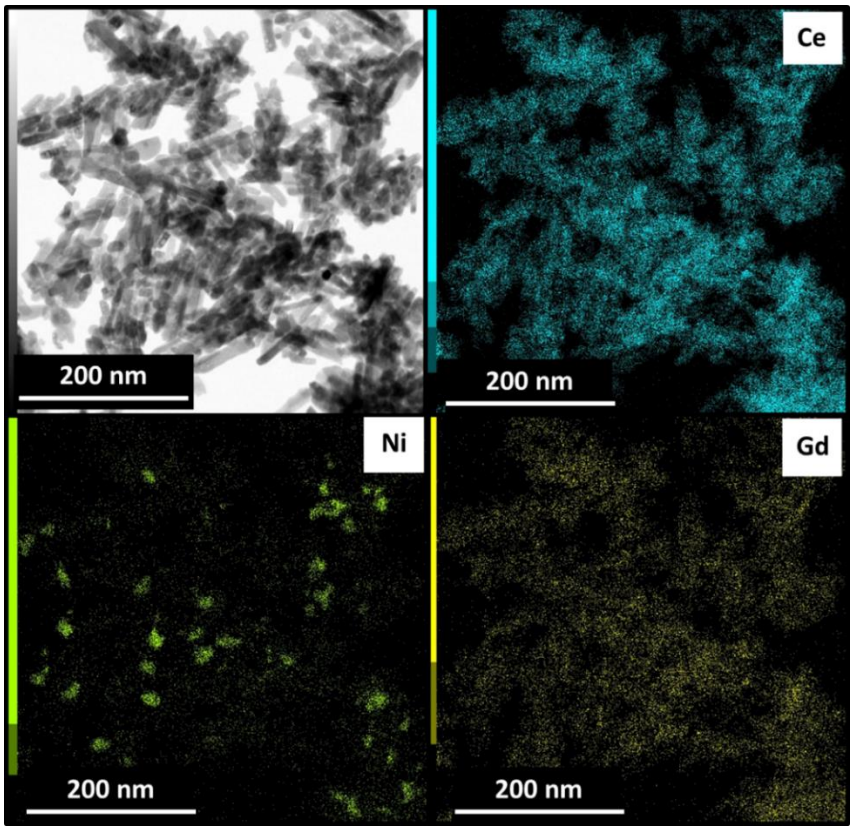

Fig. 3.23 TEM-EDS mapping for 5Ni/CGO-NR catalyst after heat treatment at 800 °C.

The synthesized nanomaterials were studied for ethanol steam reforming (ESR)**.** The ethanol conversion obtained for the ethanol steam reforming reactions at 600 °C with H_2O:EtOH = 3:1 (molar ratio) is shown in **Fig. 3.24.** Both catalysts (without heat treatment) showed 100% ethanol conversion during 25 h of reaction. The 5Ni/CGO-NR catalyst heated at 800 °C showed 100% conversion of ethanol upon 15 hours of reaction and a very small deactivation with increasing reaction time (~99% at 25 h). On the other hand, 5Ni/CGO-NC catalyst heated at 800 °C showed an initial ethanol conversion of 97%, followed by a fast loss of activity up to 5 hours of reaction and a relatively stable conversion (~87%) with increasing reaction time. The 5Ni/CGO-NR catalyst heated at 900 °C showed 100% initial conversion of ethanol and a fast deactivation in the initial five hours of reaction, followed by a continuous loss of activity with increasing reaction time (~83% at 25 h).

The heat treatment at high temperatures changes the morphology and decreases the CGO support surface area, particularly the CGO-NR, and the coarsening of the Ni particles, resulting in fewer active sites for the catalytic

reaction. The results shown in **Fig. 3.24** indicate that the 5Ni/CGO-NR remains active even after heat treatment at 800 °C, possibly due to higher surface area and dispersion of Ni in the support. Nonetheless, when the 5Ni/CGO-NR catalyst is heated to 900 °C, there is a morphological change in the support, as shown in **Fig. 3.21** (e), and grain growth of the Ni particles occurs, reducing the active sites and leading to a significant deactivation of the catalyst. Although the 5Ni/CGO-NC catalyst's morphology and surface area do not significantly change after heat treatment at 800 °C, the initial relatively low specific surface area inhibits a high dispersion of Ni nanoparticles (**Fig. 3.22**). This feature can promote the agglomeration and coarsening of the Ni particles.

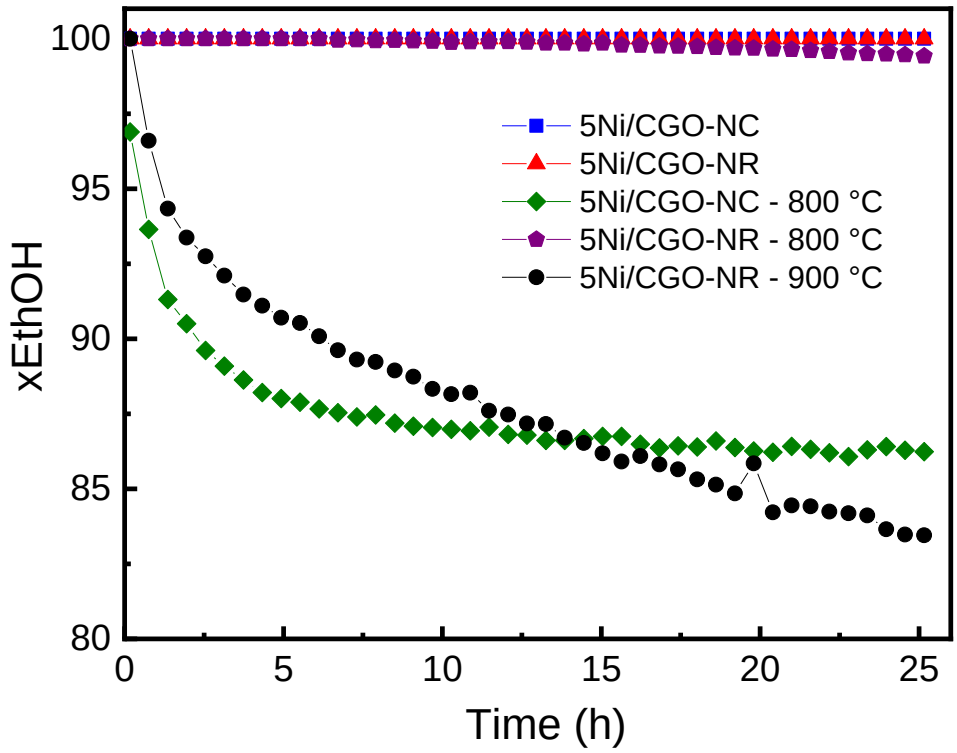

Fig. 3.24 Ethanol conversion obtained for the catalysts after ethanol steam reforming reactions at 600 °C and H_2O/EtOH molar ratio of 3.

The time-dependence of the product distribution during the 25 h reforming reactions is shown in **Fig. 3.25**. All reactions start with ~70% of selectivity to H_2. For the catalysts, 5Ni/CGO-NC, 5Ni/CGO-NR, 5Ni/CGO-NR-800 °C, **Fig. 3.25** (a), (c), and (d), respectively, the product distribution remains stable. As for the 5Ni/CGO-NC-800 °C catalyst (**Fig. 3.25** (b)), during the first 2 h of the reaction,

there is a decrease in the initial H_2 selectivity by 2% correlated with an increase in acetaldehyde selectivity, also by 2%. Further, in the ESR, the selectivity of the products remains stable. Such stability is not observed for the 5Ni/CGO-NR-900 °C catalyst (**Fig. 3.25** (e)), in which the initial drop in the H_2 selectivity in the first two hours develops as a continuous decrease of H_2 selectivity coupled with a continuous increase of acetaldehyde formation. The observed deactivation of the catalytic activity of the 5Ni/CGO-NR heated at 900 °C is related to the significant microstructural change observed in **Fig. 3.21**.

Regarding the distribution of products, in **Fig. 3.25**, the formation of H_2, CO, CO_2 and traces of CH_4, was detected in all catalysts [202]. Besides the ethanol steam reforming (Equation 1.15), several reactions can occur in parallel, such as: (i) the decomposition of ethanol (Equation 3.7), (ii) the dehydrogenation of ethanol to acetaldehyde (Equation 3.8), (iii) the steam reforming of acetaldehyde (Equation 3.9) and (iv) the water gas shift reaction (Equation 3.10). The results obtained for the catalysts suggest that the ethanol reforming, the dehydrogenation of ethanol to acetaldehyde followed by the steam reforming of acetaldehyde and the water gas shift reactions were favoured in these catalysts. The deactivation of the catalysts upon heat treatment was accompanied by the formation of acetaldehyde and a drop in H_2 selectivity. As the catalyst needs metallic sites to break the C-C bond, it is suggested that the catalysts that exhibited deactivation and increasing acetaldehyde selectivity at the expense of H_2 were losing metallic active sites.

$$\mathrm{CH_3CH_2OH} \rightleftharpoons \mathrm{CO} + \mathrm{H_2} + \mathrm{CH_4} \tag{3.7}$$

$$\mathrm{C_2H_5OH} \rightleftharpoons \mathrm{C_2H_4O} + \mathrm{H_2} \tag{3.8}$$

$$C_2H_4O + H_2O \rightleftharpoons 2CO + 3H_2 \tag{3.9}$$

$$CO + H_2O \rightleftharpoons CO_2 + H_2 \tag{3.10}$$

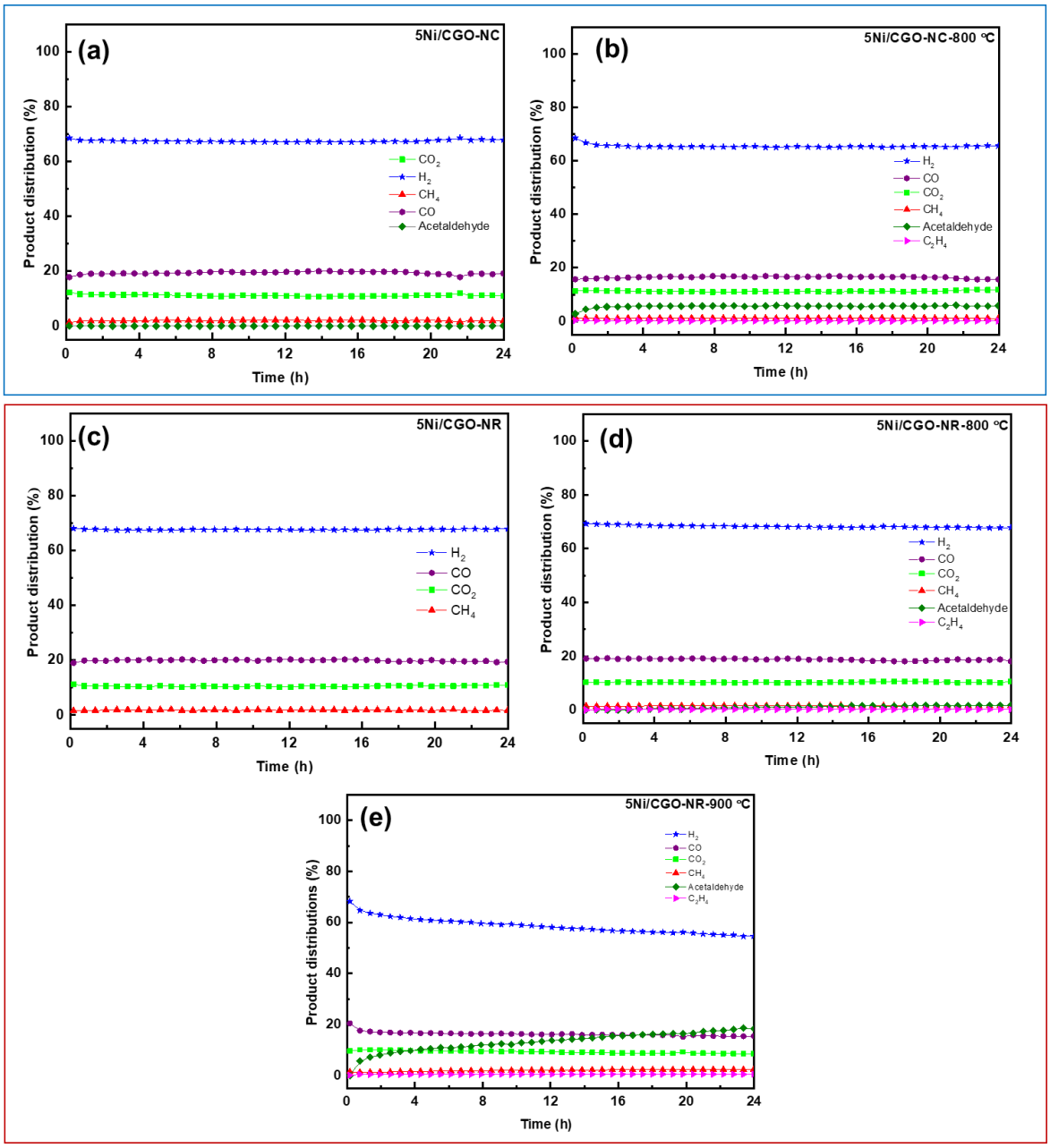

Fig. 3.25 Product distribution obtained for the catalysts after ethanol steam reforming reactions at 600 °C and H_2O/ethanol molar ratio of 3, for (a) 5Ni/CGO-NC, (b) 5Ni/CGO-NC-800 °C, (c) 5Ni/CGO-NR, (d) 5Ni/CGO-NR-800 °C and (e) 5Ni/CGO-NR-900 °C.

Fig. 3.26 shows the thermogravimetric analysis (TGA) of spent catalysts carried out to investigate possible carbon formation in the catalysts surface during ESR at 600 °C. The calcined 5Ni/CGO-NC catalyst presented a small decrease in mass, while the same catalyst with heat treatment at 800 °C showed the highest mass loss. The peaks in the derivative of mass loss develop between 620 and

590 °C, indicating the oxidation of carbonaceous species [233]. The 5Ni/CGO-NR catalyst exhibit no mass loss indicating absence of carbon deposits. For the 5Ni/CGO-NR catalyst heated at 800 °C a very small peak is identified at 575 °C. These results are consistent with the ethanol conversion (**Fig. 3.24**), in which the catalyst 5Ni/CGO-NC heat treated at 800 °C showed the larger activity loss. The TGA data suggests that the deactivation of the catalyst was caused by carbon formation on catalyst's surface, a feature that is likely to occur in small surface area/low dispersion catalysts.

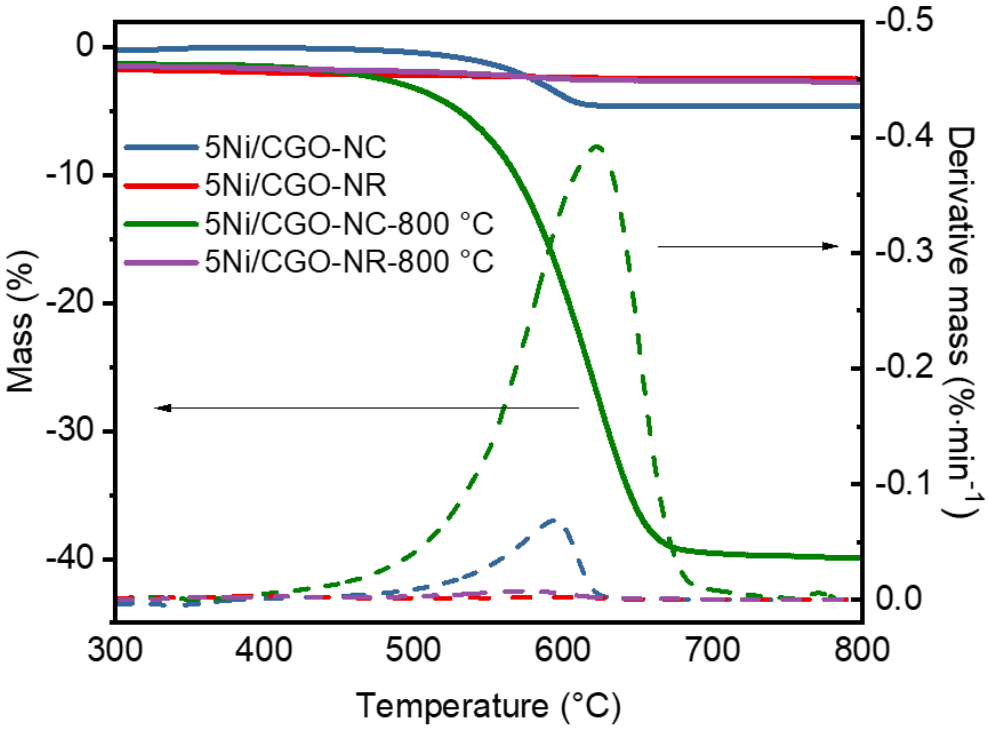

Fig. 3.26 TGA, with mass and derivative of mass of spent 5Ni/CGO-NC and 5Ni/CGO-NR catalysts after ESR at 600 °C.

The experimental results showed that the high specific surface area of CGO-NR promoted a high dispersion of Ni nanoparticles that contributed to a high catalytic activity at 600 °C towards ethanol steam reforming. It is interesting to note that the CGO-NR exhibited a more pronounced microstructural change upon heating at 800 °C. Nevertheless, upon heating both Ni-impregnated CGO supports (NR and NC), the nanorods were observed to retain better catalytic properties for

the ESR at 600 °C. Thus, the 5Ni/CGO-NR catalyst was chosen to be applied as a catalytic layer for the direct ethanol SOFC tests.

Fig. 3.27 shows the 5Ni/CGO-NR catalytic layer deposited to the anode and heated at 800 °C for adhesion of the layer. A total thickness of 50 µm was obtained for the catalytic layer by depositing 7 $mg \cdot cm^{-2}$ of the 5Ni/CGO-NR ink. The image shows that by heating at 800 °C a good adhesion of the catalytic layer to the anode support was ensured. Hence, those conditions were used for the application of the catalytic layer to the commercial ASC, submitted to a durability test under fuel cell condition with ethanol as a fuel.

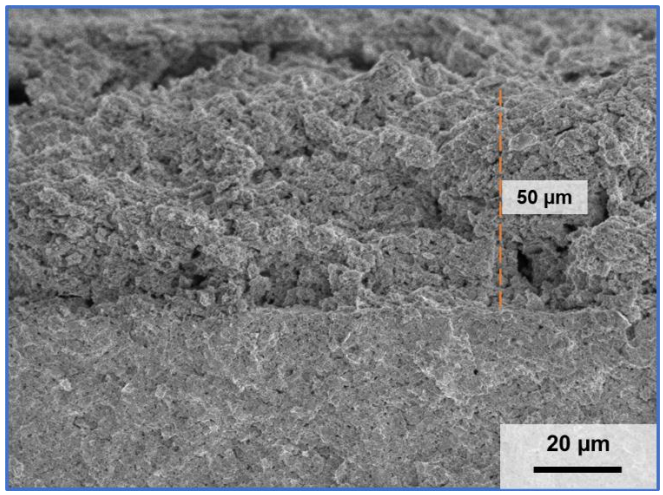

Fig. 3.27 Secondary electron SEM images of a fractured surface of the 5Ni/CGO-NR catalytic layer deposited the anode and heated at 800 °C. The dotted line indicates the thickness of the catalytic layer.

To investigate the effect of the catalytic layer on the electrochemical performance of fuel cell directly fed with anhydrous ethanol, a short-term durability test was carried out for 130 h at 700 °C and 0.6 V (**Fig. 3.28** (a)). The test was run under flow of synthetic air on the cathode side, and at first hydrogen was used as a fuel and then it was changed to ethanol. The flow rates were calculated to carry an equivalent theoretical number of electrons to the anode. A 1/6 ratio between ethanol and H_2 was set while keeping a constant total flow rate of 6 $L \cdot h^{-1}$. Therefore, 78% H_2 balanced in N_2 was switched to 13% ethanol, by keeping the temperature of ethanol's thermal bath at 48 °C, according to the Clapeyron's law.

In the first 20 h under hydrogen the cell experienced a degradation rate of -2.8 $mA \cdot h^{-1}$. By changing the fuel to ethanol there was drop in the current output from ~1.6 $A \cdot cm^{-2}$ under hydrogen to ~0.8 $A \cdot cm^{-2}$ under anhydrous ethanol. Such a

decrease in current could be explained by many parameters of the complex reaction taking place at both the anode and catalytic layers. The Faradaic efficiency for ethanol is possibly lower than that of H_2, the larger molecule size of ethanol imposes restrictions to mas transport in the porous layers, moreover the catalytic conversion of ethanol to hydrogen is limited to ~70% of selectivity as seen in **Fig. Fig. 3.25** (d). Residence time is also a key parameter for the catalytic reaction. The higher the residence time, the higher the ethanol conversion and H_2 yield [234]. A possible cause for the current drop is related to incomplete conversion of ethanol that may be associated with a lower residence time (spatial velocity) in the fuel cell test rig compared to the catalytic reactor for ESR. In the catalytic reactor ethanol flows (30 $ml \cdot min^{-1}$) through the volume of the packed catalyst powder soaked in the quartz tube, whilst in the fuel cell system the ethanol is blown to the surface of the catalytic layer at a higher flow rate (100 $ml \cdot min^{-1}$). Such different configuration may result in a weaker interaction of the ethanol with the catalytic layer in the fuel cell system.

After 6 h under ethanol, the fuel cell stabilizes the current output to 0.65 $A \cdot cm^{-2}$ and remains practically stable for 110 h of operation with dry ethanol. During the ethanol stability test the fuel cell exhibits a relatively lower degradation rate of -0.76 $mA \cdot h^{-1}$. After completing >110 h under ethanol, the fuel is changed back to hydrogen and the current increases to 1.4 $A \cdot cm^{-2}$. It is interesting to note that by extrapolating the initial degradation ratio under H_2 to 130 h of operation results in a final current close to 1.4 $A \cdot cm^{-2}$, indicating that operation under ethanol promoted no additional degradation of the fuel cell's performance. Moreover, it is important to consider that degradation due to carbon deposit is likely to occur within relatively shorter time of operation than that of the stability test (<110 h). Such an excellent result demonstrate that the active catalyst based on CGO-NR and Ni is capable of sustaining ethanol steam reforming at 700 °C, using the water produced through the catalytic reaction of the electrochemical oxidation of H_2.

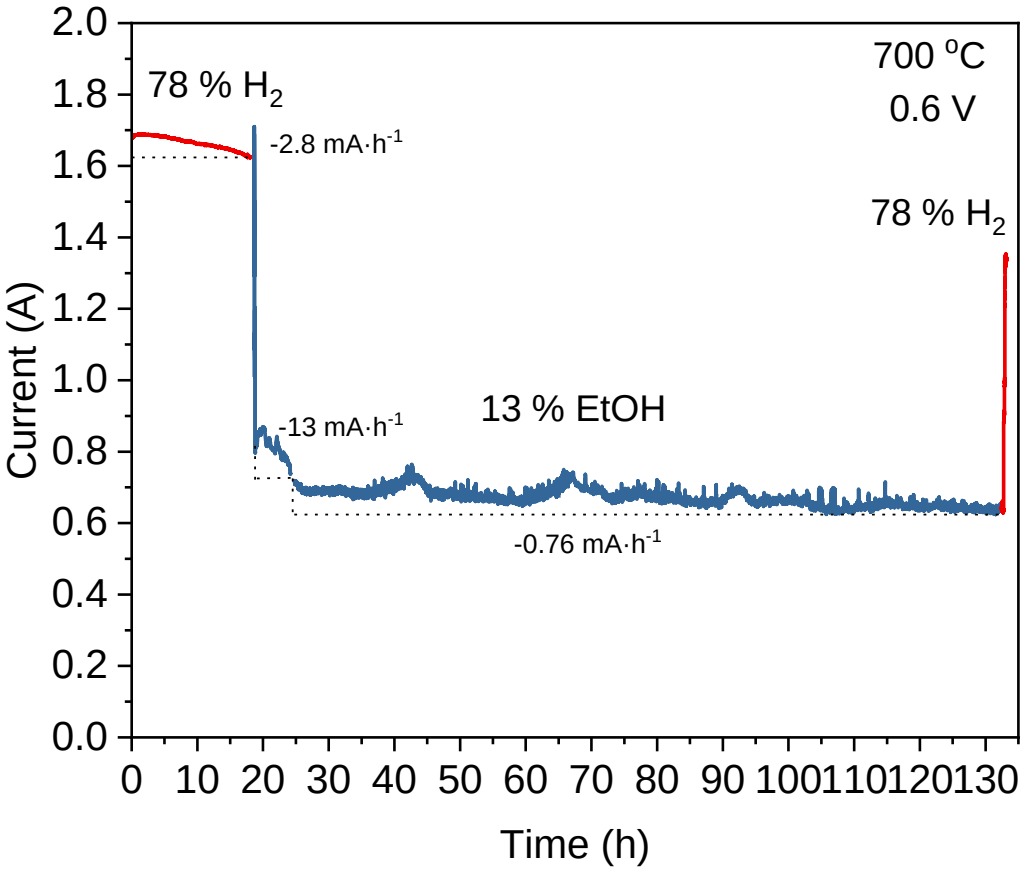

Fig. 3.28 Durability test of the anode-supported single cell with the 5Ni/CGO-NR catalytic layer, 130 h at 700 °C, applied voltage of 0.6 V, under 6 $L \cdot h^{-1}$ synthetic air at the cathode side and at the anode side dry hydrogen for the first 20 h, then dry ethanol for the next 110 h and finishing with hydrogen. A total flux of 6 $L \cdot h^{-1}$ was flown through the anode compartment.

Polarization curves and EIS data were collected at both the beginning and the end of the durability test, as shown in **Fig. 3.29** and **Fig. 3.30**. The estimated values: series resistance (R_s) and the total resistances (R_{total}), are shown in **Table 3.3**.

At the beginning of the test, under H_2, the cell has an OCV of 1.04 V and a maximum power density of 1.06 $W \cdot cm^{-2}$ 2, as shown in the I-V curve in **Fig. 3.29** (a). The I-V curve measured after 130 h of operation shows a decrease in both OCV and power density. A decrease in OCV is usually associated with a leakage in the system, through the electrolyte or through the sealing of the fuel cell testing unit. Besides the I-V curve the EIS can be used to better understand the electrochemical behaviour of the cell. The EIS diagram under 0.6 V polarization is

shown in **Fig. 3.29** (b). The series resistance, R_s, attributed to the ohmic resistance is the main component (~70%) to the total resistance of the fuel cell. The R_s value increases 20% after the durability test. The polarization resistance shows two main arcs: at a high frequency ~10^3 Hz and one at a low frequency ~10 Hz; however, the low frequency end is not well defined. Nonetheless, R_{ptotal} is estimated and assigned to the polarization resistance. Considering the R_{ptotal} values there is a small increase of ~3% polarization resistance after the fuel cell operation. These results showed that the electrodes suffered little degradation after 110 h operating under ethanol. Indicating that there was none or no significant carbon formation on the anode of the fuel cell, and that the decrease in power density of the cell can be attributed to a loss in gas tightness.

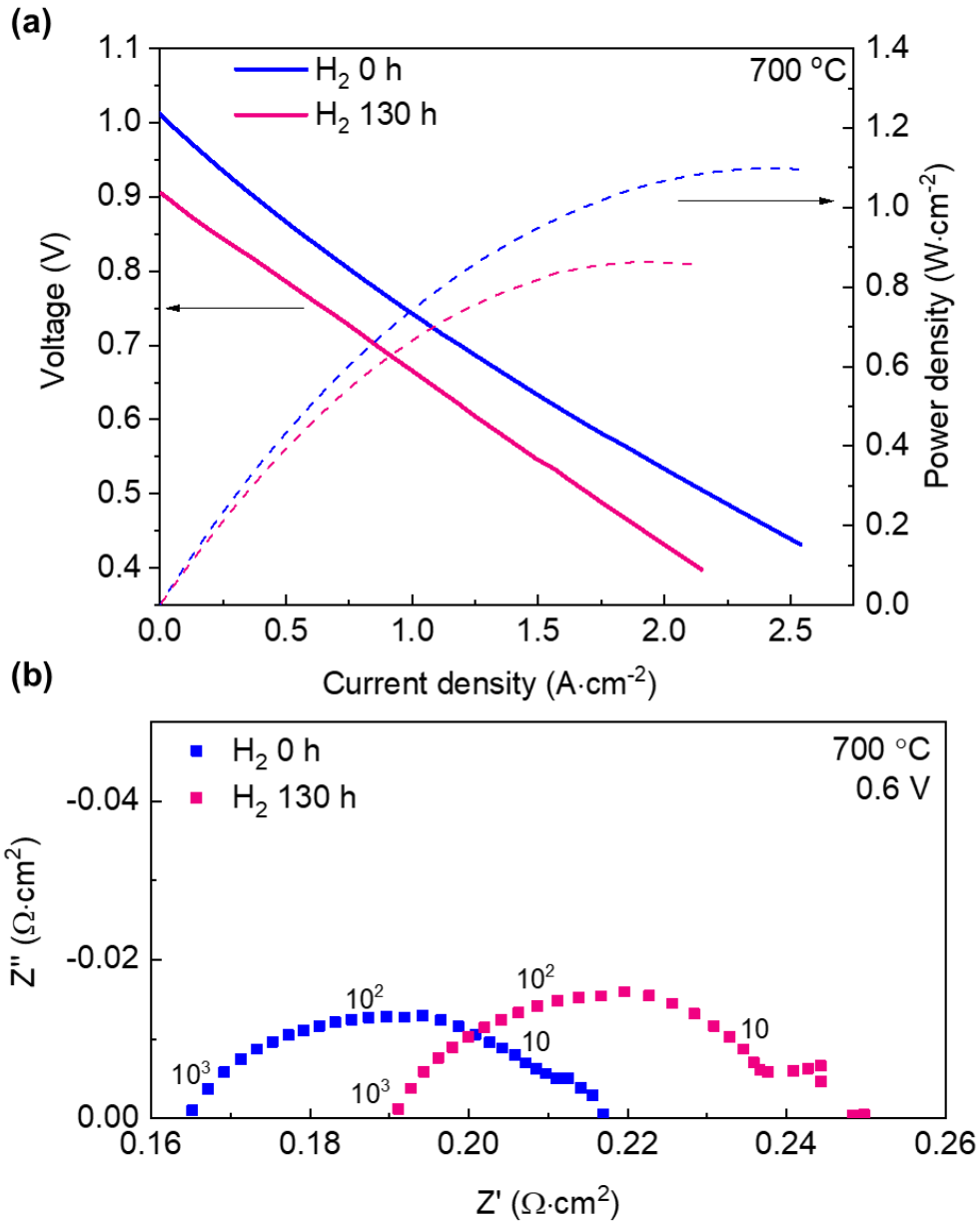

Fig. 3.29 Electrochemical characterization of the fuel cell under hydrogen before and after the durability test of 130 h operation (20 h H_2 and 110 h EtOH) at 700 °C under 0.6 V polarization: (a) I-V curve and (b) complex impedance diagrams at 0.6 V.

Fig. 3.30 (a) shows the I-V curves of the fuel cell under ethanol, measured both at the beginning and end of operation under ethanol. The I-V curves were measured between 0.6 V and 0.4 V to ensure the production of H_2O for the direct internal reforming of ethanol. A significant decrease in maximum power density is noted when the fuel is changed from H_2 to ethanol, in agreement with the current drop observed in **Fig. 3.28**. Under ethanol a more pronounced decrease in power

density takes place in the first 6 hours, possibly due to stabilization of the system under ethanol. After 110 h of operation the maximum power density decreased from 0.47 $W \cdot cm^{-2}$ to 0.39 $W \cdot cm^{-2}$. The EIS data from **Fig. 3.30** (b) indicates an increase in series resistance after 110 h of operation, whereas the polarization resistances are similar.

The EIS diagrams before and after the durability test revealed that the main component contributing to the increased total resistance of the fuel cell is the ohmic resistance. A similar feature was observed in the **Fig. 3.29** (b) in which the EIS data under H_2 showed an increase in the ohmic resistance as the main responsible for the performance degradation of the fuel cell. Therefore, such an increase of the ohmic resistance measured under both fuels is possibly associated with electrochemical degradation process of the fuel cell and, apparently, it is not directly related to the use of ethanol as fuel.

Comparing the obtained resistances from **Fig. 3.29** (b) and **Fig. 3.30** (b), as shown in **Table 3.3**, an increase in both series (R_s) and polarization resistances (R_{ptotal}) is observed. The R_s value increased by almost 2-fold, whereas there is more than a 4-fold increase in R_{ptotal}. Indicating that the reactions occurring at the electrodes are more affected by the change in fuel. Nevertheless, the EIS spectra did not indicate an increase in the polarization resistance with the cell's operation, on the contrary, there was some improvement in the R_{ptotal}. Nonetheless, the total resistance increased slightly from 0.5347 $\Omega \cdot cm^2$ to 0.5592 $\Omega \cdot cm^2$, due to the increase in R_s. Further pointing out that the anode did not deteriorate and that the catalytic layer was able to supress carbon formation on the anode.

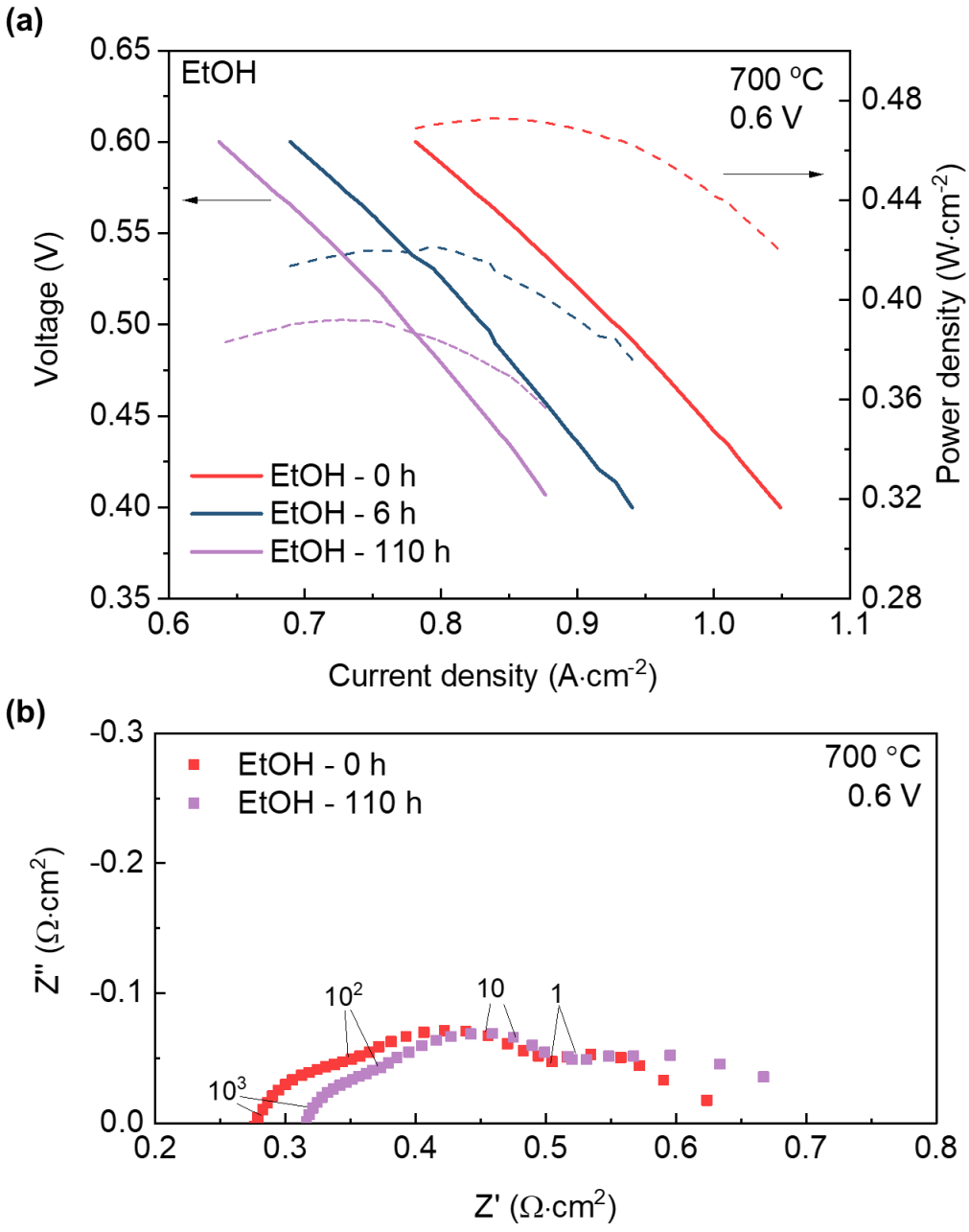

Fig. 3.30 Electrochemical analyses of the cell under ethanol at the start of the ethanol introduction (after 20 h under H_2) and after (20 h H_2 and 110 h EtOH) with 0.6 V polarization at 700 °C (a) I-V curve starting at 0.6 V (b) EIS diagrams at 0.6 V.

Table 3. 3 Resulting fitting parameters of series resistances (R_s) and total polarization resistances (R_{ptotal}) and total resistances (R_{total}) of the EIS diagram of the anode supported cell with catalytic layer at 700 °C under 0.6 V, with H_2 and ethanol as fuels, at the start and at the end of the durability test.

Fuel-time	R_s ($\Omega \cdot cm^2$)	R_{ptotal} ($\Omega \cdot cm^2$)	R_{total} ($\Omega \cdot cm^2$)
H_2-0 h	1.52E-01	6.02E-02	2.12E-01
H_2-130 h	1.82E-01	6.20E-02	2.44E-01
EtOH-0h	2.65E-01	2.70E-01	5.35E-01
EtOH-110 h	3.06E-01	2.53E-01	5.59E-01

Fig. 3.31 shows the SEM image of the fractured cell showing the interface between the anode and the catalytic layer after the durability test. The interface shows no sign of delamination between the layers and no carbon deposits, filaments, or whiskers, were detected.

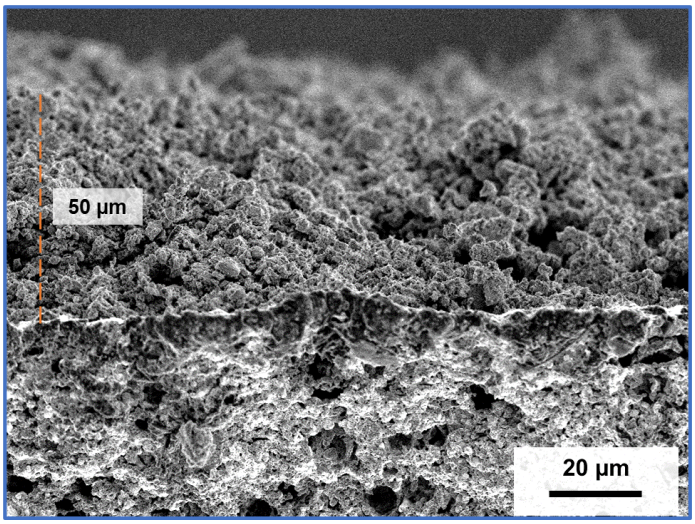

Fig. 3.31 Secondary electron SEM image of the fractured cell showing the interface between 5Ni/CGO-NR catalytic layer and the anode support after the durability test at 700 °C under ethanol. The dotted line indicates the thickness of the catalytic layer.

3.4 Summary

3.4.1 Shape-controlled synthesis of CGO by hydrothermal route

The hydrothermal method was successfully used to synthesize CGO with different morphologies: nanorods and nanocubes. The characterization revealed that the samples exhibited different degrees of crystallinity and distinctive thermal evolution. By increasing the sintering temperature, the CGO-NR structure evolves rapidly, showing an intense densification at 1050 °C, whereas for the NC diffusion is inhibited and there is no retraction, which is confirmed by the porous microstructure at 1400 °C. Such results are attributed to high surface energy of the NRs that promotes mass diffusion and leads to a rapid rod to sphere transformation. On the other hand, the stability of the NCs upon thermal treatment was ascribed to a lower surface energy, befitting the reconstruction of more stable ceria {111} surface. Due to the high sintering activity of the NR, a CGO-NR sample was sintered at 1200 °C and it presented electrical conductivity compatible with a CGO sample sintered at 1500 °C.

These results indicated the possibility of controlling the behaviour of CGO by defining the shape of nanoparticles. These findings show that microstructural control of ceria can lead to its application for a different purpose in an SOFC. Thus, the applications of the NR and NC CGO were evaluated both in electrolyte-supported ceria-based SOFC and as the catalyst support for SOFC operating directly with ethanol.

3.4.2 Application of CGO nanorods as electrolyte support in an SOFC

A ceria-based electrolyte supported solid oxide fuel cell was successfully fabricated at a sintering temperature of 1150 °C. The morphology of gadolinium-doped ceria nanorods was essential in promoting the densification of the electrolyte at such a low temperature. The I-V curves indicate that sintering at 1150 °C resulted in IT-SOFC with good gas tightness, low electrode polarization, and power output limited by the electrolyte thickness. The experimental results evidenced that shape control synthesis of doped ceria is a promising route to

promote significant cost reduction and increased fabrication flexibility to ceria-based solid oxide fuel cells.

3.4.3 Evaluation of Ni/CGO nanocubes and nanorods as catalyst for ethanol steam reforming and application as catalytic layer for SOFC

Shape-controlled CGO nanoparticles, nanocube and nanorod, were studied as Ni support catalysts aiming at ethanol steam reforming reaction at intermediate temperature (600-700 °C). The morphology of the support was shown to have an important role in controlling the conversion of ethanol and carbon formation on the surface of the catalyst. The catalyst Ni/CGO-NR was shown to have the highest activity due to the highest surface area of the support that favoured a high dispersion of Ni. The heat treatment at temperatures close to those necessary to attach the catalytic layer onto the anode of solid oxide fuel cell had a striking effect on the catalytic properties of the Ni/CGO. The high surface area of the CGO-NR was crucial to favour a high dispersion of Ni in the ceramic support. Such high surface area of the calcined material resulted in high catalytic activity sustained even after heating the catalyst at 800 °C. Further heating the CGO-NR to 900 °C resulted in activity loss, similarly to the observed for CGO-NC heated at 800 °C.

Thus, the Ni/CGO-NR was applied as a catalytic layer in the anode-supported SOFC. The durability of the direct internal reforming of ethanol was evaluated at 700 °C. The fuel cell exhibited a decrease in the current output when the fuel was changed from H_2 to ethanol which was linked to an incomplete conversion of ethanol to H_2. Nonetheless, the most important result is the stable performance of the fuel cell for more than 110 hours of continuous operation under dry ethanol. The electrochemical characterization suggested that operating the fuel cell under ethanol had no additional degradation mechanism as compared to H_2. Moreover, no sign of carbon deposits was detected on the surface of the anode after running the fuel cell on dry ethanol. The results showed a promising strategy for the stable operation of direct ethanol solid oxide fuel cells at intermediate temperature.

Chapter 4

Functional ceria-based thin film deposited by pulsed laser deposition as cathode/electrolyte interlayers

4.1 Introduction

In the intermediate temperature solid oxide fuel cells (IT-SOFC), the electrochemical reactions such as ORR and ion transport occurring at the cathode and cathode/electrolyte interface, are hindered with the typical state-of-the-art (SoA) materials. It is precisely at this interface where phenomena of reactivity between phases and diffusion between cations occur, promoting the decrease in the fuel cell's performance and durability. Thus, the performance of the fuel cell will be greatly influenced by those interfaces. To achieve a high performance and durability of an IT-SOFC it is a requirement to increase the cathodic activity and to decrease the interfacial resistance between cathode and electrolyte.

Currently, the LSCF perovskite cathode materials reacts with the YSZ electrolyte [52–54], therefore doped-ceria barrier layer (BL) is introduced to inhibit the interdiffusion processes [10,38,39,235–237]. However, there are still challenges for the optimization of the BL: its thickness must be minimized, and its microstructure optimized to reduce ohmic resistance contribution. Pulsed laser deposition (PLD) has shown to be the most promising method to apply a thin dense, and continuous BL [57,59,238]. Doped-ceria barrier layers deposited by PLD have improved the performance by 70% compared to SoA fuel cells and shown good stability under continuous operation [119].

Besides the BL, adjusted nanostructured layers can be deposited by the PLD technique to enhance the ORR by creating an interface rich of reaction sites. A possible strategy to increase the interface for ORR is to create a nanocomposite cathode combining an electronic conductor and ionic conductor. The strontium-doped lanthanum manganite (LSM), the standard cathode material for high temperature SOFC (800-1000 °C), is widely studied due to electronic properties, chemical stability, and specially its good compatibility with the YSZ electrolyte [239]. However, due to its poor oxygen surface exchange and diffusivity causing a limited extension of reaction beyond the TPB, single-phase LSM is not an appropriate choice as a cathode when intermediate temperatures of operation are

targeted [240] [241]. The generation of nanocomposite electrodes combining structures of LSM with an ionic conductor such as samarium doped ceria (SDC) [242], which has a high oxygen conductivity, has been shown to increase the length of active area, and improve ORR kinetics [243].

In recent years, a novel approach based on nano-scaled structures have been applied between cathode and electrolyte to decrease the oxygen electrode resistance [21–27]. Su et al. [243] and Yoon et al. [63] have successfully grown nanocomposite structures of LSM/YSZ and LSCO/CGO, respectively, reporting an improvement in electrochemical properties. Develos-Bagarinao et al. [244] proposed a dense multilayer heteroepitaxial cathode of LSC and GDC with interface-induced enhancement of oxygen surface exchange and oxygen ion diffusivity resulting in a superior fuel cell performance. While fuel cells comprising nanocomposite layers may exhibit enhanced power density by improving adhesion properties, increasing the density of the active surface area to facilitate the migration of oxygen ions, charge transfer processes, and long-term thermochemical stability remain a challenge [13,245,248]. In this regard, a previous report investigated the fundamental electrochemical properties of LSM-SDC vertically aligned nanocomposites (VANs) deposited on model single crystal electrolytes.[249] These VANs showed a greatly improved long-term thermal stability with respect to SoA electrode materials by suppressing the Sr segregation to the surface, along with enhanced oxygen kinetics as a consequence of fast diffusion and incorporation pathways promoted by the microstructural alignment [249]. Moreover, unlike standard multilayer films, VANs are self-assembled structures, with stable interfaces formed at growth temperature, that exhibit good microstructural stability at operation temperatures.

In the present study an SDC barrier layer combined with an LSM-SDC nanostructured functional layer (NFL), both deposited by pulsed laser deposition (PLD), were applied in a SoA anode supported cell. The role of such bilayer placed between the YSZ electrolyte and LSCF current collector layer (CCL) was investigated. The SDC BL will help minimizing cation interdiffusion while the composite’s interface will enlarge the electrochemically active surface area for the ORR. The nanostructured layers applied by the PLD technique were fine-tuned to obtain dense and thin interlayers. The goal is to better understand the role of

nanometric interlayers to enhance the overall performance of the cell and its durability.

4.2 Experimental

Initial studies were carried out on symmetrical cells prepared by deposition of thin layers by pulsed laser deposition (PLD) on a 150 μm thick substrate of 8YSZ (Kerafol), as shown in **Fig.**7.1. Specifically, a bilayer formed by a SDC barrier layer (BL) and a nanocomposite functional layer (NFL) of LSM - SDC was deposited by PLD in a multitarget chamber from PVD Products (PVD5000) with a KrF excimer laser (λ = 248 nm). The targets used for this purpose were of $Sm_{0.2}Ce_{0.8}O_{1.9}$ (Kceracell) for the BL and 50:50 wt% $(La_{0.8}Sr_{0.2})_{0.98}MnO_3$ (Kceracell) and $Sm_{0.2}Ce_{0.8}O_{1.9}$ (Kceracell) for the NFL target. An energy fluency of around 1 $J \cdot cm^{-2}$ was used for the ablation of the targets and a frequency of 10 Hz for the BL and of 2 Hz for the NFL. During the deposition process, the distance between the substrate and the target was 90 mm, the temperature of the chamber was kept at 750 °C under an oxygen partial pressure of 0.7 Pa.

A cathode current collector layer (CCL) of $(La_{0.6}Sr_{0.4})_{0.97}Co_{0.2}Fe_{0.8}O_3$ (LSCF) (Kceracell) was deposited on top of the as-deposited PLD layers and directly on the YSZ substrate by a 3-axis automated airbrush (Print3D Solutions). The ink was prepared according to a formulation developed by the IREC group [213]. Accordingly, ethanol, LSCF and polyvinylpyrrolidone (PVP, Sigma Aldrich, Mw ~55000) with the proportion of 10:1:0.1 wt% respectively, were mixed under magnetic stirring for 12 h, followed by ultrasonication for 1 h. The thickness of the LSCF CCL deposited was controlled by its weight (~8 mg of LSCF on each side of the cell). A schematic representation of the symmetrical cells is shown in **Fig. 4.1.**

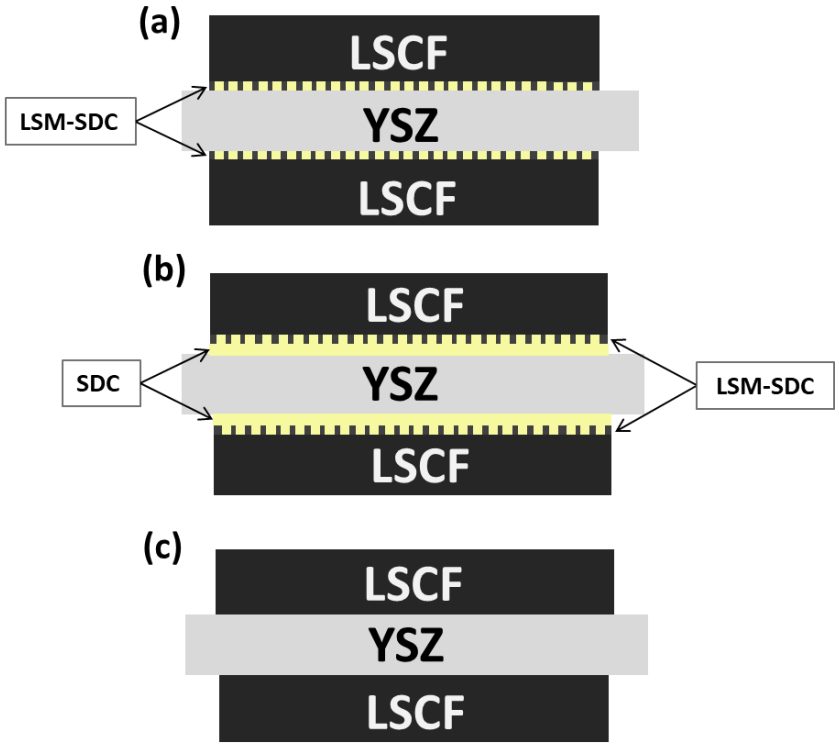

Fig. 4.1 Schematic representation of the three symmetrical cells (a) YSZ/LSM-SDC/LSCF, (b) YSZ/SDC/LSM-SDC/LSCF, and (c) YSZ/LSCF.

The evolution of the NFL layer and the interface with the LSCF CCL was studied by direct deposition of the NFL on YSZ tape. A set of cells with only the NFL (no CCL) and another set with NFL and LSCF CCL were treated at 900, 1000 and 1100 °C, to determine the stability of the bilayer and the optimal sintering temperature by electrochemical impedance spectroscopy (EIS).

The crystalline phases of the PLD and NFL layers (as-deposited and after heat treatment) were characterized by X-ray diffraction (XRD) on a Bruker-D8 Advance instrument using Cu Kα radiation with a nickel filter and a Lynx Eye detector.

The symmetric cells with the different interlayers and sintering temperatures were electrochemically characterized. Gold paste was hand brushed on top of the electrodes and cured at 800 °C to ensure current collection. The station used was the ProboStat™ (NorECS) which was placed inside a high-temperature vertical tube furnace. Gold paste and mesh were used for current collection. The impedance spectroscopy measurements (EIS) were carried using a Novocontrol spectrometer (NOVOCONTROL Technologies GmbH & Co. KG) at temperatures

ranging from 550 to 800 °C under synthetic air flow. According to the EIS analysis of the symmetric cells with NFL, 1000 ºC was defined as the optimal temperature. Likewise, the samples with the bilayer BL+NFL as interlayers and without the bilayer were sintered at 1000 °C.

Complete SOFCs were prepared to evaluate the performance and the durability of a Ni-YSZ/YSZ/SDC/LSM-SDC/LSCF single cell. A state-of-the-art anode supported half-cell was used as substrate. The same deposition procedures, as described in the symmetrical cell, were used for the complete cell, a schematic diagram of the complete cell is shown in **Fig. 4.2**. Accordingly, the SDC barrier layer followed by the LSM-SDC ceramic nanocomposite layer were deposited by PLD on top of the electrolyte, and the LSCF cathode was airbrushed on top of the NFL. A ProboStat™ (NorECS) system placed inside a high temperature tube furnace was used to test the complete cells. Ceramabond™ (Aremco) paste was used to seal the cell. The electrochemical characterization, impedance spectroscopy (EIS) and I-V curves were carried out using the PARSTAT® 2273 potentiostat. The long-term durability test was done using a M9700 electronic load from Maynuo Electronic Co. Ltd. The measurements of the complete single cells were done under dry H_2 fuel in the anodic compartment and synthetic air in the cathode with a flow density of 22.22 $Nml \cdot min^{-1} \cdot cm^{-2}$. The EIS data were obtained at OCV and with a current density of 0.2 $A \cdot cm^{-2}$ at 700, 750, and 800 °C. The long-term durability test was carried out for 700 h at 750 °C with a current density of 0.3 $A \cdot cm^{-2}$.

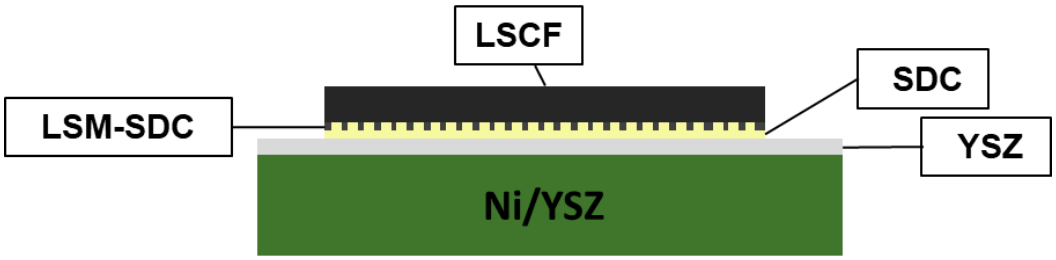

Fig. 4.2 Schematic representation of the complete cell Ni-YSZ/YSZ/SDC/LSM-SDC/LSCF.

The microstructural characterization of the cells before and after operation was obtained from lamellae of the samples prepared with focused ion beam

scanning electron microscope (FIB-SEM) Dual Beam Helios 650. The SEM images were obtained from Dual Beam Helios 650, and transmission electron microscopy analyses of the lamellae and EDS mapping were carried out using the JEOL 2010F TEM equipment.

4.3 Results and discussion

X-ray diffraction was used to confirm the crystalline phases of the thin functional layers of SDC (BL), LSM-SDC (NFL) and the bilayer SDC + LSM-SDC (BL+NFL) deposited by PLD on YSZ substrates. The obtained patterns are shown in **Fig. 4.3**. The diffraction patterns revealed the cubic structure of both the YSZ substrate and the SDC. The LSM diffraction peaks are clearly visible and match with pseudo-cubic structure typical of thin film LSM layers [250].

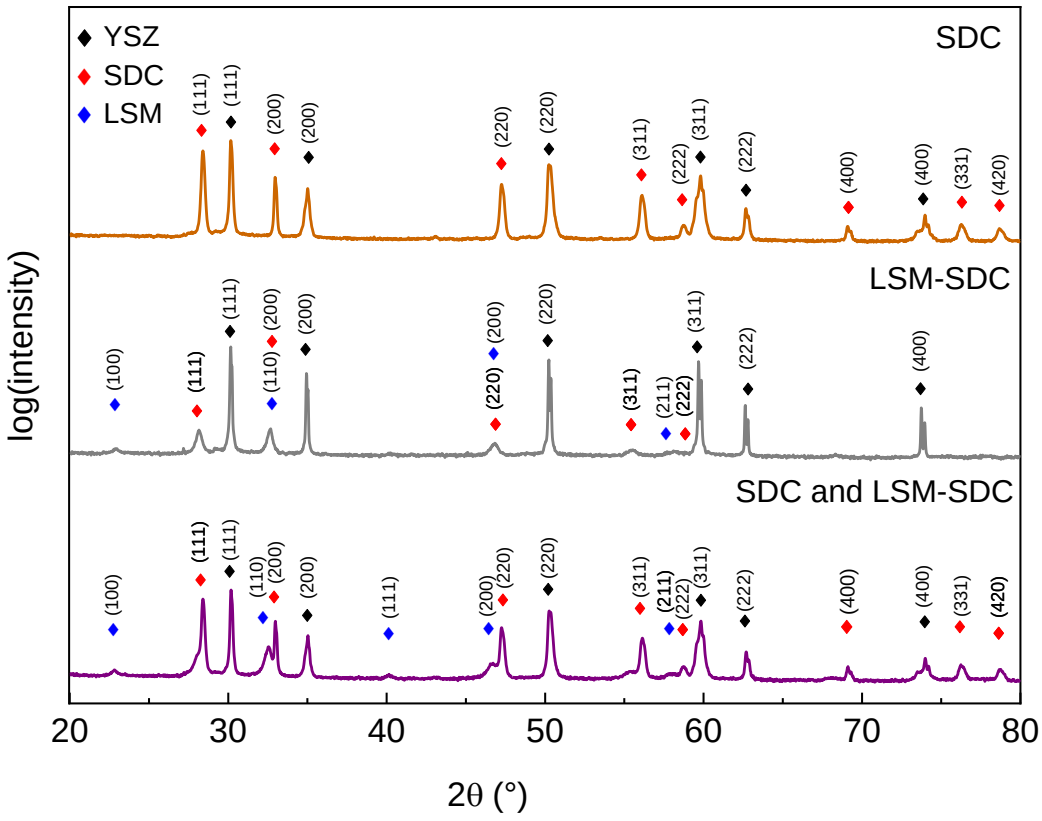

Fig. 4.3 XRD patterns of PLD layers on YSZ. Top to bottom: SDC, SDC+LSM-SDC and LSM-SDC as-deposited.

Samples with the NFL were treated at 900, 1000 and 1100 °C, to determine the stability of the bilayer. The XRD analysis is shown in **Fig. 4.4**. Interestingly, the XRD analysis of the samples show no formation of additional phases nor substantial peak shifts, confirming the stability of the PLD layers after thermal treatment.

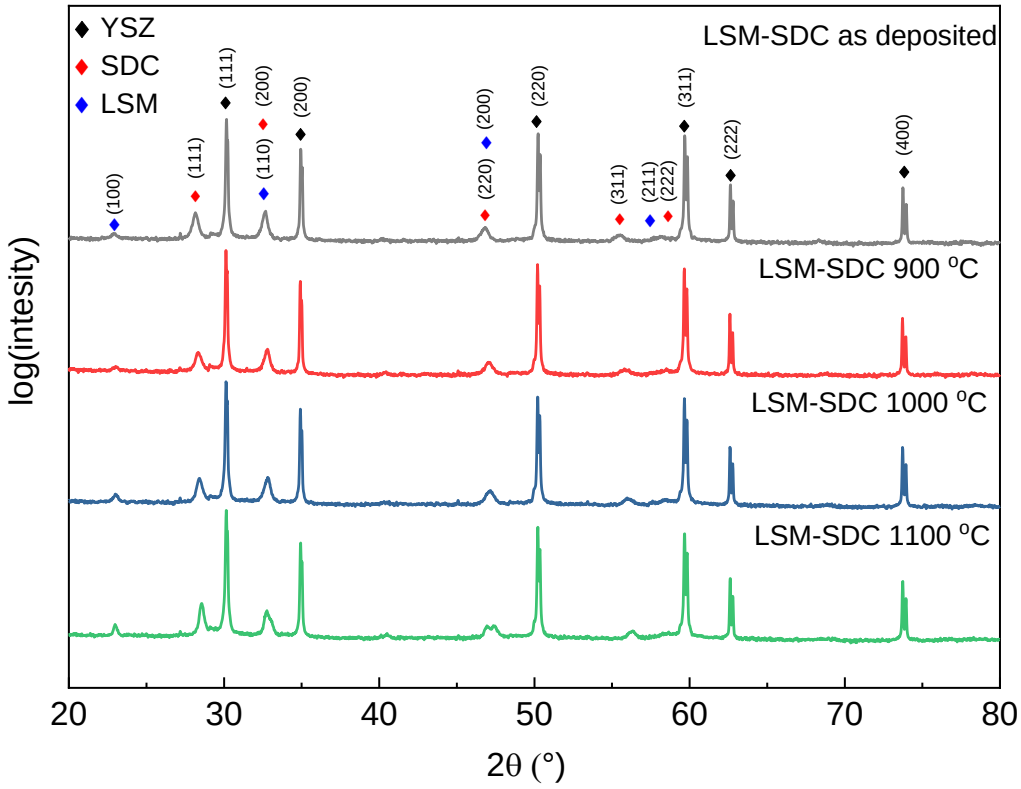

Fig. 4.4 XRD patterns of LSM-SDC layers on YSZ treated at different temperatures (900, 1000 and 1100 °C).

To determine the morphological characteristics of the final electrolyte-electrode interface microstructure, SEM cross-section images were obtained as shown in **Fig. 4.5** (a). The SEM image shows the BL+NFL sandwiched between the YSZ substrate and airbrushed LSCF layer. It is interesting to note that the mesostructure was preserved after sintering at 1000 °C. The images show a 400 nm thick homogeneous bilayer of both SDC (200 nm) and LSM-SDC (200 nm). The layers exhibit high density and are well attached to both the YSZ electrolyte and the LSFC cathode. The chemical composition of the nanostructured interface was assessed by high resolution EDS mapping, which was carried out on the area

of the cross-section interface as shown in **Fig. 4.5** (b). From the elemental analyses, the BL and the NFL are clearly distinguishable. It is possible to identify a clear vertical periodicity (200 nm column spacing) of the Ce and Sm signals in the NFL layer confirming the alternate periodic growth of SDC and LSM. Notably, unlike typical PLD nanocomposite model systems [251], vertical alternation was here obtained without the need of a well-defined substrate orientation, as the BL is highly polycrystalline (cf. **Fig. 4.3**).

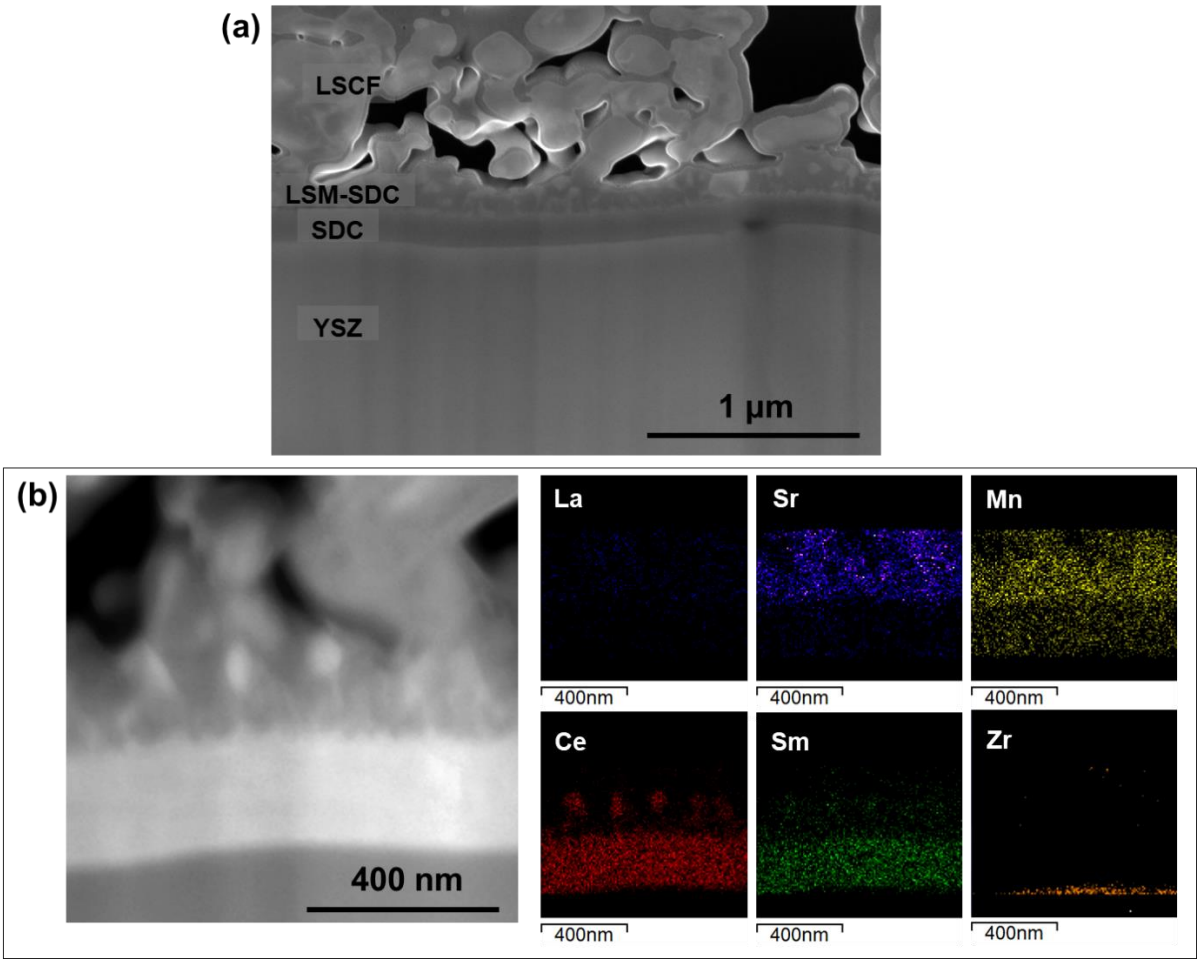

Fig. 4.5 (a) Cross-sectional SEM image of SDC BL and LSM-SDC NFL deposited on YSZ support with LSCF sintered at 1000 °C (b) STEM image of the cross-section with EDSmapping of the deposited thin films.

The EIS analyses were firstly carried out of the samples with the configuration YSZ/LSM-SDC/LSCF (**Fig. 4.1** (a)) treated at 900, 1000 and 1100 °C to define the optimal sintering temperature of the LSCF layer. **Fig. 4.6** (a) shows the impedance data at 750 °C. The experimental data were fitted with the equivalent circuit $LR_S(R_{P1}CPE_{P1})$ $(R_{P2}CPE_{P2})$, shown in **Fig. 4.6** (b), where L refers

to the inductive contribution due to the setup, R_S is the series resistance, ascribed to the ohmic contributions including the ionic resistance of the electrolyte and contact resistances and the electrode polarization arcs at higher frequencies were fitted with a resistance and a constant phase element (CPE) connected in parallel ($R_{Pi}CPE_{Pi}$).

The temperature dependence of the series (ASR_{series}) and polarization (ASR_{pol}) area-specific resistances for the different cells is reported in **Fig. 4.6** (c) and **Fig. 4.6** (d), respectively. The ASR_{series} was determined by the value of the fitting of the series resistance (R_s) in the EIS diagram, which is equivalent to the x-intercept at the high frequency end of the diagram. The ASR_{pol} was obtained from the sum of the polarization resistances (R_{p1} + R_{p2}) which are equivalent to the resistance of the two arcs in the EIS diagram.

Small differences between the ASR_{series} of the three samples were observed, and the same value of activation energy (E_a ~0.85 eV) was calculated. The samples treated at 1000 °C display the lowest resistance. Considering the ASR_{pol} the sample sintered at 1100 °C display a significant increase in the polarization resistance associated with a higher activation energy (E_a=1.69 eV). Such resistive behaviour can be attributed to the high temperature sintering temperature of 1100 °C, which is known to promote the formation of resistive phases at the YSZ/LSCF interface [119]. This high temperature coupled with the limitation due to the thickness of the layer (200 nm), might activate parallel interdiffusion processes between the cathode and the electrolyte leading to the formation of insulating phases and decomposition of the electrode material [55,59].

The lowest resistance at the cell operating temperature (~750 °C) was obtained by the heat treatment at 1000 °C. Thus, such a temperature was selected as the optimal one to produce the symmetrical cell with the additional BL (**Fig. 4.1** (b)) and without any interlayer (**Fig. 4.1** (c)).

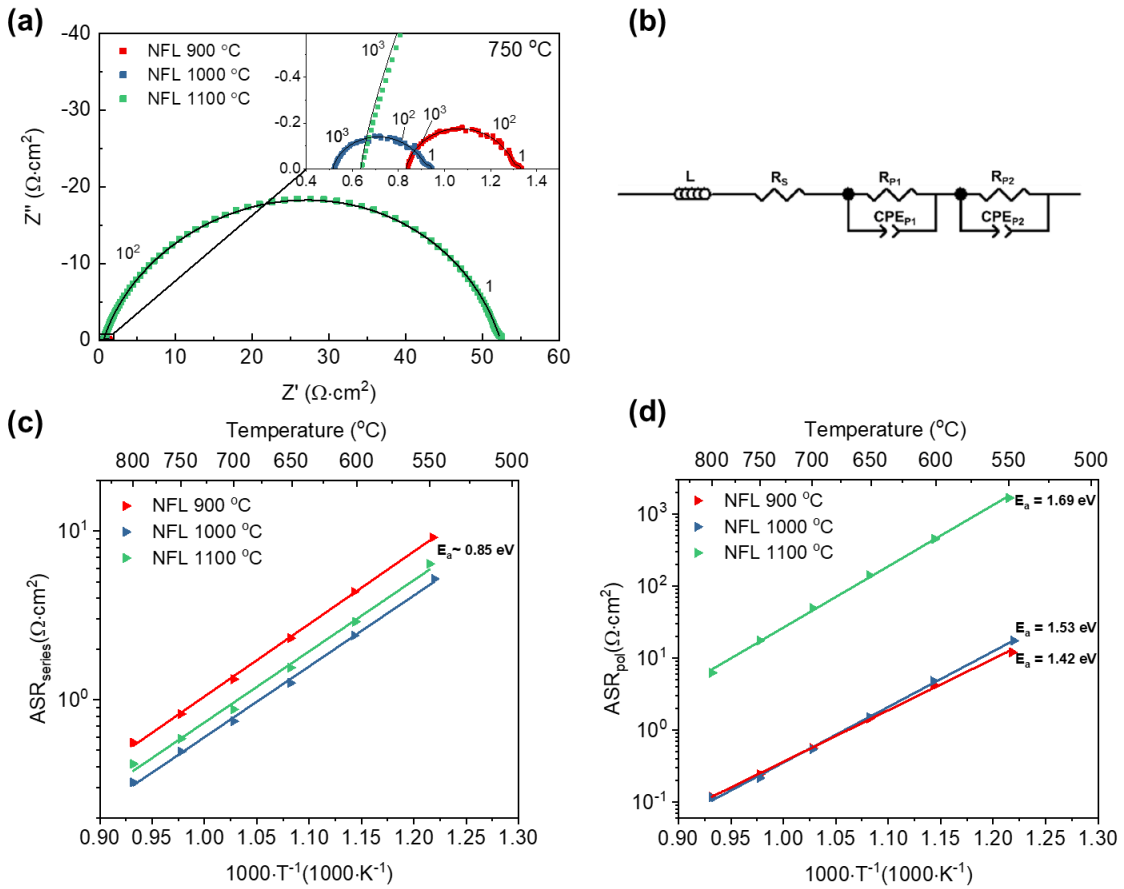

Fig. 4.6 (a) EIS diagrams of the symmetrical cells with NFL (YSZ/LSM-SDC/LSCF) sintered at different temperatures measured at 750 °C. The inset shows the high-frequency portion of the diagrams. (b) equivalent circuit used to fit the impedance data. (c) and (d) Arrhenius plots of the series and polarization ASR, respectively, of the symmetrical cells.

The EIS diagram and the total area specific resistance (ASR_{total}) of the cells with the additional BL and without the bilayer sintered at 1000 °C are shown in **Fig. 4.7** (a) and (b). The EIS data were fitted with the same circuit shown in **Fig. 4.6** (b). The cell without the bilayer exhibits more than a 40-fold increase in ASR compared to the cell with a bilayer (BL + NFL). The increase occurs mostly in the polarization resistance, as seen in the impedance diagram (**Fig. 4.7** (a)). This result emphasizes the importance of the ceria barrier layer to hinder the interface reactions between LSCF and YSZ.

Notably, the addition of a BL (sample BL + NFL) was found to determine a significant decrease in the total resistance as compared with the sample with just the NFL. Such a decrease was associated with a greater impact on the polarization resistance, which decreased almost by an order of magnitude, as

seen when comparing the impedance diagrams of the cells treated at the same temperature in **Fig 4.6** (a) and **Fig. 4.7** (a). It is observed that the most important difference is in the arc of polarization resistance formed at high frequency (R_{p1}). The R_{p1} value obtained from the fitted diagram is 0.43 $\Omega \cdot cm^2$ for the NFL at 1000 °C and 0.06 $\Omega \cdot cm^2$ when the BL is added. The arc formed at high frequency can be attributed to interfacial impedance contributions at the electrode-electrolyte interface [43,252]. It is assumed that the presence of the BL favours oxygen ion transport from the electrode to the electrolyte.

Fig. 4.7 (c) shows the area specific resistances, series and polarization, of the BL+NFL cell. The polarization resistances are in accordance with previous reported experimental results of LSCF cathodes [222,246]. A low activation energy is observed for both series (0.86 eV) and polarization area specific resistances (1.23 eV). The low polarization activation energy obtained of 1.23 eV (in comparison with ~1.4 eV for LSCF cathodes) [192,222,253,254] suggests that the PLD interlayer facilitates the ORR.

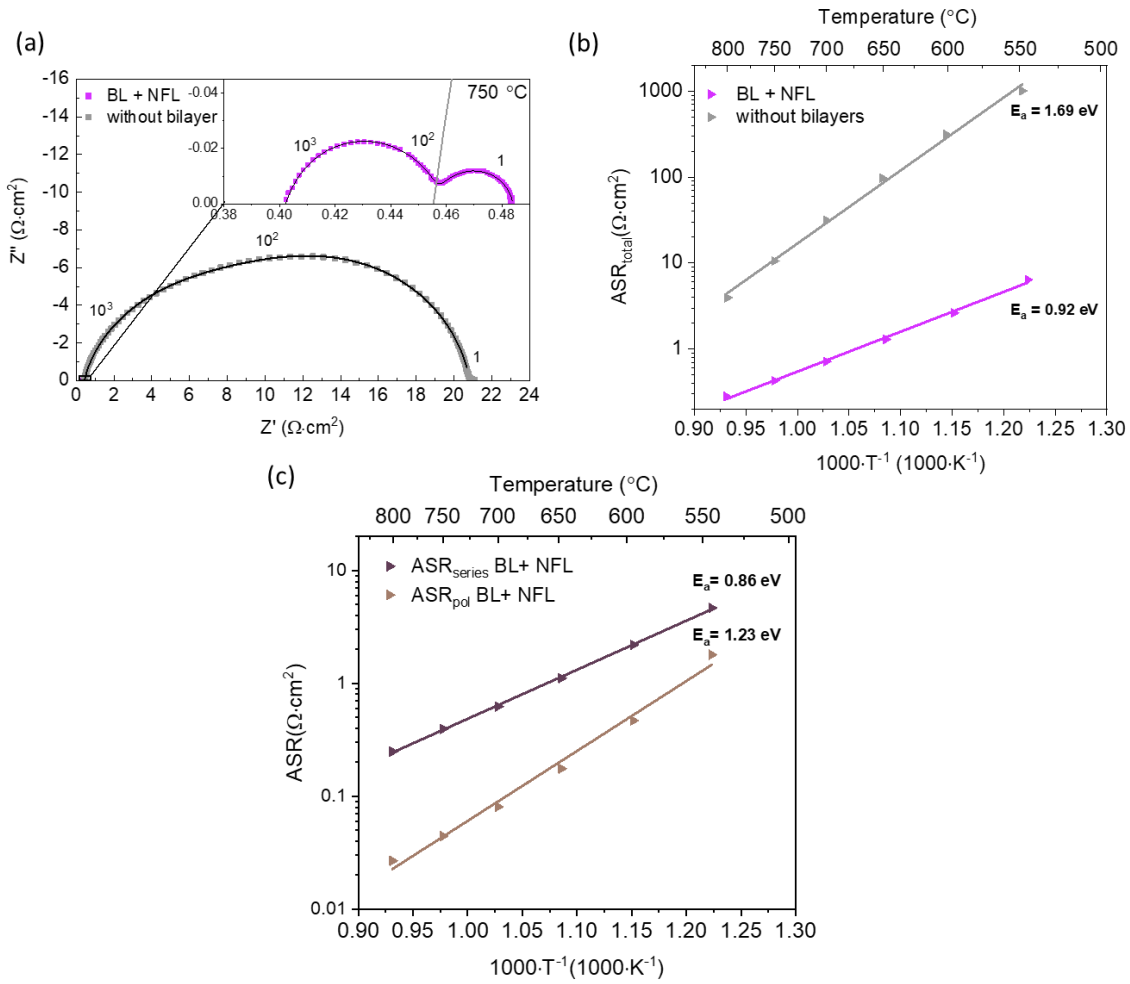

Fig. 4.7 (a) EIS diagrams of the symmetrical cells with BL + NFL (YSZ/SDC/LSM-SDC/LSCF) and without the bilayer sintered at 1000 °C. The inset shows the expanded high frequency portion of the diagram. (b) Arrhenius plots of the total ASR of the symmetrical cells with NFL +BL and without the bilayer sintered at 1000 °C. (c) Arrhenius plots of the series and polarization ASR of the symmetrical cell with BL+NFL sintered at 1000 °C.

To demonstrate the effect of the PLD interlayers on the electrochemical performance of the fuel cell, an anode-supported single cell with the interlayers (BL and the NFL) and LSCF sintered at 1000 °C was tested. **Fig. 4.8** (a) shows the current-voltage (I-V) and current-power (I-P) curves of the anode-supported cell at 700, 750, and 800 °C under synthetic air and dry hydrogen. The fuel cell presents an OCV of 1.1 V as expected for the selected temperature range and reaches a power density at 0.6 V of 0.38 W·cm^{-2}, 0.29 W·cm^{-2}, and 0.23 W·cm^{-2} at 800, 750, and 700 °C, respectively. The reported values on the I-V curve are

not achieving the maximum power density; however, the curve has been extrapolated, showing the maximum power density values up to 0.41 W·cm^{-2}, 0.31 W·cm^{-2} and 0.24 W·cm^{-2} at temperatures of 800, 750, and 700 °C, respectively. The cell exhibited superior performance than anode supported cells reported by the literature with LSCF cathode [60,255].

Fig. 4.8 (b) and (c) show the impedance plots both under OCV and applying 0.2 A·cm^{-2} respectively at 700, 750, and 800 °C. **Table 4.1** exhibits the fitting results, series and polarization resistances (R_s, R_{p1}, R_{p2}) from the impedance plots in **Fig. 4.8**. Additionally, the capacitances (C_{p1} and C_{p2}) of the semicircles, calculated from the obtained CPE elements using Equation 4.1 are also shown in **Table 4.1**.

$$C_p = Q^{1/n} \times R_{pi}^{(1-n)/n} \quad (4.1)$$

where *Q* and *n* are parameters of the CPE element. *Q* is associated to the true capacitance, and *n* (0 < *n* < 1) is related to the deviation of the semicircle to the 90° angle of a perfect capacitor.

The measurements carried out at OCV show a large contribution of the polarization resistance to the total ASR. Under a bias, this contribution is decreased as the applied current activates most of the electrochemical reactions. A 3-fold decrease of polarization resistance is observed under biased measurements for all the temperatures analysed. At 800 °C, the polarization resistance R_{p2} rapidly decreases from 0.70 Ω·cm^2, at OCV, to 0.18 Ω·cm^2 at 0.2 A·cm^{-2}. Similar behaviour is observed at all temperatures. Considering the obtained values for the C_{p1} and C_{p2} and the characteristic frequencies, the high frequency arcs can be ascribed to charge transfer process at the electrodes/interfaces and to the oxygen reduction reaction, and the lower frequency arcs are attributed to mass diffusion mechanisms [223,224].

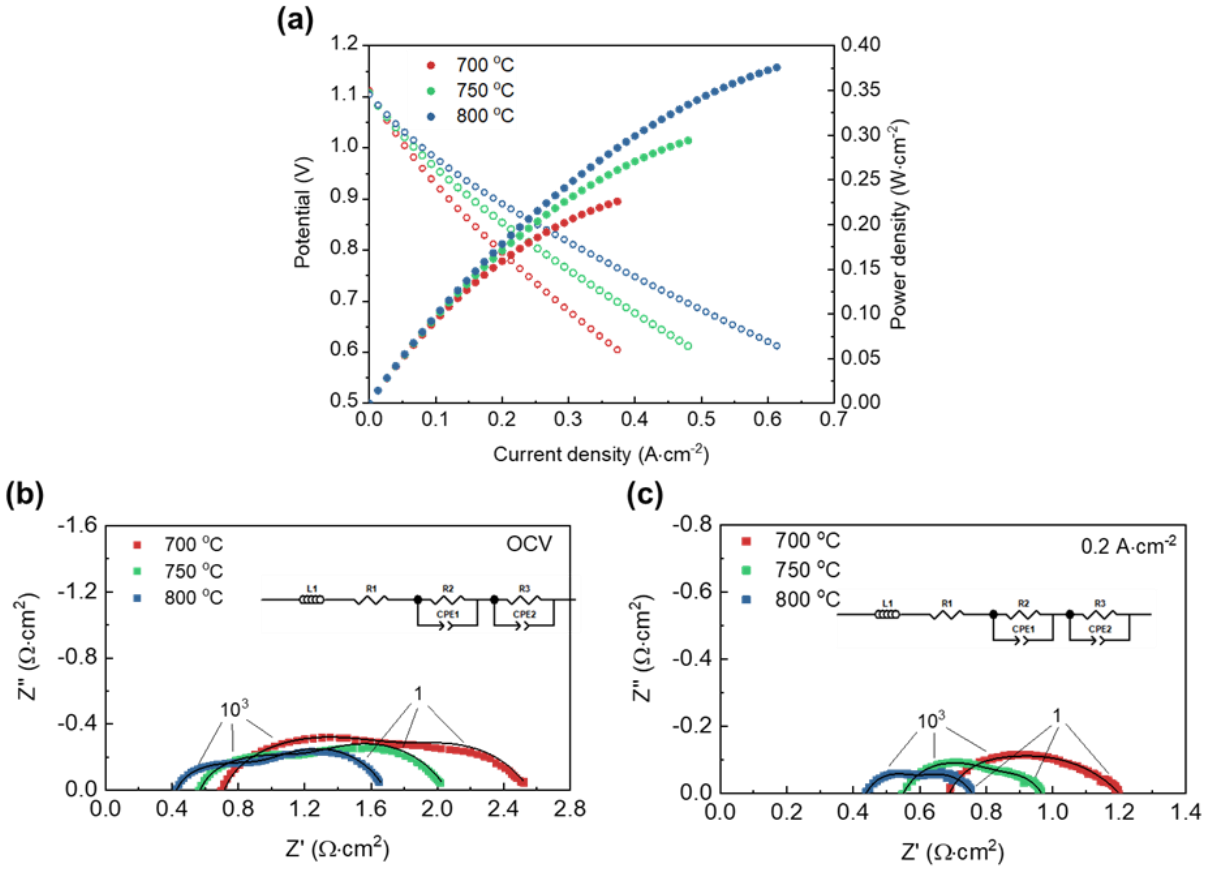

Fig. 4.8 (a) I-V curve and EIS diagrams at (b) OCV and (c) 0.2 A·cm^{-2} of the anode-supported single cell with the BL+ NFL interlayers at 700, 750, and 800 °C under synthetic air and dry hydrogen.

Table 4.1 Fitting parameters of series resistances (R_s), polarization resistances (R_{p1} and R_{Pp2}) and capacitances (C_{p1} and C_{p2}) at OCV and at 0.2 A·cm^{-2} of the EIS diagram of the anode-supported single cell with the BL+ NFL interlayers at 700, 750, and 800 °C.

	OCV					0.2 A·cm^{-2}				
T (°C)	**R_s (Ω·cm²)**	**R_{p1} (Ω·cm²)**	**C_{p1} (F·cm^{-2})**	**R_{p2} (Ω·cm²)**	**C_{p2} (F·cm^{-2})**	**R_s (Ω·cm²)**	**R_{p1} (Ω·cm²)**	**C_{p1} (F·cm^{-2})**	**R_{p2} (Ω·cm²)**	**C_{p2} (F·cm^{-2})**
700	0.57	1.19	6.9E-4	8.35E-1	1.12E-1	5.72E-1	3.61E-1	2.49E-2	2.5E-1	1.49E-1
750	0.44	8.85E-1	8.82E-4	7.42E-1	9.61E-2	4.64E-1	3.01E-1	9.37E-3	2.21E-1	1.57E-1
800	0.30	6.94E-1	8.56E-4	7.01E-1	1.15E-1	3.71E-1	2.21E-1	1.19E-2	1.85E-1	1.29E-1

To investigate the effect of the bilayer on the long-term electrochemical performance, a durability test shown in **Fig. 4.9** (a) was carried out for 700 h under

synthetic air and dry hydrogen atmospheres with a flow of 22 $Nml \cdot min^{-1} \cdot cm^{-2}$ and a current density of 0.3 $A \cdot cm^{-2}$. Remarkably, an improvement of 267 $m \cdot V \cdot kh^{-1}$ was observed during the first 200 h of the test followed by a slight degradation of 41.9 $m \cdot V \cdot kh^{-1}$ during the following 500 h. Throughout 700 h of operation, the fuel cell has improved 225 $m \cdot V \cdot kh^{-1}$. The reported improvement in the cell provides evidence that the interfaces are still dynamic, and the nanostructured layers might have rearrangements leading the system to evolve towards a stable microstructure. Notably, a decrease in ASR for the LSM-SDC nanocomposite model system under thermal degradation (OCV conditions) was highlighted previously [249]. Here, a similar behaviour is observed under SOFC operating conditions.

The voltage drops that occur after ~600 h in **Fig. 4.9** (a) can be possibly attributed to a crack in the ceramic sealing of the fuel cell allowing a change in the pO_2 of the chambers and could have a relation to the decrease in OCV after the 700-h test, as seen in **Fig. 4.9** (b). It can be seen from the I-V curve of **Fig. 4.9** (b), and from the EIS, **Fig. 4.9** (c), that the electrochemical performance of the cell was practically constant during the 700 h of operation. This interesting behaviour led to a further microstructural analysis of the cell before and after 700 h of operation.

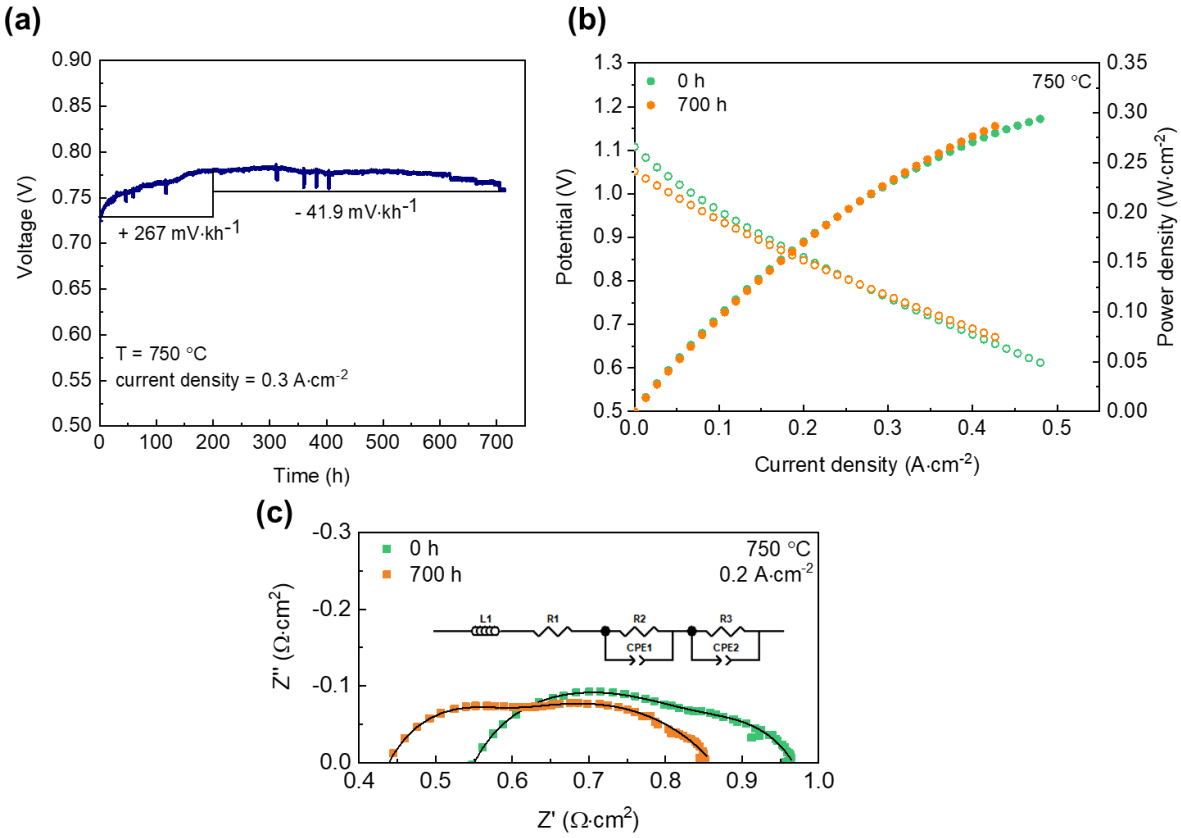

Fig. 4.9 (a) Long-term durability test of the anode-supported single cell with the BL+NFL interlayers for 700 h at 750 °C, a current density of 0.3 A·cm^{-2}, under synthetic air and dry hydrogen, (b) I-V curves and (c) EIS diagrams at 0.2 A·cm^{-2} of the cell at 0 h and 700 h of operation measured at 750 °C under the same conditions.

A TEM analysis with EDS mapping was carried out before **Fig. 4.10** (a) and after the 700-h durability test **Fig. 4.10** (b). In the obtained TEM image and on the EDS analysis of the cell as prepared, **Fig. 4.10** (a), one can observe the good adhesion and uniformity of the layers, and a clear distinction between the elements of each layer. After 700 h of operation, the layers are still well aligned. However, cation diffusion is observed. There is a significant rearrangement of the species in the thin film layers of the tested cell as seen by EDS mapping (**Fig. 4.10** (b)). There is a well-described mechanism of activation of the LSM cathode by cathodic polarization that occurs by surface modification and leads to an increase of the oxygen vacancies and facilitates ORR [256]. The activation is partially due to the reduction of $Mn^{3+/4+}$ to Mn^{2+} that cations diffuse to the electrolyte surface under biased providing high electronic conductivity in the zirconia surface, and the electrolyte becomes active for oxygen incorporation [257]. Consistently, a

substantial diffusion of the Mn element is observed; the species are seen throughout the barrier layer and reach the electrolyte surface. This could possibly lead to an improvement in the first 200 h of operation. Interestingly, spontaneous cationic diffusion in LSM-SDC nanocomposites was directly put in relation with improved structural stability (suppressed Sr segregation in LSM), according to recent investigations [249]. Nevertheless, it is not possible to point out exactly the mechanisms that were involved in enhancing the fuel cell's performance and in the final long-term stability. However, it is noted that cations rearrangement under biased and through the operation of the cell can have a positive effect on the durability of the cell, not only be the cause of degradation [252].

Interestingly, the image **Fig. 4.10** (b) shows the formation of microvoids along the electrolyte-BL interface. Those microvoids are known to be produced by the preferential Ce diffusion into the YSZ layer [258] and could be an origin for degradation phenomena. Nonetheless, the resistive phase has been contained in the barrier layer and did not seem to have a substantial effect on the degradation of the cell.

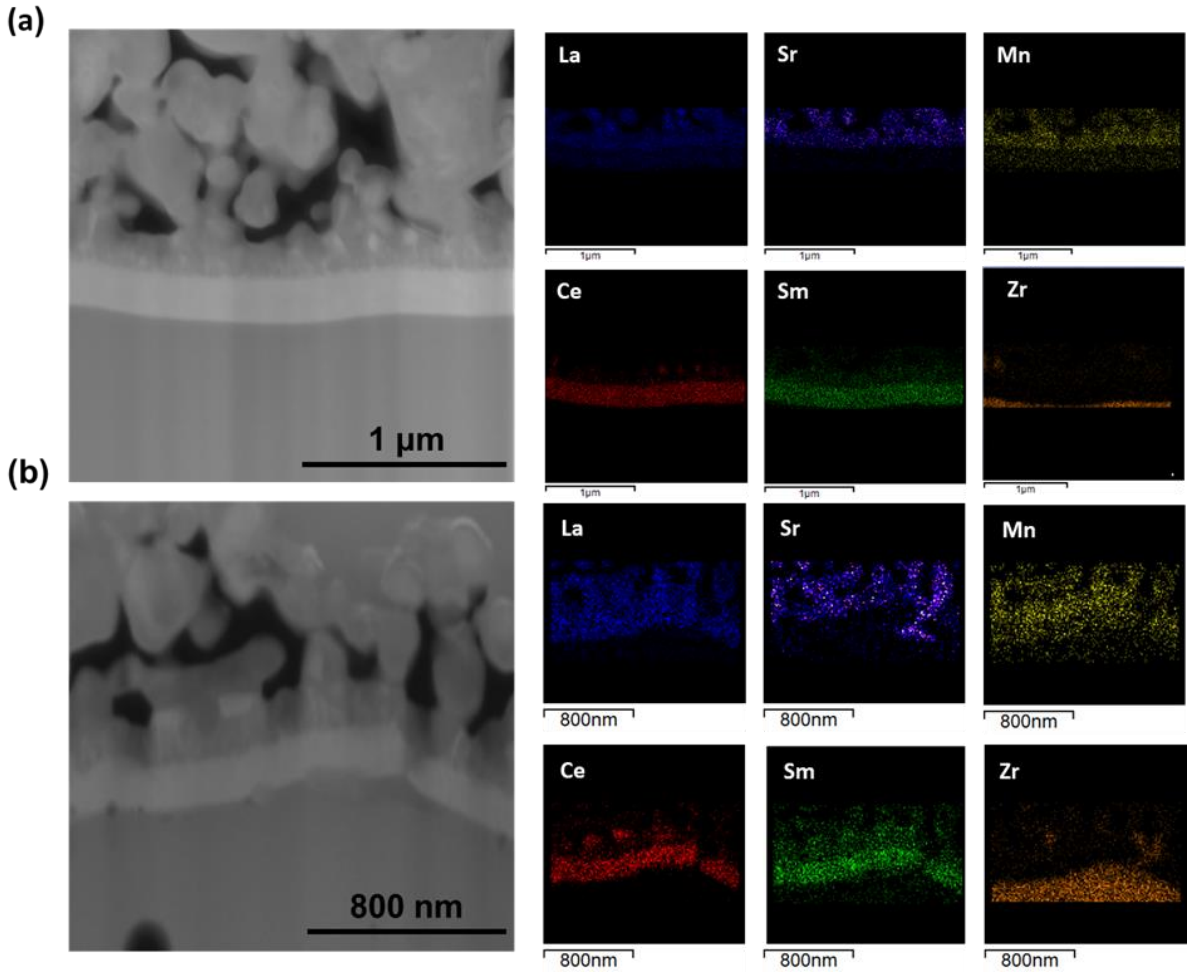

Fig. 4.10 TEM images and EDS mapping of the anode-supported single cell with the BL+NFL and LSCF cathode before (a) and after (b) 700 h of operation at 750 °C and 0.3 A.cm^{-2}.

4.4 Summary

Bilayers of Sm-doped ceria and self-assembled vertical aligned LSM-SDC nanocomposites were successfully fabricated by the PLD technique. The layers showed a dense morphology with a thickness of ~200 nm each with a vertical periodicity of the materials in the nanocomposite layer. Such functional layers, upon optimization on symmetric cells, have been employed in anode-supported fuel cells, which demonstrated a stable performance through a durability test of 700 h with and an improvement of 225 m·V·kh^{-1} during the 700-h operation. Such a performance enhancement can be arguably attributed to the rearrangement of cations in the interlayers, as observed in the TEM images and EDS analyses.

There is a synergistic contribution of an effective dense diffusion barrier that impedes undesired cation migration between the cathode and electrolyte interface. Along with a more efficient charge exchange promoted by the composite functional layer, in which having an assembly of an ionic conductor (SDC) with a typical electronic conducting phase (LSM) with rationalized microstructure, facilitates oxygen reduction reaction. Further understanding of the dynamics involved in interfaces under operating conditions is suggested to achieve further knowledge in engineering advanced interfaces.

Conclusion

The studies carried out in this thesis demonstrate the effects of controlling nanostructured gadolinia-doped ceria properties for the efficient processing of SOFC functional layers. Simple chemical routes for the synthesis of nanometric ceria and advanced physical deposition techniques were approached. Important contributions to SOFC technology include the demonstration that by processing functional layers, either using controlled chemical syntheses of nanopowders or using physical deposition for nanolayers fabrication, multi-fuel and durable high-performance fuel cells are achieved.

Reducing the sintering temperature used for SOFC fabrication is a critical issue to both reduce cost and avoid degradation. Iron as a sintering aid effectively decreased the sintering temperature of CGO to ~1200 °C, an important achievement for the CGO diffusion barrier (bi-electrolytes). In this study, by using a selective lixiviation process it was possible to advance the understanding of how the Fe_2O_3 sintering aid distributes on both the solid-solid and solid-gas interfaces of CGO nanopowders promoting densification. Iron segregates preferentially at grain boundaries (solid-solid interface). With increasing sintering temperature, the surface specific area of the grain boundary (solid-solid interface) decreases with grain growth causing the precipitation of Fe-rich phase. Understanding the mechanism by which Fe alters the mass diffusion process is of the utmost value optimizing CGO sintering and using it as a component in an SOFC.

A hydrothermal route for the synthesis of shape-controlled was shown to be an efficient approach to control mass diffusion and densification mechanisms of the CGO. Nanorods and nanocubes of CGO were produced by simply controlling the synthesis temperature. The CGO nanorods exhibited a high surface specific area with a highly defective surface that promotes mass diffusion at low temperatures. Conversely, the CGO nanocubes had a very low sintering activity, attributed to the higher stability of the cubic crystallographic planes exposed at the cube facets. Nanocubes remained porous after high temperature sintering. Such characteristics were explored for processing fuel cells.

The sinterability of CGO nanorods was used to fabricate an electrolyte-supported SOFC fully sintered at 1150 °C. The electrochemical analyses of the

fuel cell indicated good gas tightness, and low electrode polarization, mainly due to the ohmic resistance associated with the thickness of the electrolyte. The results demonstrated that by controlling the shape of doped-ceria, the sintering temperature of a fuel cell can be reduced, consequently, lowering the production cost, saving energy, and increasing the flexibility of the use of ceria on SOFC.

Both the CGO nanorods and the nanocubes were evaluated as support materials for Ni-based catalysts in the steam reforming reaction of ethanol at intermediate temperature. The morphology of the support was shown to have an important role in the catalytic activity, particularly when the necessary heat treatment to fuel cell layer preparation is considered. Herein, the Ni catalyst on the CGO nanorod support displayed the highest activity, even after heat treatment at 800 °C, and was therefore applied as catalytic layer in an SOFC for direct operation with ethanol. The fuel cell operated under a continuous flow of anhydrous ethanol at 700 °C and exhibited a stable performance for 100 hours, without any sign of degradation due to carbon deposition. Such a result showed the potential of direct ethanol fuel cells operating at intermediate temperatures using an active catalytic layer.

The pulsed layer deposition method was used to apply CGO both as a barrier layer and as a nanofunctional cathode layer, combining CGO and LSM, in the interface between the YSZ electrolyte and LSCF current collector cathode. The deposition of the bilayer was shown to enhance the cell’s performance, having an important role in reducing the ohmic resistance and increasing the oxygen reduction reaction area. It was demonstrated that nanostructured functional films have an important role in minimizing interfacial resistances and promoting increased durability.

In summary, this thesis establishes innovative approaches to tailor functional layers using doped-ceria for the high-performance components of intermediate temperature SOFC operating with a renewable and readily available biofuel with good stability. The experimental results showed that controlling the nanostructured properties of a key component material, either by wet-chemistry synthesis and/or physical methods, represents a powerful strategy to tune the properties towards application in solid state catalytic and electrochemical devices.

Appendix 1

Development of the tape casting technique for SOFC electrolytes and anode supported SOFC fabricated through lamination and co-sintering.

A1.1 Introduction

There are several techniques to process ceramic materials for use in SOFCs. Among them, tape casting is chosen by many SOFC industrial developers because it is a low-cost, easily scalable process that allows the production of tapes with various morphologies [259,260]. An important advantage of using tape casting is that the green tapes can be superimposed by the technique of lamination or by sequential tape casting to form a multilayer component which can then be co-sintered, reducing the number of heat treatments and the final cost. The lamination process consists of pressing green tapes, usually utilizing a mechanical press, and sequential tape casting consists of casting a tape above the other. Lamination can be a challenging process and lead to several problems such as the formation of pores and defects such as delamination and cracks upon firing decreasing interfacial strength [4]. Cassidy et al. [261] have successfully used the sequential tape casting to produce a triple cast structure with a dense YSZ electrolyte sandwiched between two porous YSZ scaffolds, which were co-sintered and impregnated with the electrode materials. Menzler et al. [262] have produced half-cells by sequential tape casting of a two anode layers (support and functional) cast on top of a thin electrolyte tape followed by co-sintering. The cell was completed by screen printing an LSM cathode. Electrochemical tests proved the fuel cell stack ability and operational functionality.

The biggest challenge of producing a tape casted component is the development of suspensions with adequate formulation for the ceramic particles to be well dispersed and have adequate viscosity to control the solvent evaporation and diffusion rate through the tape. After casting a crucial step for multi-layered tape is the co-sintering of the components due to the shrinkage mismatches of the different materials layers. The shrinkage mismatch brings mechanical stress and resulting in warping, non-uniform shrinkage, delamination, and cracking. To avoid these undesired issues, the sintering

behaviour of each layer should be analysed, such that the induced stress level can be controlled within the acceptable range.

During this Ph.D., the processing technique of tape casting for fabrication of SOFC was developed. This project initiated with the production of YSZ electrolytes by tape casting to use as a support in electrolyte supported (ECS) SOFC. Then, progress was made in preparing the slurry of the Ni/YSZ anodes. SOFC anode supported half-cells (ASC) were obtained by laminating the YSZ tapes with those of Ni/YSZ and these materials were co-sintered. The tape casting development presented here further advances to sequential tape casting developed by the student MSc. Student Lays Nunes Rodriguez as a more effective method than the lamination to obtain half-cells [263].

A1.2 Experimental

To prepare the slurry for tape casting, the ceramic materials 8 mol% yttria-stabilized zirconia (YSZ, Tosoh) and the cermet precursor of NiO and YSZ (60:40 vol%), were prepared by the liquid mixture [211,212]. Accordingly, nickel (II) acetate tetrahydrate (9%, Sigma-Aldrich) and YSZ (Tosoh) were mixed with 200 mL ethanol and heated under constant stirring at a temperature of ~70 °C until complete evaporation of the ethanol. The powder was then calcined at 450 °C for 5 h.

The formulation of the electrolyte and anode slurry was based on a study carried out by the student at the University of St Andrews [261,263,264]. The formulation of the anode was adapted taking into consideration the specific surface area (SSA) of the synthesized NiO/YSZ anode powder. The SSA of the anode powder was measured by the BET method using the Quantachrome ChemBET-Pulsar. Before the analysis, the sample was treated under He flow at 300 °C for 3 h.

The ceramic powders of interest, 12 vol% YSZ for the electrolyte and 8 vol% NiO/YSZ + 4 vol% of graphite (micrograph 99507 LJ) for the anode, were placed in a polyethylene (PE) bottle with 20 zirconia balls (10 mm diameter) and 70 vol% (~20 ml) of the solvent containing a ratio 3:2 of methyl ethyl ketone: ethanol. The PE bottle was set on a ball mill at 100 rpm and left milling for 16 h to ensure homogeneity and break up the agglomerates. Then 8 vol% of the binder polyvinyl butyral (PVB, Butvar-98) and 5 vol% of the two plasticizers, polyethylene glycol

(PEG, Mw 400, Sigma Aldrich) and dibutyl phthalate (DBP, Sigma Aldrich) were added to the suspension. Finally, the slurry was stirred in the ball mill for an additional 16 h.

Tape casting was performed on an STC-14A machine (Hansung) with a doctor blade (MTC02A) (**Fig. A1.1**), containing two levelling blades adjusted according to the final thickness of the intended inserts. The doctor blade was set to 0.3 mm for both the electrolyte support and for the anode support, and for the thin electrolyte of the anode-supported cell (ASC), it was set to 0.1 mm.

Fig. A1.1 Tape casting system (left) and doctor blade (right).

The ceramic suspension was poured into the reservoir of the doctor blade, and the treadmill was set in motion for 2.355 $cm \cdot s^{-1}$. The tape was cast on a polyester film and left to dry. To obtain thicker supports, the anode and electrolyte were laminated in a uniaxial press set to 50 °C and 1 $ton \cdot cm^{-2}$. Typically, five electrolyte tapes were laminated for the electrolyte support and for the anode supported four anode green tapes were laminated with one thin electrolyte green tape. The tapes were cut with a 25 mm round hole puncher and heat treatments were carried out. The calcining temperatures were established by thermogravimetric analyses (Setaram Labsys), between room temperature and 1300 °C with a heating rate of 10 $°C \cdot min^{-1}$ under synthetic air flow. The sintering and co-sintering steps were adapted from [261,263,264].

The electrolyte support calcining/sintering was carried out in two steps: first the cell was heated to 500 °C at a ramp rate of 0.5 $°C \cdot min^{-1}$ and dwell time of 1 h,

then it was heated to 1500 °C at a ramp rate of 0.5 °C·min^{-1} and dwell time of 2 h. The co-sintering of the anode support with the laminated electrolyte was also carried out in two stages, first the calcination stage following a ramp rate of 0.3 °C·min^{-1} until 850 °C and dwell time of 1 h followed by the sintering stage with a ramp rate of 0.3 °C·min^{-1} until 1450 °C and dwell time of 1 h. The apparent porosity of the tape was measured through the standard test method for apparent porosity [210].

Complete fuel cells were made by the deposition of anode and cathode inks for the ESC and cathode ink for the ASC. Herein, functional layers (FL) and current collection layers (CCL) of both anode and cathode were prepared following a previously developed method [265]. The anode inks consisted of NiO/YSZ prepared by the liquid mixture method with compositions of 40 vol% NiO for the FL and 60 vol% NiO for the CCL. To the FL and to the CCL inks, the pore former graphite (micrograph 99507 LJ) was added in the proportions of 5 wt% and 9 wt%, respectively. The anode inks were prepared by ball milling for 24 h at 100 rpm the ceramic powders + graphite with 1 wt% PVP, 4 wt% ethylene glycol, 2 wt% PVB, 27 wt% terpineol and 30 wt% ethanol. The grinding media consisted of zirconia spheres with 3 mm diameter. The cathode was also made of a FL, 50 wt% LSM (Fuel Cell Materials) and 50 wt% YSZ (Tosoh), and a CCL of LSM. The inks were prepared by mixing the 30 wt% the ceramics with a commercial ink-vehicle (Fuel Cell Materials) in a planetary mill (Fritsch - Pulverisette) for three cycles of 5 minutes at 3000 rpm. The grinding media used were zirconia spheres with ~1 mm diameter.

The inks were deposited using the spin coating (Laurel, model WS-400-6NPP-LITE) method [265]. The substrates, i.e., the electrolyte support and the anode supported half-cell, were fixed in the spin coater by vacuum. The suspensions were deposited on top of the substrate, and the spin coater was put to rotation at 6000 rpm for 10 s, to evenly spread the inks. Each deposition was followed by a drying step, where the tapes were placed under an incandescent lamp (200 W), at a 20 cm distance, and left drying overnight. Typically, 1 FL and 5 CCL of electrode inks were deposited by this method.

For the ESC, the anode layers were deposited at first, followed by a heat treatment at 1400 °C, heating rate of 5 °C·min^{-1} and dwell time of 1 h. Then the

cathode layers were deposited and submitted to a heat treatment to 1150 °C, heating rate of 0.5 °C·min^{-1} and a dwell time of 1 h. The same heat treatment was followed for the cathode in the ASC. The heat treatments, ink composition and deposition were optimized by the group and will not be the focus of this study.

The microstructure of the ASC and the ESC were analysed using a scanning electron microscope SEM JSM-6010LA.

The electrochemical properties of the ESC and the ASC were tested in the open flange test set-up from Fiaxell SOFC Technologies™. The current collection was carried out by gold wires connected to a gold mesh (diameter 37mm) in the air outlet and by a nickel mesh on the fuel side. The electrochemical measurements were carried out at 850 °C under H_2 and synthetic air, both with a flow rate of 12 L·h^{-1}, by a Zahner IM6 electrochemical workstation. The impedances under the open circuit conditions were measured in the frequency range of 1 MHz to 1Hz with an ac amplitude of 10 mV.

A1.3 Results and discussion

The specific surface area (SSA) of the ceramics was measured and used to formulate the slurry recipe. The SSA for YSZ is 13 m^2·g^{-1}, as obtained from the manufacturer, and for NiO/YSZ powder the SSA is 18 m^2·g^{-1} as calculated through the BET method. The SSA helped defining the ceramic loading in the formulation, and it was established as 12 vol% YSZ for the electrolyte and 8 vol% NiO/YSZ.

A thermogravimetric analysis (**Fig. A1.2**) of the green tapes was carried out to establish the calcination or pre-sintering temperatures. The materials exhibited a similar mass loss behaviour until 500 °C. A first mass loss occurs from 30 to 150 °C associated with the release of residual solvent or adsorbed water, and a second mass loss from 200 to 500 °C related to the decomposition of the binder and the plasticizers from the tapes. For the anode tape, an additional mass loss is observed at ~800 °C was ascribed to the decomposition of graphite pore former [266].

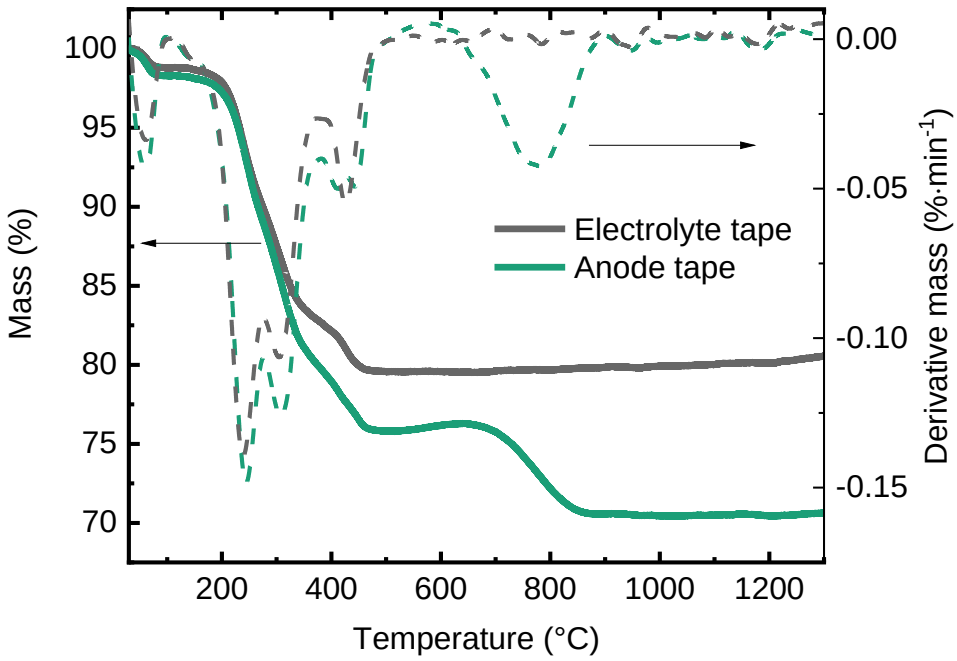

Fig. A1.2 TGA analysis, with mass and the derivative of mass, of the electrolyte and anode tape obtained under synthetic airflow and 10 °C·min^{-1} heating rate.

For the ESC, the lamination technique was used to increase the thickness and thus the mechanical resistance of the electrolyte support. In **Fig. A1.3**, a dense electrolyte of ~300 µm thickness is shown in the inset magnified image closed pores are observed. But these should not overly interfere with the electrolyte's performance. A high relative density of 97% was obtained for the electrolyte, emphasizing the high density and lack of open porosity for the electrolyte. Nonetheless, the lamination of the green tapes can lead to delamination upon sintering, evidenced by the arrows in **Fig. A1.3**, which could cause the electrolyte to crack. The elimination of such defects on the tape or upon sintering is one of the biggest challenges in the tape casting process.

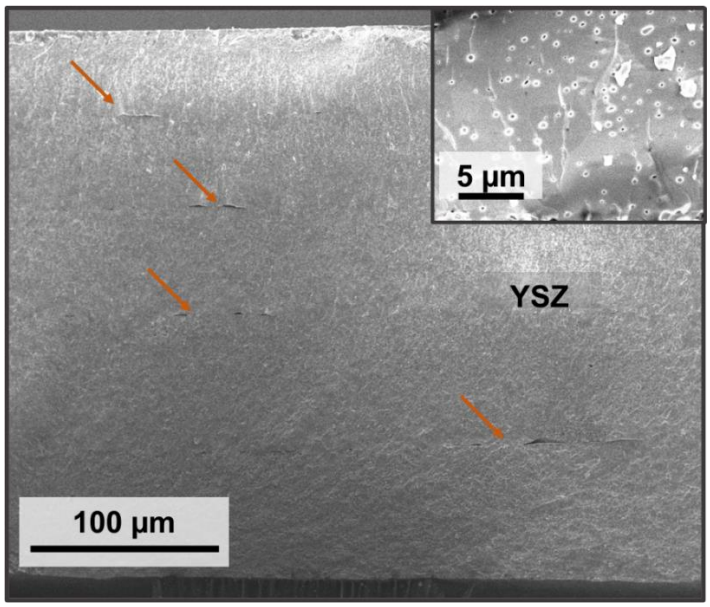

Fig. A1.3 Secondary electron SEM images of a fractured cross-section of the YSZ electrolyte with a magnified view of the porosity of the electrolyte.

Fig. A1.4 shows the sintered ESC. The electrolyte has ~300 µm thickness and the cathode and anode have a thickness of ~40 µm and ~60 µm, respectively. Those thicknesses were within the typical range used and in agreement with the procedure optimized by the group [265]. The image also evidences good adhesion of anode and the cathode to the electrolyte and a homogeneous interface.

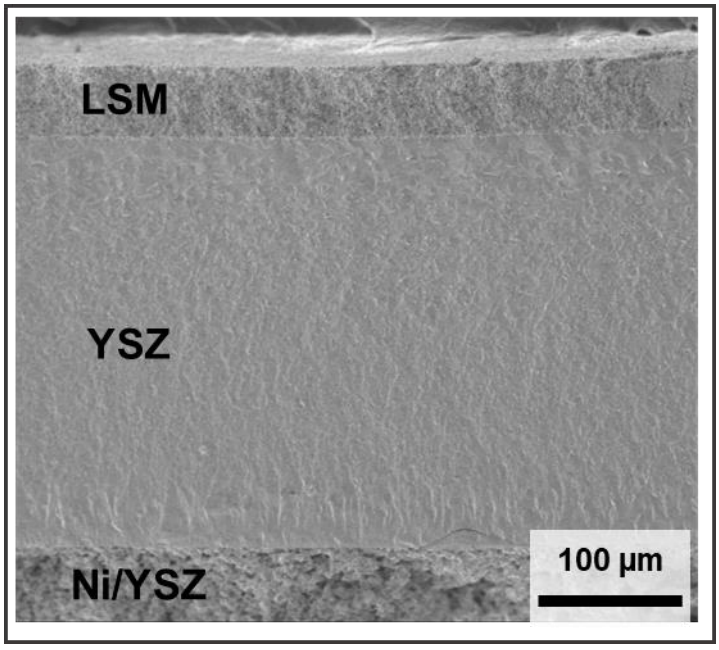

Fig. A1.4 Secondary electron SEM images of a fractured cross-section of the ESC.

Fig. A1.5 shows the images of the ASC with laminated electrolyte and anode tapes. The cross-section shown in **Fig. A1.5** (a) reveals homogeneous interfaces and a good attachment between the layers. The anode support has ~350 µm thickness, the electrolyte ~55 µm, and the cathode ~40 µm. The SEM image of the anode **Fig. A1.5** (b) shows a detailed view of the anode support, exhibiting open porosity. The calculated apparent relative open porosity of the sintered anode tape was of 22%. Such interconnected porosity is still low for an ASC, and should ideally be superior to 30% [267]. In an ASC, the interconnected porosity of the anode should be maximized to allow gas diffusion through the thick anode layer to the TPB [4,268,269]. The cathode **Fig. A1.5** (c) exhibits interconnected porosity and good adhesion to the electrolyte. **Fig. A1.5** (d) shows a magnified view of the dense electrolyte, where a few closed pores with an average size of 200 nm can be observed but should not be detrimental to the cell's performance.

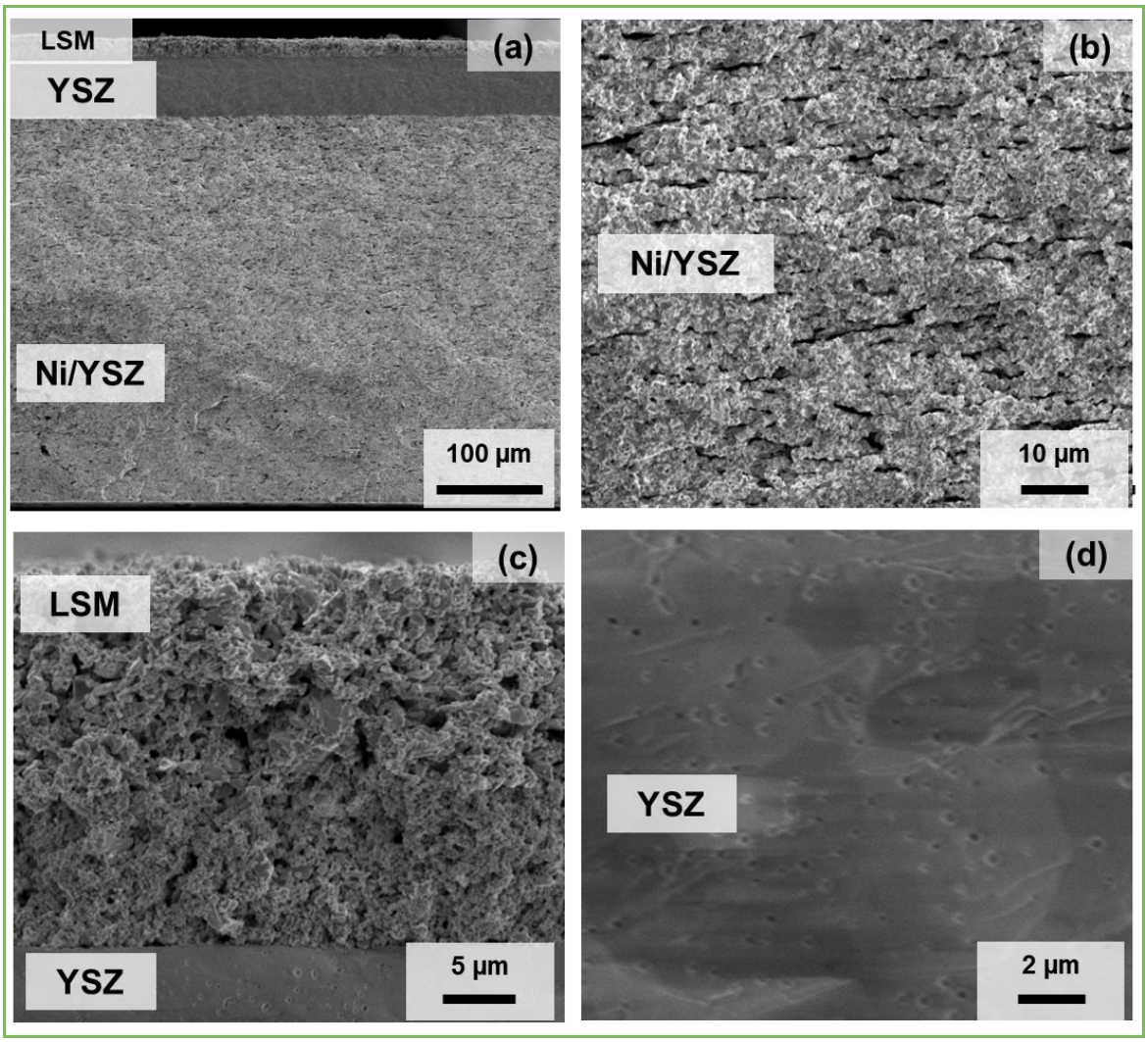

Fig. A1.5 Secondary electron SEM images of a fractured cross section of the tape casted ASC (a) general view (b) detail of the anode (c) anode and cathode interfaces, and (d) detail of the electrolyte.

Fig. A1.6 shows the I-V and current density power density (I-P) curves measured at 850 °C under synthetic air and dry hydrogen. A maximum power density of 139 $mW \cdot cm^{-2}$ and 234 $mW \cdot cm^{-2}$ were obtained by the ESC and the ASC, respectively. The OCV of both cells is ~1 V, demonstrating a good gas tightness for both cells, in agreement with the high density observed by the SEM images. The processing techniques successfully produced a highly dense, stable electrolyte layer. Nevertheless, the power densities obtained are still inferior to the state-of-the-art fuel cells reported for ESC [270] and ASC with similar configurations [271]. However, it is important to consider that ASCs typically have electrolyte thickness in the 5-10 µm range, which is considerably smaller than that

(~55 µm) in the ASC shown in **Fig. A1.5**. Such results evidence the importance of further optimization of the techniques for electrode depositions.

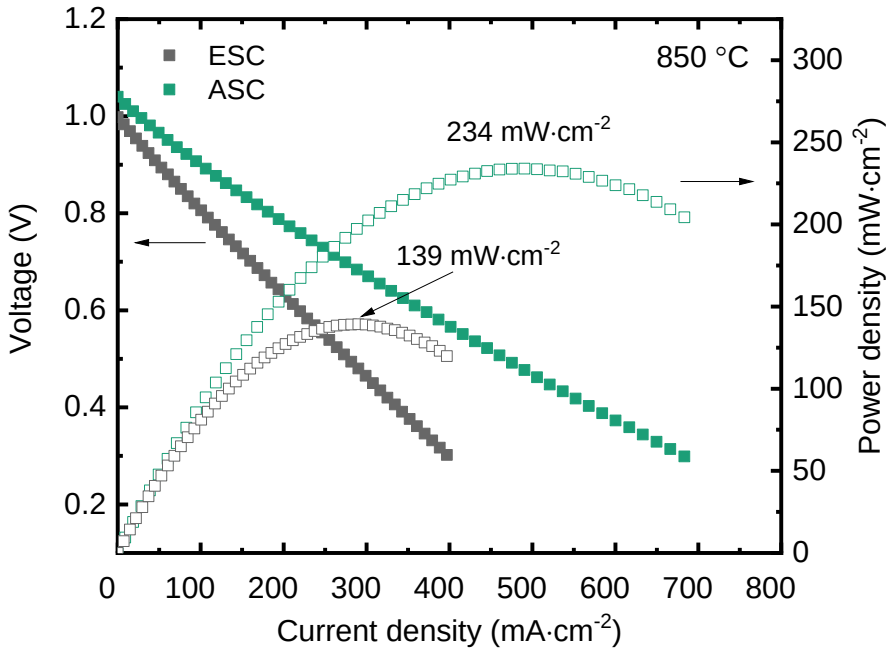

Fig. A1.6 Current-voltage (I-V) and current-polarization (I-P) curves of the ESC and ASC at 850 °C under synthetic air and dry hydrogen.

The EIS diagrams of the ESC and ASC at OCV and 850 °C are shown in **Fig. A1.7**. The EIS data were fitted with the equivalent circuit $LR_s(R_{p1}CPE_{p1})(R_{p2}CPE_{p2})$. The series resistances (R_s), the polarization resistances (R_{p1} and R_{p2}) and total resistance (R_{total}) attained through the fitting are exhibited in **Table A1.1**.

The series resistance (R_s), related to the ion transport in the electrolyte and ohmic interfacial resistances, corresponds to 58% of the total resistance in the ECS and to 41% in the ACS, emphasizing the important relationship between ohmic resistance and electrolyte thickness. The circuit was also fitted with two arcs, the first at high frequency ~10^3 Hz and the second at lower frequency ~10 Hz. The high frequency arcs are usually ascribed to the charge transfer process at the electrode/electrolyte interfaces and to the oxygen reduction reaction, occurring in the cathode [222,224]. The fitting of the equivalent circuit resulted in higher R_{p1} value for the ESC, corresponding to an area specific

resistance of 0.614 Ω·cm^2 higher than obtained for the ASR (0.281 Ω·cm^2), indicating faster reactions occurring at the interfaces of the ASC. Nonetheless, a higher value R_{p2} is obtained for the ASR. The phenomena occurring at this characteristic frequency are typically assigned to the mass diffusion, which is usually dominated by gas and H_2O diffusion in the anode of an ASC [222–224]. The impedance spectroscopy has shown that the largest influence on the resistance originated in the ESC originated from ohmic resistance, whereas in the ASC, it comes from the polarization resistances. Thus, the strategy to decrease the polarization resistance of the ASC is to increase the porosity of the anode layer, which was found to be below the optimal level.

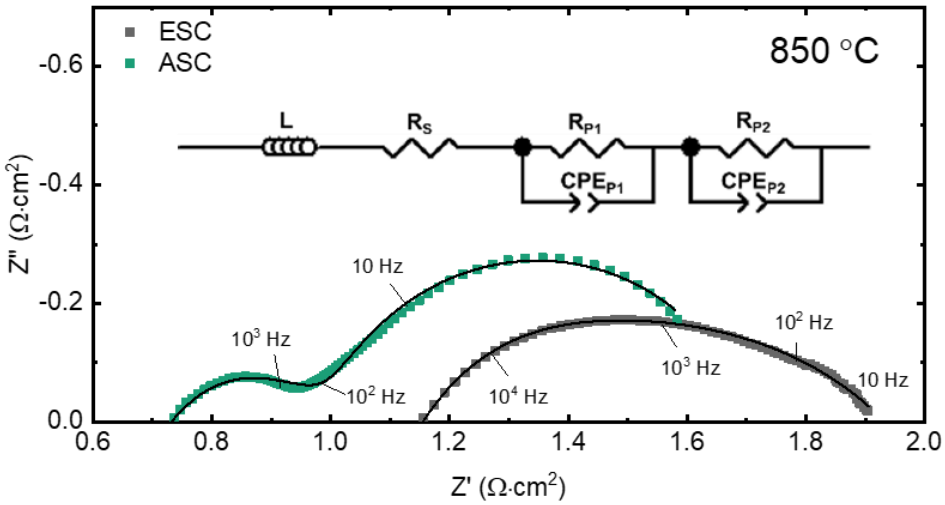

Fig. A1.7 EIS diagrams at OCV of the ESC and ASC at 850 °C under synthetic air and dry hydrogen.

Table A1.1 Resulting fitting parameters of series resistances (R_s), polarization resistances (R_{p1} and R_{p2}) and total resistance (R_{total}) of the ESC and ASC at OCV, at 850 °C.

Cell	R_s (Ω·cm^2)	R_{p1} (Ω·cm^2)	R_{p2} (Ω·cm^2)	R_{total} (Ω·cm^2)
ESC	1.12	6.14E-1	1.94E-1	1.93
ASC	6.85E-01	2.81E-1	7.10E-1	1.68

A1.4 Conclusion

The development of the tape casting processing method was successful in producing the electrolyte and anode layers. As a results, the ASC exhibited the highest power density and the lowest total resistance. Nonetheless, the cell's performance can be optimized by increasing the interconnected porosity of the anode layer and decreasing the electrolyte thickness to achieve high power densities (~1 $W \cdot cm^{-2}$). Additionally, the lamination step of the green tapes was challenging and resulted in some delamination of the tapes.

Scientific contribution

Scientific journals

Rodrigues, Lays Nunes; Machado, Marina; Moraes, Leticia Poras Reis; Thyssen, Vivian Vazquez; Fonseca, Fabio Coral. Development of Anode-Supported Solid Oxide Fuel Cell by Sequential Tape-Casting and Co-Sintering. ECS TRANSACTIONS, v. 103, p. 2245-2251, 2021.

Esposito, Vincenzo; Kabir, Ahsanul; Rosa, Massimo; Van Nong, Ngo; Rodrigues, Thenner S.; Rodrigues, Lays N.; Machado, Marina F. S.; Moraes, Letícia P. R.; Marani, Debora; Fonseca, Fabio Coral. Tuning diffusion paths in shaped ceria nanocrystals. CRYSTENGCOMM, v. 21, n. 27, p. 4025–4029, 2019.

Machado, Marina; Moraes, Leticia P. R.; Rodrigues, Lays Nunes; Tabanez, Miguel; Ferrazoli, Marcela; Fonseca, Fabio C. Evaluation of Fe-Doped CGO Electrolyte for Application in IT-SOFCs. ECS TRANSACTIONS, v. 91, p. 1209-1216, 2019.

Machado, Marina; Moraes, Leticia P. R.; Rodrigues, Lays; Rodrigues, Thenner; Fonseca, Fabio C. Lowering the Sintering Temperature of a SOFC by Morphology Control of the Electrolyte Powder. ECS TRANSACTIONS, v. 91, p. 1193-1199, 2019.

Machado, Marina F. S.; Moraes, Leticia P. R.; Monteiro, Natalia; Esposito, Vincenzo; De Florio, Daniel; Marani, Debora and Fonseca, Fabio C. Low Temperature Synthesis and Properties of Gadolinium-Doped Cerium Oxide Nanoparticles. ECS TRANSACTIONS, v. 78, p. 387-394, 2017.

Submitted scientific work

Machado, Marina; Baiutti, Federico; Bernadet, Lucile; Morate, Alex; Nuñez, Marc; Ouweltjes, Jan Pieter; Fonseca, Fabio C.; Torrell, Marc and Tarancón, Albert. Functional thin films as cathode/electrolyte interlayers: a strategy to enhance the performance and durability of solid oxide fuel cells (Submitted to Journal of Materials Chemistry A, May 2022).

Scientific work in elaboration

Machado, Marina; da Silva Andre L.; Moraes Leticia P. R; Rodrigues Lays N.; Caliman, Lorena B.; Gouvêa, Douglas and Fonseca, Fabio C. *Interface segregation of Fe-doped CGO electrolyte and its influence on sintering and electrochemical properties.*

Machado, Marina; Moraes, Tamara S; Rodrigues, Lays N; Vilela, Vanessa; and Fonseca, Fabio C. *Evaluation of Ni/CGO nanocubes and nanorods as catalyst for ethanol steam reforming and application as catalytic layer for SOFC.*

Conferences

Machado, Marina; Moraes, L. P. R., Rodrigues, L. N.; Fonseca, F. C. Synthesis, and characterization of shape-controlled ceria-based nanoparticles. In: Sustainable Gas Research and Inovation, São Paulo. SGRI, 2018. (Oral)

Machado, M. F. S.; Moraes, Leticia P. R.; Nunes, L.; Fonseca, F. C. Effect of iron doping nano-GDC synthesized via low temperature heterogeneous precipitation. In: 7th International Congress on Ceramics, 2018, Foz do Iguaçú. (Oral)

Moraes, Leticia P.R.; Monteiro, N. K.; Machado, M. F. S.; De Florio, D. Z.; Esposito, V.; Marani, D.; Fonseca, F. C. Low temperature synthesis of gadolinium-doped cerium oxide nanoparticles. In: XV Encontro da SBPMat, 2016, Campinas. (Poster)

References

[1] S. Arrhenius, On the influence of carbonic acid in the air upon the temperature of the ground, The London, Edinburgh, and Dublin Philosophical Magazine and Journal of Science. 41 (1896) 237–276. https://doi.org/10.1080/14786449608620846.

[2] V. Masson-Delmotte, P. Zhai, A. Pirani, S.L. Connors, C. Péan, S. Berger, N. Caud, Y. Chen, L. Goldfarb, M.I. Gomis, M. Huang, K. Leitzell, E. Lonnoy, J.B.R. Matthews, T.K. Maycock, T. Waterfield, O. Yelekçi, R. Yu, B. Zhou, IPCC, 2021: Climate Change 2021: The Physical Science Basis. Contribution of Working Group I to the Sixth Assessment Report of the Intergovernmental Panel on Climate Change, (2021).

[3] United Nations Framework Convention on Climate Change. Paris Agreement. Article 2(a), (2015). https://unfccc.int/process-and-meetings/the-paris-agreement/the-paris-agreement.

[4] P.A. Connor, X. Yue, C.D. Savaniu, R. Price, G. Triantafyllou, M. Cassidy, G. Kerherve, D.J. Payne, R.C. Maher, L.F. Cohen, R.I. Tomov, B.A. Glowacki, R.V. Kumar, J.T.S. Irvine, Tailoring SOFC Electrode Microstructures for Improved Performance, Advanced Energy Materials. 8 (2018) 1800120. https://doi.org/10.1002/aenm.201800120.

[5] L. Fan, B. Zhu, P.-C. Su, C. He, Nanomaterials and technologies for low temperature solid oxide fuel cells: Recent advances, challenges and opportunities, Nano Energy. 45 (2018) 148–176. https://doi.org/10.1016/j.nanoen.2017.12.044.

[6] S.A. Saadabadi, A. Thallam Thattai, L. Fan, R.E.F. Lindeboom, H. Spanjers, P.V. Aravind, Solid Oxide Fuel Cells fueled with biogas: Potential and constraints, Renewable Energy. 134 (2019) 194–214. https://doi.org/10.1016/j.renene.2018.11.028.

[7] D.J.L. Brett, A. Atkinson, N.P. Brandon, S.J. Skinner, Intermediate temperature solid oxide fuel cells, Chemical Society Reviews. 37 (2008) 1568. https://doi.org/10.1039/b612060c.

[8] S.U. Costilla-Aguilar, M.I. Pech-Canul, M.J. Escudero, R.F. Cienfuegos-Pelaes, J.A. Aguilar-Martínez, Gadolinium doped ceria nanostructured oxide for intermediate temperature solid oxide fuel cells, Journal of Alloys and Compounds. 878 (2021) 160444. https://doi.org/10.1016/j.jallcom.2021.160444.

[9] R. Fuentes, R. Baker, Synthesis and properties of Gadolinium-doped ceria solid solutions for IT-SOFC electrolytes, International Journal of Hydrogen Energy. 33 (2008) 3480–3484. https://doi.org/10.1016/j.ijhydene.2007.10.026.

[10] C. Nicollet, J. Waxin, T. Dupeyron, A. Flura, J.-M. Heintz, J.P. Ouweltjes, P. Piccardo, A. Rougier, J.-C. Grenier, J.-M. Bassat, Gadolinium doped ceria interlayers for Solid Oxide Fuel Cells cathodes: Enhanced reactivity with sintering aids (Li, Cu, Zn), and improved densification by infiltration, Journal of Power Sources. 372 (2017) 157–165. https://doi.org/10.1016/j.jpowsour.2017.10.064.

[11] H. Inaba, Ceria-based solid electrolytes, Solid State Ionics. 83 (1996) 1–16. https://doi.org/10.1016/0167-2738(95)00229-4.

[12] A.V. Coles-Aldridge, R.T. Baker, Ionic conductivity in multiply substituted ceria-based electrolytes, Solid State Ionics. 316 (2018) 9–19. https://doi.org/10.1016/j.ssi.2017.12.013.

[13] B.S. Kang, A. Inoishi, A. Takagaki, T. Ishihara, Pr2Ni0.71Cu0.24Ga0.05O4-$Sm_{0.2}C_{e0.8}O_{1.9}$ composite film as active cathodic layer for intermediate temperature solid oxide fuel cells, Solid State Ionics. 327 (2018) 59–63. https://doi.org/10.1016/j.ssi.2018.10.027.

[14] W.R. Grove, XXIV. *On voltaic series and the combination of gases by platinum*, The London, Edinburgh, and Dublin Philosophical Magazine and Journal of Science. 14 (1839) 127–130. https://doi.org/10.1080/14786443908649684.

[15] H.-H. Möbius, On the history of solid electrolyte fuel cells, Journal of Solid State Electrochemistry. 1 (1997) 2–16. https://doi.org/10.1007/s100080050018.

[16] A.B. Stambouli, E. Traversa, Solid oxide fuel cells (SOFCs): a review of an environmentally clean and efficient source of energy, Renewable and Sustainable Energy Reviews. 6 (2002) 433–455. https://doi.org/10.1016/S1364-0321(02)00014-X.

[17] W.H. Kan, A.J. Samson, V. Thangadurai, Trends in electrode development for next generation solid oxide fuel cells, J. Mater. Chem. A. 4 (2016) 17913–17932. https://doi.org/10.1039/C6TA06757C.

[18] E.D. Wachsman, K.T. Lee, Lowering the Temperature of Solid Oxide Fuel Cells, Science. 334 (2011) 935–939. https://doi.org/10.1126/science.1204090.

[19] W. Winkler, P. Nehter, Thermodynamics of Fuel Cells, in: R. Bove, S. Ubertini (Eds.), Modeling Solid Oxide Fuel Cells: Methods, Procedures and Techniques, Springer Netherlands, Dordrecht, 2008: pp. 13–50. https://doi.org/10.1007/978-1-4020-6995-6_2.

[20] E.G.G. Services, Fuel cell handbook, US Department of Energy, 2004.

[21] S.J. Skinner, J.A. Kilner, Oxygen ion conductors, Materials Today. 6 (2003) 30–37. https://doi.org/10.1016/S1369-7021(03)00332-8.

[22] S.M. Haile, Materials for fuel cells, Materials Today. 6 (2003) 24–29. https://doi.org/10.1016/S1369-7021(03)00331-6.

[23] L. Navarro, n-Type Conductivity in Gadolinia-Doped Ceria, J. Electrochem. Soc. 144 (1997) 267. https://doi.org/10.1149/1.1837395.

[24] H. Yahiro, Y. Eguchi, K. Eguchi, H. Arai, Oxygen ion conductivity of the ceria-samarium oxide system with fluorite structure, J Appl Electrochem. 18 (1988) 527–531. https://doi.org/10.1007/BF01022246.

[25] B. Steele, Appraisal of $Ce_{1-y}Gd_yO_{2-y/2}$ electrolytes for IT-SOFC operation at 500°C, Solid State Ionics. 129 (2000) 95–110. https://doi.org/10.1016/S0167-2738(99)00319-7.

[26] K. Momma, F. Izumi, VESTA 3 for three-dimensional visualization of crystal, volumetric and morphology data, Journal of Applied Crystallography. 44 (2011) 1272–1276. https://doi.org/10.1107/S0021889811038970.

[27] L.P.R. Moraes, Desenvolvimento de nanoestruturas 2D à base de céria para deposição de camadas finas aplicadas a células a combustível de óxido sólido, PhD thesis, University of São Paulo, 2021.

[28] J. Faber, C. Geoffroy, A. Roux, A. Sylvestre, P. Abélard, A Systematic investigation of the dc electrical conductivity of rare-earth doped ceria, Appl. Phys. A. 49 (1989) 225–232. https://doi.org/10.1007/BF00616848.

[29] D.A. Andersson, S.I. Simak, N.V. Skorodumova, I.A. Abrikosov, B. Johansson, Optimization of ionic conductivity in doped ceria, Proc Natl Acad Sci U S A. 103 (2006) 3518–3521. https://doi.org/10.1073/pnas.0509537103.

[30] S. (Rob) Hui, J. Roller, S. Yick, X. Zhang, C. Decès-Petit, Y. Xie, R. Maric, D. Ghosh, A brief review of the ionic conductivity enhancement for selected oxide electrolytes, Journal of Power Sources. 172 (2007) 493–502. https://doi.org/10.1016/j.jpowsour.2007.07.071.

[31] H.J. Avila-Paredes, K. Choi, C.-T. Chen, S. Kim, Dopant-concentration dependence of grain-boundary conductivity in ceria: A space-charge analysis, J. Mater. Chem. 19 (2009) 4837. https://doi.org/10.1039/b904583j.

[32] N. Jaiswal, K. Tanwar, R. Suman, D. Kumar, S. Upadhyay, O. Parkash, A brief review on ceria based solid electrolytes for solid oxide fuel cells, Journal of Alloys and Compounds. 781 (2019) 984–1005. https://doi.org/10.1016/j.jallcom.2018.12.015.

[33] A.V. Coles-Aldridge, R.T. Baker, Oxygen ion conductivity in ceria-based electrolytes co-doped with samarium and gadolinium, Solid State Ionics. 347 (2020) 115255. https://doi.org/10.1016/j.ssi.2020.115255.

[34] J. Huang, Z. Gao, Z. Mao, Effects of salt composition on the electrical properties of samaria-doped ceria/carbonate composite electrolytes for low-temperature SOFCs, International Journal of Hydrogen Energy. 35 (2010) 4270–4275. https://doi.org/10.1016/j.ijhydene.2010.01.063.

[35] B. Wang, B. Zhu, S. Yun, W. Zhang, C. Xia, M. Afzal, Y. Cai, Y. Liu, Y. Wang, H. Wang, Fast ionic conduction in semiconductor CeO2-δ electrolyte fuel cells, NPG Asia Mater. 11 (2019) 51. https://doi.org/10.1038/s41427-019-0152-8.

[36] M. Akbar, B. Jin, Z. Tu, J. Gao, M. Yousaf, N. Mushtaq, X. Wang, W. Dong, B. Wang, Y. Cai, C. Xia, High-performing and stable non-doped ceria electrolyte with amorphous carbonate coating layer for low-temperature solid oxide fuel cells, Electrochimica Acta. 393 (2021) 139067. https://doi.org/10.1016/j.electacta.2021.139067.

[37] D. Beckel, A. Bieberle-Hütter, A. Harvey, A. Infortuna, U.P. Muecke, M. Prestat, J.L.M. Rupp, L.J. Gauckler, Thin films for micro solid oxide fuel cells, Journal of Power Sources. 173 (2007) 325–345. https://doi.org/10.1016/j.jpowsour.2007.04.070.

[38] A. Tsoga, A. Gupta, A. Naoumidis, P. Nikolopoulos, Gadolinia-doped ceria and yttria stabilized zirconia interfaces: regarding their application for SOFC technology, Acta Materialia. 48 (2000) 4709–4714. https://doi.org/10.1016/S1359-6454(00)00261-5.

[39] A. Mai, V. Haanappel, F. Tietz, D. Stover, Ferrite-based perovskites as cathode materials for anode-supported solid oxide fuel cellsPart II. Influence of the CGO interlayer, Solid State Ionics. 177 (2006) 2103–2107. https://doi.org/10.1016/j.ssi.2005.12.010.

[40] C.-C. Chao, C.-M. Hsu, Y. Cui, F.B. Prinz, Improved Solid Oxide Fuel Cell Performance with Nanostructured Electrolytes, ACS Nano. 5 (2011) 5692–5696. https://doi.org/10.1021/nn201354p.

[41] Z. Gao, L.V. Mogni, E.C. Miller, J.G. Railsback, S.A. Barnett, A perspective on low-temperature solid oxide fuel cells, Energy Environ. Sci. 9 (2016) 1602–1644. https://doi.org/10.1039/C5EE03858H.

[42] S.B. Adler, Electrode Kinetics of Porous Mixed-Conducting Oxygen Electrodes, Journal of The Electrochemical Society. 143 (1996) 3554. https://doi.org/10.1149/1.1837252.

[43] S.B. Adler, Factors Governing Oxygen Reduction in Solid Oxide Fuel Cell Cathodes, Chem. Rev. 104 (2004) 4791–4844. https://doi.org/10.1021/cr020724o.

[44] J.A. Kilner, M. Burriel, Materials for Intermediate-Temperature Solid-Oxide Fuel Cells, Annual Review of Materials Research. 44 (2014) 365–393. https://doi.org/10.1146/annurev-matsci-070813-113426.

[45] T. Tsai, S.A. Barnett, Effect of LSM-YSZ cathode on thin-electrolyte solid oxide fuel cell performance, Solid State Ionics. 93 (1997) 207–217. https://doi.org/10.1016/S0167-2738(96)00524-3.

[46] A. Tarancón, Strategies for Lowering Solid Oxide Fuel Cells Operating Temperature, Energies. 2 (2009) 1130–1150. https://doi.org/10.3390/en20401130.

[47] D. Clematis, A. Barbucci, S. Presto, M. Viviani, M.P. Carpanese, Electrocatalytic activity of perovskite-based cathodes for solid oxide fuel cells, International Journal of Hydrogen Energy. 44 (2019) 6212–6222. https://doi.org/10.1016/j.ijhydene.2019.01.128.

[48] S.J. Skinner, Recent advances in Perovskite-type materials for solid oxide fuel cell cathodes, International Journal of Inorganic Materials. 3 (2001) 113–121. https://doi.org/10.1016/S1466-6049(01)00004-6.

[49] D. Marinha, J. Hayd, L. Dessemond, E. Ivers-Tiffée, E. Djurado, Performance of $(La,Sr)(Co,Fe)O_{3-x}$ double-layer cathode films for intermediate temperature solid oxide fuel cell, Journal of Power Sources. 196 (2011) 5084–5090. https://doi.org/10.1016/j.jpowsour.2011.01.063.

[50] A. Petric, P. Huang, F. Tietz, Evaluation of La–Sr–Co–Fe–O perovskites for solid oxide fuel cells and gas separation membranes, Solid State Ionics. 135 (2000) 719–725. https://doi.org/10.1016/S0167-2738(00)00394-5.

[51] S.P. Jiang, Development of lanthanum strontium cobalt ferrite perovskite electrodes of solid oxide fuel cells – A review, International Journal of Hydrogen Energy. 44 (2019) 7448–7493. https://doi.org/10.1016/j.ijhydene.2019.01.212.

[52] S. Uhlenbruck, T. Moskalewicz, N. Jordan, H.-J. Penkalla, H.P. Buchkremer, Element interdiffusion at electrolyte–cathode interfaces in ceramic high-temperature fuel cells, Solid State Ionics. 180 (2009) 418–423. https://doi.org/10.1016/j.ssi.2009.01.014.

[53] G. Kostogloudis, Chemical reactivity of perovskite oxide SOFC cathodes and yttria stabilized zirconia, Solid State Ionics. 135 (2000) 529–535. https://doi.org/10.1016/S0167-2738(00)00433-1.

[54] S. Simner, Interaction between La(Sr)FeO_3 SOFC cathode and YSZ electrolyte, Solid State Ionics. 161 (2003) 11–18. https://doi.org/10.1016/S0167-2738(03)00158-9.

[55] S. Molin, J. Karczewski, B. Kamecki, A. Mroziński, S.-F. Wang, P. Jasiński, Processing of $Ce_{0.8}Gd_{0.2}O_{2-\delta}$ barrier layers for solid oxide cells: The effect of preparation method and thickness on the interdiffusion and electrochemical performance, Journal of the European Ceramic Society. 40 (2020) 5626–5633. https://doi.org/10.1016/j.jeurceramsoc.2020.06.006.

[56] X.-D. Zhou, B. Scarfino, H.U. Anderson, Electrical conductivity and stability of Gd-doped ceria/Y-doped zirconia ceramics and thin films, Solid State Ionics. 175 (2004) 19–22. https://doi.org/10.1016/j.ssi.2004.09.040.

[57] R. Knibbe, J. Hjelm, M. Menon, N. Pryds, M. Søgaard, H.J. Wang, K. Neufeld, Cathode-Electrolyte Interfaces with CGO Barrier Layers in SOFC: Cathode-Electrolyte Interfaces in IT-SOFCs, Journal of the American Ceramic Society. 93 (2010) 2877–2883. https://doi.org/10.1111/j.1551-2916.2010.03763.x.

[58] J.-S. Shin, M. Saqib, M. Jo, K. Park, K.M. Park, J.S. Ahn, H.-T. Lim, J.-Y. Park, Degradation Mechanisms of Solid Oxide Fuel Cells under Various Thermal Cycling Conditions, ACS Appl. Mater. Interfaces. 13 (2021) 49868–49878. https://doi.org/10.1021/acsami.1c13779.

[59] M. Morales, V. Miguel-Pérez, A. Tarancón, A. Slodczyk, M. Torrell, B. Ballesteros, J.P. Ouweltjes, J.M. Bassat, D. Montinaro, A. Morata, Multi-scale analysis of the diffusion barrier layer of gadolinia-doped ceria in a solid oxide fuel cell operated in a stack for 3000 h, Journal of Power Sources. 344 (2017) 141–151. https://doi.org/10.1016/j.jpowsour.2017.01.109.

[60] L. Adijanto, R. Küngas, F. Bidrawn, R.J. Gorte, J.M. Vohs, Stability and performance of infiltrated La0.8Sr0.2CoxFe1−xO3 electrodes with and without $Sm_{0.2}Ce_{0.8}O_{1.9}$ interlayers, Journal of Power Sources. 196 (2011) 5797–5802. https://doi.org/10.1016/j.jpowsour.2011.03.022.

[61] J.Y. Koo, T. Mun, J. Lee, M. Choi, S.J. Kim, W. Lee, Enhancement of oxygen reduction reaction kinetics using infiltrated yttria-stabilized zirconia interlayers at the electrolyte/electrode interfaces of solid oxide fuel cells, Journal of Power Sources. 472 (2020) 228606. https://doi.org/10.1016/j.jpowsour.2020.228606.

[62] K. Develos-Bagarinao, T. Ishiyama, H. Kishimoto, H. Shimada, K. Yamaji, Nanoengineering of cathode layers for solid oxide fuel cells to achieve superior power densities, Nature Communications. 12 (2021). https://doi.org/10.1038/s41467-021-24255-w.

[63] J. Yoon, S. Cho, J.-H. Kim, J. Lee, Z. Bi, A. Serquis, X. Zhang, A. Manthiram, H. Wang, Vertically Aligned Nanocomposite Thin Films as a Cathode/Electrolyte Interface Layer for Thin-Film Solid Oxide Fuel Cells, Adv. Funct. Mater. 19 (2009) 3868–3873. https://doi.org/10.1002/adfm.200901338.

[64] Y. Liu, Z. Shao, T. Mori, S.P. Jiang, Development of nickel based cermet anode materials in solid oxide fuel cells – Now and future, Materials Reports: Energy. 1 (2021) 100003. https://doi.org/10.1016/j.matre.2020.11.002.

[65] A. Atkinson, S. Barnett, R.J. Gorte, J.T.S. Irvine, A.J. McEvoy, M. Mogensen, S.C. Singhal, J. Vohs, Advanced anodes for high-temperature fuel cells, Nature Materials. 3 (2004) 17–27. https://doi.org/10.1038/nmat1040.

[66] P.I. Cowin, C.T.G. Petit, R. Lan, J.T.S. Irvine, S. Tao, Recent Progress in the Development of Anode Materials for Solid Oxide Fuel Cells, Advanced Energy Materials. 1 (2011) 314–332. https://doi.org/10.1002/aenm.201100108.

[67] R.J. Gorte, J.M. Vohs, Nanostructured anodes for solid oxide fuel cells, Current Opinion in Colloid & Interface Science. 14 (2009) 236–244. https://doi.org/10.1016/j.cocis.2009.04.006.

[68] K. Chen, X. Chen, Z. Lue, N. Ai, X. Huang, W. Su, Performance of an anode-supported SOFC with anode functional layers, Electrochim. Acta. 53 (2008) 7825–7830. https://doi.org/10.1016/j.electacta.2008.05.063.

[69] J.E. Velandia Vargas, J.E.A. Seabra, Fuel-cell technologies for private vehicles in Brazil: Environmental mirage or prospective romance? A comparative life cycle assessment of PEMFC and SOFC light-duty vehicles, Science of The Total Environment. 798 (2021) 149265. https://doi.org/10.1016/j.scitotenv.2021.149265.

[70] M.C. Steil, S.D. Nobrega, S. Georges, P. Gelin, S. Uhlenbruck, F.C. Fonseca, Durable direct ethanol anode-supported solid oxide fuel cell, Applied Energy. 199 (2017) 180–186. https://doi.org/10.1016/j.apenergy.2017.04.086.

[71] N. Laosiripojana, S. Assabumrungrat, Catalytic steam reforming of methane, methanol, and ethanol over Ni/YSZ: The possible use of these fuels in internal reforming SOFC, Journal of Power Sources. 163 (2007) 943–951. https://doi.org/10.1016/j.jpowsour.2006.10.006.

[72] S.M. de Lima, A.M. da Silva, L.O.O. da Costa, U.M. Graham, G. Jacobs, B.H. Davis, L.V. Mattos, F.B. Noronha, Study of catalyst deactivation and reaction mechanism of steam reforming, partial oxidation, and oxidative steam reforming of ethanol over Co/CeO_2 catalyst, Journal of Catalysis. 268 (2009) 268–281. https://doi.org/10.1016/j.jcat.2009.09.025.

[73] J.C. Vargas, S. Libs, A.-C. Roger, A. Kiennemann, Study of Ce-Zr-Co fluorite-type oxide as catalysts for hydrogen production by steam reforming of bioethanol, Catalysis Today. 107–108 (2005) 417–425. https://doi.org/10.1016/j.cattod.2005.07.118.

[74] M. Compagnoni, A. Tripodi, A. Di Michele, P. Sassi, M. Signoretto, I. Rossetti, Low temperature ethanol steam reforming for process intensification: New Ni/M_xO–ZrO_2 active and stable catalysts prepared by flame spray pyrolysis, International Journal of Hydrogen Energy. 42 (2017) 28193–28213. https://doi.org/10.1016/j.ijhydene.2017.09.123.

[75] A.A.A. da Silva, N. Bion, F. Epron, S. Baraka, F.C. Fonseca, R.C. Rabelo-Neto, L.V. Mattos, F.B. Noronha, Effect of the type of ceria dopant on the performance of Ni/CeO_2 SOFC anode for ethanol internal reforming, Applied Catalysis B: Environmental. 206 (2017) 626–641. https://doi.org/10.1016/j.apcatb.2017.01.069.

[76] C. Thanomjit, Y. Patcharavorachot, P. Ponpesh, A. Arpornwichanop, Thermodynamic analysis of solid oxide fuel cell system using different ethanol reforming processes, International Journal of Hydrogen Energy. 40 (2015) 6950–6958. https://doi.org/10.1016/j.ijhydene.2015.03.155.

[77] T.S. Rodrigues, A.B.L. de Moura, F.A. e Silva, E.G. Candido, A.G.M. da Silva, D.C. de Oliveira, J. Quiroz, P.H.C. Camargo, V.S. Bergamaschi, J.C. Ferreira, M. Linardi, F.C. Fonseca, Ni supported $Ce_{0.9}Sm_{0.1}O_{2-\delta}$ nanowires: An efficient catalyst for ethanol steam reforming for hydrogen production, Fuel. 237 (2019) 1244–1253. https://doi.org/10.1016/j.fuel.2018.10.053.

[78] T.S. Moraes, R.C.R. Neto, M.C. Ribeiro, L.V. Mattos, M. Kourtelesis, X. Verykios, F.B. Noronha, Effects of Ceria Morphology on Catalytic Performance of Ni/CeO2 Catalysts for Low Temperature Steam Reforming of Ethanol, Top Catal. 58 (2015) 281–294. https://doi.org/10.1007/s11244-015-0369-x.

[79] B.L. Augusto, F.B. Noronha, F.C. Fonseca, F.N. Tabuti, R.C. Colman, L.V. Mattos, Nickel/gadolinium-doped ceria anode for direct ethanol solid oxide fuel cell, International Journal of Hydrogen Energy. 39 (2014) 11196–11209. https://doi.org/10.1016/j.ijhydene.2014.05.088.

[80] S. McIntosh, R.J. Gorte, Direct Hydrocarbon Solid Oxide Fuel Cells, Chem. Rev. 104 (2004) 4845–4866. https://doi.org/10.1021/cr020725g.

[81] A.A.A. da Silva, M.C. Steil, F.N. Tabuti, R.C. Rabelo-Neto, F.B. Noronha, L.V. Mattos, F.C. Fonseca, The role of the ceria dopant on Ni / doped-ceria anodic layer cermets for direct ethanol solid oxide fuel cell, International Journal of Hydrogen Energy. 46 (2021) 4309–4328. https://doi.org/10.1016/j.ijhydene.2020.10.155.

[82] R. Muccillo, E.N.S. Muccillo, F.C. Fonseca, D.Z. de Florio, Characteristics and Performance of Electrolyte-Supported Solid Oxide Fuel Cells under Ethanol and Hydrogen, J. Electrochem. Soc. 155 (2008) B232. https://doi.org/10.1149/1.2828024.

[83] M. Cimenti, J.M. Hill, Direct utilization of methanol and ethanol in solid oxide fuel cells using Cu–Co(Ru)/$Zr_{0.35}Ce_{0.65}O_{2-\delta}$ anodes, Journal of Power Sources. 195 (2010) 3996–4001. https://doi.org/10.1016/j.jpowsour.2009.12.122.

[84] J.P. Breen, R. Burch, H.M. Coleman, Metal-catalysed steam reforming of ethanol in the production of hydrogen for fuel cell applications, Appl. Catal. B-Environ. 39 (2002) 65–74. https://doi.org/10.1016/S0926-3373(02)00075-9.

[85] B. Zhang, X. Tang, Y. Li, W. Cai, Y. Xu, W. Shen, Steam reforming of bio-ethanol for the production of hydrogen over ceria-supported Co, Ir and Ni catalysts, Catal. Commun. 7 (2006) 367–372. https://doi.org/10.1016/j.catcom.2005.12.014.

[86] B.J.M. Sarruf, J.-E. Hong, R. Steinberger-Wilckens, P.E.V. de Miranda, Ceria-Co-Cu-based SOFC anode for direct utilisation of methane or ethanol as fuels, International Journal of Hydrogen Energy. 45 (2020) 5297–5308. https://doi.org/10.1016/j.ijhydene.2019.04.075.

[87] L.O.O. da Costa, A.M. da Silva, F.B. Noronha, L.V. Mattos, The study of the performance of Ni supported on gadolinium doped ceria SOFC anode on the steam reforming of ethanol, International Journal of Hydrogen Energy. 37 (2012) 5930–5939. https://doi.org/10.1016/j.ijhydene.2012.01.008.

[88] S.D. Nobrega, M.V. Galesco, K. Girona, D.Z. de Florio, M.C. Steil, S. Georges, F.C. Fonseca, Direct ethanol solid oxide fuel cell operating in gradual internal reforming, Journal of Power Sources. 213 (2012) 156–159. https://doi.org/10.1016/j.jpowsour.2012.03.104.

[89] N.K. Monteiro, F.B. Noronha, L.O.O. da Costa, M. Linardi, F.C. Fonseca, A direct ethanol anode for solid oxide fuel cell based on a chromite-manganite with catalytic ruthenium nanoparticles, International Journal of Hydrogen Energy. 37 (2012) 9816–9829. https://doi.org/10.1016/j.ijhydene.2012.03.157.

[90] P. Vernoux, J. Guindet, M. Kleitz, Gradual Internal Methane Reforming in Intermediate-Temperature Solid-Oxide Fuel Cells, J. Electrochem. Soc. 145 (1998) 3487. https://doi.org/10.1149/1.1838832.

[91] S.D. Nobrega, P. Gelin, S. Georges, M.C. Steil, B.L. Augusto, F.B. Noronha, F.C. Fonseca, A Fuel-Flexible Solid Oxide Fuel Cell Operating in Gradual Internal Reforming, J. Electrochem. Soc. 161 (2014) F354. https://doi.org/10.1149/2.107403jes.

[92] L. Guerrero, S. Castilla, M. Cobo, Advances in ethanol reforming for the production of hydrogen, Quím. Nova. 37 (2014) 850–856.

[93] H. Yoshida, R. Yamaoka, M. Arai, Stable Hydrogen Production from Ethanol through Steam Reforming Reaction over Nickel-Containing Smectite-Derived Catalyst, Int J Mol Sci. 16 (2014) 350–362. https://doi.org/10.3390/ijms16010350.

[94] P. Zhang, Z. Yang, Y. Jin, C. Liu, Z. Lei, F. Chen, S. Peng, Progress report on the catalyst layers for hydrocarbon-fueled SOFCs, International Journal of Hydrogen Energy. 46 (2021) 39369–39386. https://doi.org/10.1016/j.ijhydene.2021.09.198.

[95] M. Liao, W. Wang, R. Ran, Z. Shao, Development of a Ni–$Ce_{0.8}Zr_{0.2}O_2$ catalyst for solid oxide fuel cells operating on ethanol through internal reforming, Journal of Power Sources. 196 (2011) 6177–6185. https://doi.org/10.1016/j.jpowsour.2011.03.018.

[96] V.A. Hackley, C.F. Ferraris, The use of nomenclature in dispersion science and technology, US Department of Commerce, Technology Administration, National Institute of Standards and Technology, 2001.

[97] C. Dhand, N. Dwivedi, X.J. Loh, A.N. Jie Ying, N.K. Verma, R.W. Beuerman, R. Lakshminarayanan, S. Ramakrishna, Methods and strategies for the synthesis of diverse nanoparticles and their applications: a comprehensive overview, RSC Adv. 5 (2015) 105003–105037. https://doi.org/10.1039/C5RA19388E.

[98] J.J. De Yoreo, P.G. Vekilov, Principles of Crystal Nucleation and Growth, Reviews in Mineralogy and Geochemistry. 54 (2003) 57–93. https://doi.org/10.2113/0540057.

[99] N.T.K. Thanh, N. Maclean, S. Mahiddine, Mechanisms of Nucleation and Growth of Nanoparticles in Solution, Chem. Rev. 114 (2014) 7610–7630. https://doi.org/10.1021/cr400544s.

[100] V.K. LaMer, R.H. Dinegar, Theory, Production and Mechanism of Formation of Monodispersed Hydrosols, J. Am. Chem. Soc. 72 (1950) 4847–4854. https://doi.org/10.1021/ja01167a001.

[101] M. Lin, Z.Y. Fu, H.R. Tan, J.P.Y. Tan, S.C. Ng, E. Teo, Hydrothermal Synthesis of CeO2 Nanocrystals: Ostwald Ripening or Oriented Attachment?, Crystal Growth & Design. 12 (2012) 3296–3303. https://doi.org/10.1021/cg300421x.

[102] H. Zhang, B. Yang, H. Li, C. Wu, W. Wang, B. Zhang, Q. Zhang, C. Zhang, Controllable Synthesis and Growth Mechanism of Ceria Nanocubes by Template-Free Hydrothermal Method, Crystal Research and Technology. 53 (2018) 1700233. https://doi.org/10.1002/crat.201700233.

[103] J.A. Marqusee, J. Ross, Theory of Ostwald ripening: Competitive growth and its dependence on volume fraction, The Journal of Chemical Physics. 80 (1998) 536. https://doi.org/10.1063/1.446427.

[104] D. Li, M.H. Nielsen, J.R.I. Lee, C. Frandsen, J.F. Banfield, J.J. De Yoreo, Direction-specific interactions control crystal growth by oriented attachment, Science. 336 (2012) 1014–1018. https://doi.org/10.1126/science.1219643.

[105] T. Taniguchi, K. Katsumata, S. Omata, K. Okada, N. Matsushita, Tuning Growth Modes of Ceria-Based Nanocubes by a Hydrothermal Method, Crystal Growth & Design. 11 (2011) 3754–3760. https://doi.org/10.1021/cg101585b.

[106] A. Layek, G. Mishra, A. Sharma, M. Spasova, S. Dhar, A. Chowdhury, R. Bandyopadhyaya, A Generalized Three-Stage Mechanism of ZnO Nanoparticle Formation in Homogeneous Liquid Medium, The Journal of Physical Chemistry C. 116 (2012) 24757–24769. https://doi.org/10.1021/jp211613b.

[107] Z. Shao, W. Zhou, Z. Zhu, Advanced synthesis of materials for intermediate-temperature solid oxide fuel cells, Progress in Materials Science. 57 (2012) 804–874. https://doi.org/10.1016/j.pmatsci.2011.08.002.

[108] G. Accardo, L. Spiridigliozzi, R. Cioffi, C. Ferone, E. Di Bartolomeo, S.P. Yoon, G. Dell'Agli, Gadolinium-doped ceria nanopowders synthesized by urea-based homogeneous co-precipitation (UBHP), Materials Chemistry and Physics. 187 (2017) 149–155. https://doi.org/10.1016/j.matchemphys.2016.11.060.

[109] O.S. Polezhaeva, N.V. Yaroshinskaya, V.K. Ivanov, Formation mechanism of nanocrystalline ceria in aqueous solutions of cerium(III) nitrate and

hexamethylenetetramine, Inorg Mater. 44 (2008) 51–57. https://doi.org/10.1134/S0020168508010081.

[110] P.-L. Chen, I.-W. Chen, Reactive Cerium(IV) Oxide Powders by the Homogeneous Precipitation Method, J American Ceramic Society. 76 (1993) 1577–1583. https://doi.org/10.1111/j.1151-2916.1993.tb03942.x.

[111] J.-G. Li, Y. Wang, T. Ikegami, T. Mori, T. Ishigaki, Reactive 10mol% RE_2O_3 (RE=Gd and Sm) doped CeO2 nanopowders: Synthesis, characterization, and low-temperature sintering into dense ceramics, Materials Science and Engineering: B. 121 (2005) 54–59. https://doi.org/10.1016/j.mseb.2005.03.001.

[112] M. Rafique, H. Nawaz, M. Shahid Rafique, M. Bilal Tahir, G. Nabi, N. r. Khalid, Material and method selection for efficient solid oxide fuel cell anode: Recent advancements and reviews, International Journal of Energy Research. 43 (2019) 2423–2446. https://doi.org/10.1002/er.4210.

[113] K. Wu, L.-D. Sun, C.-H. Yan, Recent Progress in Well-Controlled Synthesis of Ceria-Based Nanocatalysts towards Enhanced Catalytic Performance, Advanced Energy Materials. 6 (2016) 1600501. https://doi.org/10.1002/aenm.201600501.

[114] H.-X. Mai, L.-D. Sun, Y.-W. Zhang, R. Si, W. Feng, H.-P. Zhang, H.-C. Liu, C.-H. Yan, Shape-Selective Synthesis and Oxygen Storage Behavior of Ceria Nanopolyhedra, Nanorods, and Nanocubes, The Journal of Physical Chemistry B. 109 (2005) 24380–24385. https://doi.org/10.1021/jp055584b.

[115] C. Papadopoulos, K. Kappis, J. Papavasiliou, J. Vakros, M. Kuśmierz, W. Gac, Y. Georgiou, Y. Deligiannakis, G. Avgouropoulos, Copper-promoted ceria catalysts for CO oxidation reaction, Catalysis Today. 355 (2020) 647–653. https://doi.org/10.1016/j.cattod.2019.06.078.

[116] S. Yang, F. Zhou, Y. Liu, L. Zhang, Y. Chen, H. Wang, Y. Tian, C. Zhang, D. Liu, Morphology effect of ceria on the performance of CuO/CeO_2 catalysts for hydrogen production by methanol steam reforming, International Journal of Hydrogen Energy. 44 (2019) 7252–7261. https://doi.org/10.1016/j.ijhydene.2019.01.254.

[117] D. Pergolesi, E. Fabbri, A. D'Epifanio, E. Di Bartolomeo, A. Tebano, S. Sanna, S. Licoccia, G. Balestrino, E. Traversa, High proton conduction in grain-boundary-free yttrium-doped barium zirconate films grown by pulsed laser deposition, Nature Mater. 9 (2010) 846–852. https://doi.org/10.1038/nmat2837.

[118] F. Chiabrera, Interface Engineering in Mixed Ionic Electronic Conductor Thin Films for Solid State Devices, PhD thesis, University of Barcelona, 2019. www.tdx.cat.

[119] M. Morales, A. Pesce, A. Slodczyk, M. Torrell, P. Piccardo, D. Montinaro, A. Tarancón, A. Morata, Enhanced Performance of Gadolinia-Doped Ceria Diffusion Barrier Layers Fabricated by Pulsed Laser Deposition for Large-Area Solid Oxide Fuel Cells, ACS Appl. Energy Mater. 1 (2018) 1955–1964. https://doi.org/10.1021/acsaem.8b00039.

[120] P. Plonczak, A. Bieberle-Hütter, M. Søgaard, T. Ryll, J. Martynczuk, P.V. Hendriksen, L.J. Gauckler, Tailoring of $La_x Sr_{1-x} Co_y Fe_{1-y} O_{3-\delta}$ Nanostructure by Pulsed Laser Deposition, Adv. Funct. Mater. 21 (2011) 2764–2775. https://doi.org/10.1002/adfm.201100251.

[121] S. Ryu, S. Lee, W. Jeong, A. Pandiyan, S.B. Krishna Moorthy, I. Chang, T. Park, S.W. Cha, Pulsed laser deposition of BaCo0.4Fe0.4Zr0.1Y0.1O3-δ cathode for solid oxide fuel cells, Surface and Coatings Technology. 369 (2019) 265–268. https://doi.org/10.1016/j.surfcoat.2019.01.034.

[122] H.-S. Noh, J.-W. Son, H. Lee, H.-I. Ji, J.-H. Lee, H.-W. Lee, Suppression of Ni agglomeration in PLD fabricated Ni-YSZ composite for surface modification of SOFC anode, Journal of the European Ceramic Society. 30 (2010) 3415–3423. https://doi.org/10.1016/j.jeurceramsoc.2010.07.035.

[123] I. Garbayo, D. Pla, A. Morata, L. Fonseca, N. Sabaté, A. Tarancón, Full ceramic micro solid oxide fuel cells: towards more reliable MEMS power generators operating at high temperatures, Energy Environ. Sci. 7 (2014) 3617–3629. https://doi.org/10.1039/C4EE00748D.

[124] M. Jabbari, R. Bulatova, A.I.Y. Tok, C.R.H. Bahl, E. Mitsoulis, J.H. Hattel, Ceramic tape casting: A review of current methods and trends with emphasis on rheological behaviour and flow analysis, Materials Science and Engineering: B. 212 (2016) 39–61. https://doi.org/10.1016/j.mseb.2016.07.011.

[125] L.N. Rodrigues, Desenvolvimento de célula a combustível de óxido sólido pelo método de colagem de fita e co-sinterização, University of São Paulo, 2022.

[126] L.N. Rodrigues, M. Machado, L.P.R. Moraes, V.V. Thyssen, F.C. Fonseca, Development of Anode-Supported Solid Oxide Fuel Cell by Sequential Tape-Casting and Co-Sintering, Meet. Abstr. MA2021-03 (2021) 245–245. https://doi.org/10.1149/MA2021-031245mtgabs.

[127] S.-J.L. Kang, Sintering: Densification, Grain Growth and Microstructure, Elsevier, 2004.

[128] M.N. Rahaman, 2 - Kinetics and mechanisms of densification, in: Z.Z. Fang (Ed.), Sintering of Advanced Materials, Woodhead Publishing, 2010: pp. 33–64. https://doi.org/10.1533/9781845699949.1.33.

[129] M.F. Ashby, A first report on sintering diagrams, Acta Metallurgica. 22 (1974) 275–289. https://doi.org/10.1016/0001-6160(74)90167-9.

[130] J. Pan, H. LE, S. Kucherenko, J. Yeomans, A Model for Sintering of Spherical Particles of Different Sizes by Solid State Diffusion, Acta Materialia. 46 (1998) 4671–4690. https://doi.org/10.1016/S1359-6454(98)00144-X.

[131] R.L. Coble, Sintering Crystalline Solids. I. Intermediate and Final State Diffusion Models, Journal of Applied Physics. 32 (1961) 787–792. https://doi.org/10.1063/1.1736107.

[132] J.S. Moya, C. Baudín, P. Miranzo, Sintering, in: R.A. Meyers (Ed.), Encyclopedia of Physical Science and Technology (Third Edition), Academic Press, New York, 2003: pp. 865–878. https://doi.org/10.1016/B0-12-227410-5/00694-3.

[133] R.H.R. Castro, D. Gouvêa, Sintering and Nanostability: The Thermodynamic Perspective, Journal of the American Ceramic Society. 99 (2016) 1105–1121. https://doi.org/10.1111/jace.14176.

[134] D. Gouvea, R. Castro, Sintering: The Role of Interface Energies, Applied Surface Science - APPL SURF SCI. 217 (2003) 194–201. https://doi.org/10.1016/S0169-4332(03)00539-7.

[135] R.H.R. Castro, G.J. Pereira, D. Gouvêa, Surface modification of SnO_2 nanoparticles containing Mg or Fe: Effects on sintering, Applied Surface Science. 253 (2007) 4581–4585. https://doi.org/10.1016/j.apsusc.2006.10.010.

[136] R.H.R. Castro, Interfacial energies in nanocrystalline complex oxides, Current Opinion in Solid State and Materials Science. 25 (2021) 100911. https://doi.org/10.1016/j.cossms.2021.100911.

[137] H. Peng, Z. Jian, F. Liu, Review of thermo-kinetic correlation during grain growth in nanocrystalline materials, International Journal of Ceramic Engineering & Science. 2 (2020) 49–65. https://doi.org/10.1002/ces2.10040.

[138] Z. Gao, D. Kennouche, S.A. Barnett, Reduced-temperature firing of solid oxide fuel cells with zirconia/ceria bi-layer electrolytes, Journal of Power Sources. 260 (2014) 259–263. https://doi.org/10.1016/j.jpowsour.2014.03.025.

[139] S.L. Reis, E.C.C. Souza, E.N.S. Muccillo, Solid solution formation, densification and ionic conductivity of Gd- and Sm-doped ceria, Solid State Ionics. 192 (2011) 172–175. https://doi.org/10.1016/j.ssi.2010.06.017.

[140] V. Esposito, D.W. Ni, D. Marani, F. Teocoli, K.T. Sune Thydén, D.Z. De Florio, F.C. Fonseca, Accelerated ceria–zirconia solubilization by cationic diffusion inversion at low oxygen activity, Journal of Materials Chemistry A. 4 (2016) 16871–16878. https://doi.org/10.1039/C6TA06308J.

[141] J. Guerrero-Caballero, T. Kane, N. Haidar, L. Jalowiecki-Duhamel, A. Löfberg, Ni, Co, Fe supported on Ceria and Zr doped Ceria as oxygen carriers for chemical looping dry reforming of methane, Catalysis Today. 333 (2019) 251–258. https://doi.org/10.1016/j.cattod.2018.11.064.

[142] A. Sin, Preparation and sintering of $Ce_{1-x}Gd_xO_{2-x/2}$ nanopowders and their electrochemical and EPR characterization, Solid State Ionics. 175 (2004) 361–366. https://doi.org/10.1016/j.ssi.2004.03.034.

[143] J.-G. Cheng, S.-W. Zha, J. Huang, X.-Q. Liu, G.-Y. Meng, Sintering behavior and electrical conductivity of $Ce_{0.9}Gd_{0.1}O_{1.95}$ powder prepared by the gel-casting process, Materials Chemistry and Physics. 78 (2003) 791–795. https://doi.org/10.1016/S0254-0584(02)00384-X.

[144] L. Miao, J. Hou, K. Dong, W. Liu, A strategy for improving the sinterability and electrochemical properties of ceria-based LT-SOFCs using bismuth oxide additive, International Journal of Hydrogen Energy. 44 (2019) 5447–5453. https://doi.org/10.1016/j.ijhydene.2018.10.223.

[145] S. Taub, R.E.A. Williams, X. Wang, D.W. McComb, J.A. Kilner, A. Atkinson, The effects of transition metal oxide doping on the sintering of cerium gadolinium oxide, Acta Materialia. 81 (2014) 128–140. https://doi.org/10.1016/j.actamat.2014.06.041.

[146] V. Esposito, A. Kabir, M. Rosa, N.V. Nong, T.S. Rodrigues, L.N. Rodrigues, M.F.S. Machado, L.P.R. Moraes, D. Marani, F.C. Fonseca, Tuning diffusion paths in

shaped ceria nanocrystals, CrystEngComm. 21 (2019) 4025–4029. https://doi.org/10.1039/C9CE00414A.

[147] I. Shajahan, H.P. Dasari, P. Govardhan, Dilatometer studies of praseodymium doped ceria: Effect of synthesis methods on sintering behaviour, Materials Chemistry and Physics. 240 (2020) 122211. https://doi.org/10.1016/j.matchemphys.2019.122211.

[148] M.-F. Han, S. Zhou, Z. Liu, Z. Lei, Z.-C. Kang, Fabrication, sintering and electrical properties of cobalt oxide doped $Gd_{0.1}Ce_{0.9}O_{2-\delta}$, Solid State Ionics. 192 (2011) 181–184. https://doi.org/10.1016/j.ssi.2010.06.019.

[149] A.K. Baral, H.P. Dasari, B.-K. Kim, J.-H. Lee, Effect of sintering aid (CoO) on transport properties of nanocrystalline Gd doped ceria (GDC) materials prepared by co-precipitation method, Journal of Alloys and Compounds. 575 (2013) 455–460. https://doi.org/10.1016/j.jallcom.2013.05.191.

[150] J. Nicholas, L. Dejonghe, Prediction and evaluation of sintering aids for Cerium Gadolinium Oxide, Solid State Ionics. 178 (2007) 1187–1194. https://doi.org/10.1016/j.ssi.2007.05.019.

[151] T.H. Santos, J.P.F. Grilo, F.J.A. Loureiro, D.P. Fagg, F.C. Fonseca, D.A. Macedo, Structure, densification and electrical properties of Gd^{3+} and Cu^{2+} co-doped ceria solid electrolytes for SOFC applications: Effects of Gd_2O_3 content, Ceramics International. 44 (2018) 2745–2751. https://doi.org/10.1016/j.ceramint.2017.11.009.

[152] Y. Zheng, M. Zhou, L. Ge, S. Li, H. Chen, L. Guo, Effect of Fe_2O_3 on Sm-doped ceria system solid electrolyte for IT-SOFCs, Journal of Alloys and Compounds. 509 (2011) 546–550. https://doi.org/10.1016/j.jallcom.2010.09.103.

[153] C.J. Fu, Q.L. Liu, S.H. Chan, X.M. Ge, G. Pasciak, Effects of transition metal oxides on the densification of thin-film GDC electrolyte and on the performance of intermediate-temperature SOFC, Int. J. Hydrog. Energy. 35 (2010) 11200–11207. https://doi.org/10.1016/j.ijhydene.2010.07.049.

[154] J. Cheng, C. Tian, J. Yang, Effects of Fe2O3 addition on the electrical properties of SDC solid electrolyte ceramics, Journal of Materials Science: Materials in Electronics. 30 (2019) 16613–16620. https://doi.org/10.1007/s10854-019-02040-2.

[155] J.H. Choi, T. Lee, M. Choi, Y.-S. Yoo, S.-W. Baek, J. Bae, Long-term performance of anode-supported SOFC integrated with metal interconnect by joining process, International Journal of Hydrogen Energy. 35 (2010) 4285–4291. https://doi.org/10.1016/j.ijhydene.2010.02.062.

[156] H.J. Avila-Paredes, S. Kim, The effect of segregated transition metal ions on the grain boundary resistivity of gadolinium doped ceria: Alteration of the space charge potential, Solid State Ionics. 177 (2006) 3075–3080. https://doi.org/10.1016/j.ssi.2006.08.017.

[157] D. Pérez-Coll, P. Núñez, J.C.C. Abrantes, D.P. Fagg, V.V. Kharton, J.R. Frade, Effects of firing conditions and addition of Co on bulk and grain boundary properties of CGO, Solid State Ionics. 176 (2005) 2799–2805. https://doi.org/10.1016/j.ssi.2005.06.023.

[158] R.H.R. Castro, Controlling sintering and grain growth of nanoceramics, Cerâmica. 65 (2019) 122–129. https://doi.org/10.1590/0366-69132019653732573.

[159] P. Wynblatt, G.S. Rohrer, F. Papillon, Grain boundary segregation in oxide ceramics, Journal of the European Ceramic Society. 23 (2003) 2841–2848. https://doi.org/10.1016/S0955-2219(03)00308-X.

[160] A.L. da Silva, D.N.F. Muche, L.B. Caliman, J. Bettini, R.H.R. Castro, A. Navrotsky, D. Gouvêa, TiO_2 Surface Engineering to Improve Nanostability: The Role of Interface Segregation, The Journal of Physical Chemistry C. 123 (2019) 4949–4960. https://doi.org/10.1021/acs.jpcc.8b12160.

[161] M.F.S. Machado, L.P.R. Moraes, N.K. Monteiro, V. Esposito, D.Z. de Florio, D. Marani, F.C. Fonseca, Low Temperature Synthesis and Properties of Gadolinium-Doped Cerium Oxide Nanoparticles, ECS Transactions. 78 (2017) 387–394. https://doi.org/10.1149/07801.0387ecst.

[162] D.C.O.S. Neves, A.L. da Silva, R.C. de Oliveira Romano, D. Gouvêa, Fe_2O_3-doped SnO_2 membranes with enhanced mechanical resistance for ultrafiltration application, Journal of the European Ceramic Society. 40 (2020) 5959–5966. https://doi.org/10.1016/j.jeurceramsoc.2020.06.077.

[163] A.L. Da Silva, L. Wu, L.B. Caliman, R.H.R. Castro, A. Navrotsky, D. Gouvêa, Energetics of CO_2 and H_2O adsorption on alkaline earth metal doped TiO2, Physical Chemistry Chemical Physics. 22 (2020) 15600–15607. https://doi.org/10.1039/d0cp01787f.

[164] A.L. da Silva, D. Hotza, R.H.R. Castro, Surface energy effects on the stability of anatase and rutile nanocrystals: A predictive diagram for Nb2O5-doped-TiO2, Applied Surface Science. 393 (2017) 103–109. https://doi.org/10.1016/j.apsusc.2016.09.126.

[165] L. Wu, S. Dey, M. Gong, F. Liu, R.H.R. Castro, Surface segregation on manganese doped ceria nanoparticles and relationship with nanostability, Journal of Physical Chemistry C. 118 (2014) 30187–30196. https://doi.org/10.1021/jp508663p.

[166] A.A. Bernardes, L.B. Caliman, A.L. da Silva, J. Bettini, K.L. Guimarães, D. Gouvea, Li_2O-doped $MgAl_2O_4$ nanopowders: Energetics of interface segregation, Journal of the American Ceramic Society. 103 (2020) 2835–2844. https://doi.org/10.1111/jace.16942.

[167] H. Zhang, J.F. Banfield, Structural characteristics and mechanical and thermodynamic properties of nanocrystalline TiO2, Chemical Reviews. 114 (2014) 9613–9644. https://doi.org/10.1021/cr500072j.

[168] D. Gouvêa, D.C.C. do Rosário, L.B. Caliman, Surface and grain-boundary excess of ZnO-doped SnO_2 nanopowders by the selective lixiviation method, Journal of the American Ceramic Society. 100 (2017) 4331–4340. https://doi.org/10.1111/jace.14973.

[169] R.H.R. Castro, On the thermodynamic stability of nanocrystalline ceramics, Materials Letters. 96 (2013) 45–56. https://doi.org/10.1016/j.matlet.2013.01.007.

[170] R.H.R. Castro, D. Gouvêa, Sintering and Nanostability: The Thermodynamic Perspective, Journal of the American Ceramic Society. 99 (2016) 1105–1121. https://doi.org/10.1111/jace.14176.

[171] B. Cela, D.A. De MacEdo, G.L. De Souza, A.E. Martinelli, R.M. Do Nascimento, C.A. Paskocimas, NiO-CGO in situ nanocomposite attainment: One step synthesis, Journal of Power Sources. 196 (2011) 2539–2544. https://doi.org/10.1016/j.jpowsour.2010.11.026.

[172] Z. Wang, Y. Zeng, C. Li, Z. Ye, L. Cao, Y. Zhang, Structures and electrical conductivities of Gd^{3+} and Fe^{3+} co-doped cerium oxide electrolytes sintered at low temperature for ILT-SOFCs, Ceramics International. 44 (2018) 10328–10334. https://doi.org/10.1016/j.ceramint.2018.03.041.

[173] K. Neuhaus, R. Dolle, H.-D. Wiemhöfer, The Effect of Transition Metal Oxide Addition on the Conductivity of Commercially Available Gd-Doped Ceria, Journal of The Electrochemical Society. 167 (2020) 044507. https://doi.org/10.1149/1945-7111/ab729b.

[174] R.A.M.P. de Oliveira, A.L. da Silva, L.B. Caliman, D. Gouvêa, Interface excess on Li_2O-doped γ-Al_2O_3 nanoparticles, Ceramics International. 46 (2020) 10555–10560. https://doi.org/10.1016/j.ceramint.2020.01.057.

[175] V. Esposito, D.W. Ni, Z. He, W. Zhang, A.S. Prasad, J.A. Glasscock, C. Chatzichristodoulou, S. Ramousse, A. Kaiser, Enhanced mass diffusion phenomena in highly defective doped ceria, Acta Materialia. 61 (2013) 6290–6300. https://doi.org/10.1016/j.actamat.2013.07.012.

[176] R.L. Coble, Sintering Crystalline Solids. I. Intermediate and Final State Diffusion Models, Journal of Applied Physics. 32 (1961) 787–792. https://doi.org/10.1063/1.1736107.

[177] D.N.F. Muche, A.L. da Silva, K. Nakajima, D. Gouvêa, R.H.R. Castro, Simultaneous segregation of lanthanum to surfaces and grain boundaries in MgAl2O4 nanocrystals, Applied Surface Science. 529 (2020) 147145. https://doi.org/10.1016/j.apsusc.2020.147145.

[178] F. Liu, R. Kirchheim, Nano-scale grain growth inhibited by reducing grain boundary energy through solute segregation, Journal of Crystal Growth. 264 (2004) 385–391. https://doi.org/10.1016/j.jcrysgro.2003.12.021.

[179] D. Pérez-Coll, E. Sánchez-López, G.C. Mather, Influence of porosity on the bulk and grain-boundary electrical properties of Gd-doped ceria, Solid State Ionics. 181 (2010) 1033–1042. https://doi.org/10.1016/J.SSI.2010.06.006.

[180] V. V. Kharton, A. V. Kovalevsky, A.P. Viskup, A.L. Shaula, F.M. Figueiredo, E.N. Naumovich, F.M.B. Marques, Oxygen transport in $Ce_{0.8}Gd_{0.2}O_{2-\delta}$-based composite membranes, Solid State Ionics. 160 (2003) 247–258. https://doi.org/10.1016/S0167-2738(03)00183-8.

[181] D.P. Fagg, V. V Kharton, J.R. Frade, P-Type Electronic Transport in $Ce_{0.8}Gd_{0.2}O_{2-\delta}$: The Effect of Transition Metal Oxide Sintering Aids, Journal of Electroceramics. 9 (2002) 199–207. https://doi.org/10.1023/A:1023269326651.

[182] P. Sudarsan, S.B. Krishnamoorthy, Grain boundary scavenging through reactive sintering of strontium and iron in samarium doped ceria electrolyte for ITSOFC applications, Materials Research Bulletin. 100 (2018) 446–457. https://doi.org/10.1016/J.MATERRESBULL.2017.12.047.

[183] H. Inaba, Ceria-based solid electrolytes, Solid State Ionics. 83 (1996) 1–16. https://doi.org/10.1016/0167-2738(95)00229-4.

[184] W. Lai, S.M. Haile, Impedance Spectroscopy as a Tool for Chemical and Electrochemical Analysis of Mixed Conductors: A Case Study of Ceria, Journal of the American Ceramic Society. 88 (2005) 2979–2997. https://doi.org/10.1111/J.1551-2916.2005.00740.X.

[185] S. Wang, T. Kobayashi, M. Dokiya, T. Hashimoto, Electrical and Ionic Conductivity of Gd-Doped Ceria, Journal of The Electrochemical Society. 147 (2000) 3606. https://doi.org/10.1149/1.1393946.

[186] S. Taub, K. Neuhaus, H.D. Wiemhöfer, N. Ni, J.A. Kilner, A. Atkinson, The effects of Co and Cr on the electrical conductivity of cerium gadolinium oxide, Solid State Ionics. 282 (2015) 54–62. https://doi.org/10.1016/J.SSI.2015.09.024.

[187] Y. Xu, S.S. Mofarah, R. Mehmood, C. Cazorla, P. Koshy, C.C. Sorrell, Design strategies for ceria nanomaterials: untangling key mechanistic concepts, Mater. Horiz. 8 (2021) 102–123. https://doi.org/10.1039/D0MH00654H.

[188] Y. Wang, Q. Shen, Y. Tong, Z. Zhan, Investigation of Ni^{2+}-doped ceria nanorods as the anode catalysts for reduced-temperature solid oxide fuel cells, International Journal of Hydrogen Energy. 47 (2022) 6827–6836. https://doi.org/10.1016/j.ijhydene.2021.12.012.

[189] H. Inaba, T. Nakajima, H. Tagawa, Sintering behaviors of ceria and gadolinia-doped ceria, Solid State Ionics. 106 (1998) 263–268. https://doi.org/10.1016/S0167-2738(97)00496-7.

[190] R. Mehmood, X. Wang, P. Koshy, J.L. Yang, C.C. Sorrell, Engineering oxygen vacancies through construction of morphology maps for bio-responsive nanoceria for osteosarcoma therapy, CrystEngComm. 20 (2018) 1536–1545. https://doi.org/10.1039/C8CE00001H.

[191] L. Torrente-Murciano, A. Gilbank, B. Puertolas, T. Garcia, B. Solsona, D. Chadwick, Shape-dependency activity of nanostructured CeO2 in the total oxidation of polycyclic aromatic hydrocarbons, Applied Catalysis B: Environmental. 132–133 (2013) 116–122. https://doi.org/10.1016/j.apcatb.2012.10.030.

[192] Özden Çelikbilek, E. Siebert, D. Jauffrès, C.L. Martin, E. Djurado, Influence of sintering temperature on morphology and electrochemical performance of LSCF/GDC composite films as efficient cathode for SOFC, Electrochimica Acta. 246 (2017) 1248–1258. https://doi.org/10.1016/j.electacta.2017.06.070.

[193] N. Hildenbrand, B.A. Boukamp, P. Nammensma, D.H.A. Blank, Improved cathode/electrolyte interface of SOFC, Solid State Ionics. 192 (2011) 12–15. https://doi.org/10.1016/j.ssi.2010.01.028.

[194] C. Xia, M. Liu, Microstructures, conductivities, and electrochemical properties of $Ce_{0.9}Gd_{0.1}O_2$ and GDC–Ni anodes for low-temperature SOFCs, Solid State Ionics. 152–153 (2002) 423–430. https://doi.org/10.1016/S0167-2738(02)00381-8.

[195] V.A. Rojek-Wöckner, A.K. Opitz, M. Brandner, J. Mathé, M. Bram, A novel Ni/ceria-based anode for metal-supported solid oxide fuel cells, Journal of Power Sources. 328 (2016) 65–74. https://doi.org/10.1016/j.jpowsour.2016.07.075.

[196] N. Oishi, A. Atkinson, N.P. Brandon, J.A. Kilner, B.C.H. Steele, Fabrication of an Anode-Supported Gadolinium-Doped Ceria Solid Oxide Fuel Cell and Its Operation at 550°C, Journal of the American Ceramic Society. 88 (2005) 1394–1396. https://doi.org/10.1111/j.1551-2916.2005.00251.x.

[197] B. Farrell, S. Linic, Direct electrochemical oxidation of ethanol on SOFCs: Improved carbon tolerance of Ni anode by alloying, Applied Catalysis B: Environmental. 183 (2016) 386–393. https://doi.org/10.1016/j.apcatb.2015.11.002.

[198] S.D. Nobrega, M.V. Galesco, K. Girona, D.Z. de Florio, M.C. Steil, S. Georges, F.C. Fonseca, Direct ethanol solid oxide fuel cell operating in gradual internal reforming, Journal of Power Sources. 213 (2012) 156–159. https://doi.org/10.1016/j.jpowsour.2012.03.104.

[199] M.D. Zhurka, A.A. Lemonidou, P.N. Kechagiopoulos, Elucidation of metal and support effects during ethanol steam reforming over Ni and Rh based catalysts supported on (CeO_2)-ZrO_2-La_2O_3, Catalysis Today. 368 (2021) 161–172. https://doi.org/10.1016/j.cattod.2020.03.020.

[200] T. Hou, B. Yu, S. Zhang, T. Xu, D. Wang, W. Cai, Hydrogen production from ethanol steam reforming over Rh/CeO_2 catalyst, Catalysis Communications. 58 (2015) 137–140. https://doi.org/10.1016/j.catcom.2014.09.020.

[201] Y.C. Sharma, A. Kumar, R. Prasad, S.N. Upadhyay, Ethanol steam reforming for hydrogen production: Latest and effective catalyst modification strategies to minimize carbonaceous deactivation, Renewable and Sustainable Energy Reviews. 74 (2017) 89–103. https://doi.org/10.1016/j.rser.2017.02.049.

[202] S. Ogo, Y. Sekine, Recent progress in ethanol steam reforming using non-noble transition metal catalysts: A review, Fuel Process. Technol. 199 (2020) 106238. https://doi.org/10.1016/j.fuproc.2019.106238.

[203] M. Greluk, W. Gac, M. Rotko, G. Słowik, S. Turczyniak-Surdacka, Co/CeO2 and Ni/CeO_2 catalysts for ethanol steam reforming: Effect of the cobalt/nickel dispersion on catalysts properties, Journal of Catalysis. 393 (2021) 159–178. https://doi.org/10.1016/j.jcat.2020.11.009.

[204] G.R. Ferreira, F.G.E. Nogueira, A.F. Lucrédio, E.M. Assaf, Ethanol Steam Reforming by Ni Catalysts for H2 Production: Evaluation of Gd Effect in CeO_2 Support, Catal Lett. (2022). https://doi.org/10.1007/s10562-021-03875-3.

[205] D.G. Araiza, A. Gómez-Cortés, G. Díaz, Effect of ceria morphology on the carbon deposition during steam reforming of ethanol over Ni/CeO_2 catalysts, Catalysis Today. 349 (2020) 235–243. https://doi.org/10.1016/j.cattod.2018.03.016.

[206] X. Du, D. Zhang, L. Shi, R. Gao, J. Zhang, Morphology dependence of catalytic properties of Ni/CeO_2 nanostructures for carbon dioxide reforming of methane, Journal of Physical Chemistry C. 116 (2012) 10009–10016. https://doi.org/10.1021/jp300543r.

[207] I.I. Soykal, B. Bayram, H. Sohn, P. Gawade, J.T. Miller, U.S. Ozkan, Ethanol steam reforming over Co/CeO_2 catalysts: Investigation of the effect of ceria morphology, Applied Catalysis A: General. 449 (2012) 47–58. https://doi.org/10.1016/j.apcata.2012.09.038.

[208] S. Anelli, F. Baiutti, A. Hornés, L. Bernadet, M. Torrell, A. Tarancón, Improved mesostructured oxygen electrodes for highly performing solid oxide cells for co-electrolysis of steam and carbon dioxide, J. Mater. Chem. A. 7 (2019) 27458–27468. https://doi.org/10.1039/C9TA07373F.

[209] W. Shi, S. Song, H. Zhang, Hydrothermal synthetic strategies of inorganic semiconducting nanostructures, Chemical Society Reviews. 42 (2013) 5714. https://doi.org/10.1039/c3cs60012b.

[210] C08 Committee, Test Methods for Apparent Porosity, Water Absorption, Apparent Specific Gravity, and Bulk Density of Burned Refractory Brick and Shapes by Boiling Water, ASTM International. https://doi.org/10.1520/C0020-00R22.

[211] F.C. Fonseca, D.Z. de Florio, V. Esposito, E. Traversa, E.N.S. Muccillo, R. Muccillo, Mixed Ionic–Electronic YSZ/Ni Composite for SOFC Anodes with High Electrical Conductivity, Journal of The Electrochemical Society. 153 (2006) A354. https://doi.org/10.1149/1.2149312.

[212] V. Esposito, D.Z. de Florio, F.C. Fonseca, E.N.S. Muccillo, R. Muccillo, E. Traversa, Electrical properties of YSZ/NiO composites prepared by a liquid mixture technique, Journal of the European Ceramic Society. 25 (2005) 2637–2641. https://doi.org/10.1016/j.jeurceramsoc.2005.03.116.

[213] S. Anelli, Advanced strategies for Solid Oxide Electrolysis cell, PhD thesis, Universitat Autonoma de Barcelona, n.d. https://www.tesisenred.net/.

[214] Z. Liu, X. Li, M. Mayyas, P. Koshy, J.N. Hart, C.C. Sorrell, Growth mechanism of ceria nanorods by precipitation at room temperature and morphology-dependent photocatalytic performance, CrystEngComm. 19 (2017) 4766–4776. https://doi.org/10.1039/C7CE00922D.

[215] C. Dong, Y. Zhou, N. Ta, W. Shen, Formation mechanism and size control of ceria nanocubes, CrystEngComm. 22 (2020) 3033–3041. https://doi.org/10.1039/D0CE00224K.

[216] JoséC. Conesa, Computer modeling of surfaces and defects on cerium dioxide, Surface Science. 339 (1995) 337–352. https://doi.org/10.1016/0039-6028(95)00595-1.

[217] O.S. Bezkrovnyi, P. Kraszkiewicz, M. Ptak, L. Kepinski, Thermally induced reconstruction of ceria nanocubes into zigzag {111}-nanofacetted structures and its influence on catalytic activity in CO oxidation, Catalysis Communications. 117 (2018) 94–98. https://doi.org/10.1016/j.catcom.2018.08.005.

[218] M. Fronzi, A. Soon, B. Delley, E. Traversa, C. Stampfl, Stability and morphology of cerium oxide surfaces in an oxidizing environment: A first-principles investigation, The Journal of Chemical Physics. 131 (2009) 104701. https://doi.org/10.1063/1.3191784.

[219] X. Wang, Z. Zak Fang, M. Koopman, The relationship between the green density and as-sintered density of nano-tungsten compacts, International Journal of Refractory Metals and Hard Materials. 53 (2015) 134–138. https://doi.org/10.1016/j.ijrmhm.2015.07.006.

[220] P.-L. Chen, I.-W. Chen, Sintering of Fine Oxide Powders: I, Microstructural Evolution, Journal of the American Ceramic Society. 79 (1996) 3129–3141. https://doi.org/10.1111/j.1151-2916.1996.tb08087.x.

[221] F. Baumann, J. Fleig, H. Habermeier, J. Maier, Impedance spectroscopic study on well-defined (La,Sr)(Co,Fe)$O_{3-\delta}$ model electrodes, Solid State Ionics. 177 (2006) 1071–1081. https://doi.org/10.1016/j.ssi.2006.02.045.

[222] E. Perry Murray, Electrochemical performance of (La,Sr)(Co,Fe)O_3–(Ce,Gd)O_3 composite cathodes, Solid State Ionics. 148 (2002) 27–34. https://doi.org/10.1016/S0167-2738(02)00102-9.

[223] E. Hernández, F. Baiutti, A. Morata, M. Torrell, A. Tarancón, Infiltrated mesoporous oxygen electrodes for high temperature co-electrolysis of H_2O and CO_2 in solid oxide electrolysis cells, Journal of Materials Chemistry A. 6 (2018) 9699–9707. https://doi.org/10.1039/C8TA01045E.

[224] M.J. Jørgensen, M. Mogensen, Impedance of Solid Oxide Fuel Cell LSM/YSZ Composite Cathodes, J. Electrochem. Soc. 148 (2001) A433. https://doi.org/10.1149/1.1360203.

[225] J.R. McBride, K.C. Hass, B.D. Poindexter, W.H. Weber, Raman and x-ray studies of $Ce_{1-x}RE_xO_{2-y}$, where RE=La, Pr, Nd, Eu, Gd, and Tb, Journal of Applied Physics. 76 (1994) 2435–2441. https://doi.org/10.1063/1.357593.

[226] S. Loridant, Raman spectroscopy as a powerful tool to characterize ceria-based catalysts, Catalysis Today. 373 (2021) 98–111. https://doi.org/10.1016/j.cattod.2020.03.044.

[227] I. Kosacki, T. Suzuki, V. Petrovsky, H.U. Anderson, P. Colomban, Lattice defects in nanocrystalline CeO_2 thin films, Radiation Effects and Defects in Solids. 156 (2001) 109–115. https://doi.org/10.1080/10420150108216880.

[228] H.S. Roh, K.W. Jun, W.S. Dong, J.S. Chang, S.E. Park, Y.I. Joe, Highly active and stable Ni/Ce-ZrO_2 catalyst for H_2 production from methane, Journal of Molecular Catalysis A: Chemical. 181 (2002) 137–142. https://doi.org/10.1016/S1381-1169(01)00358-2.

[229] H.C. Yao, Y.F.Y. Yao, Ceria in automotive exhaust catalysts: I. Oxygen storage, Journal of Catalysis. 86 (1984) 254–265. https://doi.org/10.1016/0021-9517(84)90371-3.

[230] A.G.M. Silva, T.S. Rodrigues, A. Dias, H.V. Fajardo, R.F. Gonçalves, M. Godinho, P.A. Robles-Dutenhefner, $Ce_{1-x}Sm_xO_{1.9-\delta}$ nanoparticles obtained by microwave-

assisted hydrothermal processing: an efficient application for catalytic oxidation of α-bisabolol, Catal. Sci. Technol. 4 (2014) 814. https://doi.org/10.1039/c3cy00788j.

[231] I.I. Soykal, H. Sohn, U.S. Ozkan, Effect of Support Particle Size in Steam Reforming of Ethanol over Co/CeO_2 Catalysts, ACS Catal. 2 (2012) 2335–2348. https://doi.org/10.1021/cs3004159.

[232] G. Shi, Q. Chen, Q. Zhang, W. Cai, Z. Li, S. Zhai, H. Yu, F. Tan, Y. Wang, Morphology effect of ZnO support on the performance of Cu toward methanol production from CO2 hydrogenation, Journal of Saudi Chemical Society. 24 (2020) 42–51. https://doi.org/10.1016/j.jscs.2019.09.002.

[233] A.L. Alberton, M.M.V.M. Souza, M. Schmal, Carbon formation and its influence on ethanol steam reforming over Ni/Al_2O_3 catalysts, Catalysis Today. 123 (2007) 257–264. https://doi.org/10.1016/j.cattod.2007.01.062.

[234] L.V. Mattos, F.B. Noronha, Hydrogen production for fuel cell applications by ethanol partial oxidation on Pt/CeO_2 catalysts: the effect of the reaction conditions and reaction mechanism, Journal of Catalysis. 233 (2005) 453–463. https://doi.org/10.1016/j.jcat.2005.04.022.

[235] P. Plonczak, M. Joost, J. Hjelm, M. Søgaard, M. Lundberg, P.V. Hendriksen, A high performance ceria based interdiffusion barrier layer prepared by spin-coating, Journal of Power Sources. 196 (2011) 1156–1162. https://doi.org/10.1016/j.jpowsour.2010.08.108.

[236] L. dos Santos-Gómez, J. Hurtado, J.M. Porras-Vázquez, E.R. Losilla, D. Marrero-López, Durability and performance of CGO barriers and LSCF cathode deposited by spray-pyrolysis, Journal of the European Ceramic Society. 38 (2018) 3518–3526. https://doi.org/10.1016/j.jeurceramsoc.2018.03.024.

[237] Z. Gao, V.Y. Zenou, D. Kennouche, L. Marks, S.A. Barnett, Solid oxide cells with zirconia/ceria Bi-Layer electrolytes fabricated by reduced temperature firing, J. Mater. Chem. A. 3 (2015) 9955–9964. https://doi.org/10.1039/C5TA01964H.

[238] L. Bernadet, C. Moncasi, M. Torrell, A. Tarancón, High-performing electrolyte-supported symmetrical solid oxide electrolysis cells operating under steam electrolysis and co-electrolysis modes, International Journal of Hydrogen Energy. 45 (2020) 14208–14217. https://doi.org/10.1016/j.ijhydene.2020.03.144.

[239] J. Kim, Characterization of LSM–YSZ composite electrode by ac impedance spectroscopy, Solid State Ionics. 143 (2001) 379–389. https://doi.org/10.1016/S0167-2738(01)00877-3.

[240] S. Carter, A. Selcuck, R.J. Chater, J. Kajda, J.A. Kilner, B.C.H. Steele, Oxygen transport in selected nonstoichiometric perovskite-structure oxides, Solid State Ionics. 53–56 (1992) 597–605. https://doi.org/10.1016/0167-2738(92)90435-R.

[241] E. Ivers-Tiffée, A. Weber, D. Herbstritt, Materials and technologies for SOFC-components, Journal of the European Ceramic Society. 21 (2001) 1805–1811. https://doi.org/10.1016/S0955-2219(01)00120-0.

[242] J. Lane, J.A. Kilner, Oxygen surface exchange on gadolinia doped ceria, Solid State Ionics. 136–137 (2000) 927–932. https://doi.org/10.1016/S0167-2738(00)00530-0.

[243] Q. Su, D. Yoon, Z. Sisman, F. Khatkhatay, Q. Jia, A. Manthiram, H. Wang, Vertically aligned nanocomposite $La_{0.8}Sr_{0.2}MnO_{3-\delta}/Zr_{0.92}Y_{0.08}O_{1.96}$ thin films as electrode/electrolyte interfacial layer for solid oxide reversible fuel cells, International Journal of Hydrogen Energy. 38 (2013) 16320–16327. https://doi.org/10.1016/j.ijhydene.2013.09.128.

[244] K. Develos-Bagarinao, J. De Vero, H. Kishimoto, T. Ishiyama, K. Yamaji, T. Horita, H. Yokokawa, Multilayered LSC and GDC: An approach for designing cathode materials with superior oxygen exchange properties for solid oxide fuel cells, Nano Energy. 52 (2018) 369–380. https://doi.org/10.1016/j.nanoen.2018.08.014.

[245] W. Ma, J.J. Kim, N. Tsvetkov, T. Daio, Y. Kuru, Z. Cai, Y. Chen, K. Sasaki, H.L. Tuller, B. Yildiz, Vertically aligned nanocomposite $La_{0.8}\ Sr_{0.2}CoO_3$ /$(La_{0.5}Sr_{0.5})_2CoO_4$ cathodes – electronic structure, surface chemistry and oxygen reduction kinetics, J. Mater. Chem. A. 3 (2015) 207–219. https://doi.org/10.1039/C4TA04993D.

[246] Q. Su, D. Yoon, Y.N. Kim, W. Gong, A. Chen, S. Cho, A. Manthiram, A.J. Jacobson, H. Wang, Effects of interlayer thickness on the electrochemical and mechanical properties of bi-layer cathodes for solid oxide fuel cells, Journal of Power Sources. 218 (2012) 261–267. https://doi.org/10.1016/j.jpowsour.2012.06.094.

[247] J.C. De Vero, K. Develos-Bagarinao, H. Kishimoto, T. Ishiyama, K. Yamaji, T. Horita, H. Yokokawa, Enhanced stability of solid oxide fuel cells by employing a modified cathode-interlayer interface with a dense $La_{0.6}\ Sr_{0.4}Co_{0.2}Fe_{0.8}O_{3-\delta}$ thin film, Journal of Power Sources. 377 (2018) 128–135. https://doi.org/10.1016/j.jpowsour.2017.12.010.

[248] L. dos Santos-Gómez, S. Sanna, P. Norby, N. Pryds, E.R. Losilla, D. Marrero-López, V. Esposito, Electrochemical stability of $(La,Sr)CoO_{3-\delta}$ in $(La,Sr)CoO_{3-\delta}$ /$(Ce, Gd)O_{2-\delta}$ heterostructures, Nanoscale. 11 (2019) 2916–2924. https://doi.org/10.1039/C8NR08528E.

[249] F. Baiutti, F. Chiabrera, M. Acosta, D. Diercks, D. Parfitt, J. Santiso, X. Wang, A. Cavallaro, A. Morata, H. Wang, A. Chroneos, J. MacManus-Driscoll, A. Tarancon, A high-entropy manganite in an ordered nanocomposite for long-term application in solid oxide cells, Nat Commun. 12 (2021) 2660. https://doi.org/10.1038/s41467-021-22916-4.

[250] L. Yan, K.R. Balasubramaniam, S. Wang, H. Du, P.A. Salvador, Effects of crystallographic orientation on the oxygen exchange rate of $La_{0.7}Sr_{0.3}MnO_3$ thin films, Solid State Ionics. 194 (2011) 9–16. https://doi.org/10.1016/j.ssi.2011.05.004.

[251] J. Huang, J.L. MacManus-Driscoll, H. Wang, New epitaxy paradigm in epitaxial self-assembled oxide vertically aligned nanocomposite thin films, Journal of Materials Research. 32 (2017) 4054–4066. https://doi.org/10.1557/jmr.2017.281.

[252] J.T.S. Irvine, D. Neagu, M.C. Verbraeken, C. Chatzichristodoulou, C. Graves, M.B. Mogensen, Evolution of the electrochemical interface in high-temperature fuel cells

and electrolysers, Nat Energy. 1 (2016) 15014. https://doi.org/10.1038/nenergy.2015.14.

[253] A. Esquirol, N.P. Brandon, J.A. Kilner, M. Mogensen, Electrochemical Characterization of $La_{0.6}Sr0.{}_4Co_{0.2}Fe_{0.8}O_3$ Cathodes for Intermediate-Temperature SOFCs, J. Electrochem. Soc. 151 (2004) A1847. https://doi.org/10.1149/1.1799391.

[254] S. Jiang, A comparison of O2 reduction reactions on porous (La,Sr)MnO3 and (La,Sr)(Co,Fe)O3 electrodes, Solid State Ionics. 146 (2002) 1–22. https://doi.org/10.1016/S0167-2738(01)00997-3.

[255] W.-H. Kim, H.-S. Song, J. Moon, H.-W. Lee, Intermediate temperature solid oxide fuel cell using (La,Sr)(Co,Fe)O_3-based cathodes, Solid State Ionics. 177 (2006) 3211–3216. https://doi.org/10.1016/j.ssi.2006.07.049.

[256] G.J. la O', R.F. Savinell, Y. Shao-Horn, Activity Enhancement of Dense Strontium-Doped Lanthanum Manganite Thin Films under Cathodic Polarization: A Combined AES and XPS Study, J. Electrochem. Soc. 156 (2009) B771. https://doi.org/10.1149/1.3116228.

[257] M. Backhaus-Ricoult, K. Adib, T. St.Clair, B. Luerssen, L. Gregoratti, A. Barinov, In-situ study of operating SOFC LSM/YSZ cathodes under polarization by photoelectron microscopy, Solid State Ionics. 179 (2008) 891–895. https://doi.org/10.1016/j.ssi.2008.02.033.

[258] H. Mitsuyasu, Y. Nonaka, K. Eguchi, Analysis of solid state reaction at the interface of yttria-doped ceria/yttria-stabilized zirconia, Solid State Ionics. 113–115 (1998) 279–284. https://doi.org/10.1016/S0167-2738(98)00293-8.

[259] F.G.E. Jones, J.T.S. Irvine, Preparation of thin films using the tape-casting process for use in the solid oxide fuel cell, Ionics. 8 (2002) 339–343. https://doi.org/10.1007/BF02376046.

[260] M. Boaro, J.M. Vohs, R.J. Gorte, Synthesis of Highly Porous Yttria-Stabilized Zirconia by Tape-Casting Methods, Journal of the American Ceramic Society. 86 (2003) 395–400. https://doi.org/10.1111/j.1151-2916.2003.tb03311.x.

[261] M. Cassidy, P. Connor, M. Etches, Y. Kalecheff, M. Machado, J. Nairn, J. Irvine, Thick Film Processing Challenges in the Realisation of a Co-Fired Solid Oxide Fuel Cell Roll, Advances in Science and Technology. 87 (2014) 98–104. https://doi.org/10.4028/www.scientific.net/AST.87.98.

[262] N.H. Menzler, J. Malzbender, P. Schoderböck, R. Kauert, H.P. Buchkremer, Sequential Tape Casting of Anode-Supported Solid Oxide Fuel Cells, Fuel Cells. 14 (2014) 96–106. https://doi.org/10.1002/fuce.201300153.

[263] M. Cassidy, M. Machado, J. Nairn, C. Ni, J.T.S. Irvine, Co-fired SOFC Roll Support with Impregnated Catalysts Produced by Sequential Tape Casting, in: A1102, Lucerne, Switzerland, 2014.

[264] C. Ni, Optimisation and testing of large ceramic-impregnated solid oxide fuel cells (SOFCs), PhD Doctor of Philosophy, University of St Andrews, 2015.

[265] S.D. da Nobrega, N.K. Monteiro, F. Tabuti, D.Z. de Florio, F.C. Fonseca, Optimization of spin-coated electrodes for electrolyte-supported solid oxide fuel cells, Matéria (Rio de Janeiro). 22 (2017). https://doi.org/10.1590/s1517-707620170001.0136.

[266] G. Zhang, M. Wen, S. Wang, J. Chen, J. Wang, Insights into thermal reduction of the oxidized graphite from the electro-oxidation processing of nuclear graphite matrix, RSC Advances. 8 (2018) 567–579. https://doi.org/10.1039/C7RA11578D.

[267] M. Chen, B.H. Kim, Q. Xu, O.J. Nam, J.H. Ko, Synthesis and performances of Ni–SDC cermets for IT-SOFC anode, Journal of the European Ceramic Society. 28 (2008) 2947–2953. https://doi.org/10.1016/j.jeurceramsoc.2008.05.009.

[268] A. Atkinson, S. Barnett, R.J. Gorte, J.T.S. Irvine, A.J. McEvoy, M. Mogensen, S.C. Singhal, J. Vohs, Advanced anodes for high-temperature fuel cells, Nature Materials. 3 (2004) 17–27. https://doi.org/10.1038/nmat1040.

[269] S. Lee, K. Lee, Y. Jang, J. Bae, Fabrication of solid oxide fuel cells (SOFCs) by solvent-controlled co-tape casting technique, International Journal of Hydrogen Energy. 42 (2017) 1648–1660. https://doi.org/10.1016/j.ijhydene.2016.07.066.

[270] T. Suzuki, M. Awano, P. Jasinski, V. Petrovsky, H.U. Anderson, Composite (La, Sr)MnO_3–YSZ cathode for SOFC, Solid State Ionics. 177 (2006) 2071–2074. https://doi.org/10.1016/j.ssi.2005.12.016.

[271] H.J. Ko, J. Myung, S.-H. Hyun, J.S. Chung, Synthesis of LSM–YSZ–GDC dual composite SOFC cathodes for high-performance power-generation systems, J Appl Electrochem. 42 (2012) 209–215. https://doi.org/10.1007/s10800-012-0390-8.

INSTITUTO DE PESQUISAS ENERGÉTICAS E NUCLEARES
Diretoria de Pesquisa, Desenvolvimento e Ensino
Av. Prof. Lineu Prestes, 2242 – Cidade Universitária CEP: 05508-000
Fone/Fax(0XX11) 3133-8908
SÃO PAULO – São Paulo – Brasil
http://www.ipen.br

O IPEN é uma Autarquia vinculada à Secretaria de Desenvolvimento, associada
à Universidade de São Paulo e gerida técnica e administrativamente pela
Comissão Nacional de Energia Nuclear, órgão do
Ministério da Ciência, Tecnologia, Inovações e Comunicações.